

PL-TR-96-2112

GLOBAL IONOSPHERIC WEATHER

Dwight T. Decker
Patricia H. Doherty

Boston College
Institute for Scientific Research
Chestnut Hill, MA 02167

1 June 1996

Final Report
1 March 1993 - 28 February 1996

Approved for public release; distribution unlimited



PHILLIPS LABORATORY
Directorate of Geophysics
AIR FORCE MATERIEL COMMAND
HANSCOM AIR FORCE BASE, MA 01731-3010

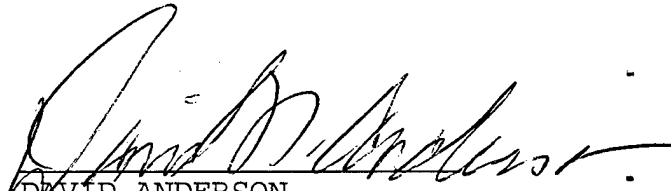
DTIC QUALITY INSPECTED 3

19961002 021

"This technical report has been reviewed and is approved for publication."



JOHN RETTERER
Contract Manager



DAVID ANDERSON
Branch Chief



CHARLES PIKE
Division Director

This report has been reviewed by the ESC Public Affairs Office (PA) and is releasable to the National Technical Information Service (NTIS).

Qualified requestors may obtain additional copies from the Defense Technical Information Center (DTIC). All others should apply to the National Technical Information Service (NTIS).

If your address has changed, if you wish to be removed from the mailing list, or if the addressee is no longer employed by your organization, please notify PL/IM, 29 Randolph Road, Hanscom AFB, MA 01731-3010. This will assist us in maintaining a current mailing list.

Do not return copies of this report unless contractual obligations or notices on a specific document require that it be returned.

REPORT DOCUMENTATION PAGE

Form Approved
OMB No. 0704-0188

Public reporting burden for this collection of information is estimated to average 1 hour per response, including the time for reviewing instructions, searching existing data sources, gathering and maintaining the data needed, and completing and reviewing the collection of information. Send comments regarding this burden estimate or any other aspect of this collection of information, including suggestions for reducing this burden, to Washington Headquarters Services, Directorate for Information Operations and Reports, 1215 Jefferson Davis Highway, Suite 1204, Arlington, VA 22202-4302, and to the Office of Management and Budget, Paperwork Reduction Project (0704-0188), Washington, DC 20503.

1. AGENCY USE ONLY (Leave blank)		2. REPORT DATE 1 June 1996	3. REPORT TYPE AND DATES COVERED Final (1 Mar 1993 - 28 Feb 1996)
4. TITLE AND SUBTITLE GLOBAL IONOSPHERIC WEATHER			5. FUNDING NUMBERS PE 63707F PR 4643 TA GL WUAA
6. AUTHOR(S) Dwight T. Decker Patricia H. Doherty			Contract: F19628-93-K-0001
7. PERFORMING ORGANIZATION NAME(S) AND ADDRESS(ES) Boston College Institute for Scientific Research 140 Commonwealth Avenue Chestnut Hill MA 02167			8. PERFORMING ORGANIZATION REPORT NUMBER
9. SPONSORING / MONITORING AGENCY NAME(S) AND ADDRESS(ES) Phillips Laboratory 29 Randolph Road Hanscom AFB MA 01731-3010 Contract Manager: John Retterer/GPIM			10. SPONSORING / MONITORING AGENCY REPORT NUMBER PL-TR-96-2112
11. SUPPLEMENTARY NOTES			
12a. DISTRIBUTION / AVAILABILITY STATEMENT Approved for public release; distribution unlimited			12b. DISTRIBUTION CODE
13. ABSTRACT (Maximum 200 words) We have studied several issues that are critical for understanding ionospheric weather. Work on global F-region modeling has consisted of participation in the Phillips Laboratory Low-Latitude Ionospheric Tomography Campaign, testing of the Global Theoretical Ionospheric Model (GTIM), and testing of the Parameterized Ionospheric Model (PIM). Analysis of TEC data and comparisons with other ionospheric models had been successfully conducted. A range of issues concerning the use of GPS observations have been studied. The topics have included limitations in determining TEC from dual-frequency GPS measurements, limitations to WAAS, solar cycle dependence of GPS TEC, and the statistics of time rate of change of TEC. Software has been developed to process RINEX formatted GPS data into TEC. Work comparing our electron-proton-H atom model to both observations and other models has been very successful. We have also successfully modeled the creation of polar cap patches and boundary blobs using time varying convection.			
14. SUBJECT TERMS ionospheric weather, global F-region modeling, total electron content, GPS, TEC, tomography, aurora, electron transport, proton-H atom transport, plasma structure, blobs			15. NUMBER OF PAGES 224
			16. PRICE CODE
17. SECURITY CLASSIFICATION OF REPORT UNCLASSIFIED	18. SECURITY CLASSIFICATION OF THIS PAGE UNCLASSIFIED	19. SECURITY CLASSIFICATION OF ABSTRACT UNCLASSIFIED	20. LIMITATION OF ABSTRACT SAR

TABLE OF CONTENTS

1. INTRODUCTION	1
2. GLOBAL F REGION MODELING	1
2.1 Total Electron Content Over the Pan American Longitudes: March-April 1994	1
2.2 Solar Cycle Dependencies in Mid-Latitude Total Electron Content	1
2.3 Improving IRI90 Low Latitude Ionospheric Specification	1
2.4 June 1991 Storm Analysis	2
2.5 Day-to-Day Comparison of Calculated and Observed Electron Densities at Midlatitudes	2
2.6 Theoretical Model Comparisons	9
2.7 Theoretical Modeling of the 1994 Chile/MISETA Campaign	14
2.8 Magnetic Storm Studies	15
2.9 Protonospheric Depletion and Recovery During Geomagnetic Storms	16
3. GPS OBSERVATIONS	21
3.1 Potential Ionospheric Limitations to GPS Wide-Area Augmentation System (WAAS)	21
3.2 Limitations in Determining Absolute Electron Content from Dual-Frequency GPS Group Delay Measurements	21
3.2 Statistics of Time Rate of Change of Ionospheric Electron Content	26
3.3 Ionospheric Corrections to Precise Time Transfer Using GPS	26
3.4 Static Ionospheric Test for the WADGPS Experiment	34
3.5 Ionospheric Measurements Using GPS	41
3.6 Solar Cycle Dependence of Total Electron Content	50
3.7 Absolute Real-Time Ionospheric Measurements from GPS Satellites in the Presence of Anti-Spoofing	53
4. ELECTRON BACKSCATTER AND PROTON PRECIPITATION	53
4.1 Proton-H Atom Transport Model Developments	53
4.2 Upgoing Electrons Produced in an Electron-Proton-Hydrogen Atom Aurora	54
4.3 Collisional Degradation of the Proton-H Atom Fluxes in the Atmosphere: A Comparison of Theoretical Techniques	54
4.4 Incident Proton Spectra: Ionospheric Effects of High-Energy Power Law Tails	54
4.5 Electron-Proton-H Atom Aurora: Comparison With Observations	54
5. MODELING HIGH LATITUDE F REGION BLOBS AND PATCHES	55
5.1 Modeling Polar Cap F-region Patches	55
5.2 Modeling Boundary Blobs	58
6. OPTICAL RADIATION	58
REFERENCES	59
PRESENTATIONS	61
JOURNAL ARTICLES	67

APPENDIX 1	69
Total Electron Content Over the Pan American Longitudes: March-April 1994	70
Solar Cycle Dependencies in Mid-Latitude Total Electron Content	79
Improving IRI90 Low Latitude Ionospheric Specification	83
Potential Ionospheric Limitations to GPS Wide-Area Augmentation System (WAAS)	92
Statistics of Time Rate of Change of Ionospheric Range Delay	110
Upgoing Electrons Produced in an Electron-Proton-Hydrogen Atom Aurora	133
Collisional Degradation of the Proton-H Atom Fluxes in the Atmosphere: A Comparison of Theoretical Techniques	145
Incident Proton Spectra: Ionospheric Effects of High-Energy Power Law Tails	186
Modeling Polar Cap F-Region Patches Using Time Varying Convection	192
Modeling Daytime F Layer Patches Over Sondrestrom	196
Modeling Boundary Blobs Using Time Varying Convection	216

1. INTRODUCTION

The objective of this research is to improve our ability to observe and theoretically model the ionospheric "weather". In this contract, we have studied five issues where we have had the tools and experience to make significant progress. Those issues include: 1) Global F region modeling, 2) GPS observations, 3) Electron backscatter and Proton precipitation, 4) Modeling high-latitude F-region blobs and patches, and 5) Optical Radiation.

2. GLOBAL F REGION MODELING

During this contract, we have been involved in data collection, data analysis, and the testing of the Global Theoretical Ionospheric Model (GTIM) all with the purpose of improving our ability to model the weather of the F region of the earth's ionosphere.

2.1 Total Electron Content Over the Pan American Longitudes: March - April 1994

From 28 March 94 to 15 April 94, Patricia Doherty participated in a major field data collection campaign. Participation included the installation, maintenance and operation of a Magnavox MX1502 Satellite Receiver System in Bermuda for the duration of the campaign. The prime purpose of the campaign was to observe the day-to-day variability of the *equatorial anomaly* using ionospheric tomography techniques. The anomaly region, typically between +/- 25 degrees of the magnetic equator, is that part of the world where the highest values of electron density and TEC occur. Fluctuations in the anomaly can be very intense and can affect high-frequency radio propagation. A summary of the campaign and the work done to date in analyzing the observations is contained in the paper, "Total Electron Content Over the Pan American Longitudes: March - April 1994" by P.H. Doherty, D.N. Anderson, J. Eicher, and J.A. Klobuchar. A copy of this paper is appended to this report (Appendix 1.).

2.2 Solar Cycle Dependencies in Mid-Latitude Total Electron Content

Total Electron Content data recorded at Hamilton, MA, over the last three solar cycles has been analyzed to illustrate short and long term effects of solar activity. A summary of this analysis is contained in the paper "Solar Cycle Dependencies in Mid-Latitude Total Electron Content" by P.H. Doherty and J.A. Klobuchar. A copy of this paper is appended to this report (Appendix 1.).

2.3 Improving IRI90 Low Latitude Ionospheric Specification

At low latitudes a number of comparisons between the International Reference Ionosphere (IRI90) model of F-region electron density profiles with observed profiles measured by the Jicamarca incoherent scatter radar indicate that during the daytime, the observed profile shape is much broader in altitude than that specified by IRI90 while at

night, just after sunset, observed F_2 -peak altitudes are significantly higher. We have worked on using the Parameterized Ionospheric Model (PIM) to develop an option for IRI90 that would improve its specification of the low latitude ionosphere. A summary of this work is given in the paper "Improving IRI90 Low Latitude Ionospheric Specification by A.J. Preble, D.T. Decker, and D.N. Anderson. A copy of this paper is appended to this report (Appendix 1.).

2.4 June 1991 Storm Analysis

The month of June 1991 was a period affected by major magnetic storm activity. There were six sudden commencement storms observed between June 3rd and the 16th. Total Electron Content (TEC) measurements recorded at three Air Weather Service Stations, Hamilton, MA, Kennedy AFB, FL and Ramey, Puerto Rico have been analyzed to observe the effects of this storm activity. These TEC values were obtained from continuous measurements of Faraday polarization changes of VHF radio signals emitted from geostationary satellites of opportunity.

Figure 1 illustrates the results of this analysis. Diurnal curves, from each station, are plotted for June 8th through the 13th. On June 8th, a sudden commencement storm occurred at 1500 UT (1100 LT for these 3 stations). All three stations responded to this activity with an immediate sharp rise in TEC followed by major depletions for the next two days. Continued geomagnetic disturbances resulted in very unusual, but remarkably similar, observations at Ramey and Kennedy through the 13th of June. Observations at Hamilton were also severely disturbed.

From this analysis, we conclude that the severity of the geomagnetic activity resulted in the appearance of equatorial electro dynamic effects as far north as Florida.

These measurements coincided with model results using the low-latitude portion of GTIM. GTIM is a time-dependent, theoretical model which solves the ion continuity equation for the O^+ concentration through production, loss and transport of ionization. Observed vertical drift velocities measured at the Jicamarca, Peru incoherent scatter radar facility during the storm were incorporated into the model to calculate electron density profiles as a function of dip latitude and local time. In Figure 2, we illustrate the results of the model by showing contours of NmF_2 (the F_2 peak density) as a function of dip latitude and local time. Here, the results reveal a strong poleward shift of the equatorial anomaly to as far north as 28 degrees dip latitude. In order to make detailed day to day comparisons with data, it will be necessary to modify GTIM to accept more than 24 hours of drift data. This would then allow the simulation of an entire period of pre-storm, storm and post-storm conditions.

2.5 Day-to-Day Comparison of Calculated and Observed Electron Densities at Midlatitudes

Over the last few years, there has been an increasing effort to validate various theoretical models of the earth's ionosphere. In the work done to date, the focus has been almost exclusively on comparisons between a calculation of a 24 hour day using typical or

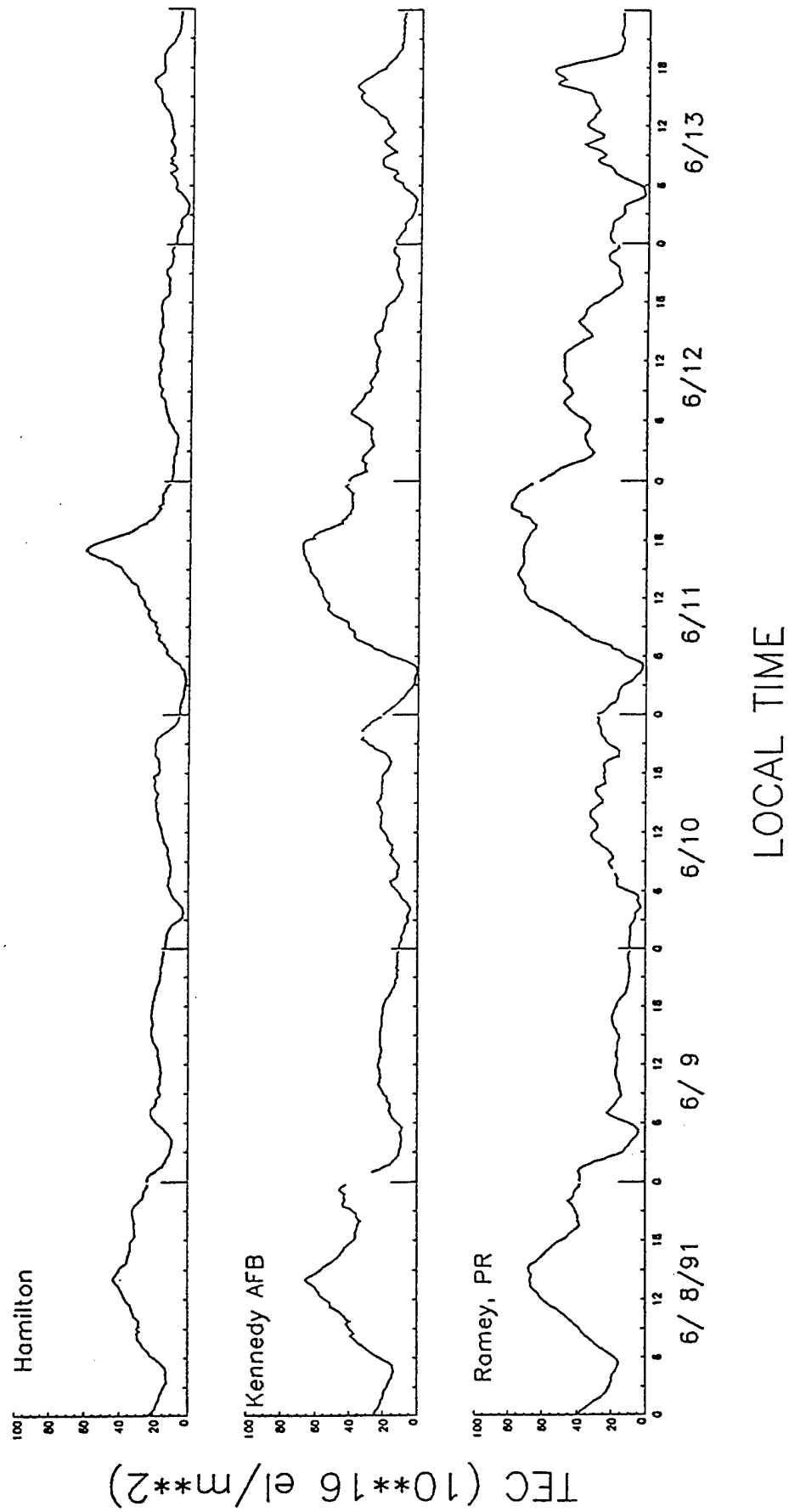


FIGURE 1

AMERICAN SECTOR - JUNE 13, 1991 - DISTURBED CONDITIONS

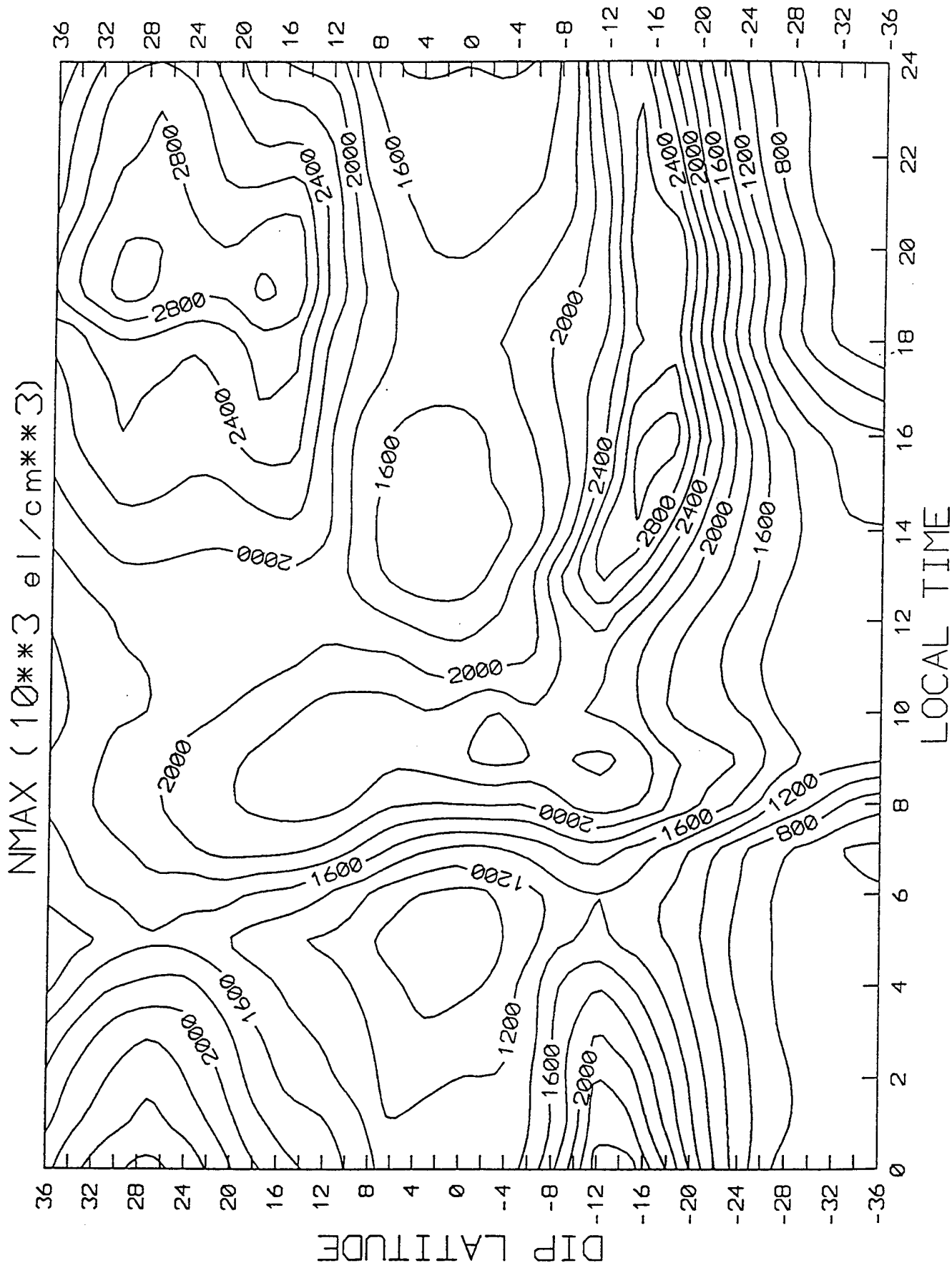


FIGURE 2

average inputs with either monthly means of observations or data from a "typical" quiet day. But, there is growing interest on how well the day to day "weather" of the ionosphere can be modeled. With that in mind, we have simulated the day to day variations for May and December 1990 at Wallops Island, Virginia.

Our initial goal was to simply see how good or bad a job GTIM does at simulating the day-to-day variability when the model is driven by statistical or empirical geophysical inputs. A follow on goal was to see how much of any discrepancy between data and theory can be understood in terms of uncertainty in the geophysical inputs. The data we used were the hourly F_2 peak parameters from digisonde measurements made at Wallops Island. GTIM is a one species F-region model that solves the ion continuity and momentum equations. In such a model, it is the day to day variation in the required geophysical inputs that causes a day to day variation in the model output. This variation in the geophysical inputs is determined by the variability in the F10.7 cm solar flux and the daily magnetic index A_p .

Of all the required geophysical inputs, it is the neutral wind that we suspect is our greatest source of day to day variability. Thus, we have simulated the entire months of December and May using three different neutral wind models. The first simulation used HWM-87 and the second used the VSH wind model. The third simulation used the approach of treating the wind as a free parameter and requiring that the model reproduce the observed $h_m F_2$. In Figure 3, we show for the first twelve days of December, 1990 the observed $N_m F_2$ compared to the results from the three simulations. The solid curve is the data, the long dashed curve is the HWM-87 simulation, the middle dashed curve the VSH results, and the shortest dashed curve is from fitting to $h_m F_2$. We see that the HWM-87 does the best, though all three simulations reproduce the gross features of the diurnal behavior. None of the simulations seem to follow the day to day variability especially around and just before noon. The fact that none of these simulations seem to follow what day to day variability there is leads us to suspect that for this month we cannot understand that variability simply in terms of uncertainties in the neutral wind.

Turning to May, we see dramatically different results. In Figure 4, we show for the first twelve days of May 1990 the observed $N_m F_2$ (solid curve) compared to a simulation using HWM-87 (dashed curve). We see that in both the data and the theory there is much less diurnal variation than in December, however the model results are obviously much too large. On some of the quieter days (day 2 and days 5-8) the data and model are in closer agreement but on magnetically active days such as days 10 and 11 the model has major difficulties. On all days, we see that the model maintains $N_m F_2$ right through until after midnight whereas on several of the days the observations show a definite decrease in $N_m F_2$ through out the pre-midnight period. In looking at the effects of different wind models, we find that the VSH model makes little difference. The results of fitting to $h_m F_2$ are shown in Figure 5, and while on certain days this procedure does produce a decay of $N_m F_2$ in the pre-midnight period, there are days in which the model still has severe problems. We conclude that the empirical geophysical inputs are simply inadequate during magnetically active periods. In particular, the problem is not confined to just the neutral winds but mostly likely involves the neutral densities and temperatures as well as possibly the electric fields and plasma temperatures.

Thus we conclude that while a GTIM driven by statistical or empirical geophysical inputs produces a day to day variation, that variation appears to have little to do with the

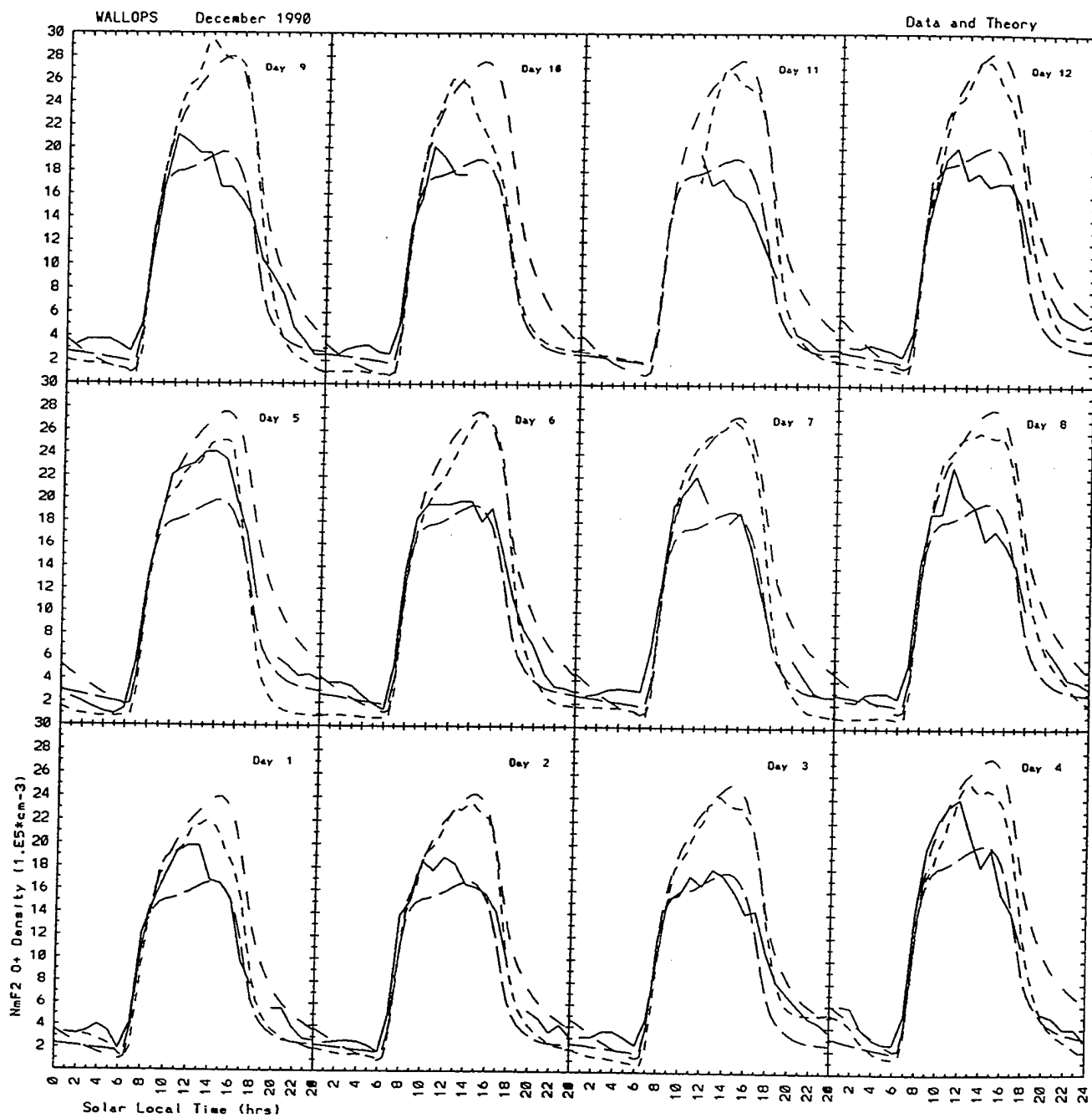


FIGURE 3

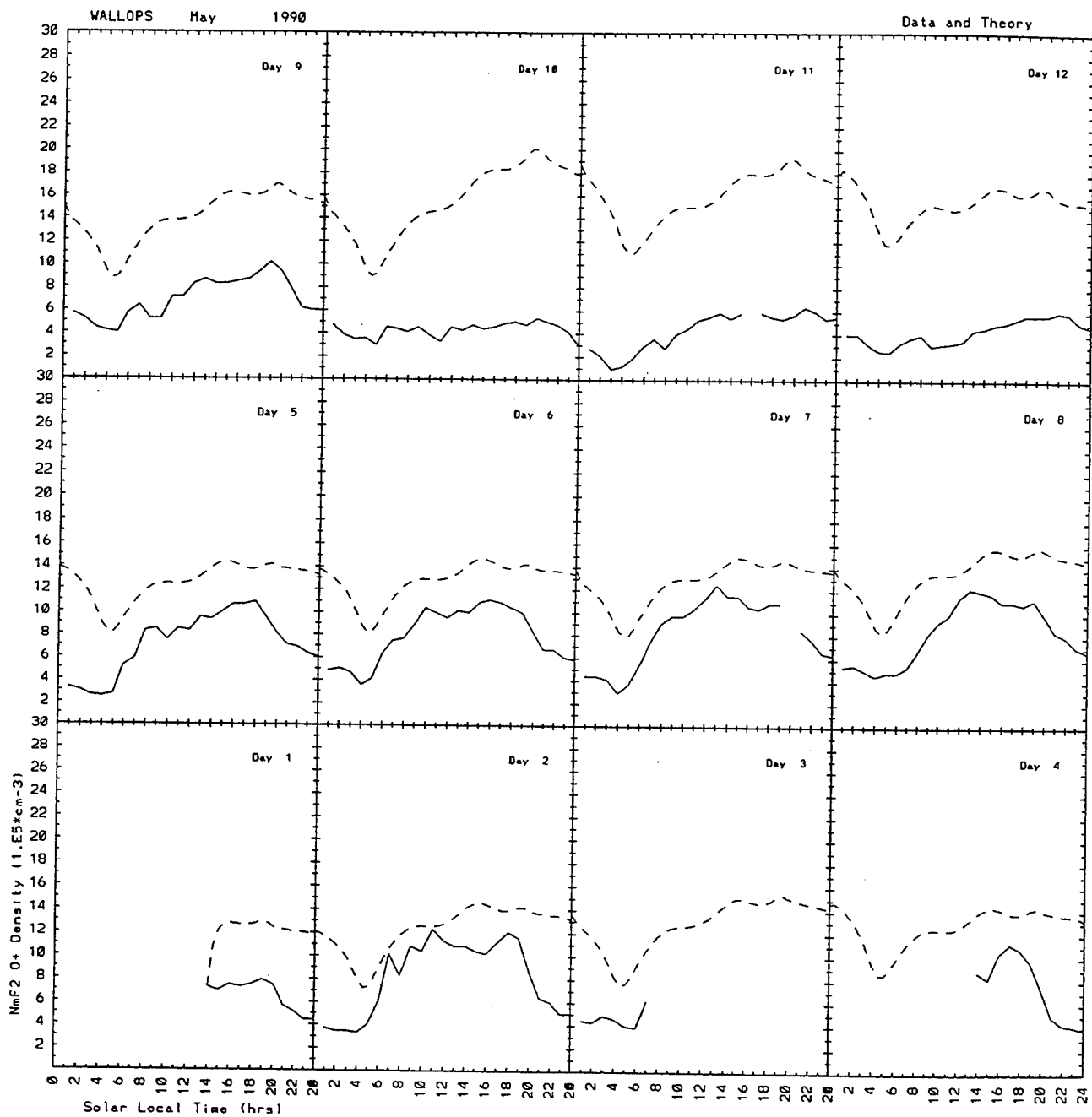


FIGURE 4

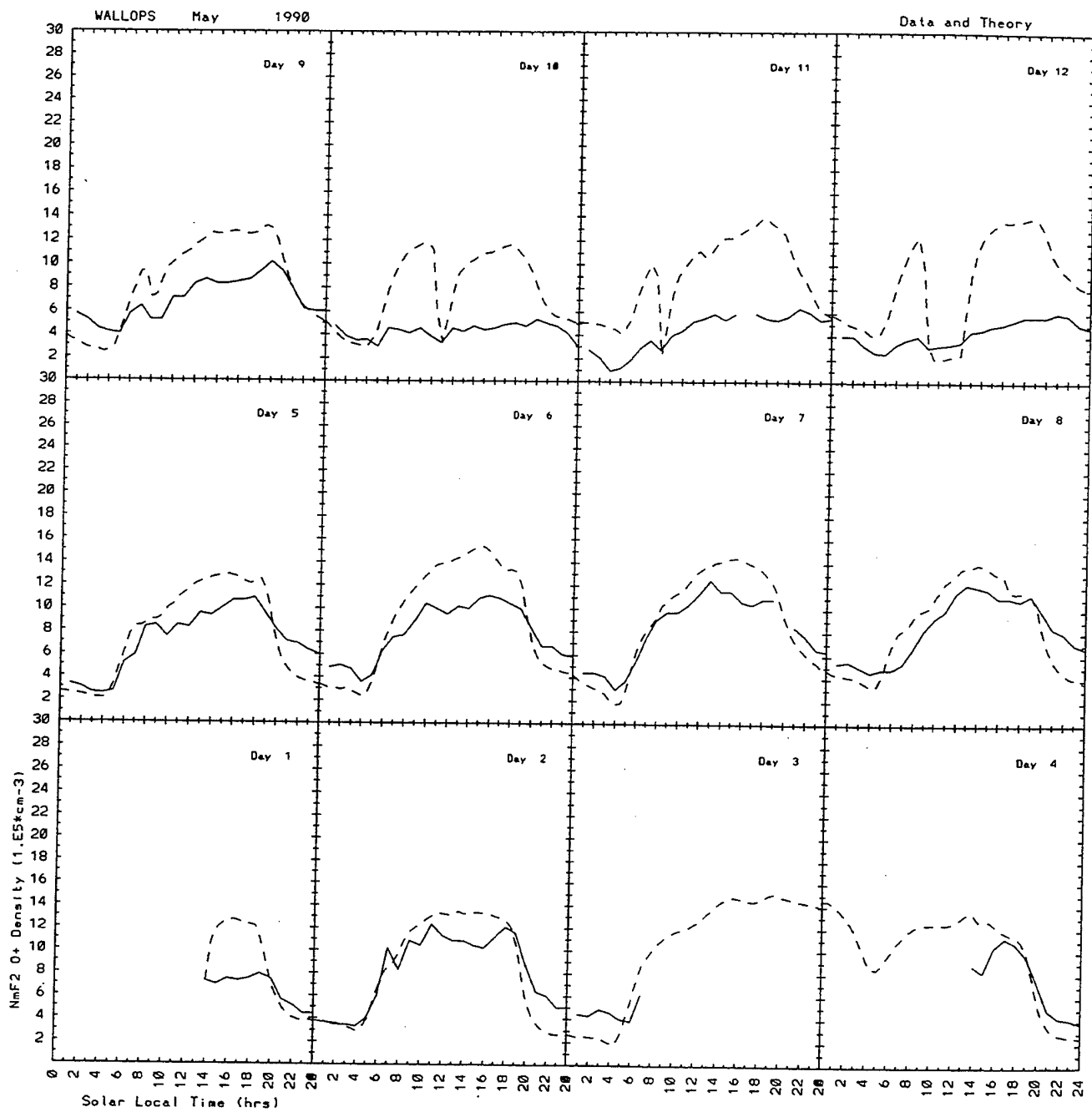


FIGURE 5

observed variations. For any specific day, we find that the observed monthly median or the GTIM calculated median is likely to be a better predictor than that day's GTIM simulation.

2.6 Theoretical Model Comparisons

As part of our effort in global modeling, we have taken part in the PRIMO workshop that has been held at the last several annual CEDAR meetings. One outcome of those meetings is that the five modeling groups involved are now working on a paper on the "Intercomparison of Physical Models and Observations of the Ionosphere". For that paper, we have begun a careful comparison between our global theoretical ionospheric model (GTIM) and the Utah State University's time dependent ionospheric model (TDIM).

As a first step in this study, we chose to compare the model's inputs at three altitudes (125, 250, and 400 km) at each UT hour for a calculation at Millstone Hill under solar maximum winter conditions. Initially the only large difference was in the source functions at 125 km. Upon examining the entire source profile from GTIM, we found an unreasonably large increase below around 125 km. This increase was the result of round off problems in the implementation of the Chapman function for calculating column densities at large solar zenith angles. This problem has now been solved and we find that all the inputs agree to within a few tens of percents.

We also began a comparisons between GTIM and the Space Environment Lab's coupled thermosphere/ionosphere model (CTIM). As is evident from its name, CTIM couples the neutral and ionized atmospheres and hence calculates ion densities as well as neutral densities, temperatures and winds. In contrast, GTIM calculates ion densities, but the neutral quantities have to be supplied as inputs. Typically those inputs come from empirical models such as MSIS-86 and HWM-87. As a first step in our study, we compared a standard GTIM run to both a CTIM run and observations. In Figures 6 and 7 we show standard runs for December 22 1990 compared to the median for the month at Millstone. The solid curve is the data, GTIM results are the long dashed curve, and CTIM results are the short dashed curve. Figure 6 shows the density of the peak of the F_2 region (NmF_2) and Figure 7 shows the altitude of the F_2 peak (HmF_2). The agreement between models and between models and observations is fairly typical of what we have seen in earlier work.

In order to make a more precise comparison between the ionospheric calculations of the two models, it is necessary to use the neutral quantities calculated by CTIM as the neutral inputs to GTIM. When we examine the neutral winds, densities, and temperatures calculated by CTIM, we find the winds weaker, the densities lower, and the temperatures cooler than the empirical models used by GTIM. In Figures 8 and 9 we present the results of using the CTIM quantities as the inputs for GTIM. The solid curve gives the CTIM F_2 peak results and the dashed curves are the various GTIM results. The longest dashed curve is the standard GTIM calculation where the neutral densities, temperatures, and winds come from empirical models. The curve of shortest dashes is the GTIM results where all the neutral quantities come from CTIM. The intermediate dashed curve is the GTIM calculation that used CTIM neutral winds but MSIS86 neutral densities and temperatures. We see that using the CTIM winds enhances the NmF_2 in the afternoon

MILLSTONE December 22 1990

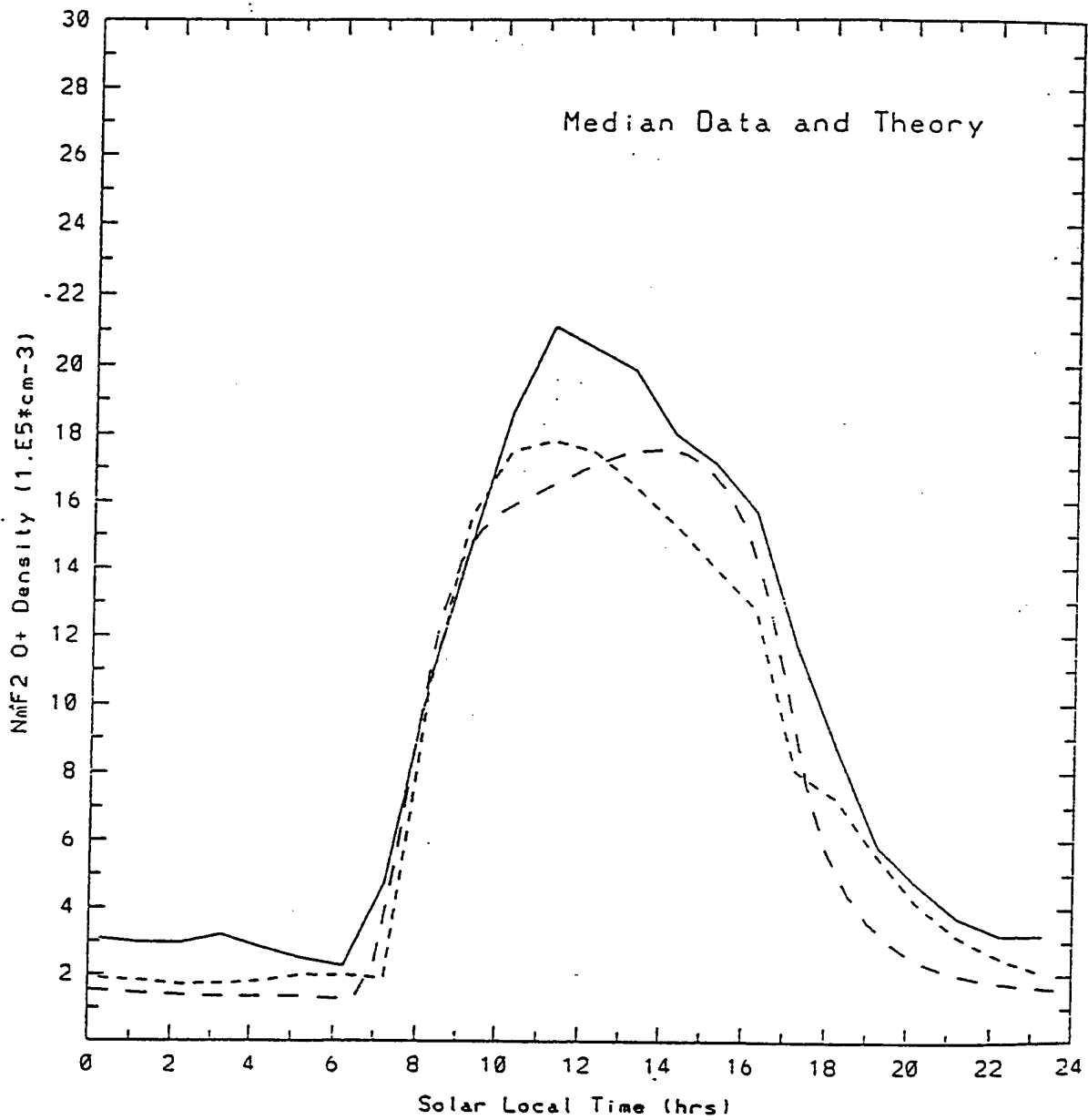


FIGURE 6

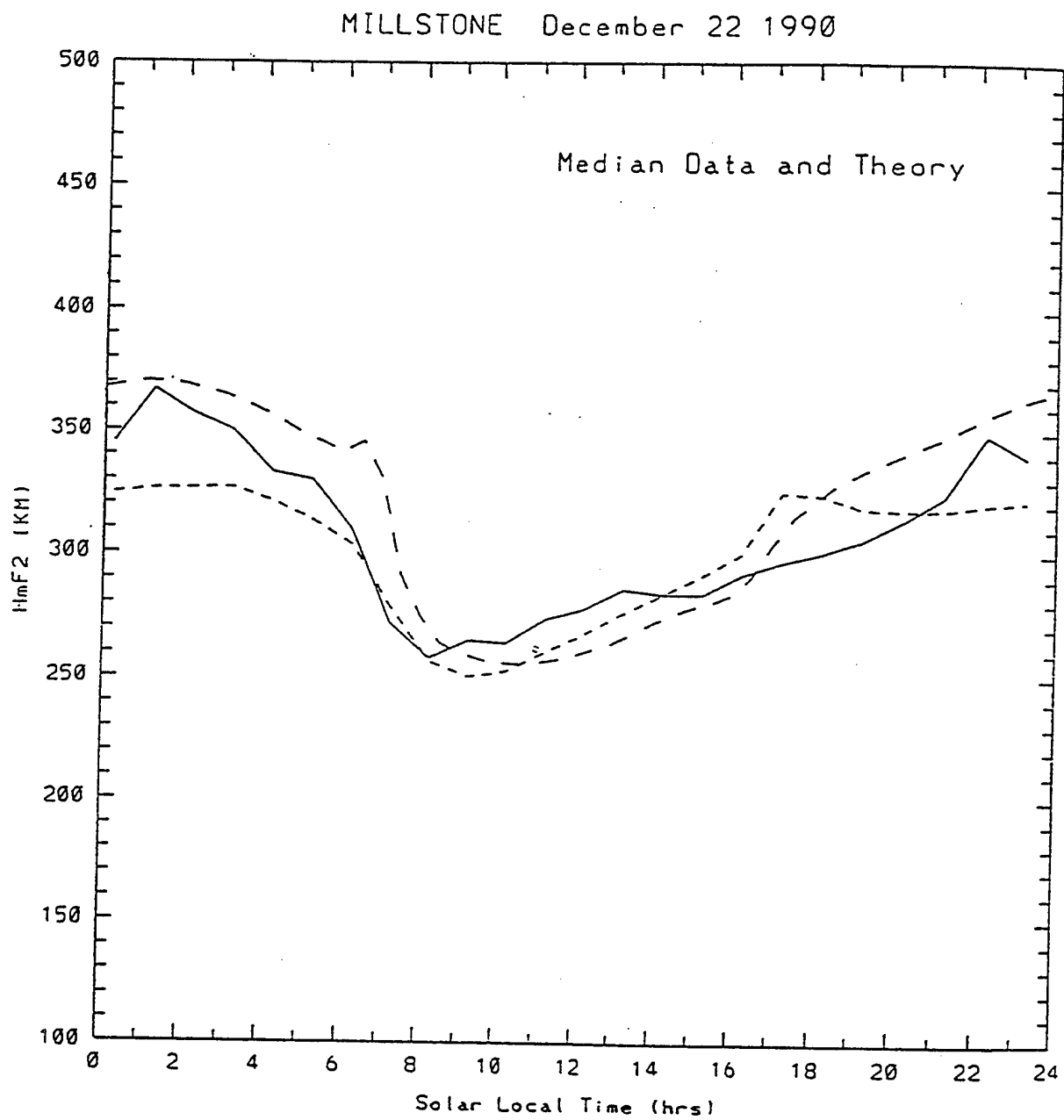


FIGURE 7

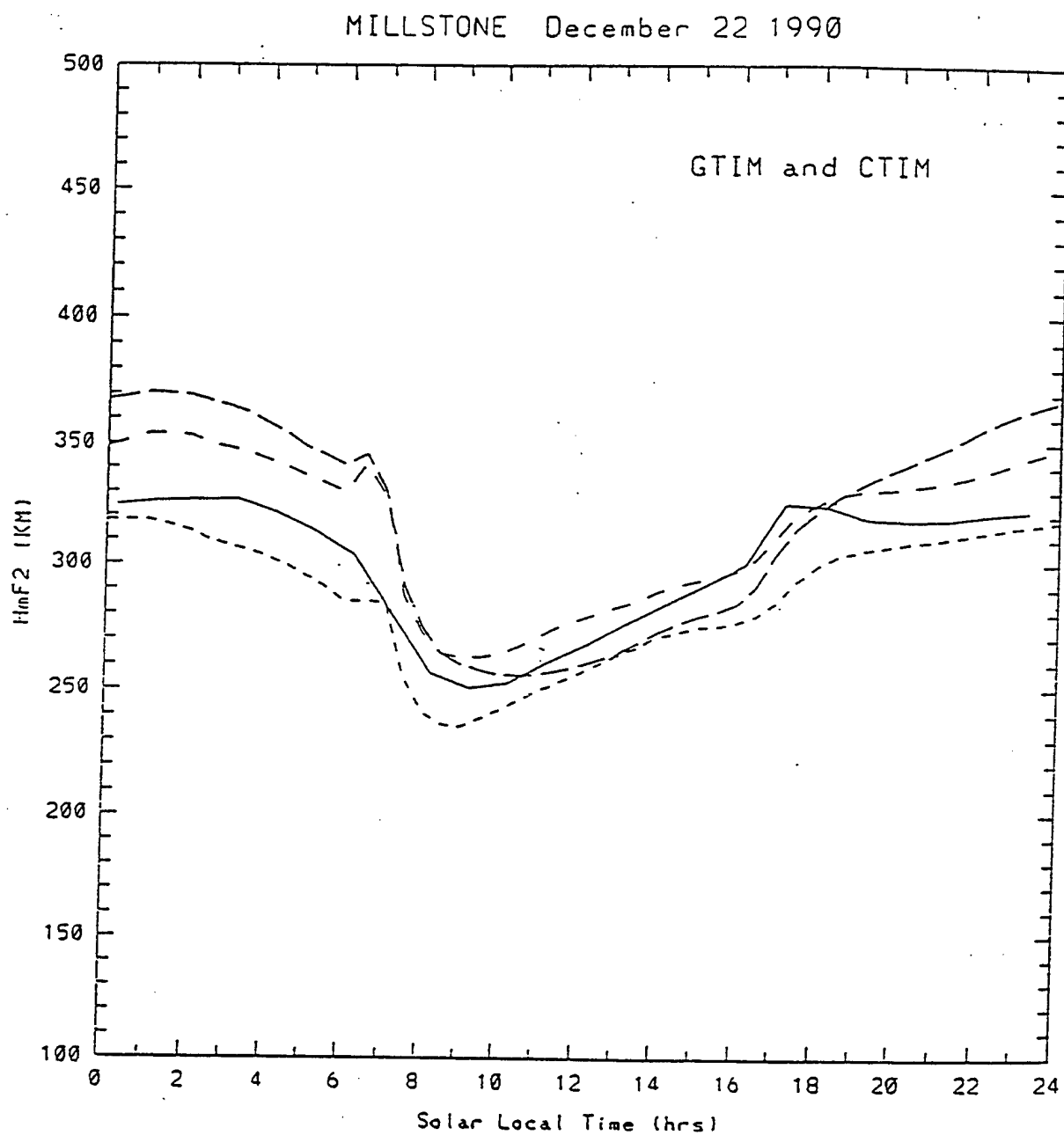


FIGURE 8

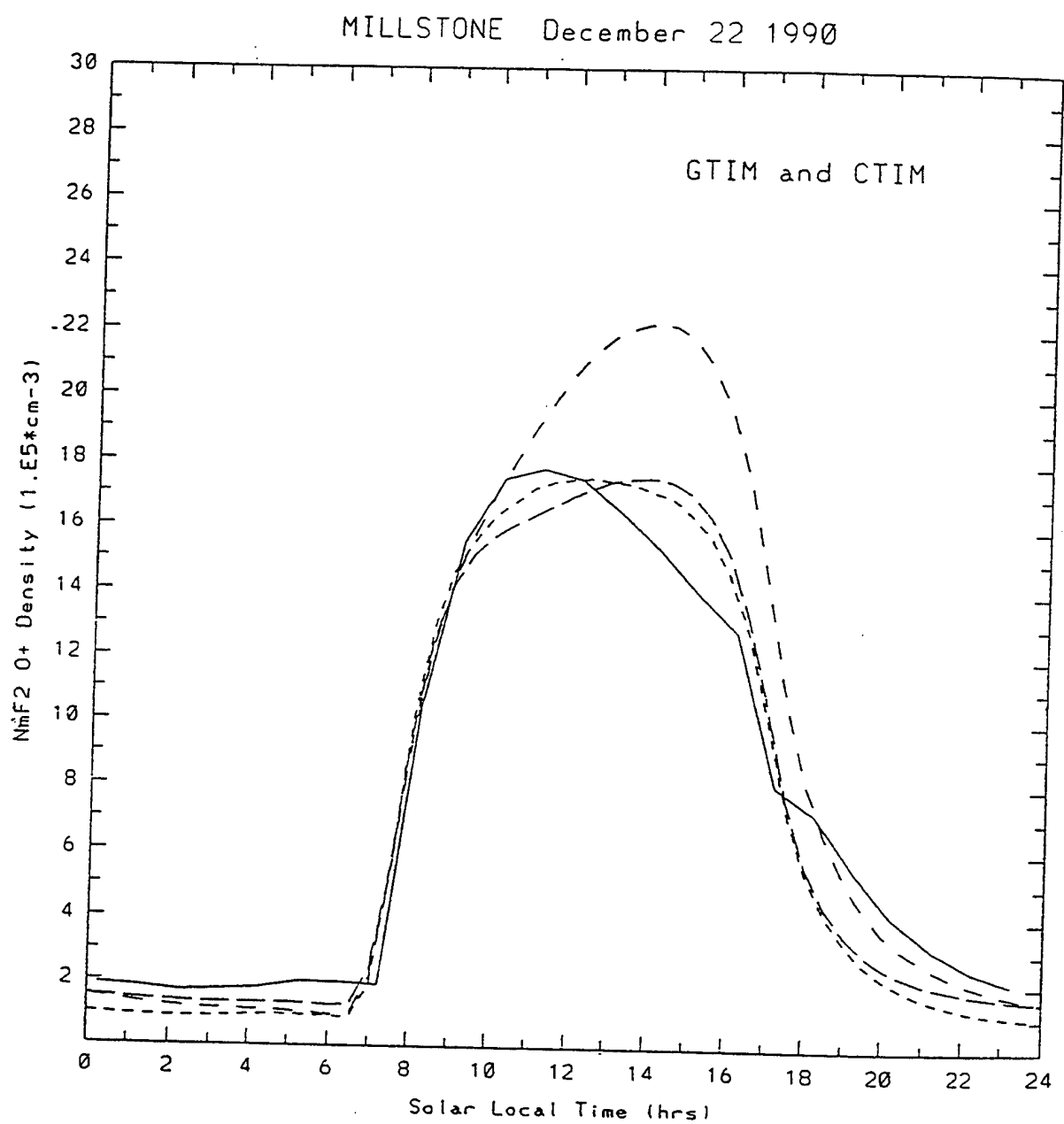


FIGURE 9

leading to poorer agreement between GTIM and CTIM. However using all the CTIM neutral quantities brings the models back into much better agreement.

While using all the CTIM neutral quantities as inputs for GTIM leads to better agreement, differences do remain between the models especially in the afternoon and early evening. Calculations performed using non-zero fluxes at the top boundary indicate that GTIM F_2 peak results are sensitive to this boundary condition. Thus we should use boundary fluxes that are consistent with what is occurring within CTIM. Also, if H^+ is important at the top altitude then either the boundary in GTIM should be lowered or the GTIM boundary flux should include the H^+ flux as well as the O^+ flux.

2.7 Theoretical Modeling of the 1994 Chile/MISETA Campaign

During the Chile/MISETA campaign, 27 Sept. to 3 Oct. 1994, a number of ground-based and satellite-borne instruments obtained data on electron density profiles, neutral wind velocities, vertical and horizontal ExB drift speeds, optical and radar signatures of equatorial bubbles and spread F/scintillation occurrences. We have performed a series of simulations of specific days from this campaign. In our first simulations, we used the Global Theoretical Ionospheric Model (GTIM) to calculate the ambient ionospheric conditions on Sept. 29 and 30, 1994. We compared with Jicamarca digisonde, Aqua Verde digisonde, and DMSP insitu observations. We also calculated flux-tube integrated generalized Rayleigh-Taylor growth rates for these two days.

The inputs for the simulations were from our standard set of empirical models. The one exception was the vertical ExB drift inputs which were based on the Jicamarca incoherent scatter radar observations of Sept 29 and 30. On Sept. 29, the observed post sunset drift was smaller than the averaged drift. On Sept 30, just the opposite was the case. On both days the calculations using the observed drifts produced hmF_2 s that were in better agreement with Jicamarca digisonde observations than calculations using average drifts. On the other hand the agreement with the F_2 peak parameters measured at Aqua Verde was poor. At 860 km, GTIM showed a similar shape in latitude as compared to DMSP insitu measurements, but well overestimated the observed magnitudes of the electron density.

Spread F was observed on Sept 30 but not on Sept 29. Calculations of the NRT growth rates were qualitatively consistent with this observations. On Sept 29, the shortest calculated e-folding time was 36 minutes at around 1900 mlt whereas on Sept 30 it was 9 minutes.

For the next set of simulations, we made several improvements to the low latitude portion of GTIM. We reorganized the selection of L shells so that the model is more robust and no longer requires that the net vertical drift over 24 hours be zero. We began using the Brace and Theis electron temperature model rather than a parameterized Millstone solar minimum electron temperature. In our linear growth rate calculation, we modified it to include the ratio of the F region Pedersen conductivity to the total Pedersen conductivity. Finally, we also added for each fluxtube the calculation of the integral over time of the growth rate. This was included to give us a parameter that would give a measure of both whether you had a positive growth rate and whether it was positive for long enough time to allow for significant growth of some initial perturbation. This was previously used as a diagnostic parameter by Kelley and Maruyama in a paper on a diagnostic model for equatorial spread F.

Simulations were performed for four days of the campaign. The agreement with digisonde measured F_2 peak parameters at Jicamarca was good. To the south closer to the anomaly, we found fair agreement with the F_2 peak parameters measured at Agua Verde. In particular, our improved electron temperature input produced much better agreement with NmF_2 in previous simulations. We also compared with vertical TEC measurements from TOPEX and found consistent agreement. By this we mean that while the observations were never directly within the Jicamarca meridian, the simulations were consistent with the character of the orbit to orbit variations seen by TOPEX.

The growth rate calculations were qualitatively consistent with the spread F observations. When spread F was observed the rates were larger and they were smaller when no spread F was observed. However, no clear difference was seen between the day that had weak bottomside spread F versus the day that had the large plumes extending to above 1000 km.

On two days of the campaign, the vertical drift data ends at around 1900 local time when spread F was observed to begin and the radar was switched into a different mode. Using the observed drift as an input to the model lead to reasonable agreement with the digisonde measured F_2 peak parameters before 1900 hours, however after this time there was poor agreement especially for hmF_2 . For both days, hmF_2 was seen to increase at between 20 and 24 hours. We decided to model this behavior by using the vertical drift as a free parameter during those times that drift measurements were unavailable. The point was not to claim that we are inferring the actual drift but to simply use the drift as a convenient parameter for fitting the observed hmF_2 . Our goal was to see how our growth rate calculations who be effected if the model more closely followed the observed F_2 peak behavior at Jicamarca. In both cases, the effect was to have the growth rate increase again after it had fallen off from its earlier high around 1900 LT. The integral of the growth rate was able to climb to over 5 e-foldings. This represents a factor of 148 increase over any initial perturbation. While this was suggestive of spread F activity, it was not as large as the 10 e-foldings seen by Kelly and Maruyama.

We also examined neutral wind data from Arequipa and found that it will be quite difficult to use as an input to the model. The problem is that it provides wind only for one location over a limited time, whereas the model needs winds over 24 hours at a large range of latitudes. How to integrate this type of data with a global wind model is an open question especially when the data is very different from what the empirical wind model predicts. We performed one calculation using a very simple merging of wind data and model. The results showed as expected that the neutral wind is a crucial parameter however the agreement with observations was poorer than when using the normal empirical wind model.

2.8 Magnetic Storm Studies

The Federal Aviation Administration (FAA) Satellite Program Office is developing a Wide Area Augmentation System (WAAS) based on the GPS system. It is intended to support enroute through precision approach flight operations. In this quarter, we have continued to study potential ionospheric effects on GPS signals that would have a major impact on the precise ranging requirements of WAAS. In order to determine "worst case"

ionospheric gradients which the WAAS Stations might encounter, we looked into ionospheric range delay changes during all the geomagnetic storms for which we could find data for the last solar maximum period. Unfortunately, we only had consistent, well calibrated TEC data from four east coast North American stations. From this data base we have attempted to assemble a “composite worst case” storm for analysis. It is important to note, however, that each geomagnetic storm has its own characteristics. This “composite worst case” storm is based on the major geomagnetic storm that occurred in March 1989. Figure 10 illustrates the March 1989 storm in which TEC measurements made for a six day period from the four east coast North American stations are shown. The storm onset occurred late on 12 March. Note the large, short lived TEC increase seen at the Ramey, Puerto Rico station late on March 13. Also, note that the data from the Kennedy AFB, FL station indicated a large increase, but that the most important portion, near 00 hours on 14 March UT, is missing. The Kennedy data is missing during that important period due to the extremely strong scintillation on the VHF signal from the geostationary satellite of opportunity being used to make these TEC observations during that period. The strong VHF scintillation which precluded the measurement of TEC at the Kennedy AFB site during that time, doesn’t imply that scintillation would have occurred on GPS frequencies.

An example of ionospheric range delays, in units of meters at L1, over the Continental United States (CONUS), for a quiet ionosphere, is shown in Figure 11. These contours are quite smooth and the operational WAAS would not have trouble in transmitting ionospheric range delays and their nominal errors to aircraft in this average environment. Figure 12 shows ionospheric range delay contours, also in units of meters of range delay at L1, during the major geomagnetic storm which occurred in March 1989. Note the large gradient south of the island of Cuba. Also shown in Figure 12 are the 5° station spacing grid points which an operational WAAS would have. Note that much of the entire large gradient in ionospheric range delay is between the grid points, and likely would be missed in determining the ionospheric delays and their errors. While this large gradient did not occur over the CONUS region, it very well could have. The reasons that this gradient occurred equatorward of the CONUS are complex, but likely are because the March 1989 storm was so severe that the largest effect, normally coming from solar particle precipitation into the auroral region, and large electric fields which drive the ionization to great heights in the ionosphere, were so intense that the largest effect was seen equatorward of the CONUS. For more moderate storms the effect would likely be smaller, and would be expected to occur further away from the equator. This storm was one of a severity which occurs once or twice during each 11 year solar cycle.

In order to sort out the effects of magnetic storms as a function of time after storm onset, differences were taken of the equivalent ionospheric range delay during a storm, minus average conditions. A plot of those differences for the Kennedy, MA station is shown in Figure 13. Note that, while the departures from average behavior are greatest during the afternoon of the day of the storm, smaller differences from average conditions still are evident several days after the storm.

2.9 Protonospheric Depletion and Recovery During Geomagnetic Storms

In the 1970’s a unique ATS6 radio beacon experiment was conducted to measure the total electron content, N_T , along the slant path from the satellite to several ground

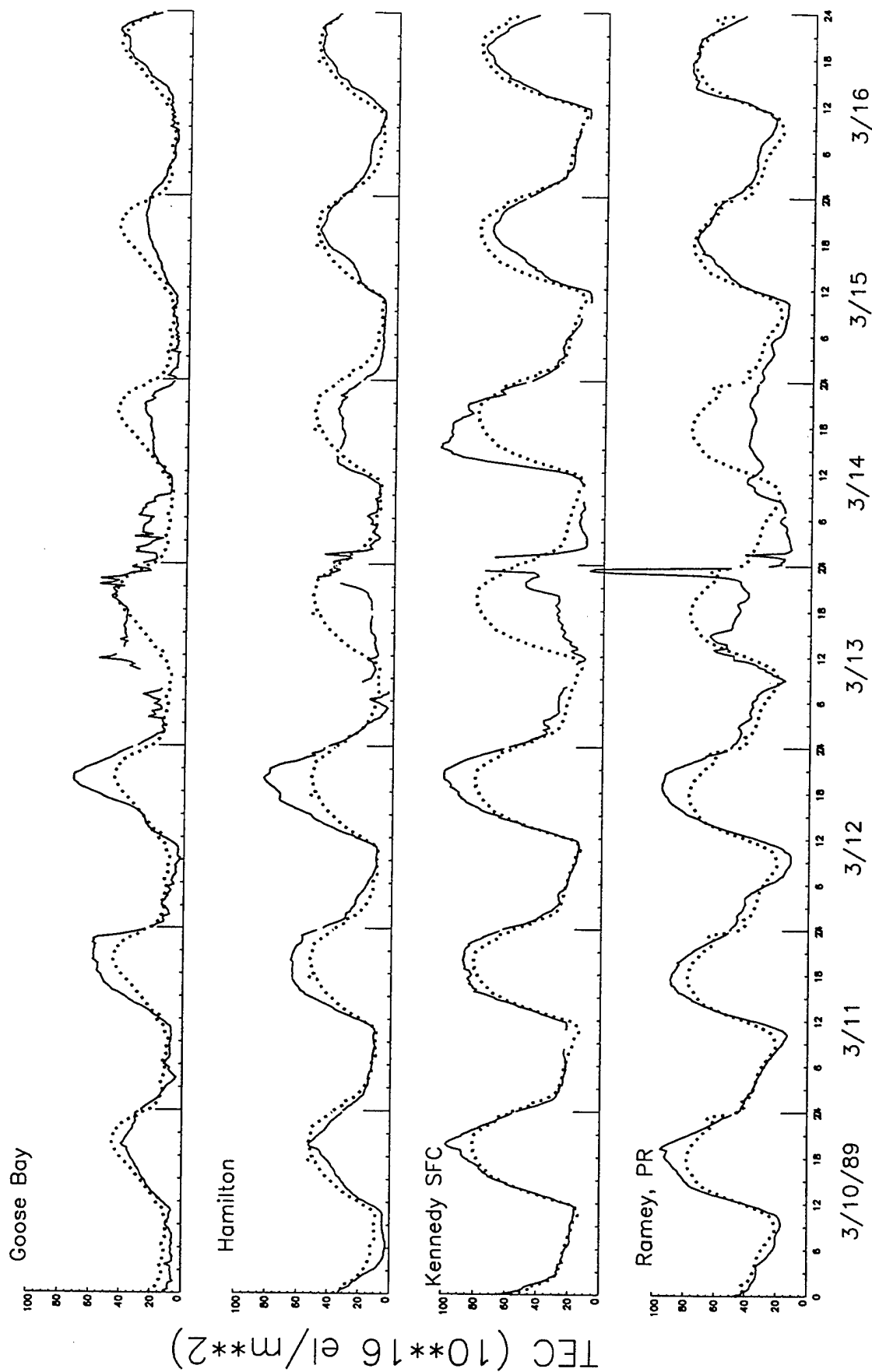


FIGURE 10

UNIVERSAL TIME

DISTURBED IONOSPHERE (MARCH 1989, F10.7=207.2, UT=20:00)

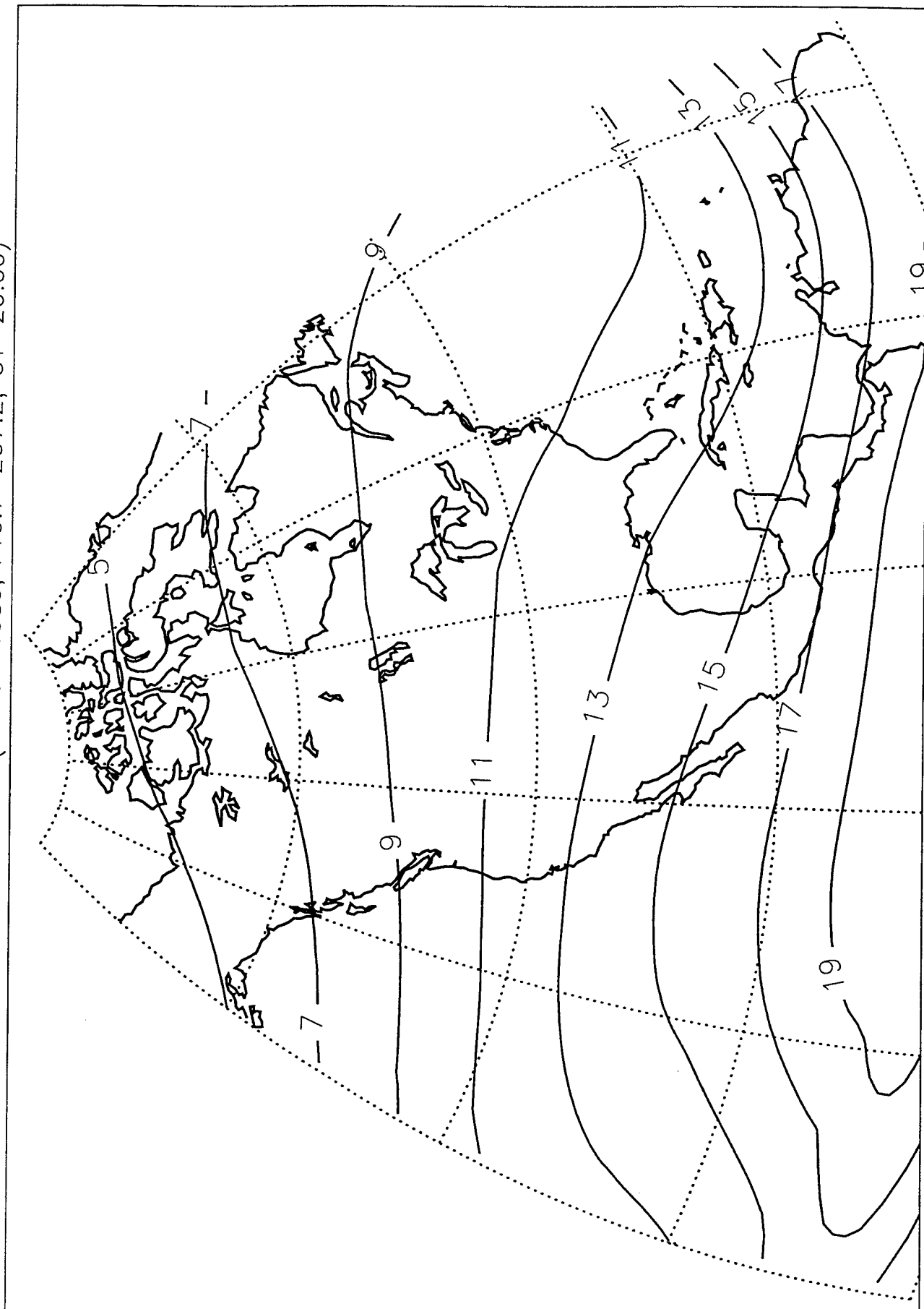


FIGURE 11

DISTURBED IONOSPHERE (MARCH 1989, F10.7=207.2, UT=20:00)

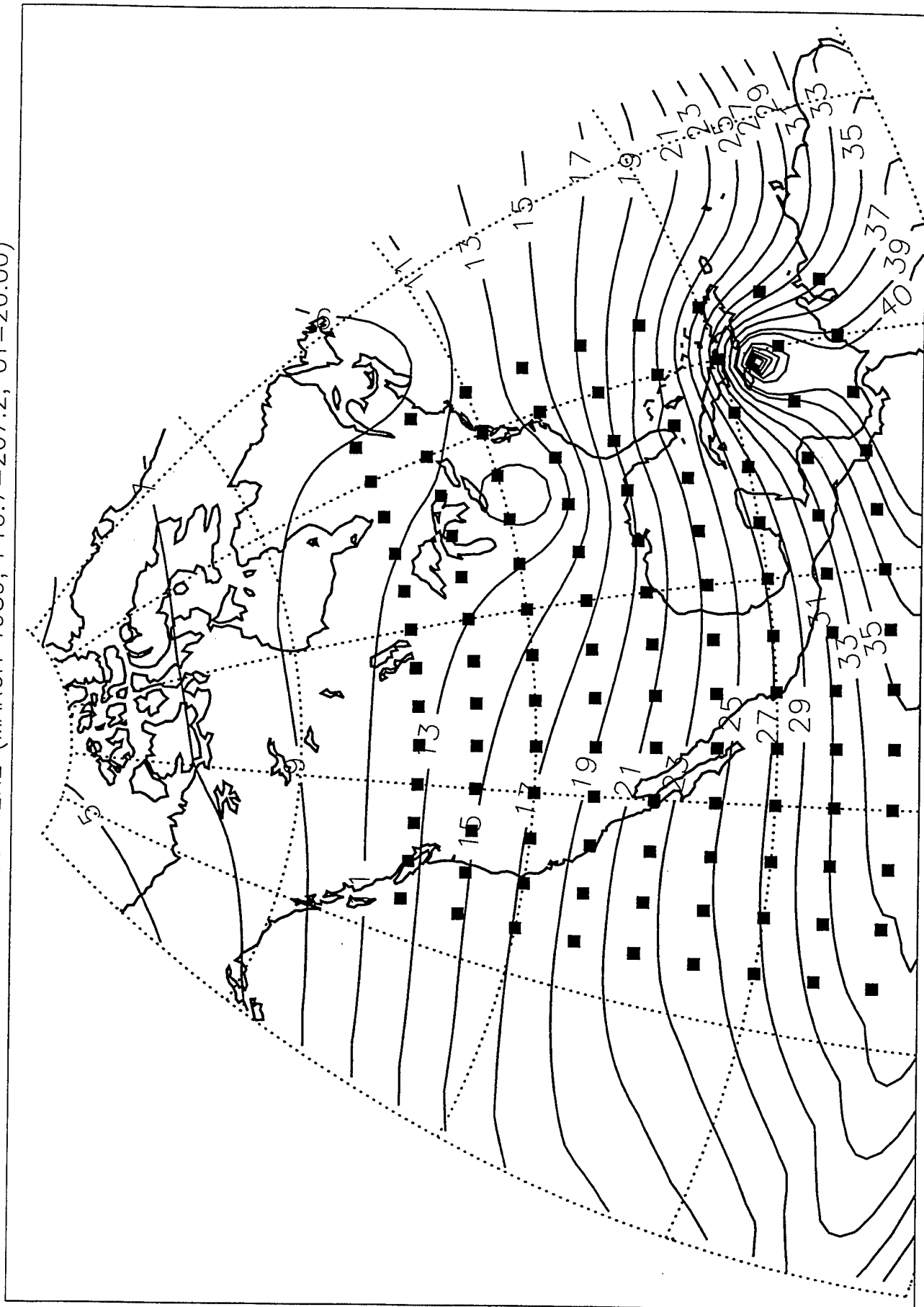


FIGURE 12

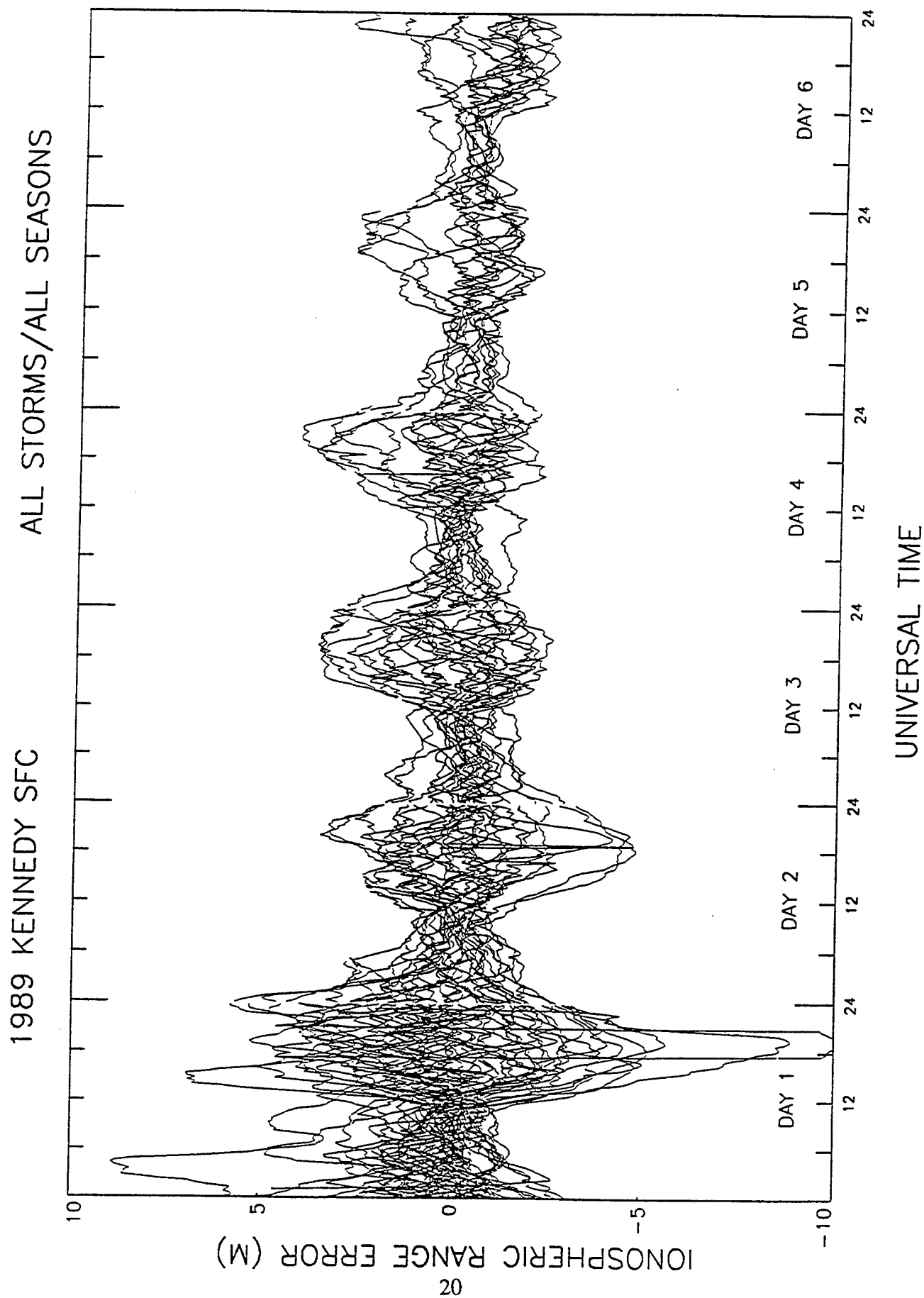


FIGURE 13

receiving stations and also the so-called Faraday content, N_F , along the slant path, typically up to an altitude of ~2000 km. The difference between simultaneous measurement of N_T and N_F yields the protonospheric contribution to total electron content, N_P . Prior research by *Kersley and Klobuchar*, [1980], have shown that the measured protonospheric contribution to TEC and its variation are sensitive functions of the ray path L shell geometry. Comparing the average response of N_P to several geomagnetic storms, measured for three different geometry's at Hamilton, MA, Boulder, CO and Aberystwyth, Wales, *Kersley and Klobuchar* have found that the greatest absolute depletions from average levels occur at stations for which the transmission path intersects the lowest L shell and the recovery time is ~6-8 days.

Much effort has been made to correct and analyze data recorded at another L shell ray path, (ATS6 to Palehua, HI), during another phase of this experiment and to compare the results with earlier research. Figure 14 illustrates this unique ray path. It is unique in the sense that it is almost traverse to the L shells, unlike in the previous study of *Kersley and Klobuchar* where the ray path becomes tangential to some L shell. To study the protonospheric content measured from Hawaii, nine significant geomagnetic storms with sufficient quiet periods between them were selected. Figure 15 represents the results of this analysis to date. This is a superposed epoch analysis, in which departures from mean behavior in N_P are plotted for several days following a storm period. Day one for each storm was selected as the day in which a significant change from mean behavior was exhibited in N_P . This figure illustrates a slow recovery period of approximately 6 days at this location. This study is still in progress but initial conclusions concur with earlier research in that absolute departures from mean behavior in N_P are higher at lower L shells.

3. GPS OBSERVATIONS

3.1 Potential Ionospheric Limitations to GPS Wide-Area Augmentation System (WAAS)

One of the potential limitations of the FAA's GPS Wide-Area Augmentation System (WAAS) is the differential ionospheric range delay over the area of visibility of various GPS satellites used in determining range and velocity (range-rate). With this in mind, we have studied the correlation distance of differences in ionospheric time delay, which is proportional to the total electron content (TEC) of the ionosphere. A summary of our findings can be found in the paper "Potential Ionospheric Limitations to GPS Wide-Area Augmentation System (WAAS)" by J.A. Klobuchar, P.H. Doherty, and M. Bakry El-ARINI. A copy of this paper is appended to this report (Appendix 1.).

3.2 Limitations in Determining Absolute Electron Content from Dual-Frequency GPS Group Delay Measurements

The greatest problem in determining absolute TEC using GPS is in the calibration of the satellite differential group delay offsets. This value is called Tgd , and can be over 10^{17} el/m², or 10 TEC units. Several ionospheric research groups have made estimates of the

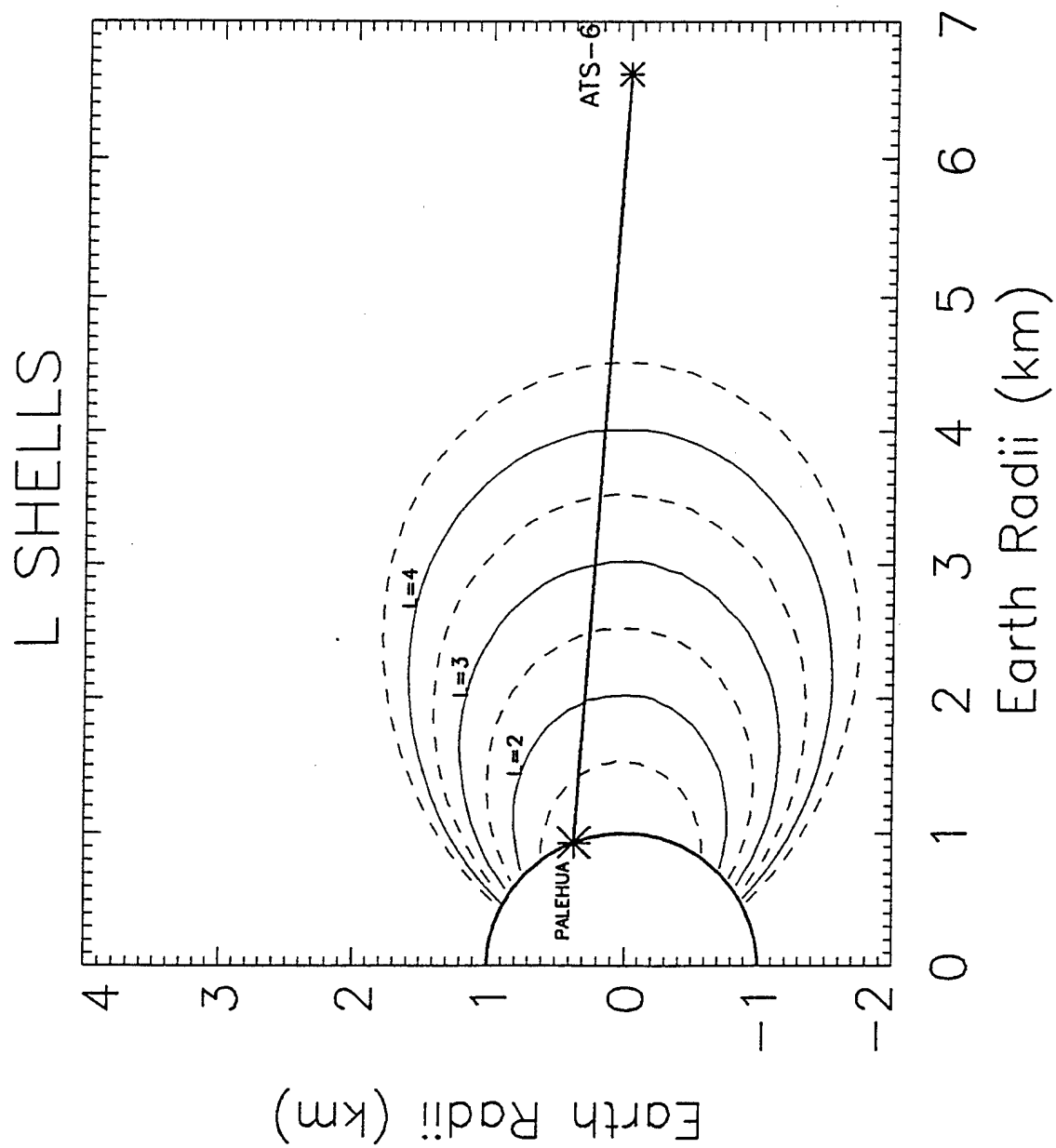


FIGURE 14

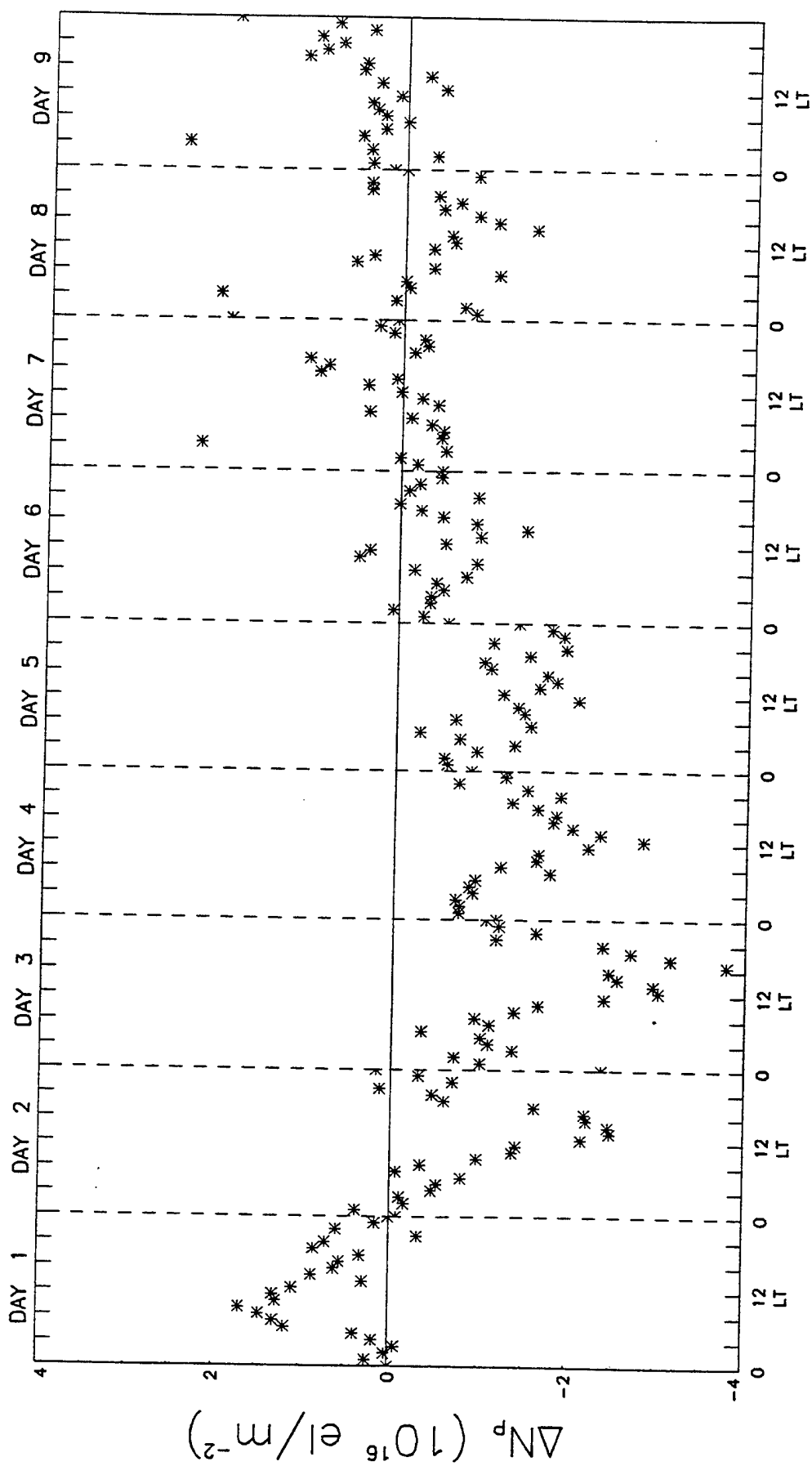


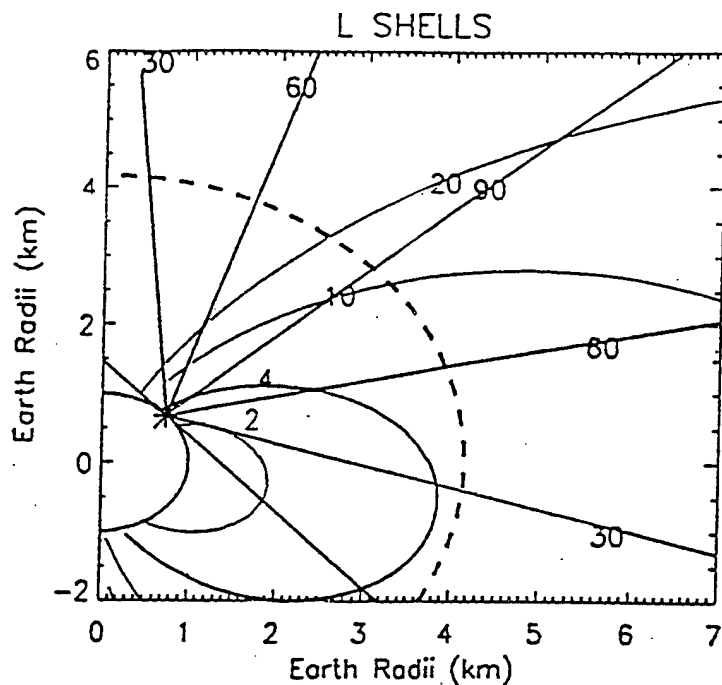
FIGURE 15

T_{gd} values for the various GPS satellites. All studies have implemented different methods to obtain the T_{gd} values and there are apparent discrepancies among the results. Over the last year, work has been done to suggest a new method of determining GPS satellite T_{gd} .

All of the methods of determining T_{gd} used by workers to date have implicitly neglected the effects of the electrons in the earth's protonosphere in their attempts to determine these values. They have all, in some form or other, used an ionospheric "shell" model, which does not include the contribution to electron content of the earth's protonosphere in different viewing directions during a typical GPS satellite pass. However, it is well known that the relative effects of the electron content of the earth's protonosphere can be up to 50% of the entire TEC during the nighttime, and 10% of the TEC during the day, *Davies, et al., 1980*. Since a typical GPS satellite observed from a station covers a widely different portion of the protonosphere over the course of its pass, it can be expected that any simple "shell" model of the ionosphere will not be an accurate representation of the actual behavior of TEC over the pass.

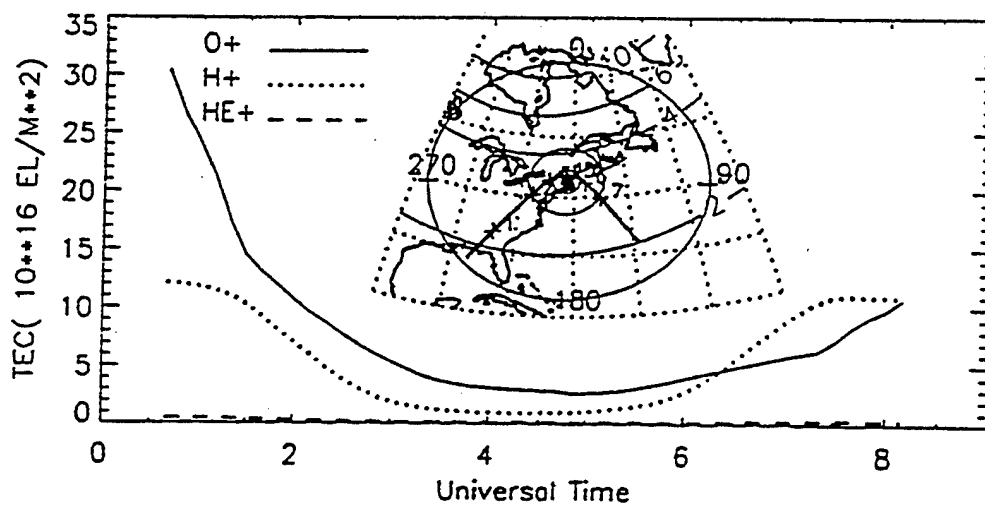
Figure 16 illustrates a cutaway view of geomagnetic L shells from the northern mid-latitude station located at Westford, MA. The L shells greater than approximately 4 are considered to be open field lines, and consequently do not contain any electrons. Note from Figure 16 that satellites viewed from Westford, MA to the north, cross only open field lines. Thus, a typical GPS pass, crossing from north to south would see completely different amounts of protonospheric electron content, ranging from zero in the north, to relatively large values when looking along the closed magnetic L shells less than 4, to the south of the station. The theoretical ionospheric model developed by *Bailey, (1990)*, has been used to calculate the contributions of the O^+ , H^+ and He^+ ions to the total TEC observed along various GPS trajectories. A representative sample of relative contributions of each of those ion species is illustrated in Figure 17 for GPS space vehicle 24. The 400 km ionospheric intersection locations from the Westford station are given in the inset in Figure 17. Note that the electron content contribution due to H^+ ions is actually greater than that from O^+ near the end of the pass. The contribution to TEC from the electron content of the H^+ protonospheric ions certainly cannot be neglected. Figure 17 illustrates that a simple "shell" model of the ionosphere, having a constant mean height, is not adequate to model changes in TEC during a GPS satellite pass.

A new method of directly measuring T_{gd} from the ground, without modeling either the protonosphere or the ionosphere, should be possible by choosing a location on the earth at a time when there is a very low TEC in both the ionosphere and the protonosphere along the path to an individual GPS satellite. Locations viewing GPS satellites above a magnetic L shell of approximately 4 should be high enough in latitude to have no contribution to TEC from the earth's protonosphere. Magnetically quiet winter nighttime in the sub-auroral latitudes can be occasions when the TEC from the F_2 region is very small. This can be confirmed by nearby ionosonde measurements of very low values of foF_2 . At those times, monitoring the relative differential phase and the relative differential group delay from a GPS satellite as it passes over the sky, should yield no changes as a function of satellite elevation angle, simply because there is little, if any, TEC to be measured. At those times, providing the receiver differential delay is known, the satellite T_{gd} can be determined directly, since there is essentially no ionosphere. For instance, an



Cutaway view of the earth along the station meridian, showing the magnetic L shells and the station elevation angles, both north and south of the station. Dashed line represents GPS orbital height.

FIGURE 16



Electron contents of O^+ , H^+ , and HE^+ for GPS SV Nr. 24 as viewed from Westford, MA.

FIGURE 17

foF₂ value of 2 MHz, corresponding to an N_{max} of $4.9 \times 10^4 \text{ el/cm}^3$, with an assumed slab thickness of 250 km, yields a TEC of only $1.2 \times 10^{16} \text{ el/m}^2$ column, not an unreasonable value for quiet winter nighttime conditions in the ionospheric trough region.

3.2 Statistics of Time Rate of Change of Ionospheric Electron Content

The time rate of change of ionospheric range delay is a potential limitation to the Wide Area Augmentation System (WAAS) in precise positioning using radio waves from Global Positioning System (GPS) satellites in the single frequency c/a mode. To assess this limitation we have studied the statistics of ionospheric range-rate changes. A summary of our findings is given in the paper "Statistics of Time Rate of Change of Ionospheric Range Delay" by P.H. Doherty, J.A. Klobuchar, and M.B. El-Arini. A copy of this paper is appended to this report (Appendix 1.).

3.3 Ionospheric Corrections to Precise Time Transfer Using GPS

The ionosphere can be the largest source of error in GPS positioning and navigation. Radio waves propagating through the ionosphere suffer an additional time delay as a result of their encounter with the free electrons in the ionosphere. TEC is a function of many variables, including geographic location, local time, solar ultraviolet radiation, season and magnetic activity. Accurate information on the behavior of TEC is important to satellite navigation and time transfer systems that correct for the time delay effects of the earth's ionosphere.

The GPS dual frequency system provides the opportunity to measure absolute TEC with a high degree of accuracy. Absolute TEC values are obtained by measuring the differential group delay of the 10.23 MHz modulation on the dual frequency signals. Relative TEC values are obtained by monitoring the differential phase of the two GPS carriers. By combining both the relative accuracy of the differential carrier phase with the absolute TEC obtained from the differential group delay, excellent absolute TEC measurements can be made. An example of this technique is illustrated in Figure 18. The group delay measurement for one complete satellite pass is plotted in Figure 18a. Note that this is an absolute measurement of time delay, however, it includes the effects of multipath and receiver noise. Figure 18b, represents the relative, but highly accurate, phase measurement for the same satellite pass. Figure 18c illustrates the results of fitting the relative phase measurement to the absolute, but noisy, group delay measurement to obtain a highly accurate measure of absolute ionospheric time delay.

We have completed a study on the variability of TEC using this technique. The data was recorded at Hanscom AFB, Ma using the four channel ICS-4Z Mini Rogue GPS dual frequency receiver. This receiver has a high performance design that is capable of tracking four satellites simultaneously using the P-codes on both frequencies, L1 and L2, in addition to the C/A code on the L1 frequency.

The GPS data used in this study was recorded from May 1992 through April 1993. Figure 19 illustrates the satellite paths of the various GPS satellites over Hanscom for one day during this period. Elevation angles of 0 through 60 degrees are represented by the

February 24, 1993

PRN# 16

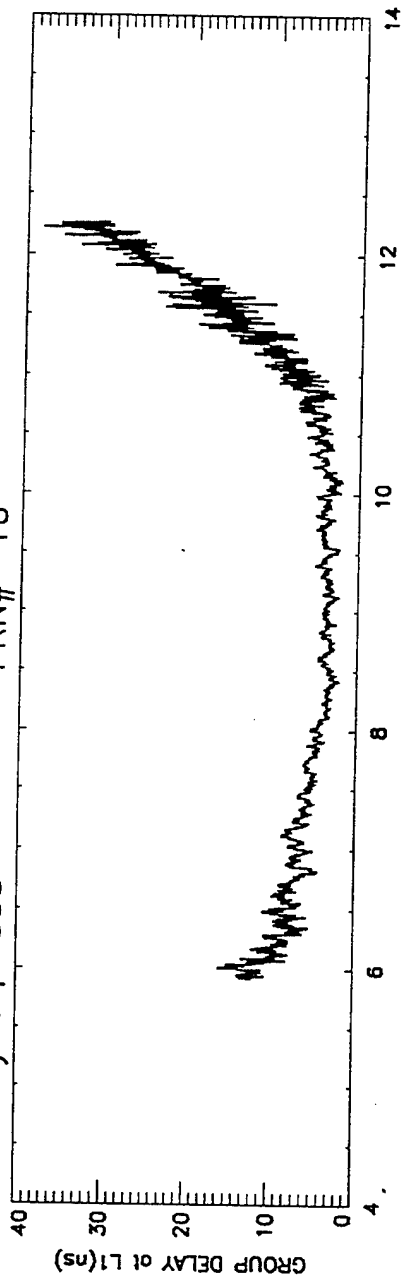


FIGURE 18a

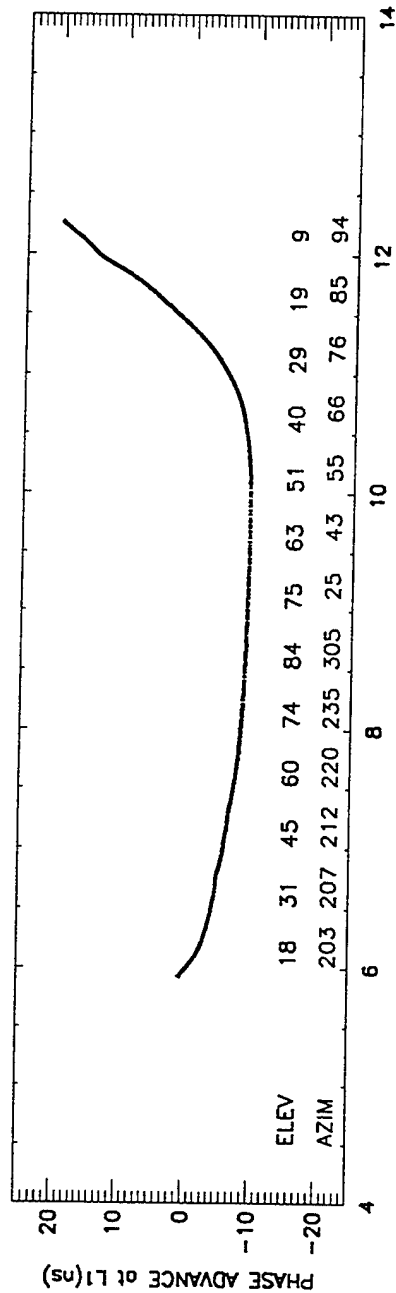


FIGURE 18b

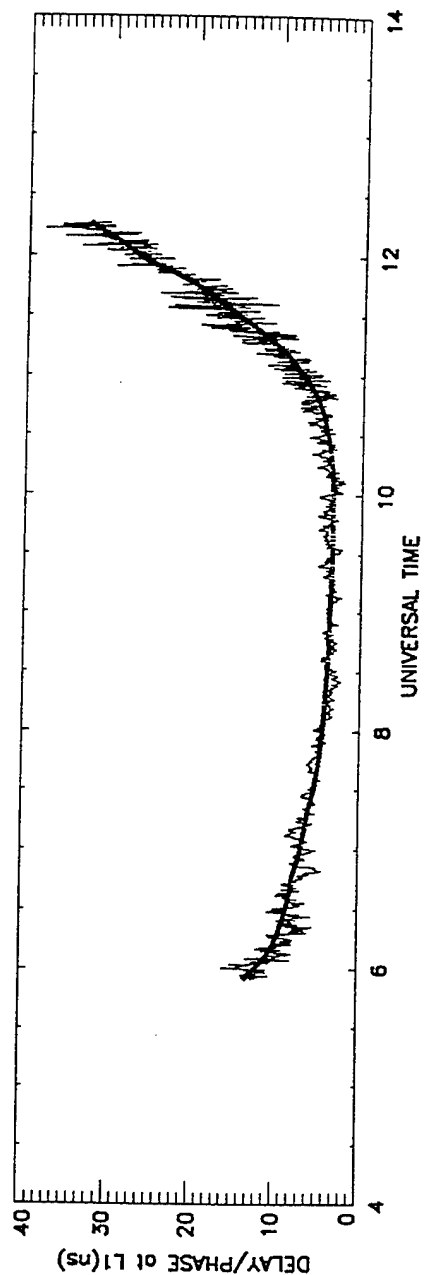


FIGURE 18c

GPS Satellite paths over Hanscom AFB, MA

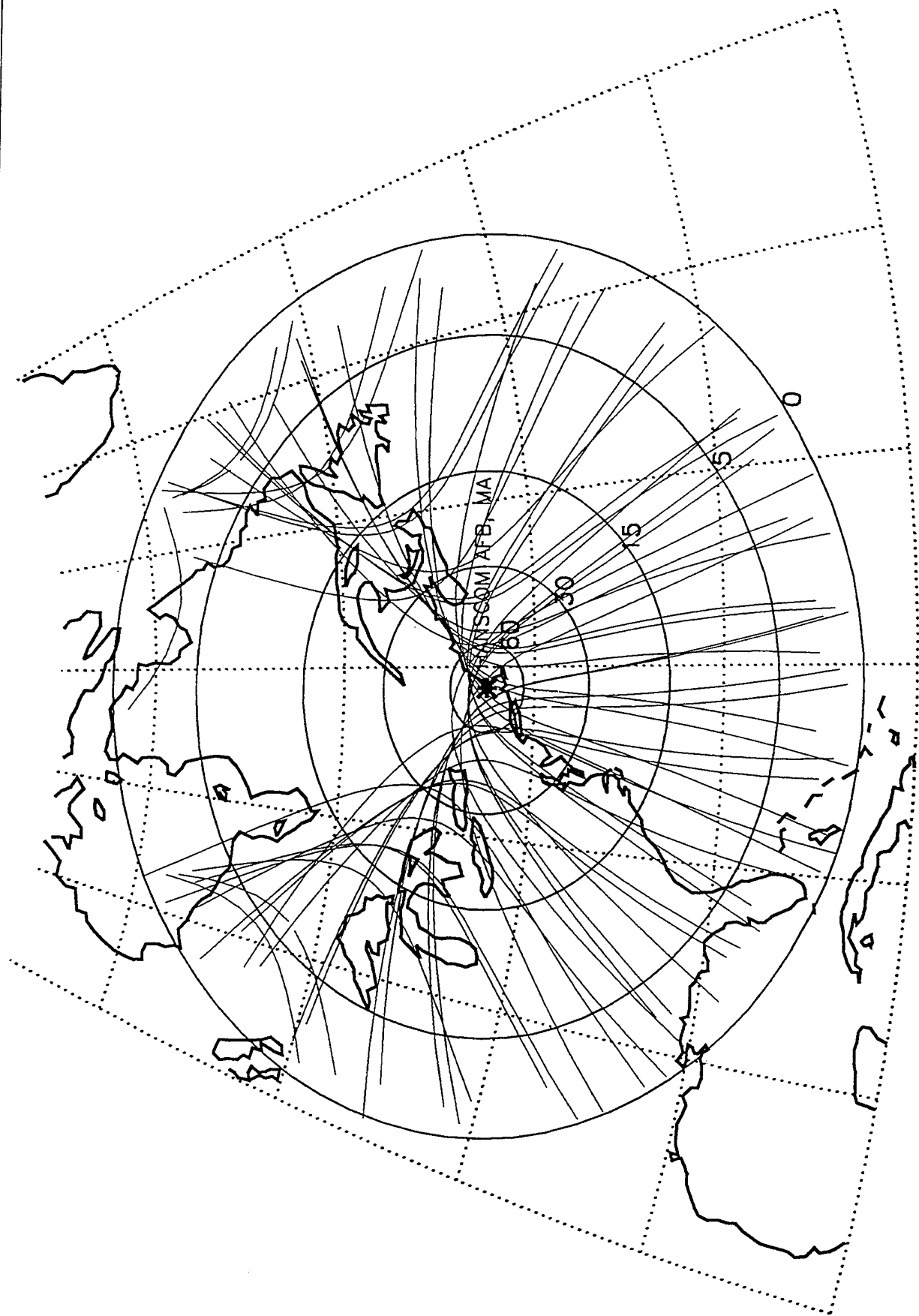


FIGURE 19

concentric rings centered around the station. Satellite signals received from widely spaced azimuth and elevation angles pass through greatly different regions of the ionosphere. Therefore, simultaneous measurements of ionospheric time delay (or TEC) along different lines of sight generally are not the same.

Figure 20 displays the observations recorded on February 24, 1993. The slant absolute delay measurements have been converted to equivalent vertical time delay in ns at L1. That is the measurement at the geographic position directly below the point where the satellite intersects the centroid of the electron density distribution with height, typically at 400km. In order to display the diurnal variation of ionospheric time delay, the data is plotted versus the local time at this sub-ionospheric intersection point. At any local site, the ionization generally peaks in the mid-afternoon hours, and drops rapidly at night. The differences between measurements made at the same local time are attributed to the ionospheric gradients encountered by satellite paths intersecting the ionosphere at different latitudes.

Ionospheric time delay is highly variable by season. Figure 21 illustrates the statistics of ionospheric time delay for three seasons during the daytime hours of 1100-1700 local time. The daytime TEC values were computed and grouped by season, summer (May through August), winter (November through February), and the combined equinoxes of March, April, September and October. The ionospheric time delay measurements are plotted against their cumulative probability so that the percentage of occurrence above and below certain probability levels can be observed. A straight line on this type of statistical plot indicates a normal distribution. The slope of the line is a measure of the standard deviation, and departures from a straight line are simply deviations from a normal distribution. This Figure indicates that the median daytime values of ionospheric time delay are highest in winter, followed closely by the equinox period. The summer values are the lowest. The winter season exhibits a significant departure from a normal curve above the 99% probability point. Departures like these are often due to the effects of magnetic storm activity.

Figure 22 illustrates the statistics of ionospheric time delay during the nighttime hours of 2300-0500 local time. Here, it is evident that the summer nighttime values are higher than those of the other two seasons. Winter and equinox have a more nearly normal distribution than summer. Summer begins to depart significantly from a normal distribution above the 95% probability level. The negative numbers below the 1% probability point are likely due to incorrect satellite biases.

Ionosphere time delay is primarily a function of solar ultraviolet radiation. A reasonable surrogate measure of the amount of ultra-violet radiation produced by the sun which is responsible for ionizing the earth's atmosphere, and producing the ionosphere, is the number of sunspots visible on the solar surface. Figure 23 illustrates the last two solar cycles with the period indicated during which the GPS measurements were made. This period was in the declining phase of the current solar cycle, therefore, the ionospheric time delay values measured are approximately half the magnitude expected at the peak of the solar cycle.

The data set used in this ionospheric variability study is the first continuous, well calibrated, dual frequency GPS ionospheric data set large enough for statistical research. The TEC parameter, however, has been studied for over twenty years using measurements of the Faraday rotation of linearly polarized radio waves transmitted from geostationary

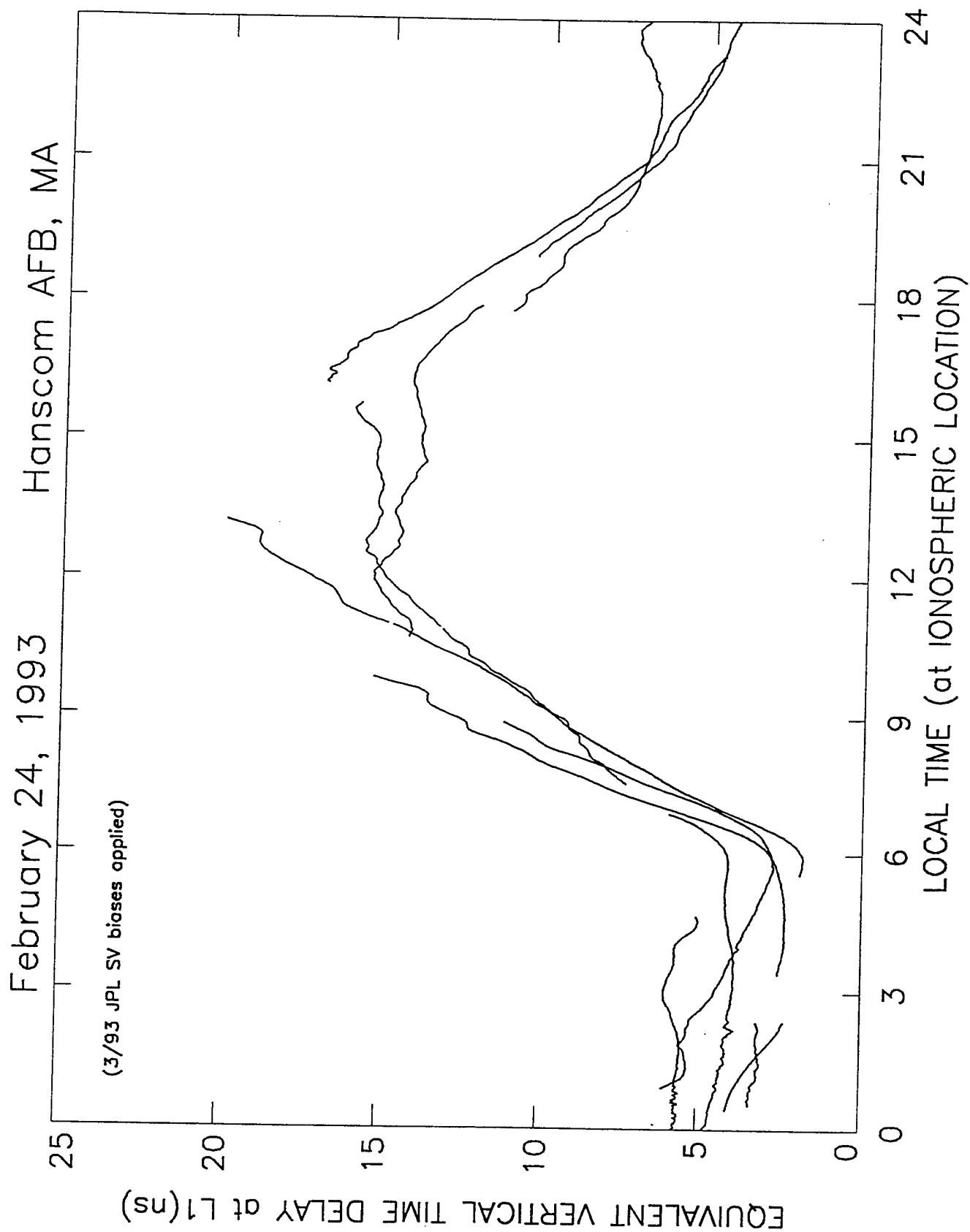


FIGURE 20

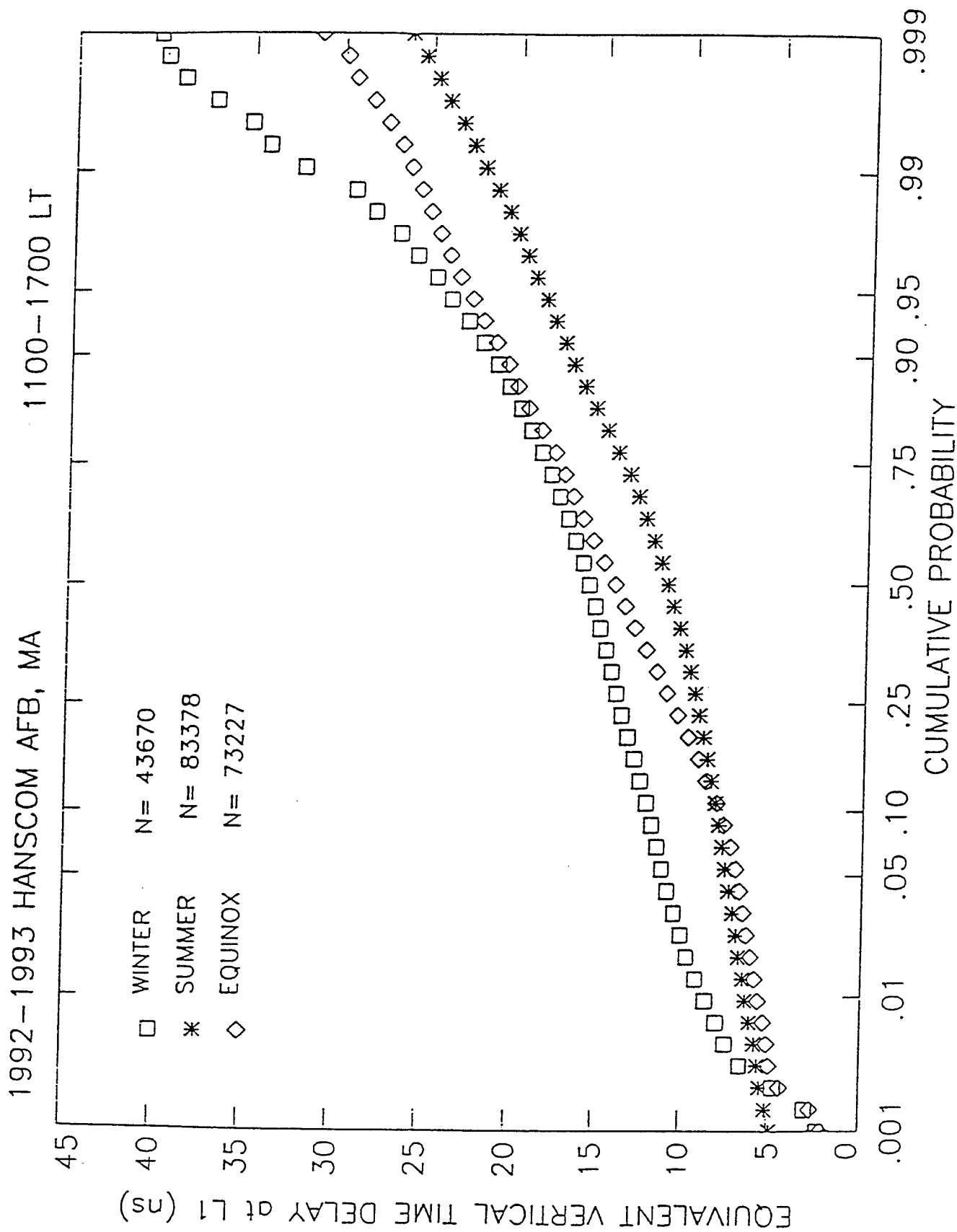


FIGURE 21

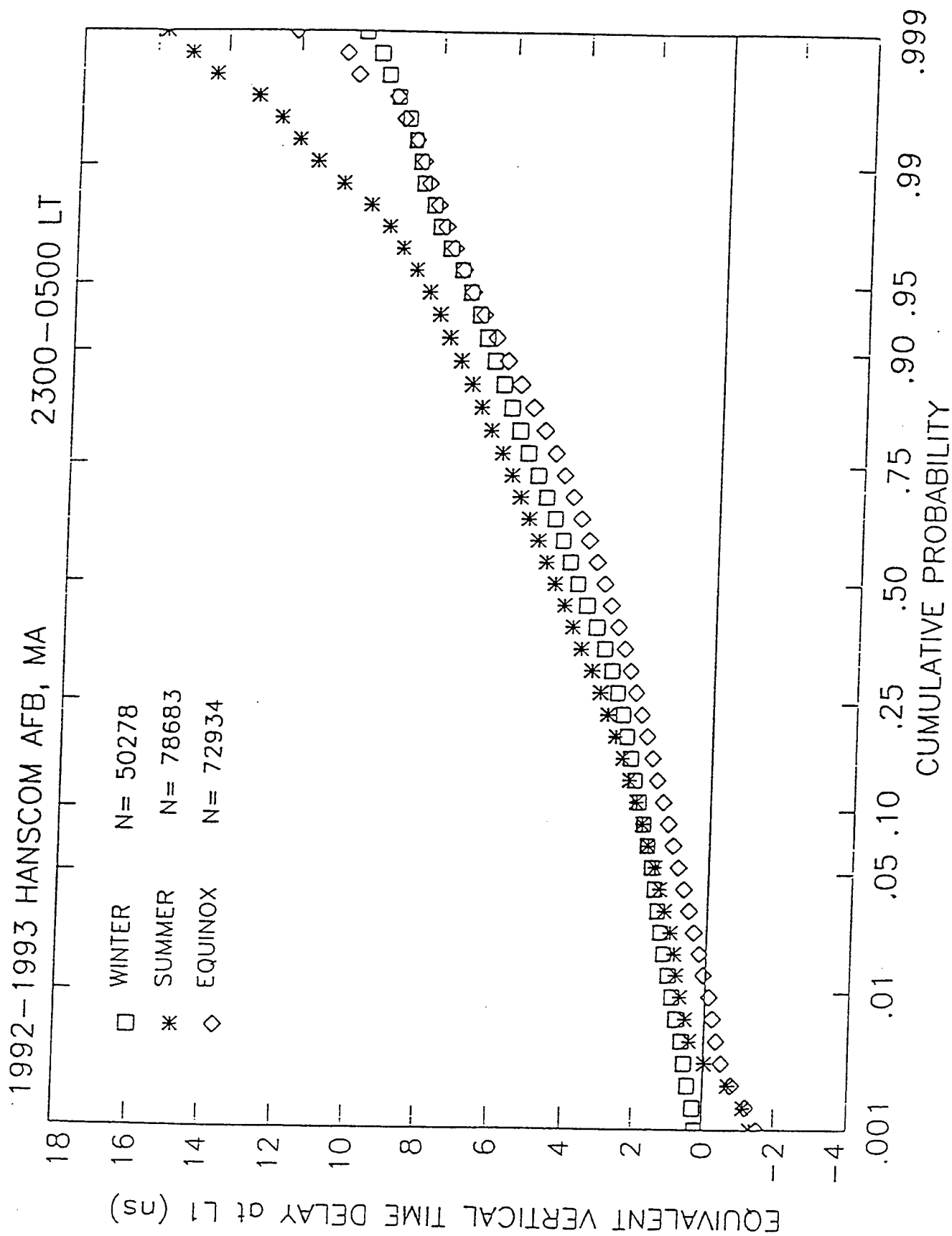


FIGURE 22

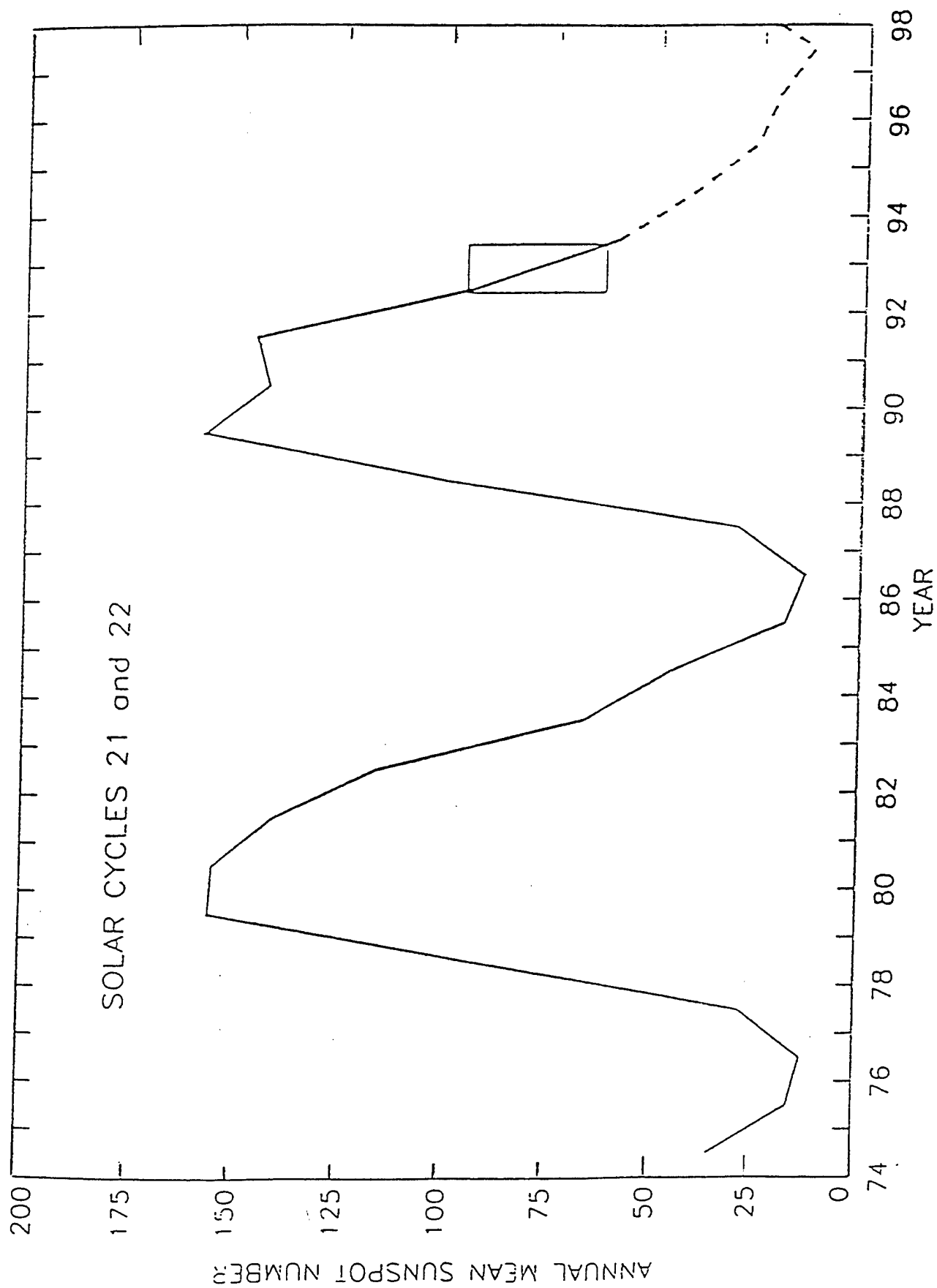


FIGURE 23

satellites. For comparison with the GPS TEC study, Figure 24, is included to represent the daytime probability of equivalent vertical ionospheric time delays at the GPS L1 frequency, as determined from the Hamilton, MA 1981 Faraday rotation data. A comparison of these 1981 results and the recent GPS daytime statistics (Figure 19) illustrates agreement in seasonal behavior with summer producing the smallest daytime values and equinox exhibiting the greatest day-to-day variability. It also illustrates the ionospheric time delay dependence on solar activity, with the 1981 data producing median values that are nearly two times those encountered during the 1992-1993 period.

3.4 Static Ionospheric Test for the WADGPS Experiment

We have supported the FAA's Phase 1 Wide Area Differential GPS (WADGPS) Satellite Navigation Testbed Experiment by operating a GPS receiver at Hanscom AFB, analyzing the measured data, and providing the results to the Mitre Corporation.

Support also consisted of delivering a revised version of the data analysis program to the FAA. The new version of the processing software improved data error detection and run time. This program is used by our site and three other sites operated by the FAA in their WADGPS experiment.

Our first study of this WADGPS data has consisted of analysis of a year's worth of data with the purpose of assessing some of the current limitations to Wide Area Differential GPS. This data was collected from May 1992 through April 1993 at the following locations:

Oldtown, ME	(44.95 North, 68.67 West)
Hanscom AFB, MA	(42.45 North, 71.27 West)
Atlantic City, NJ	(39.45 North, 74.57 West)
Dayton Airport, OH	(39.90 North, 84.22 West)
Georgetown, SC	(33.31 North, 79.32 West)

One of the major issues in WADGPS is to determine the number and placement of ionospheric monitoring stations in the Continental United States (CONUS) required to represent the ionospheric range error between stations to within a specific value. One of the potential limitations in WADGPS, is the unknown spatial variability of ionospheric range errors between locations where dual frequency GPS measurements are being made.

The important parameter in this study is the difference in range error as a function of distance. Thus, differences in the received absolute range error viewing the same GPS satellites from two different locations were computed. Pairs of points using common GPS satellites were used in order to keep the approximate same distance between the ionospheric intersection as the station spacing, since the viewing angles to the satellites are nearly parallel for stations spaced within the region of our experimental work.

Figure 25 illustrates some of the results of this study. It shows the statistical behavior of the differences in range error, in meters, for the Hanscom AFB, Atlantic City Airport station pair. Differences in range error are plotted separately for each of three seasons, summer (May through August), winter (November through February), and the combined equinoxes (March, April, September and October). The data was further separated into daytime, 11-17 hours local time, and nighttime, 23-05 hours local time.

1981 Hamilton, MA 1100-1700 LT

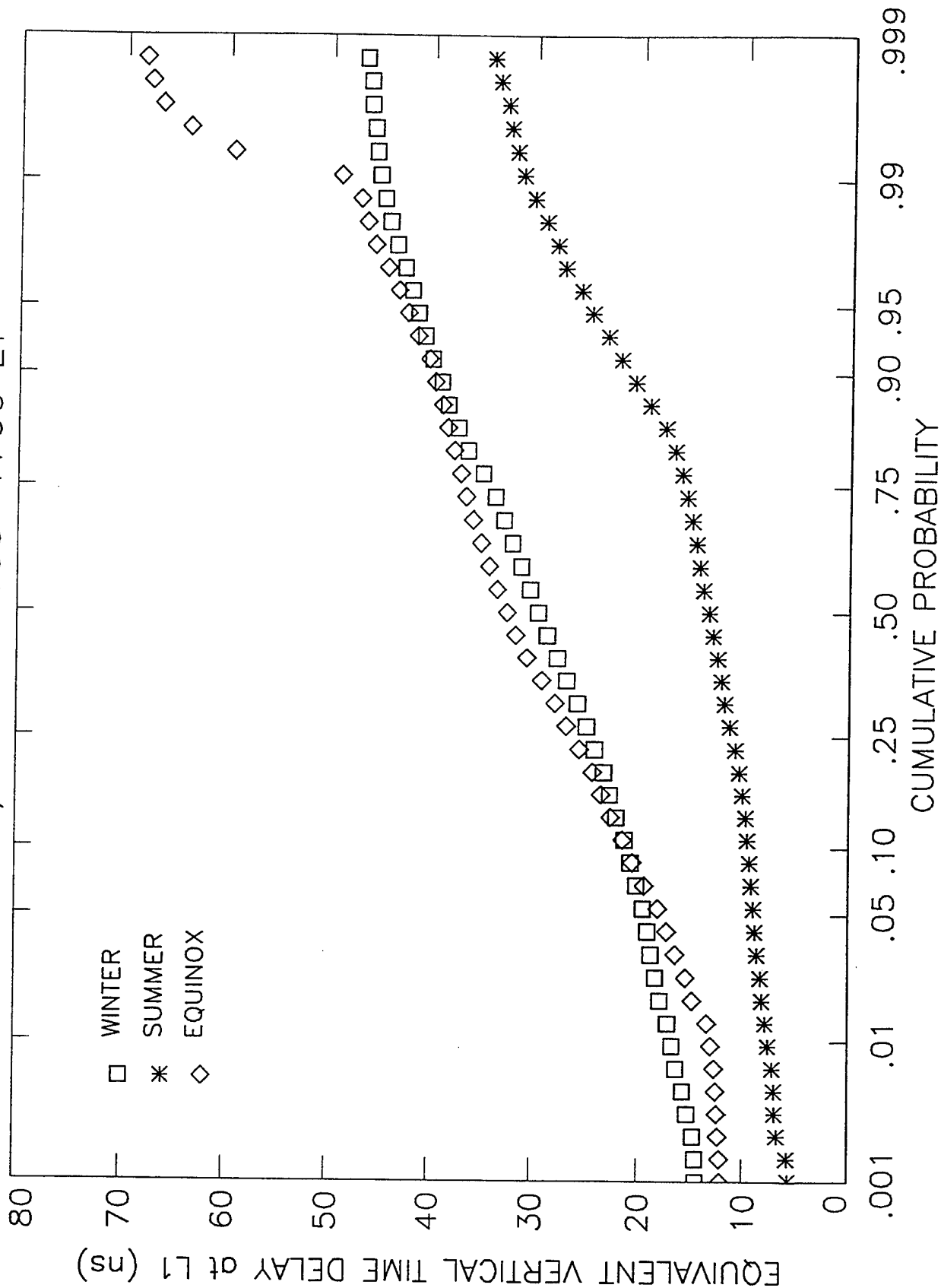


FIGURE 24

5/92 - 4/93 HAFB-ATLANTIC CITY 1100-1700 LT (0-90 degrees)

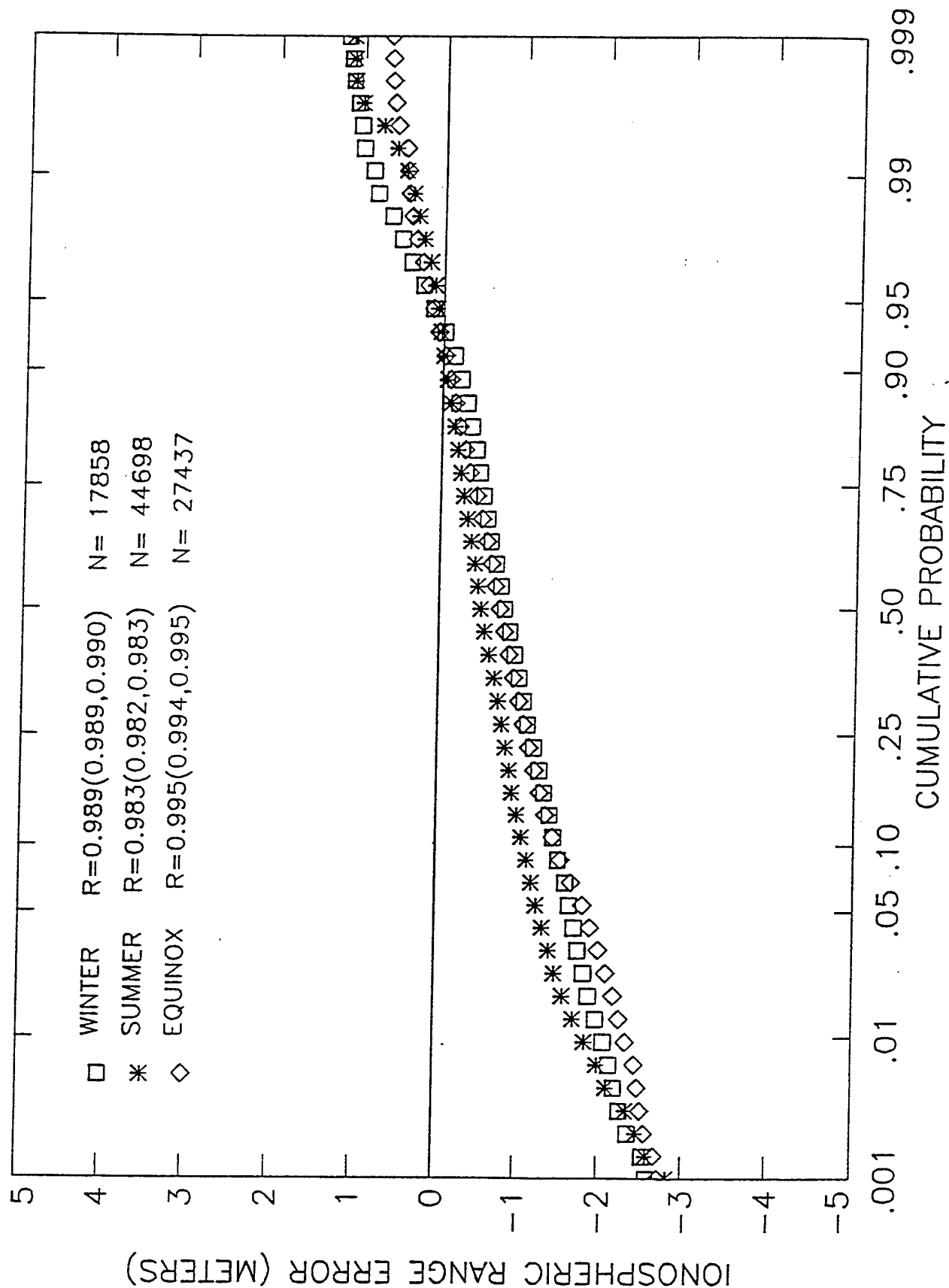


FIGURE 25

These differences are plotted against their cumulative probability so that the percentage occurrence below and above certain probability values can easily be seen. Figure 25 shows that the ionospheric range error differences at the 1% cumulative probability point are approximately -2 meters, the median difference is -1 meter and the difference at the 99.9% cumulative probability point is about 1 meter. Therefore, the absolute difference in range error for this data set was virtually always less than 2 meters. The distance between Hanscom AFB and Atlantic City Airport is approximately 434 km.

Figure 26 illustrates the results using the Dayton, Ohio and Hanscom AFB station pair. It shows that the absolute difference in range error measured at these two stations is higher than 2 meters at the 25% cumulative probability point for two seasons and exceeds 6 meters at the 1% point. The median point, however, is still less than 2 meters. The higher numbers are a results of the greater distance between this station pair. The distance between Dayton and Hanscom AFB is 1,120 km.

Similar figures are currently in process for all the station pairs listed above.

Unfortunately, the portion of the solar cycle during which our measurements were taken, was not a period of maximum solar activity, but was approximately 1/2 way down the descending phase of the current cycle of high activity. For a period of very high solar activity the range errors, and the corresponding differences in range errors between pairs of stations, will be a factor of 2 higher than those actually observed and reported in this report.

The largest values of absolute ionospheric range error, and the largest temporal and spatial gradients, generally occur during magnetic storms, especially during major magnetic storms. During the period of measurement here, from May 1992 through April 1993, there were a number of magnetic storms. None, however were considered to be major magnetic storms. During storms, the largest absolute differences in range error generally only occur during the late afternoon hours of the 1st day of the storm. If only a few major storms occur each year, and if the largest gradients occur only for a few hours during the storm, that cumulative length of time is less than one percent of the entire year. Thus, the ionospheric range error statistics will not be seriously affected except below the 1% and above the 99% levels. Little evidence of major storm effects was found at any probability point during our one year of GPS range error measurements. This is a hopeful sign. Figure 27a illustrates the cumulative probability of TEC for local daytime hours for the entire month of April at Atlantic City. Figure 27b is the same data with the exception of the two storm days. A comparison of these two figures reveal deviations from normal behavior beginning at about the 90th percentile, with a maximum of approximately 9 meters at the 99th percentile.

An example of disturbances caused by storm activity is illustrated in Figure 28. Figure 28a illustrates range error measurements recorded at Hamilton, MA during solar maximum using the Faraday technique. The large departure from a "normal" distribution above the 99% probability point is the result of a severe storm that occurred on October 18, 1981. Figure 28b illustrates the same data with the October 18th storm period removed. Thus, restoring the normal distribution.

Our initial results from the 1st year of measurements of ionospheric range error in the eastern CONUS region have shown that differential range errors are less than 2 meters for station spacings of approximately 430 km for at least 99% of the time. Thus, stations to be used in an operational WADGPS should be located no greater than 430 km apart.

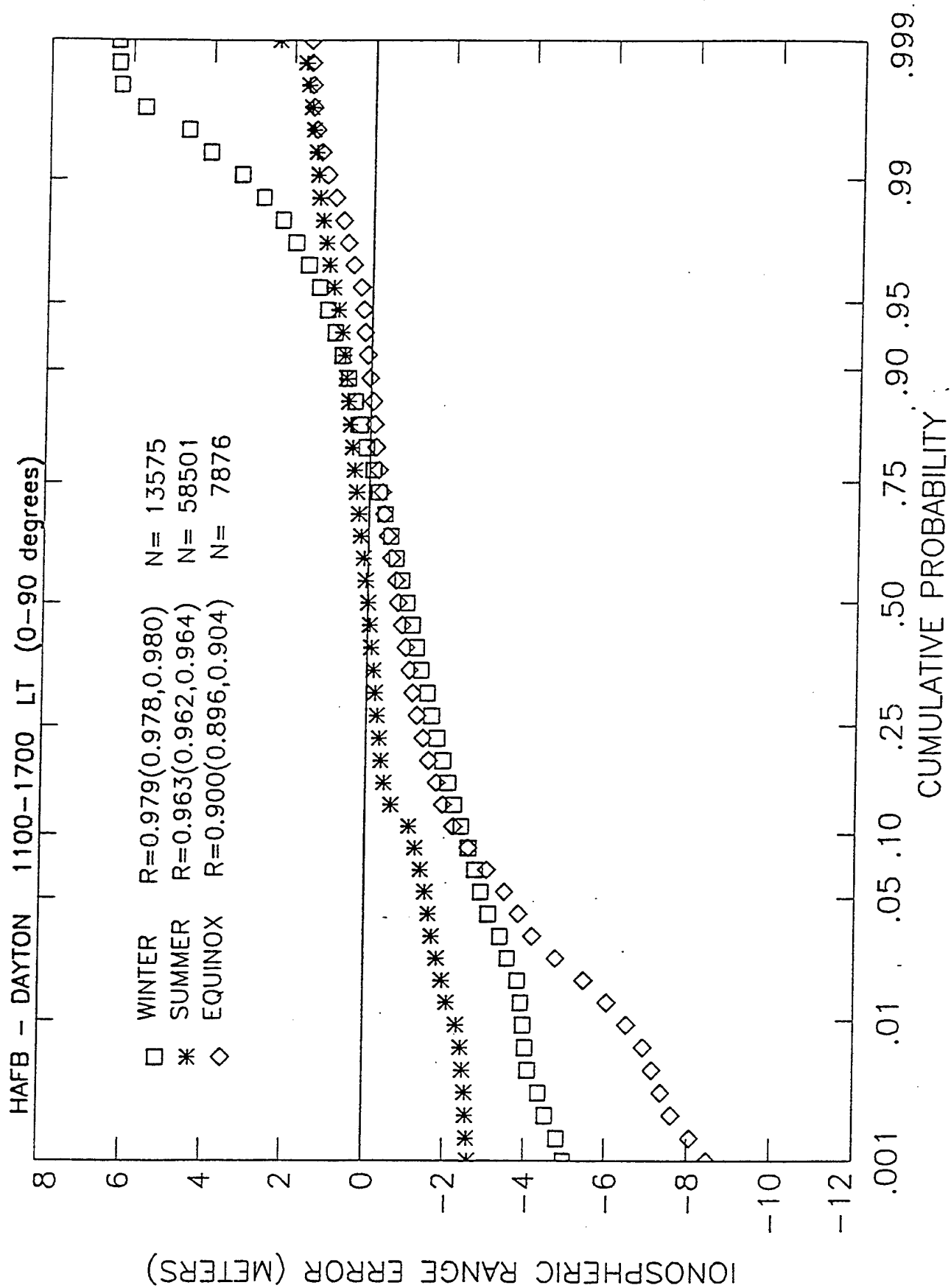


FIGURE 26

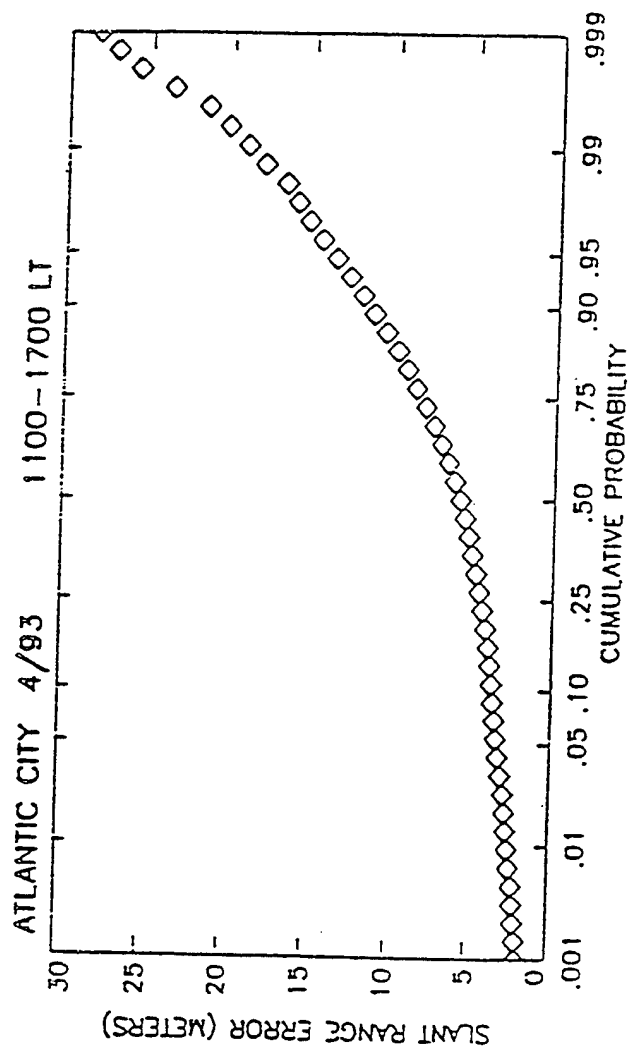


FIGURE 27a

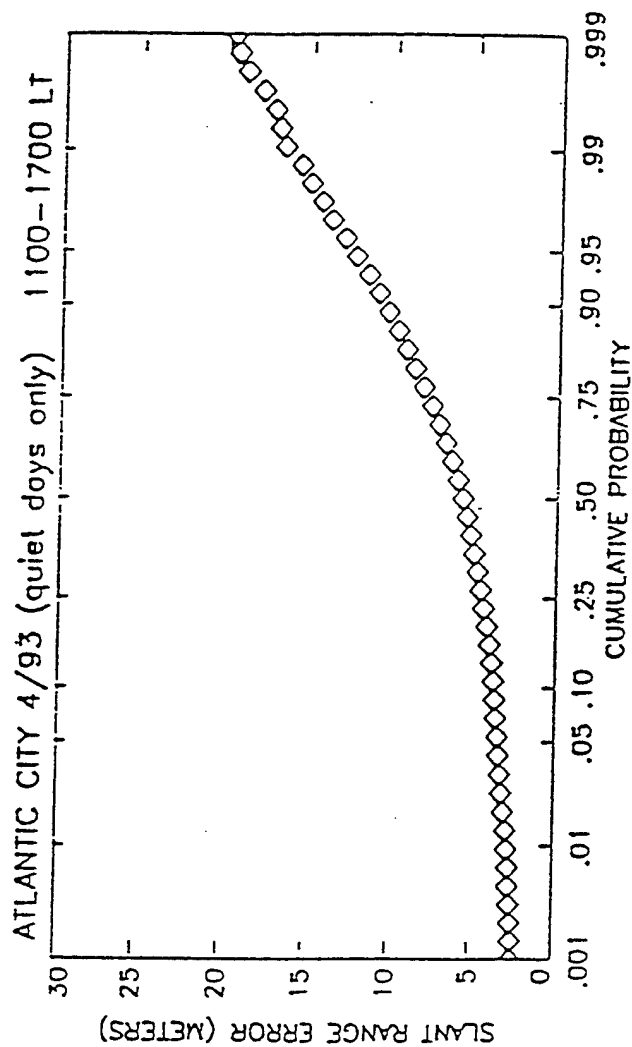


FIGURE 27b

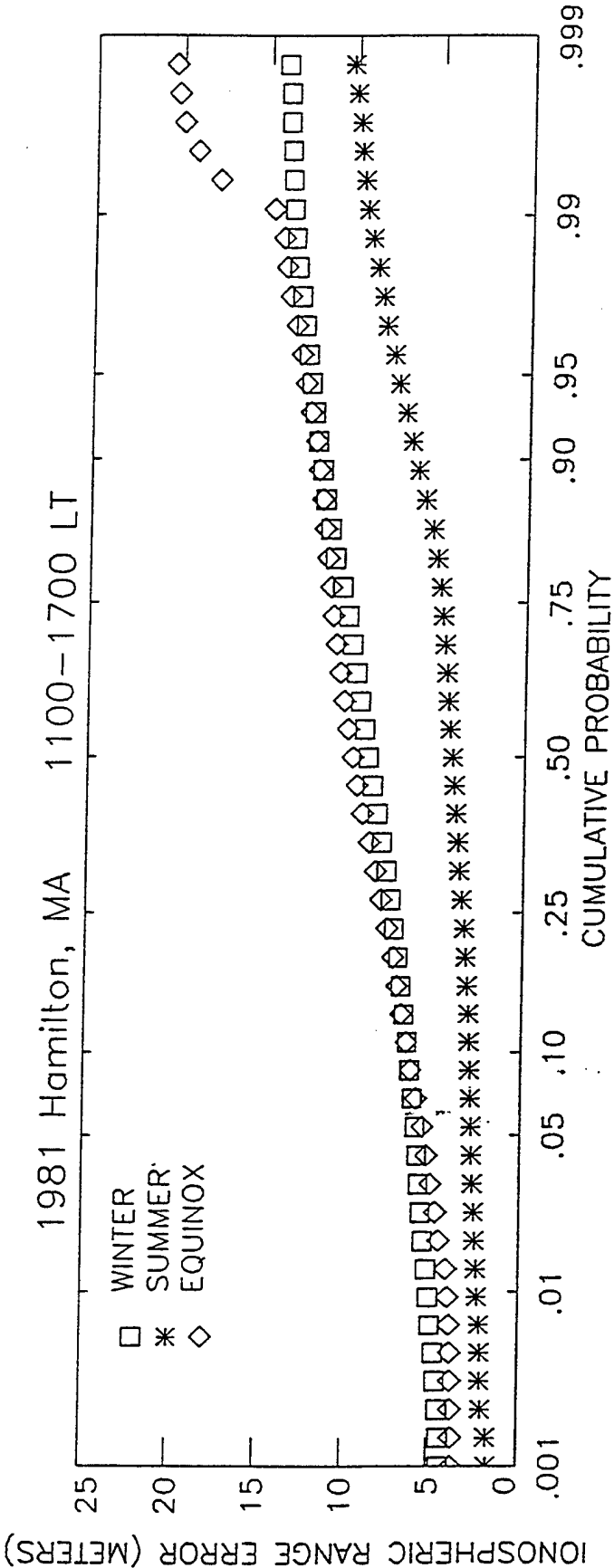


FIGURE 28a

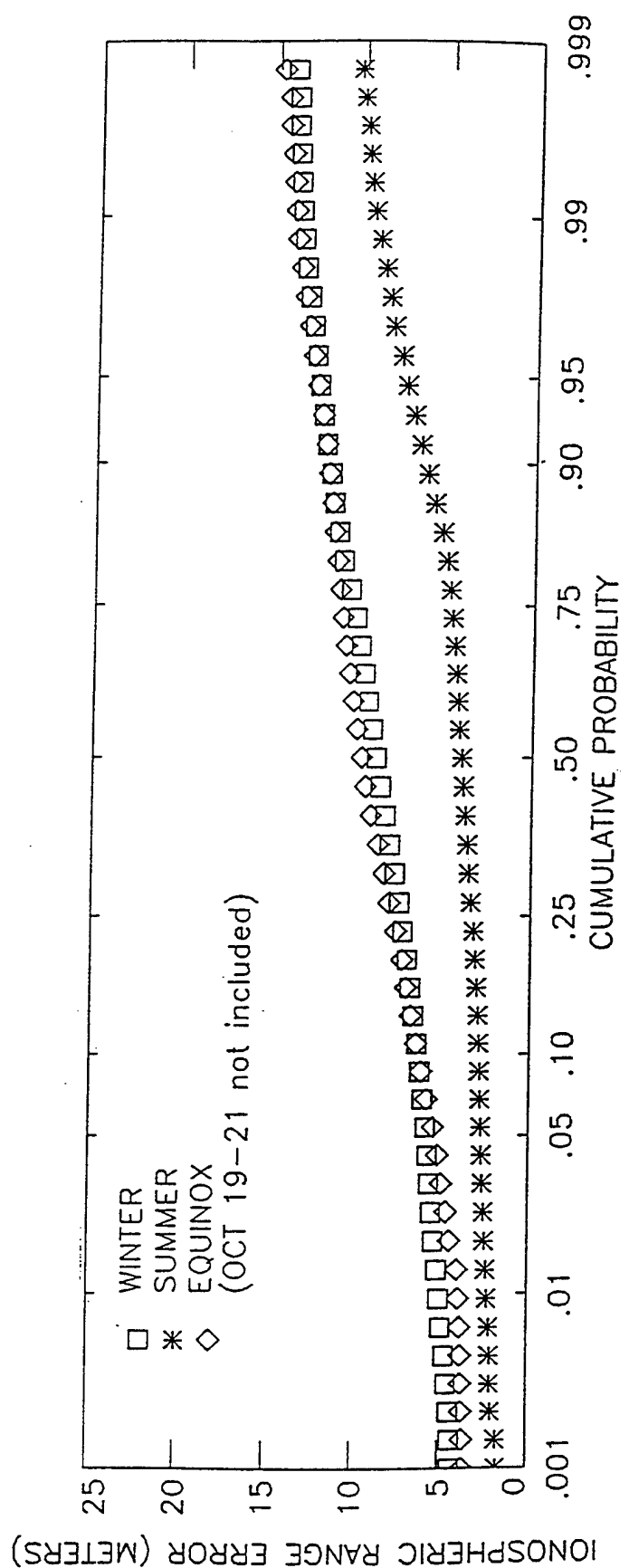


FIGURE 28b

This type of study is useful because information on the ionospheric response to magnetic activity will aid the FAA in determining operating procedures during these disturbances.

3.5 Ionospheric Measurements Using GPS

Global Positioning System (GPS) satellites provide a unique opportunity for ionospheric research. The GPS dual frequency measurements of carrier phase and group delay at both the L1 and L2 GPS frequencies make it possible to measure ionospheric Total Electron Content (TEC) and ionospheric disturbances.

The International GPS Service for Geodynamics (IGS) is a network of GPS tracking stations located worldwide. IGS was established by the International Association of Geodesy (IAG) to support geodetic and geophysical research activities that utilize the GPS technique. Presently, there are approximately 50 data stations that collect and archive daily observations. Figure 29 summarizes the geographic locations of current stations in the IGS network. The general management of the IGS network is directed by the Central Bureau located at the Telecommunications Science and Engineering Division of the Jet Propulsion Laboratory in Pasadena, CA. Most stations in the IGS network are equipped with GPS Rogue or Turbo Rogue dual frequency receivers that record both differential group delay and differential carrier phase for up to 8 satellites simultaneously. To provide data compatibility, all stations store phase and pseudorange observations in daily Receiver Independent Exchange Format (RINEX). Data sets are available from several networks including the Central Bureau via Internet. Also available from the Central Bureau are RINEX format descriptions, navigation message files, current satellite and station information and software for data compression and decompression.

The potential use of the data base in ionospheric research is extensive and has been described by *Wanniger, (1993)*. The data base has also been utilized by *Wilson, et. al., (1992)*, to generate global ionospheric maps. In addition, *Wilson and Mannucci, (1993)*, used the IGS data base to estimate instrumental biases in the GPS receivers at the various sites, as well as in the individual GPS satellite transmitters. *Doherty, et. al., (1994)*, determined statistics of the time rate of change in ionospheric range delay using six months of data from a wide range of IGS stations in the North American continent. These references are only a sample of the vast potential that the IGS network provides for ionospheric research.

This documentation provides information regarding the acquisition of data from the IGS network and the calculation of TEC using RINEX formatted data. It also describes software developed at the Air Force Phillips Laboratory to process the data. Any questions regarding this package should be addressed to:

Patricia Doherty
Institute for Space Research
Boston College
Newton, MA 02159
Internet address: doherty@plh.af.mil
Telephone: 617-377-4283

GPS TRACKING NETWORK OF THE INTERNATIONAL GPS SERVICE FOR GEODYNAMICS OPERATIONAL AND PLANNED STATIONS

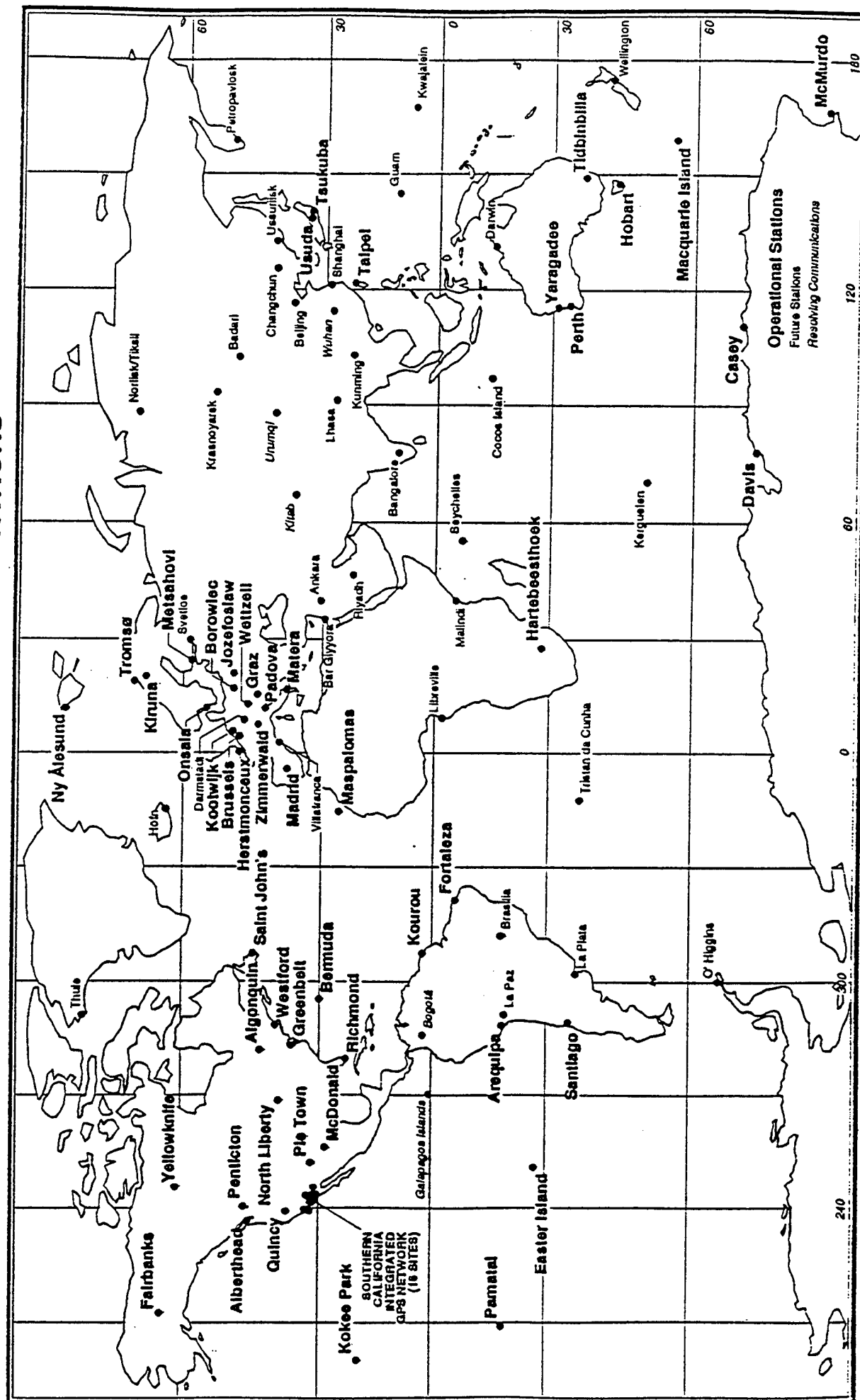


FIGURE 29

September 1994

TEC Calculations Using RINEX Data

RINEX data contains a well defined set of observables including dual frequency carrier phase, pseudorange (code) and observation time. The ionospheric range error or Total Electron Content can be determined from dual frequency pseudorange or carrier phase measurements. Figure 30 illustrates both of these measurements for a typical satellite pass recorded at Westford, MA.

The pseudorange or group delay measurement, shown in the top panel of Figure 30, represents an absolute measure of the ionospheric range error in meters. These measurements were recorded under anti-spoofing conditions and therefore exhibit excessive variations in receiver noise. This increased receiver noise is due to the low signal to noise ratio that results when a receiver is operated in a codeless mode of tracking. This noise is more evident at low elevation angles, as can easily be seen near both ends of the pass. This measurement is also susceptible to noise induced by multipath. Multipath is strongly dependent on the local environment and is also more evident at low elevation angles. To calculate differential delay (ns) from the dual frequency (or P-code) data:

- 1) convert P code in meters to ns:

$$p1(ns) = p1(m)/.3$$

$$p2(ns) = p2(m)/.3$$

- 2) calculate differential code delay(ns):

$$\text{diff. code delay}(ns) = (p2(ns) - p1(ns) - \text{HWCAL}(ns))$$

where HWCAL(ns) = hardware calibration in ns

The differential carrier phase measurement, shown in the middle panel of Figure 30, provides a much more precise measure of the ionospheric error, but only on a relative scale. This measurement is not as noisy as the group delay and is not susceptible to multipath. It is measured in whole cycles at both L1 and L2. To calculate differential delay (ns) from carrier phase:

- 1) convert cycles of L1 and L2 to ns:

$$L1(ns) = L1(\text{cycles})/1.57542$$

$$L2(ns) = L2(\text{cycles})/1.22760$$

- 2) calculate differential phase delay:

$$\text{diff. phase delay}(ns) = L1(ns) - L2(ns)$$

The user can then convert differential delay to other parameters with the following conversion factors provided by Klobuchar, (*private communication, 1994*):

- 1 nanosecond of differential delay:

$$= 2.852 \times 10^{16} \text{ el/m}^2 \text{ (TEC)}$$

$$= 1.546 \text{ nanoseconds of delay at L1}$$

$$= 0.464 \text{ meters of range error at L1}$$

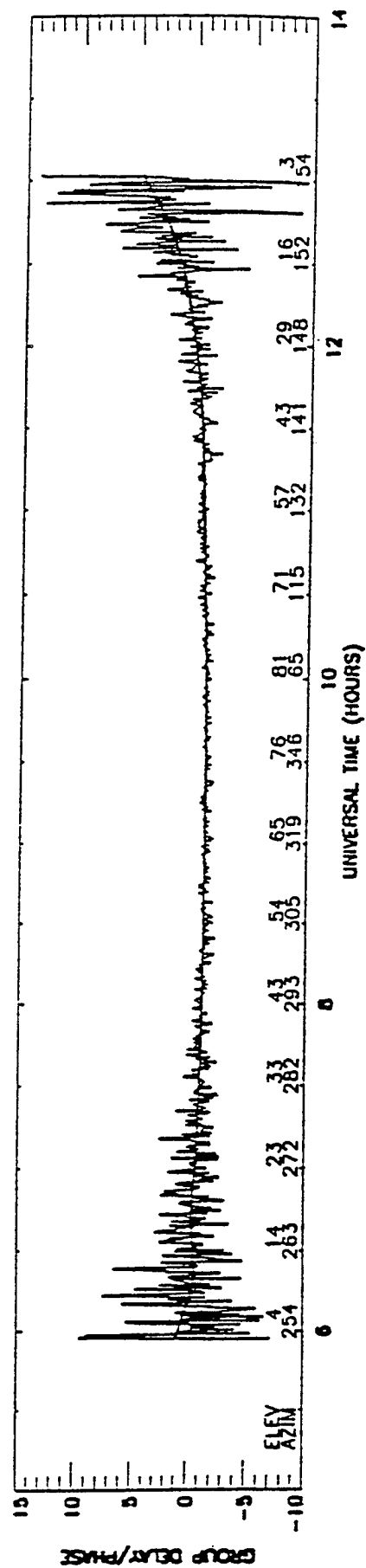
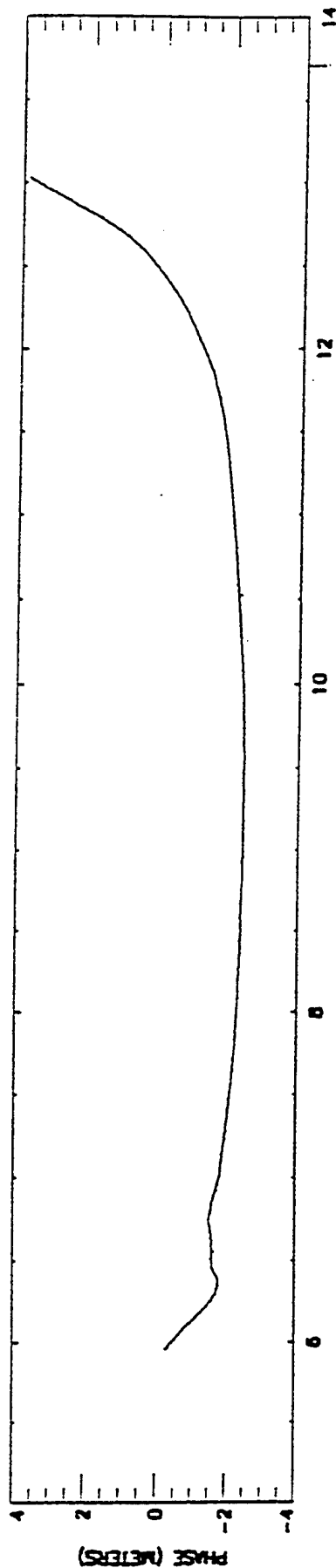
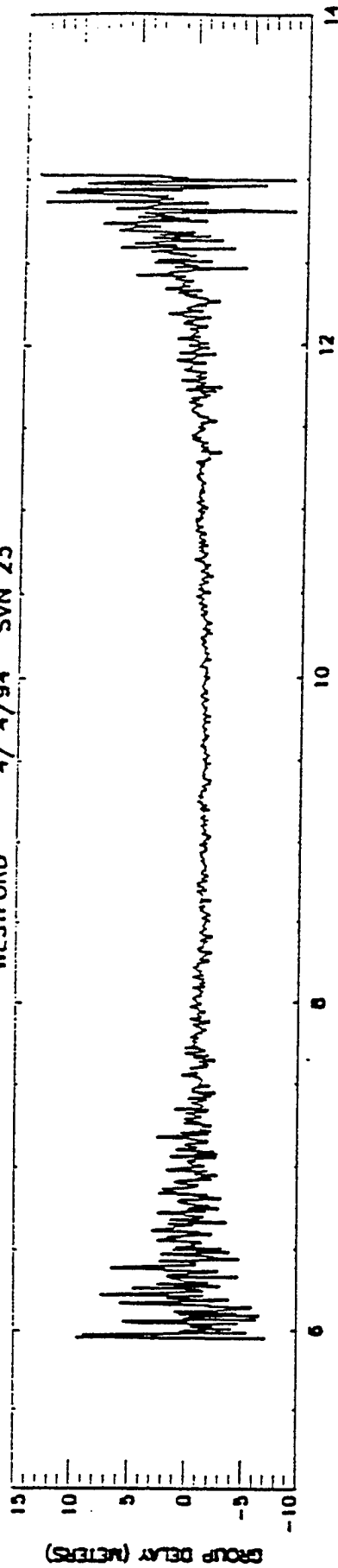


FIGURE 30

In processing the data, the accurate phase measurement is fit to the noisy pseudorange measurement to obtain an absolute and precise measurement of TEC. This fit is determined with data collected during the middle of the pass to avoid the noisy data at low elevation angles and multipath interference. Then the pseudorange measurements are discarded and we are left with the differential carrier phase data fit to the absolute scale provided by the pseudorange. The bottom panel of Figure 30 illustrates this process by showing the phase measurements fit to the group delay measurements. The approximate elevation and azimuth of the satellite is printed below the data in the bottom panel.

The IGS network also provides Navigation Message Files in RINEX format. These files contain a subset of clock and ephemeris data for each of the transmitting GPS satellites. The parameters included in this file are for the beginning of the GPS week with the exception of the Mean Anomaly which is referenced at the time of ephemeris. In processing the data, a navigation message file is required to determine elevation and azimuth positions as viewed by the recording station.

Accessing the Data

Access to the RINEX data files is through the IGS data center at JPL. Data is stored in JPL's guest computer "BODHI" in the sub-directory: /pub/rinex. Approximately 180 days of data are stored on line. Data is stored in directories indexed by the Julian day of the year. An underscore "_" after the day number indicates that data is available for that day. Each directory contains data and navigation message files for each station in operation for a single day.

Files can be accessed via anonymous ftp through internet (address: 128.149.70.66). A sample transfer session is described below. In this description, the user commands are in italics and comments regarding the user commands are in parentheses.

```
SUN [120]: ftp 128.149.70.66          (open ftp session with BODHI)
Connected to 128.149.70.66
220 bodhi FTP server (Version 1.7.109.2 Tue Jul 28 23:32:34 GMT 1992) ready.

Name(128.149.70.66:doherty): anonymous  (login is anonymous)
331 Guest Login ok, send ident as password.
Password:user@location                (password is your internet address)

ftp> cd pub/rinex                     (change directory)
ftp> binary                           (for binary transfer of data)
ftp> cd 244_                           (change directory to data stored for day 244)
                                         (the underscore _ indicates that data is
available)
ftp> get 94sep01west____r0.mnx_z        (get data recorded at Westford on 09/01/94)
                                         (multiple files can be accessed with a macro)
150 Opening BINARY mode for data connection for 94sep01west____r0.mnx_z
(612441 bytes).
226 Transfer complete.
```

local: 94sep01west____r0.rnx_z remote:94sep01west____r0.rnx_z
612411 bytes received in 42 seconds (14 Kbytes/s)
ftp> bye (end transfer session)

The IGS Central Bureau at JPL also provides information about the network through anonymous ftp at 128.149.70.41. In the directory "igsb", files can be found that outline data format and availability, station information, software and other general information.

Software to Process RINEX Data

Software has been developed at the Air Force Phillips Laboratory to process the RINEX data provided by the IGS network. The software was developed by Boston College under Air Force Contract F19628-93-K-0001. The main programs developed for processing the data are listed below:

RINEX.F - fortran program that performs all the calculations and generates three output files for further processing

PLTRNX.PRO - IDL plot routine to plot the results generated in RINEX.F

SLIP.PRO - IDL plot routine to plot out and correct potential cycle slips in phase that were not automatically corrected in RINEX.F

The fortran program is written in standard fortran and should be portable to any other system. The plot programs are written for a UNIX based system using the Interactive Data Language analysis software. If the IDL package is not available, similar graphics software can be developed to display the results generated by **RINEX.F**.

RINEX.F is the front end of the process. It requires an input file named "rinex.info" containing directives for processing the data. It must include the following information:

- line 1: rinex data filename (uncompressed ".rnx" file)
- line 2: navigation message filename (uncompressed ".eph" file)*
- line 3: month, day, year - (for the rinex data in 2 digit format)
- line 4: station name - (where rinex data was collected)
- line 5: Julian day - (day of the year corresponding to month, day, yr)
- line 6: Hardware calibration(ns) - (receiver hardware calibration)

*When accessing the network, the user will find a navigation message file for each station data file. In the processing described here, it is not necessary to provide a different ephemeris file for each station data file. The **RINEX.F** program converts the ".eph" file to a standard almanac set that can be used for any station location. In fact, the **RINEX.F** program can predict accurate satellite positions using a ".eph" file that is up to three weeks old.

After reading the input file "rinex.info", **RINEX.F** will perform the following:

- a) read in the rinex data (.rnx file)
- b) calculate the geographic location of the station
- c) convert the phase and pseudorange data to TEC units, where 1 TEC unit = 1×10^{16} e/m².
- d) calculate elevation and azimuth angles for each data sample (using the .eph file)
- e) search for time gaps that may be related to receiver drop outs
- f) search and correct apparent cycle slips in phase for individual satellite passes
- g) determine absolute TEC by fitting the smooth, relative phase data to the noisy, absolute pseudorange data using an arithmetic mean fit
- h) generate 3 output files for further processing:
 - data.file - contains the final output including phase, pseudorange, absolute fitted TEC, elevation, azimuth and time at 1 minute intervals
 - error.file - contains information on errors found in the data including gaps in time (potential drop outs) and cycle slips
 - slip.file - contains satellite passes that may contain cycle slips that were not corrected in RINEX.F.

2) **PLTRNX.PRO** is a plot routine written in IDL (Interactive Data Language). It simply reads the output file "data.file" created in RINEX.F and plots the results. Figure 31 illustrates some of these results for data recorded on 10/08/94 at Westford, MA. Each panel exhibits the carrier phase data fit to the absolute scale provided by the pseudorange measurement for separate satellite passes.

3) **SLIP.PRO** is a plot routine written in IDL. It reads and plots the "slip.file" data file created in RINEX.F. Slip.file contains problem data passes. In general, RINEX.F automatically detects and corrects for cycle slips. Passes that are written to "slip.file" are those that RINEX.F was not able to correct. SLIP.PRO is menu driven allowing options to zoom into problem areas, to correct apparent cycle slips or to accept or reject the data file. Figure 32 illustrates a simple session with SLIP.PRO. The top panel is the standard plot with the fitted phase data plotted over the pseudorange data. The middle panel shows the phase data alone with a pointer indicating an apparent cycle slip at 14.50 hours UT. The bottom panel illustrates the resulting phase curve after the cycle slip was corrected by SLIP.PRO. SLIP.PRO generates an output file containing corrected satellite passes. This file must be concatenated with the "data.file" provided by **RINEX.F**.

Summary

The programs and techniques included in this package together with the data set made available by the International GPS Service for Geodynamics provides and excellent

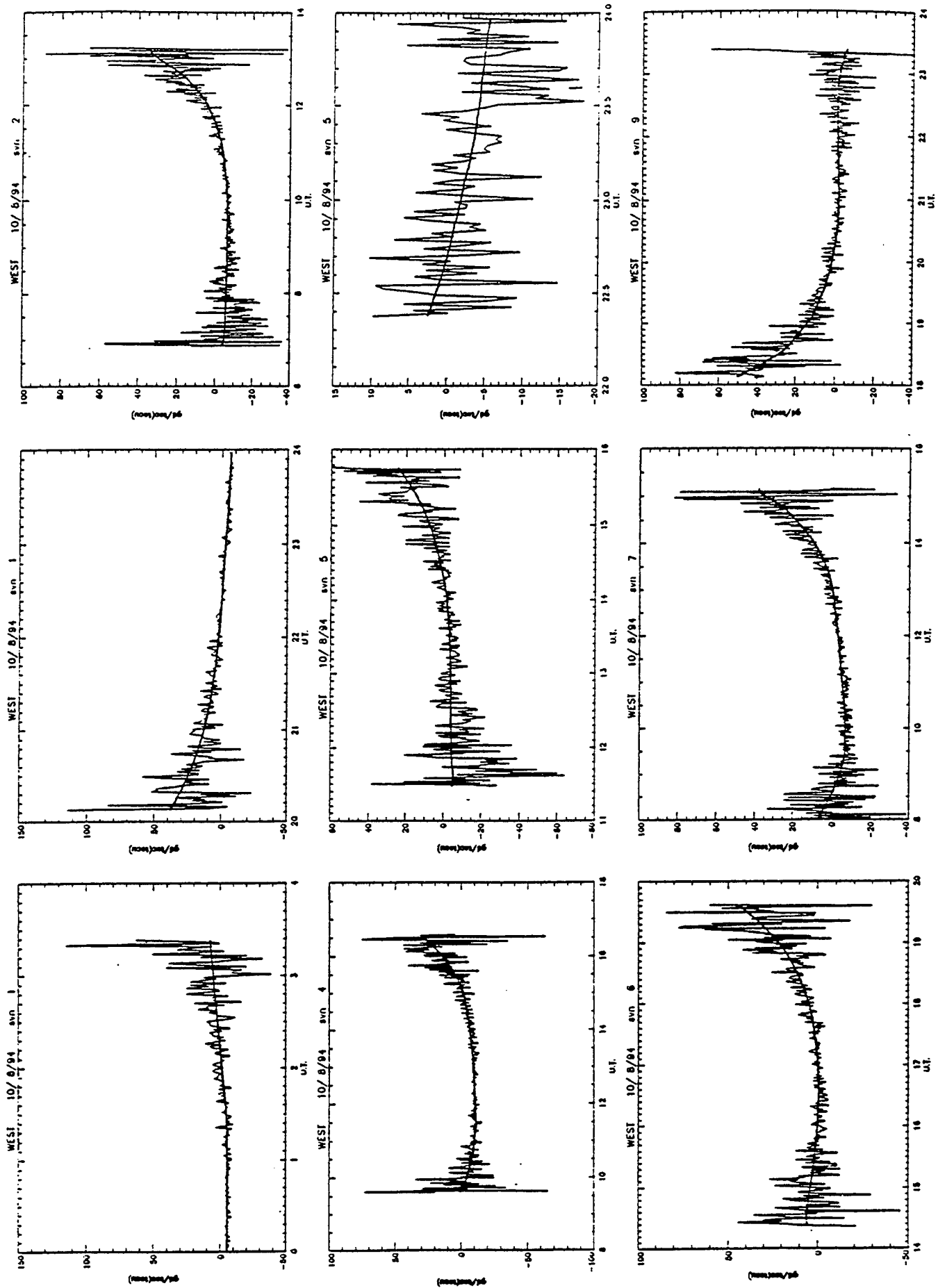


FIGURE 31

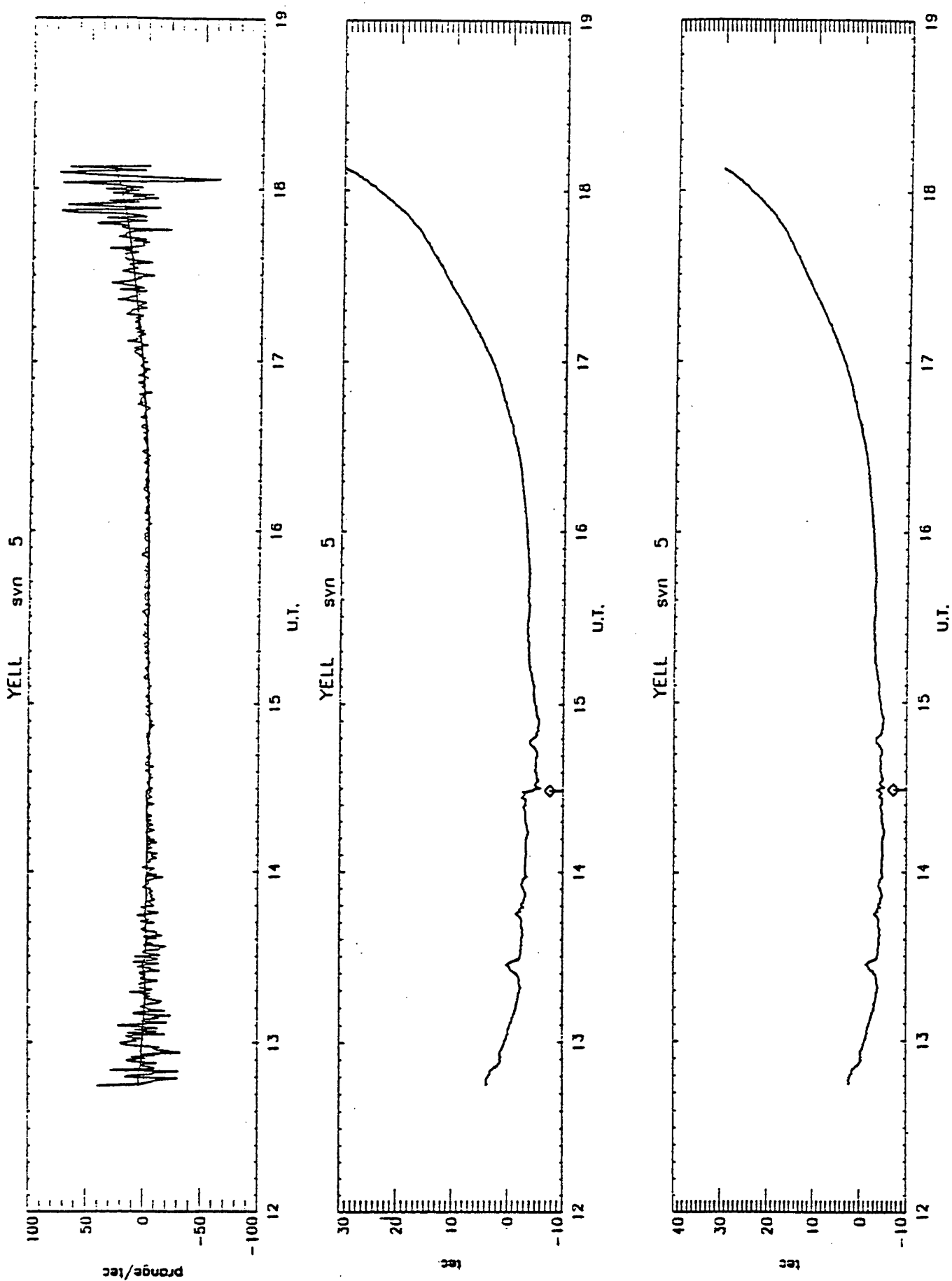


FIGURE 32

opportunity for ionospheric research. Additional software can be developed by the individual user to further analyze the data for many different applications.

The following list summarizes the steps to obtain and analyze data from the IGS network using these techniques:

- 1) login to the central network at JPL
- 2) access data files and navigation message files in binary mode
- 3) decompress data and navigation message files on your computer
- 4) create the input file named "rinex.info" required by **RINEX.F**
- 5) run the **RINEX.F** program
- 6) run **SLIP.PRO** to look at and correct problem passes in "slip.dat"
- 7) concatenate the corrected passes from **SLIP.PRO** to "data file" from **RINEX.F**
- 8) optionally plot the "data.file" with **PLTRNX.PRO**
- 9) develop additional software to study the results.

3.6 Solar Cycle Dependence of Total Electron Content

The ionosphere is the most substantial source of error in GPS positioning and navigation. While the dual frequency GPS user can correct for this error using the signals of both GPS frequencies, the single frequency user has to use the Ionospheric Correction Algorithm (ICA) that was developed to correct for approximately 50% rms of the error. The ICA was developed in 1975 using the Bent Model (Llewellyn and Bent, 1973), a state of the art empirical ionospheric model that was based on data recorded during an average solar cycle. Solar cycle maximum values since that period has been much higher. As a result, the ICA does not adequately represent periods of extremely high solar maximum activity.

There have also been several papers in the literature which claim that there is a "saturation effect" in Total Electron Content, (TEC), which is directly proportional to ionospheric range delay. Another high solar cycle maximum has been predicted to occur approximately in the year 2000, and the existing ionospheric first principle models do not satisfactorily account for the very high values of solar flux expected to occur at that time. In any case, if this saturation effect is true for high values of solar flux, we must determine how it changes with long term solar activity.

Given the need to examine the relationship between GPS TEC and solar activity, efforts have been made to collect and analyze past GPS data from the International GPS Service for Geodynamics. This service, managed by the Jet Propulsion Laboratory in Pasadena, CA, collects and archives dual-frequency GPS data from over 60 stations located worldwide. Our hope was to collect several years worth of GPS data in order to check the long-term dependence of ionospheric range delay against solar flux values. Data recorded at Kokee, HI, Goldstone, CA, Westford, MA and Tromso, Norway have been collected and analyzed up to the end of February 1996. We are still waiting for software from JPL to convert the earliest (1990 - 1991) data sets from raw data to the standard Receiver Independent Exchange, (RINEX), data format.

When this data base has been completed, we will use it to describe a relationship between GPS TEC and solar activity. However, such a database will only span part of one

solar cycle and as such would mostly likely be inadequate for determining the complete solar cycle dependence of the TEC. Our solution to this problem has been to turn to a different type of ionospheric data (ionosonde measurements) that offers coverage over nearly four complete solar cycles, but is still closely related to TEC. In particular, we have obtained a database containing routine and almost continuous measurements of ionospheric foF₂ from 125 ground based ionosonde stations. The foF₂ parameter is a frequency measurement that directly gives the electron density at the peak of the F₂ region of the ionosphere. Since much of the TEC comes from around the peak of the F₂ region, we have utilized the database to infer possible saturation effects in TEC versus solar activity at several locations. By correlating foF₂ measurements recorded at several widely spaced geographic locations with various proxies of the 10.7 cm solar flux over four solar cycles, we will be able to observe if a functional relationship between ionospheric behavior and solar activity exists. We feel that this foF₂ data base together with measurements of 10.7 cm solar flux (F_{10.7}) will best describe the functional dependence of ionospheric behavior on solar activity, including extreme levels of solar flux. During this quarter, we have processed foF₂ data from the following stations and time periods:

Station	Latitude	Longitude	Time Period
Ottawa, Canada	45.1° N	76.2° W	1956-1991
Boulder, CO	40.1° N	105.3° W	1958-1992
Slough, UK	51.5° N	.6° W	1957-1990
Wallops Island, VA	37.9° N	75.5° W	1968-1987
White Sands, NM	32.3° N	106.5° W	1957-1972
Huancayo, Peru	12.0° S	75.3° W	1957-1989
Concepcion, Chile	36.6° S	73.0° W	1957-1979
Bogota, Columbia	4.5° N	74.2° W	1957-1965

Figure 33 illustrates a sample of the results at Slough, UK during solar cycle 19. The top three graphs depict measurements of peak density (NmF₂) versus daily values of 10.7 cm solar flux. The bottom three graphs show the same peak density values versus a 27 day running average of 10.7 cm solar flux. Note that the data has been limited to geomagnetically quiet days to offset storm variations and has been separated into three seasons to account for the well documented ionospheric seasonal variability. The top three figures show an apparent saturation in NmF₂ versus daily values of solar flux during winter, with a less apparent saturation effect during summer. The equinox season does not exhibit saturation but it does have a higher degree of variability than the other seasons. The bottom figures show that if we use a 27 day average of solar flux versus daily values of NmF₂, the saturation effect during winter and summer virtually disappears and the general variability of the data is minimized. In general, all of our results exhibit similar, but not identical, behavior.

To determine if a different functional relationship exists in different regions work should continue using the foF₂ data base to compare results from stations located in different latitude and longitude regions. Also measurements of TEC from faraday rotation during one solar cycle at a mid-latitude location could be used to illustrate the connection between TEC and foF₂. Finally, examination of the GPS TEC solar activity dependence should verify the connection between GPS TEC, TEC determined from faraday rotation,

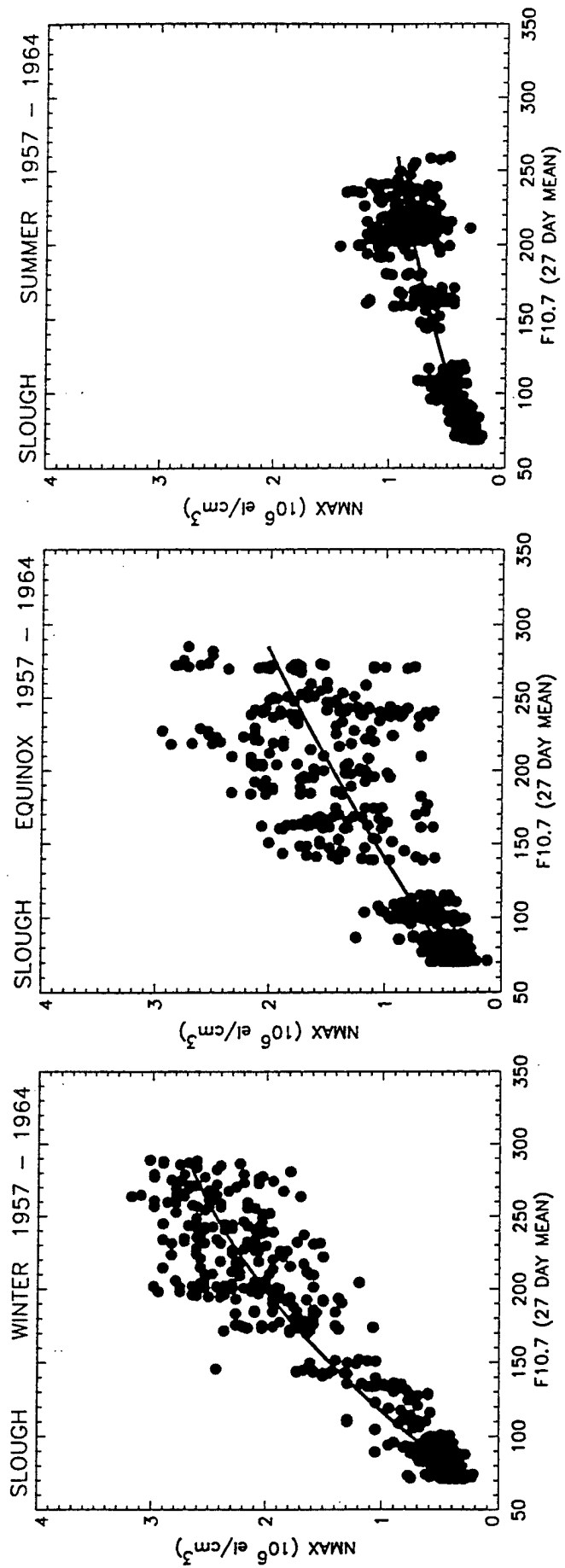
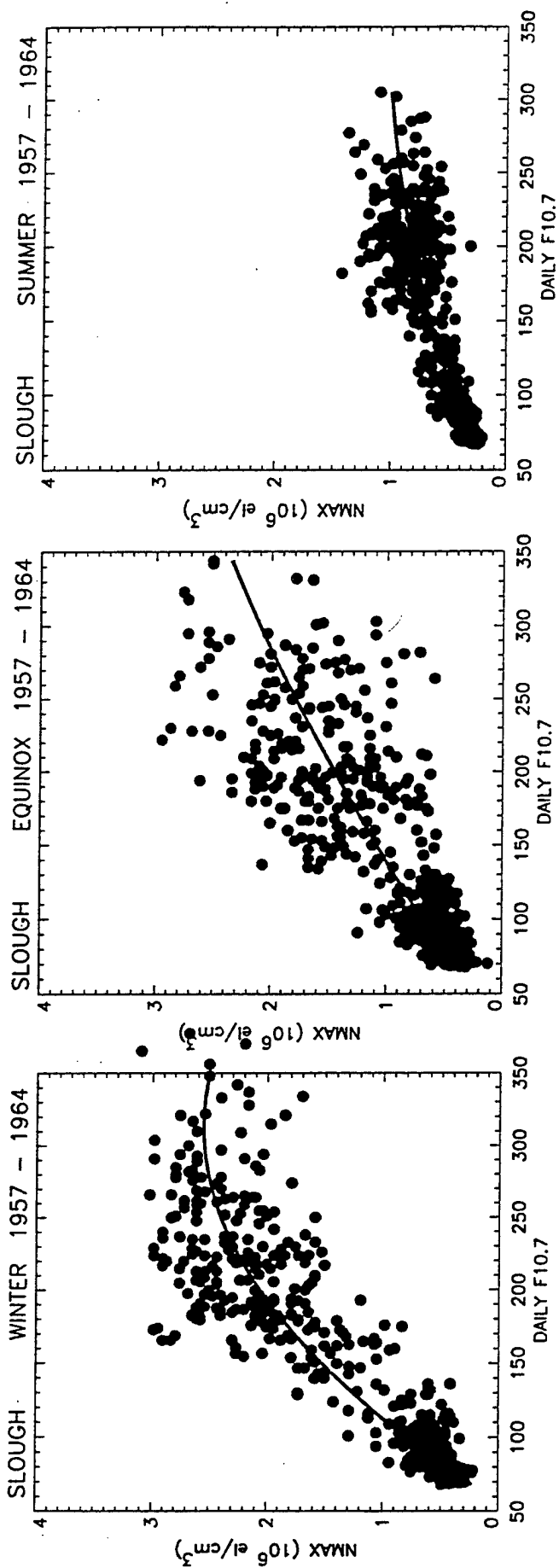


FIGURE 33

and foF₂. In this way, what is learned about the behavior of foF₂ over 4 solar cycles could be used in quantifying the relationship between TEC and solar activity.

3.7 Absolute Real-Time Ionospheric Measurements from GPS Satellites in the Presence of Anti-Spoofing

A study has been initiated to determine the possibility of using GPS measurements in real-time to determine the absolute ionospheric error. Until the onset of Anti-Spoofing, the most significant limitation for real-time GPS analysis was caused by the multi-path environment especially evident at low elevation angles. With anti-spoofing turned on, the lower signal to noise ratio additionally limits the accuracy of making absolute measurements until the satellite reaches an elevation of at least 30 degrees. We have investigated the potential accuracy of real-time analysis under both anti-spoofing on and off conditions. In addition, we began the design of a novel, non-recursive, adaptive filter that will lessen the effect of the low signal to noise ratio induced by anti-spoofing.

4. ELECTRON BACKSCATTER AND PROTON PRECIPITATION

4.1 Proton-H Atom Transport Model Developments

During the contract several issues arose concerning the Proton-H atom Transport (PHT) model. The simplest problem was that of inconsistent behavior in the secondary electron spectrum produced in a proton aurora as a function of the energy grid used. This proved to be a minor bug in the handling of the relevant cross sections and was easily corrected. Of greater concern was the question of how well does the program conserve particles and energy.

To study this problem, we carefully formulated statements of particle and energy conservation that could be used in testing the solutions of the transport model. In using our implementations of the conservation laws to study this problem, a series of bugs were found in the code. Some proved to be minor but three were crucial. One involved the conservation tests themselves and the other two the basic integration over altitudes that is performed when solving for the proton and H atom fluxes. The present code now conserves particles and energy at each altitude and pitch angle to better than 6%. At many altitudes it is better than 1%. The code is now more robust having been run from as high in altitude as 700 km and as low in energy as 100 eV. Previously, 500 eV was our lower energy limit and our top altitude had to be 600 km or below. The present limit of 100 eV is simply a result of our present cross sections having a 100 eV lower limit. Likewise, the 700 km is a limit simply because we have yet to try a higher boundary altitude.

While the initial testing of the model was performed on the Convex, the model has been ported to the VAX so it can be conveniently used with our entire suite of transport codes that reside on the VAX cluster. Another version of the proton-H atom model exists on the Convex that gives essentially the same results but has been modified to run more efficiently. It will be ported to the VAX sometime in the next year. We also ported the model to a Sun Sparc workstation.

4.2 Upgoing Electrons Produced in an Electron-Proton-Hydrogen Atom Aurora

We have performed the first test of a self-consistent theory for the combined electron-proton-hydrogen atom aurora. The results of this study are found in the paper "Upgoing electrons produced in an electron-proton-hydrogen atom aurora" by D.T. Decker, B. Basu, J.R. Jasperse, D.J. Strickland, J.R. Sharber, and J.D. Winningham. A copy of this paper is appended to this report (Appendix 1.).

4.3 Collisional Degradation of the Proton-H Atom Fluxes in the Atmosphere: A Comparison of Theoretical Techniques

Over the life of this contract, we have enjoyed a productive collaboration with the Polar Geophysical Institute in Apatity, Russia. The focus of that collaboration has been the comparison between three different theoretical models for proton-H atom transport. The results of this work can be found in manuscript titled "Collisional Degradation of the Proton-H Atom Fluxes in the Atmosphere: A Comparison of Theoretical Techniques" by D.T. Decker, B.V. Kozelov, B. Basu, J.R. Jasperse, and V.E. Ivanov. A copy of this manuscript is appended to this report (Appendix 1.).

4.4 Incident Proton Spectra: Ionospheric Effects of High-Energy Power Law Tails

Observations in the magnetosphere and the ionosphere suggest that proton spectra incident at the top of the ionosphere have nonthermal power law tails at energies above their characteristic or peak energy. We have investigated the effects these tails have in the ionosphere and summarized our results in a paper entitled "Incident Proton Spectra: Ionospheric Effects of High-Energy Power Law Tails" by B. Basu, D.T. Decker, and J.R. Jasperse. A copy of this paper is appended to this report (Appendix 1.).

4.5 Electron-Proton-H Atom Aurora: Comparison With Observations

While a model for the electron-proton-hydrogen atom aurora now exists, comparisons between theory and experiment are in their infancy. Accordingly, we searched for suitable data to use in testing the combined electron-proton-H atom auroral model. Overall, the results were discouraging. Rocket shots made in the late sixties and early seventies were disappointing in the quality of their data. The basic problem is the measurements do not provide an adequate specification of the inputs needed by the model nor many of the outputs needed for a through test of the model. Similarly, a recent rocket shot (ARIA) measured ion fluxes but the counting statistics are so poor as to make modeling an altitude profile a pointless exercise.

One brief study using the proton-H atom transport model was completed. What was done was to use the Hardy et al statistical model of auroral ion precipitation [1989] to supply the input proton fluxes to the model and then calculate the resulting H β emissions

at various latitudes, local times, and magnetic activities. This was then compared to the empirical $H\beta$ model of Creutsberg et al. [1988]. In Figure 34, we show a sample comparison where the dashed curves are from Creutsberg and the solid curves are from the model calculations. The time given at the top is the local magnetic time and results are shown for three levels of magnetic activity. Going left to right the solid curves are for $K_p = 4, 2, 0$ and the dashed curves are for $a_e = 360.1, 113.5, 25$. One can see that the general trends with magnetic activity are consistent, but clearly the model results are running up to a factor of 2 higher. Given the uncertainties concerning ground based measurements and the somewhat apples and oranges comparison that results from Hardy et al. being based on 18,000 satellite passes and Creutsberg et al being based on 14 nights, it is difficult to assess how serious a problem the model may have.

In another study, we attempted to model three emissions that were observed during the 1981 AFGL Auroral E rocket campaign. In this experiment there were upward looking photometer measurements but no successful particle measurements. This meant that we had to use one emission to determine the incident proton characteristics, another to determine the incident electron characteristics and then using the inferred inputs calculate a third emission to compare to observation. In Figure 35, we show the fit to the $H\beta$ emission assuming a 6.5 keV Maxwellian protons incident with an energy flux of .228 ergs/cm²-sec. In Figure 36, we show the fit to 3914Å assuming 1.3 keV Maxwellian electrons incident with an energy flux of 1.6 ergs/cm²-sec along with the incident protons. Finally in Figure 37 we show the VK 2762Å emission that results from using the inferred particle fluxes. The two curves come from using different O quenching factors. The S designates the aeronomically determined factor from Sharp and the P designates the laboratory determined factor from Piper. One can see that within the quenching uncertainty that we have good agreement. It should be noted that while an encouraging result, this case is not a very severe test of the proton-H atom model since most of the emission appears to come from the electrons.

5. MODELING HIGH LATITUDE F REGION BLOBS AND PATCHES

5.1 Modeling Polar Cap F-region Patches

We performed various simulations to study the formation of polar cap F-region patches. Our first efforts lead to a paper entitled "Modeling Polar Cap F Region Patches Using Time Varying convection" by J.J. Sojka, M.D. Bowline, R.W. Schunk, D.T. Decker, C.E. Valladares, R. Sheehan, D.N. Anderson, and R.A. Heelis. A copy of this paper is appended to this report (Appendix 1.).

Our next study focused on modeling daytime F layer patches over Sondrestrom and was described in the paper "Modeling Daytime F Layer Patches Over Sondrestrom" by D.T. Decker, C.E. Valladares, R. Sheehan, Su. Basu, D.N. Anderson, and R.A. Heelis. A copy of this paper is appended to this report (Appendix 1.).

We also have examined a scenario for producing density enhancements in the polar cap that was originally studied by *Anderson et al.*[1988]. Our purpose was to clarify what is happening in that scenario and verify that while it appears to be different from the scenarios described in *Sojka et al.*[1993] and *Decker et al.*[1994] in fact all three papers

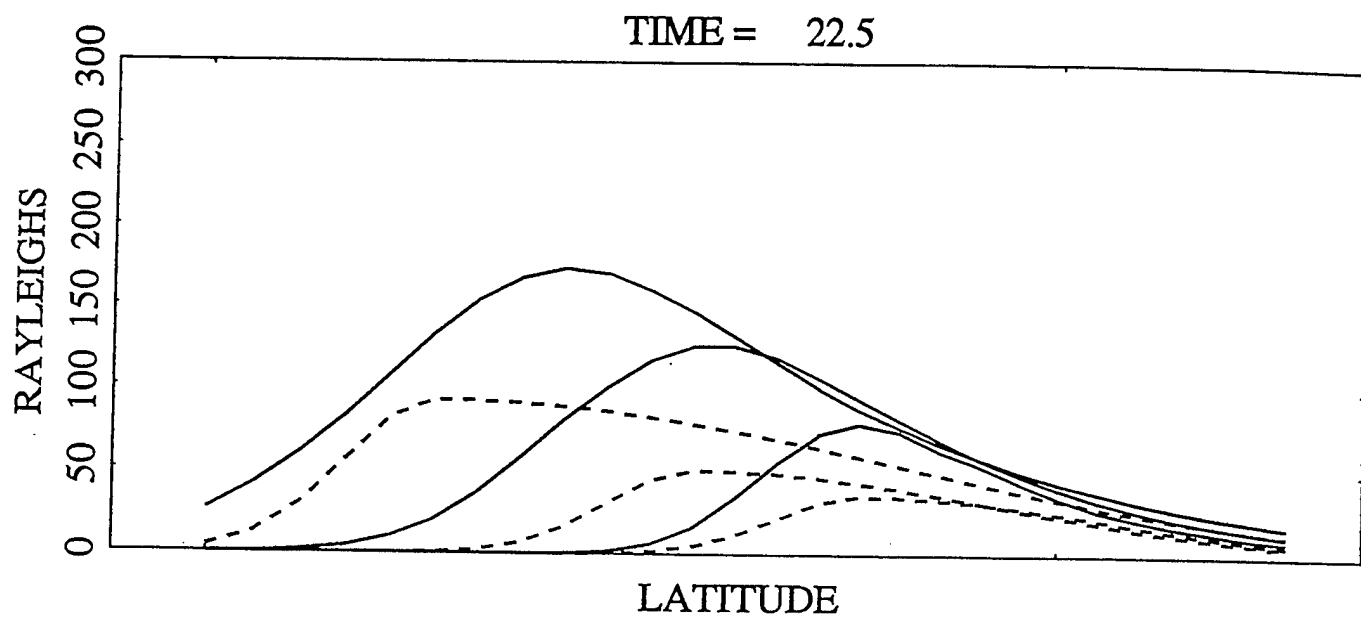


FIGURE 34

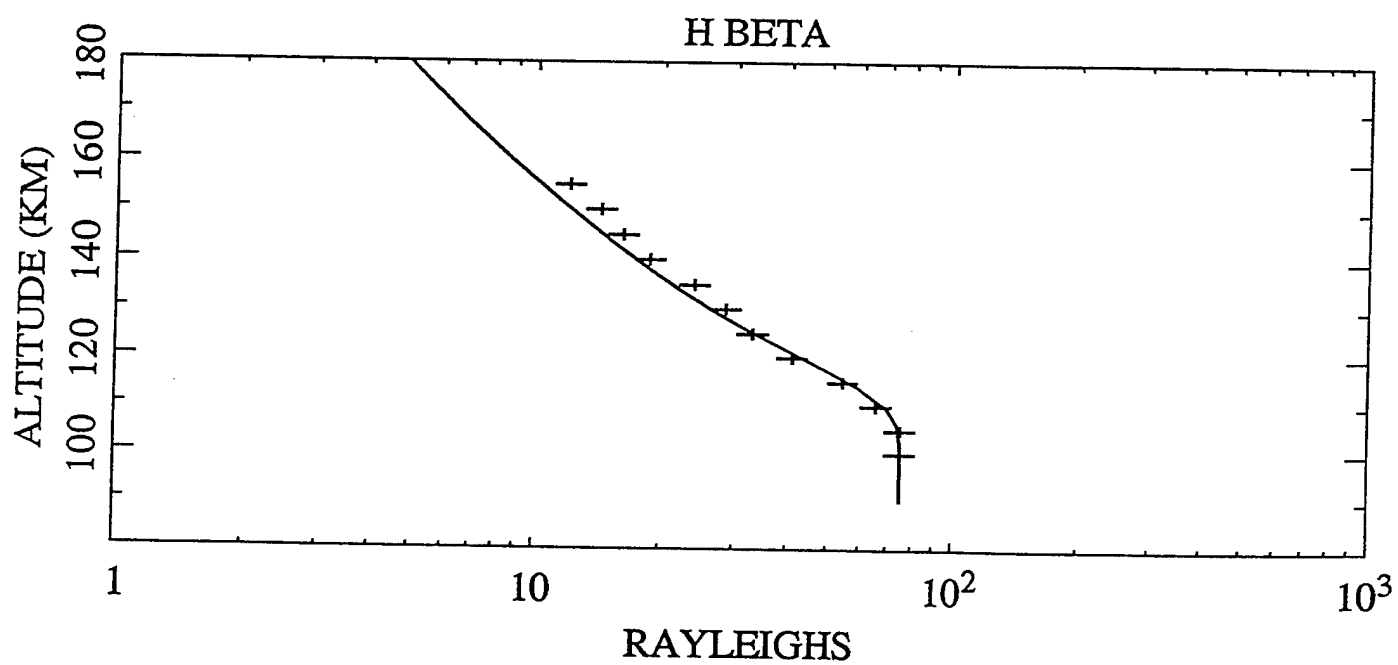


FIGURE 35

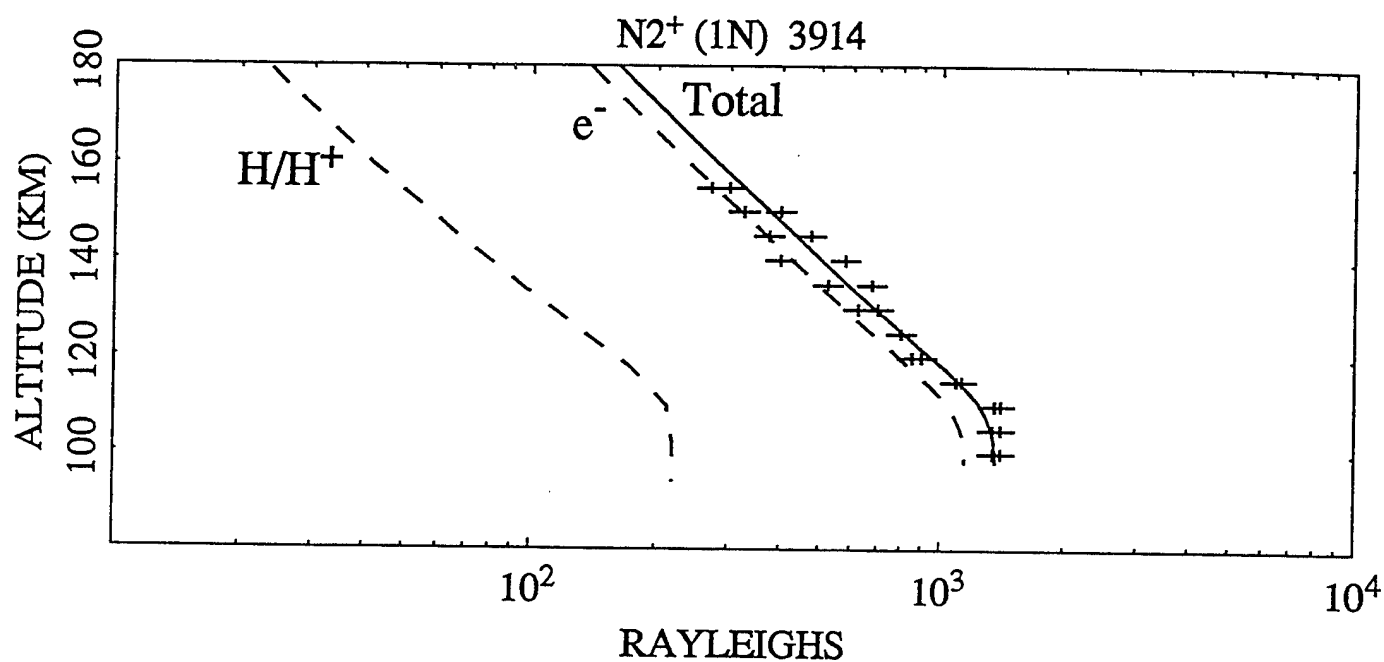


FIGURE 36

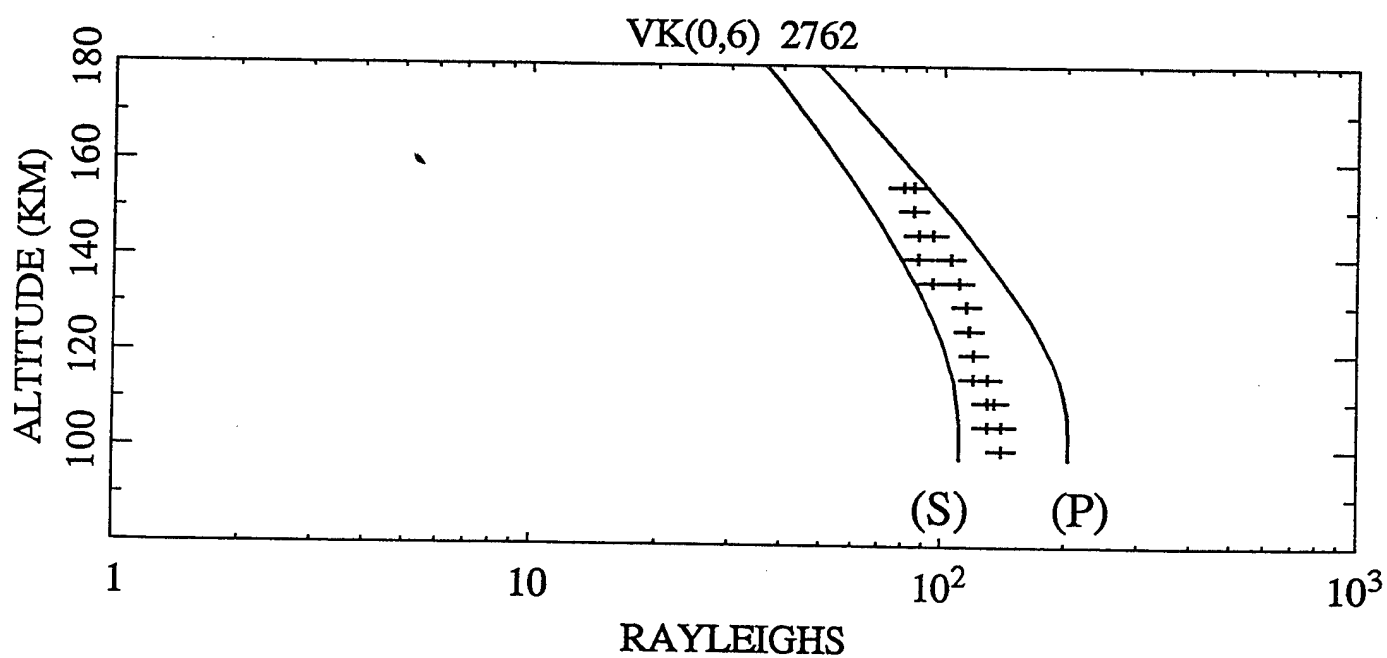


FIGURE 37

are describing essentially the same mechanism. That mechanism is one of changing in time the location of the type three trajectories. These are the trajectories where corotation and the magnetospheric potential act together to take plasma from the sunlit lower latitudes and bring it in and across the polar cap. In *Sojka et al.* [1993], the change was done by using the By dependence of the global convection pattern. In *Decker et al.* [1994], it was done by changing between Heelis patterns and Heppner/Maynard patterns. In repeating the Anderson et al. calculation, we have found that changing the polar cap radius and potential drop also changes where the type three trajectories are to be found. However the change is not one of going from a pattern that has no type three trajectories and thus creates no tongue of ionization (TOI) to a pattern that does. Rather both patterns have type three trajectories and create a TOI. What is different is that the large radius pattern creates a broader TOI as compared to that created by a small radius pattern. We also found that the signature on the ground is very sensitive to the chosen location. This indicates that under the same conditions different high latitude stations may have very different signatures of F-region structure. We also found that the structure produced was very sensitive to details of the convection pattern. It is not yet clear if this mechanism will work in general or if it is basically an artifact of the Heelis 82 convection pattern that was originally used.

5.2 Modeling Boundary Blobs

We have used GTIM to study the mechanism which generates F-region electron density enhancements known as boundary blobs. The results of our study are found in the paper "Modeling Boundary Blobs Using Time Varying Convection" by D.N. Anderson, D.T. Decker, and C.E. Valladares. A copy of this paper is appended to this report (Appendix 1.).

6. OPTICAL RADIATION

We investigated the ultraviolet radiations obtained on shuttle missions STS-4 and STS-39. The intensity of the radiations as a function of wavelength and tangent altitude have been examined. This involved the modification of programs that had been written for these flights in order to obtain the desired plots for these radiations. The SUN workstation, the gpx vax and the dsm vax were used for this purpose. As the gpx vax is no longer available, a way was found for reading the data on our optical discs. Most of the STS-4 data are now in the SUN workstation available for comparison with the AURIC code.

Phillips Laboratory began a new initiative to investigate the electrical discharges from thunderstorms that go upwards into the lower part of the ionosphere. Our part on this effort has been the design of an experiment to measure the electron temperature in the discharge. It consists of a UV/visible imager and two photometers. The radiations to be measured are H_{α} and H_{β} at 6563 and 4861 Angstroms. The theory of obtaining electron temperature from the ratio of these two radiations has been examined. It has been applied to laboratory measurements but not yet to thunderstorm discharges. Among the experimental problems that we have worked on are (a) the characteristics of the narrow band filters needed to make the measurements, (b) the simultaneous measurements of H_{α}

and H_p and computer recording of same, and (c) accurate timing signals into both sets of instruments for comparing the data obtained. A paper describing this experiment has been prepared for the meeting of the International Optical Engineering Society in August 1996.

REFERENCES

- Anderson, D.N., J. Buchau, and R.A. Heelis, Origin of density enhancements in the winter polar cap ionosphere, *Radio Sci.*, 23, 513, 1988.
- Balan, N., G. J. Bailey, and B. Jayachandran, "Ionospheric evidence for a non-linear relationship between EUV and 10.7-cm fluxes during an intense solar cycle", *Planet. Space Sci.*, 41, 141, 1993.
- Balan, N., G. J. Bailey, B. Jenkins, P. B. Rao, and R. J. Moffett, "Variations of ionospheric ionization and related solar fluxes during an intense solar cycle", *J. Geophys. Res.*, 99, 2243-2253, 1994.
- Bailey, G. J. and R. Sellek, *Annales Geophysicae*, pp171-189, 1990.
- Bilitza, D. and K. Rawer, New options for IRI electron density in the middle ionosphere, *Adv. Space Res.*, 10(11), 7-16, 1990.
- Creutzberg, F., R.L. Gattinger, F.R. Harris, S. Wozniak, and A. Vallance Jones, Auroral Studies with a Chain of Meridian Scanning Photometers 2. Mean Distributions of Proton and Electron Aurora as a Function of Magnetic Activity, *J. Geophys. Res.*, 93, 14591, 1988.
- Davies, K., *Space Science Reviews*, Vol. 25, pp 357-430, 1980.
- Decker, D.T., C.E. Valladares, R. Sheehan, Su. Basu, D.N. Anderson, and R.A. Heelis, Modeling daytime F layer patches over Sondrestrom, *Radio Science*, 29, 249, 1994.
- Doherty, P. H., E. Raffi, J. A. Klobuchar and, M. B. El-Arini, "Statistics of Time Rate of Change of Ionospheric Range Delay", *Proceedings of the 1994 ION-GPS Meeting*, Salt Lake City, Utah, September, 1994.
- Hardy, D.A., M.S. Gussenhoven, and D. Brautigam, A Statistical Model of Auroral Ion Precipitation, *J. Geophys. Res.*, 94, 370, 1989.
- Holzworth, R. H. and Meng, C. I., "Mathematical Representation of the Auroral Oval", *Geophysical Research Letters*, 2, No. 9, Sept. 1975.
- Klobuchar, J. A., private communication, 1994.

- Kersley, L. and J. A. Klobuchar, "Storm Associated Protonospheric Depletion and Recovery", *Planet. Space Sci.*, 28, pp. 453-458, 1980.
- Llewellyn, S.K. and R. B. Bent, Documentation and description of the Bent ionospheric model, Air Force Geophysics Laboratory, Report AFCRL-TR-73-0657, Hanscom AFB, Massachusetts, 1973. AD772733.
- Sojka, J.J., M.D. Bowline, R.W. Schunk, D.T. Decker, C.E. Valladares, R. Sheehan, D.N. Anderson, and R.A. Heelis, Modeling polar cap F region patches using time varying convection, *Geophys. Res. Lett.*, 20, 1783, 1993.
- Wanniger, L. "Ionospheric Monitoring Using IGS Data", presented at the 1993 Berne IGS Workshop, Berne, March 25-26, 1993.
- Wilson, B. D., Mannucci, A. J., Edwards, C. D. and Roth, T., "Global Ionospheric Maps Using a Global Network of GPS Receivers", *Proceedings of the International Beacon Satellite Symposium*, Cambridge, MA, 1992.
- Wilson, B. D. and Mannucci, A. J., "Instrumental Biases in Ionospheric Measurements Derived from GPS Data", *Proceedings of the 1993 ION-GPS Meeting*, Salt Lake City, Utah, 1993.

PRESENTATIONS AND PROCEEDINGS

We were involved in 49 presentations at various scientific meetings of which 10 appeared in published proceedings. There also 10 presentations that have been submitted to meetings that will be held within the next 6 months.

Doherty, P. H., B. Fejer, D. N. Anderson, and A. P. Creamer, "Low Latitude Ionospheric Response to Jicamarca, Storm-Time Vertical Drift Measurements", presented at the Cedar Storm Study workshop, March 1993, Millstone Hill, Westford, MA and the Spring AGU Meeting, May 1993, Baltimore, MD.

Klobuchar, J. A., S. Basu, and P. H. Doherty, "Potential Limitations in Making Absolute Ionospheric Measurements Using Dual Frequency Radio Waves from GPS Satellites", presented at the Ionospheric Effects Symposium, May 4-6, 1993, Alexandria, VA. Also appeared in the Proceedings of the Ionospheric Effects Symposium, 1993.

Jasperse, J.R., B. Basu, D.J. Strickland, R.E. Daniell, and D.T. Decker, "Combined Electron-Proton-Hydrogen Atom Aurora: Predictions of a Transport-Theoretical Model" presented at the Ionospheric Effects Symposium, May 4-6, 1993, Alexandria, VA. Also appeared in the Proceedings of the Ionospheric Effects Symposium, 1993.

Decker, D.T., D.N. Anderson, and B.W. Reinisch, "Day to Day Comparison of Calculated and Observed Electron Density Profiles at Midlatitudes" presented at Spring AGU meeting, May 1993, Baltimore MD and the XXIVth General Assembly of the International Union of Radio Science, August 1993, Kyoto, Japan.

Creamer, A.P., D.N. Anderson, P.H. Doherty, and B.G. Fejer, "Validation of the Phillips Lab Low Latitude Ionospheric Model with Jicamarca ISR Observations", presented at Spring AGU meeting, May 1993, Baltimore MD.

Decker, D.T., "Modeling the LTCS 2 and 6 Periods with the Phillips Laboratory Ionospheric Model", presented at the PRIMO Workshop, CEDAR Meeting, Boulder, CO, June 1993.

Decker, D.T., "Modeling Polar Cap Patches: The Present Status", presented at the HLPS Workshop, CEDAR Meeting, Boulder, CO, June 1993.

Decker, D.T., J.R. Jasperse, B. Basu, and D.J. Strickland, "The Theory of the Electron-Proton-Hydrogen Atom Aurora: Comparison with Observations, presented at the NATO Advance Research Workshop 20 Annual European Meeting on Atmospheric Studies by Optical Methods, September 1993, Apatity, Russia.

Klobuchar, J.A., P. Doherty, and M. El-Arini, "Potential Ionospheric Limitations to Wide Area Differential GPS", presented at ION-GPS 1993, September 21-24, 1993, Salt Lake City, Utah.

J.R. Jasperse, B. Basu, D.J. Strickland, D.T. Decker, J.R. Sharber, and J.D. Winningham, "Theory of the Electron-Proton-Hydrogen Atom Aurora: Comparison With Observations", presented at the Fall AGU meeting, December 1993, San Francisco CA.

D.T. Decker, C.E. Valladares, R. Sheehan, Su. Basu, D.N. Anderson, and R.A. Heelis, "Modeling Daytime F Layer Patches Over Sondrestrom", presented at the Fall AGU meeting, December 1993, San Francisco CA.

C.E. Valladares, D.T. Decker, R. Sheehan, Su. Basu, and D.N. Anderson, "Observations and Workstation Modeling of Large Scale Plasma Density Structures in the Cusp/Cleft Region", presented at the Fall AGU meeting, December 1993, San Francisco CA.

Snow, R.W., Osborne, A.W., Klobuchar, J.A., and Doherty, P.H., "Ionospheric Corrections to Precise Time Transfer Using GPS", presented at the Precise Time Transfer Institute meeting, December 6-9, 1993, Marina Del Ray, California.

El-Arini, M.B., Klobuchar, J.A., and Doherty, P.H., "Evaluation of the Wide-Area Differential GPS (WDGPS) Ionospheric Grid Algorithm During the Peak of the Current Solar Cycle", presented at the National Technical Meeting of the Institute of Navigation, January 24-26, 1994, San Diego, California.

D.T. Decker, J.R. Jasperse, and B. Basu, "The Status of Electron-Proton-Hydrogen Atom Transport Theory", presented at the Proton Aurora Workshop, CEDAR meeting, Boulder CO June 1994.

D.T. Decker, "GTIM/CTIM Comparisons", presented at the PRIMO Workshop, CEDAR meeting, Boulder CO, June 1994.

D.T. Decker, C.E. Valladares, D.N. Anderson, J.J. Sojka, and R.W. Schunk, "Modeling Polar Cap F-Region Patches: A Review of the Last 2 Years", presented at the Second Joint Workshop for CEDAR HLPS/STEP GAPS, June 1994, Peaceful Valley, Colorado.

D.N. Anderson, D.T. Decker, and C.E. Valladares, "Modeling Boundary Blobs Using Time Varying Convection", presented at the Second Joint Workshop for CEDAR HLPS/STEP GAPS, June 1994, Peaceful Valley, Colorado.

C. E. Valladares, D. T. Decker, R. Sheehan, D. N. Anderson and K. Fukui, Modeling the Formation of Polar Cap Patches Using Convection Elliptical Vortices, presented at the Second Joint Workshop for CEDAR HLPS/STEP GAPS, June 1994, Peaceful Valley, Colorado.

The following 7 presentations also were published in the Proceedings of the International Beacon Satellite Symposium, July, 1994.

P. H. Doherty, E. Raffi, J. Klobuchar, and M. B. EL-Arini,

"Statistics of Time Rate of Change of Ionospheric Electron Content", presented at the 1994 Beacon Satellite Symposium, July 1994, Aberystwyth, Wales.

H. Doherty, and J. A. Klobuchar, "Solar Cycle Dependencies in Mid-Latitude Total Electron Content", presented at the 1994 Beacon Satellite Symposium, July 1994, Aberystwyth, Wales.

J. A. Klobuchar, P. H. Doherty and M. B. El-Arini, "Mid-Latitude Differential TEC versus Station Spacing", presented at the 1994 Beacon Satellite Symposium, Aberystwyth, Wales, 11-15 July, 1994.

J. A. Klobuchar, P. H. Doherty, G. Bailey and K. Davies, "Limitations in Determining Absolute Total Electron Content from Dual-Frequency GPS Group Delay Measurements", presented at the 1994 Beacon Satellite Symposium, Aberystwyth, Wales, 11-15 July, 1994.

R.W. Snow, P. Romanowski, P.H. Doherty, J.A. Klobuchar, "A Comparison of Ionospheric Total Electron Content Measurements with Code and Codeless GPS Receivers", presented at the 1994 Beacon Satellite Symposium, Aberystwyth, Wales, 11-15 July, 1994.

W.A. Pakula, D.N. Anderson, M. Beaudet, J. Bendito, P.H. Doherty, J. Eicher, P.F. Fougere, L.F. Hughes, R. Inzirillo, N. Jakowski, M. Kapel, J.A. Klobuchar, H. Kuenzler, H.G. Kugland, C. Lottig, R. Leitinger, R. Maderbacher, J.R. Manzano, T.D. Raymund, V.H. Rios, R. Sheehan, B. Trepanier, C. Valladares, J. Whitfield, "Initial Total Electron Content Results from the Pan American Ionospheric Tomography Campaign", presented at the 1994 Beacon Satellite Symposium, Aberystwyth, Wales, 11-15 July, 1994.

M. Bakry El-Arini, R.S. Conker, T.W. Albertson, J.K. Reagan, J.A. Klobuchar, P.H. Doherty, "Comparison of Real-Time Ionospheric Algorithms for a GPS Wide-Area Augmentation System (WAAS)", presented at the 1994 Beacon Satellite Symposium, Aberystwyth, Wales, 11-15 July, 1994.

B.V. Kozelov, V.E. Ivanov, D.T. Decker, B. Basu, J.R. Jasperse, "Proton-Hydrogen Atom Transport in the Atmosphere: A Comparison of Computational Techniques", presented at the 21st Annual European Meeting on Atmospheric Studies by Optical Methods, London, England.

P. H. Doherty, E. Raffi, J. Klobuchar and M. B. El-Arini, "Statistics of Time Rate of Change of Ionospheric Range Delay", presented at the ION GPS-94 Conference in September 1994 in Salt Lake City, Utah. It also appeared in the Proceedings of ION GPS-94, Part 2, 1589, September 1994.

D.T. Decker, D.N. Anderson, and C.E. Valladares, "Modeling Boundary Blobs Using Time Varying Convection", presented at the 1994 Fall AGU meeting, December 1994, San Francisco, CA.

D.N. Anderson, A.J. Preble, and D. T. Decker, "Improving IRI90 Low Latitude Ionospheric Specification", presented at the 1994 AGU Fall meeting, December 1994, San Francisco, CA., the U.S. National U.S. National Radio Science Meeting, January 1995, and the IRI Workshop on Equatorial Phenomenon held in India in January 1995.

D.N. Anderson, J.A. Klobuchar, P. Doherty, P.F. Fougere, T. Raymund, W.A. Pakula, R. Leitinger, and N. Jakowski, "Tomographic Studies at Equatorial Latitudes", presented at the IRI Workshop on Equatorial Phenomenon held in India in January 1995.

David N. Anderson, D.T. Decker, and C.E. Valladares, "Modeling F-region Polar Cap Patches and Boundary Blobs", presented at the 1995 Cambridge Symposium/Workshop on Multiscale Phenomena in Space Plasmas held in Bermuda in February 1995.

J.A. Klobuchar, P.H. Doherty and M.B. El-Arini, "Correcting for the Effects of Ionospheric Range Delays on the Proposed Wide-Area Augmentation System (WAAS)", presented at the AGU Spring Meeting held in Baltimore MD in May 1995.

J. A. Klobuchar, P. H. Doherty and R. Leitinger, "Total Electron Content Over the Pan American Longitudes: March-April 1994". Presented at the International Union of Geodesy and Geophysics held in Boulder, CO in July 1995.

D.T. Decker and D.N. Anderson, "Theoretical Modeling of the 1994 Chile/MISETA Campaign", presented at the International Symposium on Equatorial Aeronomy held in Bali, Indonesia in March 1995, at the 1995 CEDAR Workshop held in Boulder, Colorado in June 1995 and at the IUGG XXI General Assembly held in Boulder, CO in July 1995.

D.T. Decker, D.N. Anderson, and C.E. Valladares, "Modeling F-region Polar Cap Patches and Boundary Blobs", presented at the IUGG XXI General Assembly held in Boulder, CO in July 1995.

R. Conker, M. B. El-Arini, T. Albertson, J. Klobuchar, and P. Doherty, "Development of Real-Time Algorithms to Estimate the Ionospheric Error Bounds fro WAAS", presented at The Institute of Navigation ION-GPS 95 Meeting held in Palm Springs, CA in September, 1995.

D. T. Decker and D. N. Anderson, "Theoretical Modeling of the 1994 Chile/MISETA Campaign", presented at the 1995 Fall American Geophysical Union meeting held in San Francisco in December, 1995 and the National Radio Science Meeting held in Boulder, Colorado in January, 1996..

R. W. Eastes, P.J. Espy, A.V. Dentamaro, D.T. Decker, "Modeling the N₂ Lyman-Birge-Hopfield bands in the dayglow: Including radiative and collisional coupling between the singlet states", presented at the 1995 Fall American Geophysical Union meeting held in San Francisco in December, 1995.

J. J. Sojka, R.W. Schunk, D.J. Crain, and P.H. Doherty, "Using RINEX TEC Observations to Determine Weather Effects in the Mid-Latitude Ionosphere", presented at the 1995 Fall American Geophysical Union meeting held in San Francisco in December, 1995.

D.N. Anderson, D.T. Decker, A.J. Preble, R.W. Schunk, and J.J. Sojka, "Comparison Between Theoretically Calculated and Observed Electron Density Profiles at Low and Mid Latitudes", presented at the National Radio Science Meeting held in Boulder, Colorado in January, 1996.

P.H. Doherty, D.N. Anderson, J. Eicher, and J.A. Klobuchar, "Total Electron Content Over the Pan American Longitudes: March-April 1994", submitted to the 8th International Ionospheric Effects Symposium to be held in Alexandria, VA, May 1996.

B. Basu, D.T. Decker, and J.R. Jasperse, "Incident Proton Spectra: Ionospheric Effects of High-Energy Power Law Tails", submitted to 8th International Ionospheric Effects Symposium to be held in Alexandria, VA, May 1996.

A.J. Preble, D.T. Decker, and D.N. Anderson, "Improving IRI90 Low Latitude Ionospheric Specification", submitted to the 8th International Ionospheric Effects Symposium to be held in Alexandria, VA in May 1996.

J.A. Vladimer, V.R. Ewell, M.C. Lee, P.H. Doherty, D.T. Decker, D.N. Anderson, and J.A. Klobuchar, "Ionospheric TEC Observations from the TOPEX Satellite", submitted to the 23rd IEEE International Conference of Plasma Science to be held in Boston, MA, June 3-5, 1996.

V.R. Ewell, J.A. Vladimer, M.C. Lee, P.H. Doherty, D.T. Decker, D.N. Anderson, and J.A. Klobuchar, "Ionospheric Equatorial Anomaly Formation Over Pacific and Atlantic Oceans Measured by the NASA TOPEX Satellite", submitted to the 23rd IEEE International Conference of Plasma Science to be held in Boston, MA, June 3-5, 1996.

D.T. Decker, C.E. Valladares, and D. N. Anderson, "Modeling F-Region Polar Cap Patches and Boundary Blobs", submitted to the 31st COSPAR Scientific Assembly to be held in Birmingham, United Kingdom in July 1996.

D. N. Anderson, D. T. Decker, and P. H. Doherty, "Global Ionospheric Modeling of Geomagnetic Storms", submitted to the 31st COSPAR Scientific Assembly to be held in Birmingham, United Kingdom in July 1996.

D. N. Anderson, D.T. Decker, and C.E. Valladares, "Modeling High Latitude F-region Mesoscale Structures", submitted to 25th General Assembly of URSI to be held in Lille, France from August 28 to September 5, 1996.

D. T. Decker and D. N. Anderson, "Simulations of GPS/MET Ionospheric Observations", submitted to 25th General Assembly of URSI to be held in Lille, France from August 28 to September 5, 1996.

P.H. Doherty, D.T. Decker, J.A. Klobuchar, and D.N. Anderson, "Observed Ionospheric Dependence on Solar Activity: Implications for an Improved Single Frequency GPS User Algorithm", submitted to ION-GPS 96 Meeting to be held in Kansas City, Missouri in September 1996.

JOURNAL ARTICLES

Sojka, J.J., M.D. Bowline, R.W. Schunk, D.T. Decker, C.E. Valladares, R. Sheehan, D.N. Anderson, and R.A. Heelis, Modeling polar cap F region patches using time varying convection, *Geophys. Res. Lett.*, 20, 1783, 1993.

Decker, D.T., C.E. Valladares, R. Sheehan, Su. Basu, D.N. Anderson, and R.A. Heelis, Modeling daytime F layer patches over Sondrestrom, *Radio Science*, 29, 249, 1994.

Jasperse, J.R., B. Basu, J.M. Retterer, D.T. Decker, and T. Chang, "High Frequency Electrostatic Plasma Instabilities and Turbulence Layers in the Lower Ionosphere", in *Space Plasmas: Coupling Between Small and Medium Scale Processes*, pp. 77-94, Geophysical Monograph 86, 1995.

Preble, A.J., D.N. Anderson, B.G. Fejer, and P.H. Doherty, Comparison Between Calculated and Observed F-Region Electron Density Profiles at Jicamarca, Peru, *Radio Science*, 29, 857-866, 1994.

Sturgis, C., UV/Visible absorption spectroscopy for atmospheric pollution measurements, in *Ultraviolet Technology V*, Proc. Int. Society for Optical Engineering, 2282, 126, July 1994.

El-Arini, M.B., R.S. Conker, T.W. Albertson, J.K. Reagan, J.A. Klobuchar, P.H. Doherty, Comparison of Real-Time Ionospheric Algorithms for a GPS Wide-Area Augmentation System (WAAS), *Navigation: Journal of The Institute of Navigation*, 41, 393, Winter 1994-1995.

Klobuchar, J.A., P.H. Doherty, and M.B. El-Arini, Potential Ionospheric Limitations to GPS Wide Area Augmentation System (WAAS)", *Navigation: Journal of The Institute of Navigation*, 42, 353-370, Summer 1995.

R.E. Daniell, Jr., L.D. Brown, D.N. Anderson, M.W. Fox, P.H. Doherty, D.T. Decker, J.J. Sojka, and R.W. Schunk, "Parameterized Ionospheric Model: A Global Ionospheric Parameterization Based on First Principles Models", *Radio Science*, 30, 1499-1510, 1995.

D.T. Decker, B. Basu, J.R. Jasperse, D.J. Strickland, J.R. Sharber, and J.D. Winningham, "Upgoing Electrons Produced in an Electron-Proton-Hydrogen Atom Aurora", *J. Geophys. Res.* 100, 21,409-21,420, 1995.

D.N. Anderson, D.T. Decker, and C.E. Valladares, "Modeling Boundary Blobs Using Time Varying Convection", *Geophys. Res. Lett.*, 23, 579-582, 1996.

C.E. Valladares, D.T. Decker, R. Sheehan, and D.N. Anderson, "Modeling the Formation of Polar Cap Patches Using Large Plasma Flows", *Geophys. Res. Lett.*, in press.

P. H. Doherty, J. A. Klobuchar and M. B. El-Arini, "Statistics of Time Rate of Change of Ionospheric Range Delay", accepted for publication in *Radio Science*.

APPENDIX 1

**Total Electron Content Over the Pan American Longitudes:
March-April 1994**

Patricia H. Doherty
Institute for Scientific Research
Boston College
Newton, MA 02159

David N. Anderson and Joseph Eicher
Phillips Laboratory
Hanscom AFB, MA 01731

John A. Klobuchar
Innovative Solutions International
Lincoln, MA 01773

Abstract

An experimental campaign to measure diurnal changes in Total Electron Content, (TEC), over the wide latitude range from approximately 50 degrees North to 40 degrees South was carried out from 28 March through 11 April, 1994 by monitoring the differential carrier phase from the US Navy TRANSIT Navigation Satellites, using a chain of ground stations aligned along the approximate 70 degree west longitude meridian. This campaign was conducted primarily to study the day-to-day variability of the equatorial anomaly region. The experimental plan included using the received values of TEC from the chain of stations to construct profiles of electron density versus latitude using tomographic reconstruction techniques, and then, to compare these reconstructions against a theoretical model of the low latitude ionosphere.

The diurnal changes in TEC along this latitude chain of stations showed a high degree of variability from day-to-day, especially during a magnetic storm which occurred near the beginning of the campaign. The equatorial anomaly in TEC, showed large changes in character in the two hemispheres, as well as differences in magnitude from day to day. The latitudinal gradients of TEC, especially in the lower mid-latitudes, also showed large differences between magnetic storm and quiet conditions. Comparisons of the TEC data with the theoretical model illustrate the sensitivity of the model calculations to changes in magnetic $E \times B$ drift, and serves to validate the strong dependence of these drifts on the formation and the strength of the equatorial anomaly regions.

Introduction

The equatorial anomaly region is characterized by the highest values of peak electron density and Total Electron Content in the worldwide ionosphere. These large values are primarily due to the daytime upward $E \times B$ drift at the magnetic equator which drives the ionization to higher altitudes. As the layer is lifted to higher altitudes, it diffuses down field lines that connect to the ionosphere north and south of the equator causing crests at latitudes approximately $\pm 15^\circ$ from the magnetic equator. The day-to-day variability of the equatorial ionosphere can be very large, due to changes in the strength of the $E \times B$ drift and from differences in the day-to-day strength of both the meridional and zonal component of neutral winds.

While many measurements of the equatorial and low latitude ionosphere have been made by various techniques, beginning with bottomside ionosondes, then by incoherent scatter radars at Jicamarca, Peru and at Kwajalein Island, later by topside sounders, and finally by a dual frequency, dispersive radar on the TOPEX/POSEIDON satellite, continuous measurements of the ionosphere over a wide latitude range, in a single longitude sector, have not been generally available. *Deshpande, et al., (1977)*, first showed the day-to-day variability of the low latitude Total Electron Content, (TEC), and later *Rastogi and Klobuchar, (1990)* showed examples of the day-to-day variability in TEC over the Indian sub-continent. Model studies by *Klobuchar, et al., (1991)*, showed that different $E \times B$ drifts could significantly change the TEC and the electron density at the F2 region peak over a wide range of latitudes, but little actual diurnal data over a wide range of latitudes has been available to check the validity of this model.

In order to measure the day-to-day variability of the ionosphere over a wide range of latitudes, a chain of stations was set up along the approximate 70 degrees west longitude meridian to make measurements of TEC using the dual frequency coherent signals from the US Navy TRANSIT Navigation, (NNSS) Satellites. Figure 1 illustrates the station chain. The sites were located at Hanscom AFB, MA, on the islands of Bermuda and Puerto Rico as well as at Merida, Venezuela, La Paz, Bolivia and Tucuman, Argentina. The planned site at Tabatinga, Brazil was not operated due to logistical difficulties and resulted in the WABS data gap, (Winterbottom 1994). Also shown in Figure 1 are typical NNSS Satellite passes, both a northbound and a southbound one, to illustrate that the station chain was nearly ideal for such measurements.

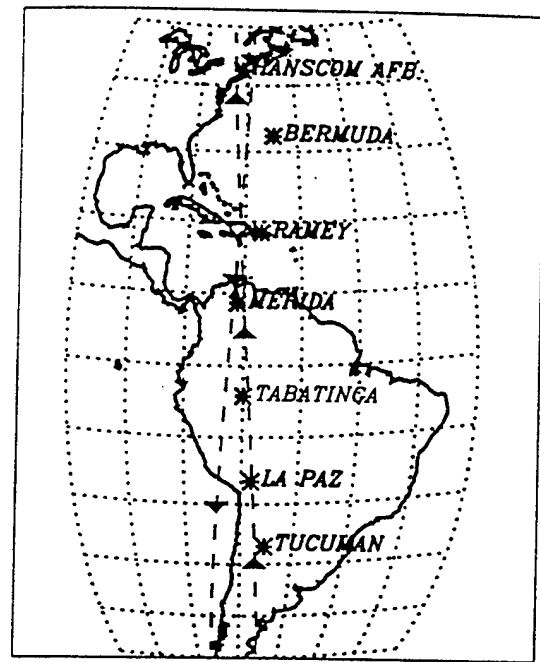


Figure 1) Map of stations along the $\approx 70^\circ$ west longitude meridian used in the campaign.

Ionospheric Measurements

The NNSS satellites transmit coherent radio beacons at 150 and 400 MHz. To determine the measurement of TEC along the 70 degree meridian, the relative differential carrier phase recorded at all sites was combined, converted to equivalent vertical TEC and changed into absolute TEC values using a visual, multi-station version of the two station method developed by *Leitinger, et al., (1975)*. There were six NNSS satellites transmitting on the operational navigation frequencies during the approximate two week period of the campaign, making it possible to record a high elevation pass from one of the NNSS satellites from the chain of stations approximately every 2 hours.

The campaign data is complemented with simultaneous measurements of TEC from dual frequency GPS and from vertical TEC measured with the TOPEX/POSEIDON satellite. GPS dual frequency data recorded at Arequipa, Peru and Santiago, Chile was obtained from the International GPS Service for Geodynamics network that is managed by the Jet Propulsion Laboratory (*IGS, 1995*). For this data set, absolute measures of TEC were made by combining the differential phase and differential group delay measurements. The slant TEC values then were converted to equivalent vertical TEC at 400 km. In addition, coincident measurements from the TOPEX/POSEIDON satellite are also presented in this study. The TOPEX satellite mission is dedicated to the study of ocean topography. The onboard dual frequency (5.2 and 13.6 Ghz) altimeter provides near global vertical TEC measurements over the ocean areas. In addition to TEC measurements, attempts have been made to detect the occurrence of phase and amplitude scintillation in the equatorial region during the campaign period. The GPS receivers at Arequipa and Santiago were used to detect phase scintillation effects while GPS receivers co-located at the NNSS monitoring sites at Merida and Tucuman were used to detect the presence of amplitude scintillation.

The measurements were made near solar minimum in late March and early April, 1994. Geomagnetic activity levels were considered quiet in the first few days of the campaign. A major magnetic storm began on April 1st, and the remainder of the period of observations had at least moderate geomagnetic activity. Data recorded during the campaign thus allowed the opportunity to study the latitudinal gradients of the ionosphere during both geomagnetically quiet and disturbed conditions.

Experimental Results

An example of equivalent vertical TEC from the full chain of six stations is shown in Figure 2. In this figure, the TEC is plotted from approximately 50° North to 40° South, a latitude span of 90° encompassing both sides of the equatorial region. At this longitude sector, the magnetic equator is located at approximately 11° South geographic latitude. This figure shows a classic case of two clearly defined anomaly regions spaced approximately 10 to 15 degrees away from the geomagnetic equator in both the northern and southern hemispheres. Note that the two stations from which the southern anomaly peak in equivalent vertical TEC is inferred give somewhat different TEC values, though they both show the peak at the same latitude. This difference in equivalent vertical TEC is due to errors in converting from the measured slant TEC to an equivalent vertical TEC when looking through gradients which are a function of elevation angle. This problem has been discussed by *Tsedilina, et al., (1994)*.

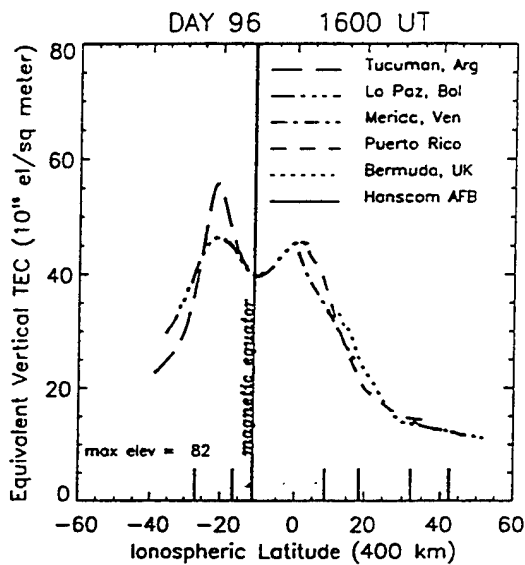


Figure 2) Equivalent Vertical TEC from the full chain of six stations at approximately 1600 UT on 6 April 1994.

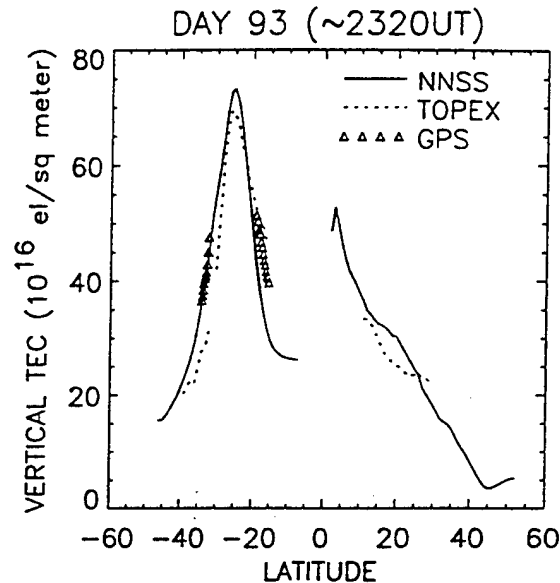


Figure 3) Comparison of TEC measurements from the NNSS, TOPEX and GPS satellite systems at approximately 2320 UT on 3 April 1994.

To access the accuracy of the TEC measurements made during the campaign, equivalent vertical TEC from GPS receivers located at Santiago, Chile and Arequipa, Peru and vertical TEC measurements made via the TOPEX/POSEIDON satellite were compared with campaign data. Figure 3 illustrates one of these comparisons. The GPS measurements shown in this figure represent simultaneous measurements of equivalent vertical TEC at 400 km. Since GPS satellites are located at an altitude greater than 20,000 km and the NNSS satellites are at 1200 km, simultaneous measurements from the two satellite systems are relatively short in local time. The TOPEX measurements in this illustration are restricted to times when the TOPEX ground track comes within one hour local time of the campaign measurements. The TOPEX satellite is located at 1300 km and provides vertical measurements of TEC to that height. This figure shows that the GPS data measured at Santiago is in good agreement with the NNSS measurements, while the GPS measurements made at Arequipa are somewhat higher. The GPS measurements near Arequipa, however, are in agreement with the TOPEX measurements. The TOPEX and NNSS calculations compare favorably in the shape and geographic location of the southern anomaly peak. The differences occur in the slight shift in the anomaly region surrounding the southern anomaly peak and the magnitude at the peak. The TOPEX calculations illustrate a peak that is approximately 6 TEC units smaller than the NNSS measurements. This difference could represent an error in the slant to vertical conversion process used for the NNSS data.

The PANAM campaign provided the unique opportunity to observe the full diurnal development and decay of the equatorial anomaly. Figure 4 illustrates measurements from a series of satellite passes for four consecutive days during the campaign. Note that each pass is offset by 15 TEC units for each hour of local time after noon to allow a visual separation between passes. In this figure, a classic response to the $E \times B$ drift is portrayed where the anomaly begins to develop by late morning, but does not peak until near 2000 hours local time. Not all six stations were operating for these days, but the

Figures 5a through 5d illustrate a comparison of the data with a sequence of model calculations. Figure 5a shows the equivalent vertical TEC measurements recorded on the 6th of April. For clarity, the approximate local time is printed near the left y axis and each curve is offset by a factor of 40 TEC units. This data shows a well defined equatorial anomaly at local noon. It peaks near 1900 local time and begins to show signs of decay at 2300 hours. The next three panels represent model calculations for comparable geomagnetic, seasonal and solar conditions. The results shown in Figure 5b are based on a climatological vertical $E \times B$ drift pattern for solar moderate conditions. Note that the local time development and the dip latitude positions of the peaks are realistic while the magnitudes of the peaks are much smaller than those exhibited in the data measurements. Initial efforts to increase the magnitude of the equatorial anomaly peaks were made by increasing the $E \times B$ drift. The results (not shown) produce larger peaks but also extend the anomaly out to higher latitudes. The base run of the model shown in Figure 5b used a temperature model that was originally developed for the mid-latitude region. Figure 5c represents the model calculations that include a more appropriate low-latitude temperature model (Brace and Theis, 1981). This modification produces sharper anomaly peaks and more realistic slopes poleward of the anomaly peaks. The dip latitude positions of the anomaly peaks are accurately maintained, but the magnitude of the peaks are still much smaller than the data calculations. The $E \times B$ vertical drift velocities used in the model are based on drift measurements made at Jicamarca, Peru. In general, they are applied in the model with no altitude dependence. Figure 5d illustrates model results when a simple linear height variation in the vertical drift is incorporated into the calculations. This modification produces more accurate peak shapes in both hemispheres and realistic slopes to higher latitudes within ± 20 degrees dip latitude. The unrealistic change induced at latitudes greater than ± 20 degrees indicates that the drift gradient needs to be refined. Although, the magnitude of the anomaly peaks have been increased they are still lower than the data measurements.

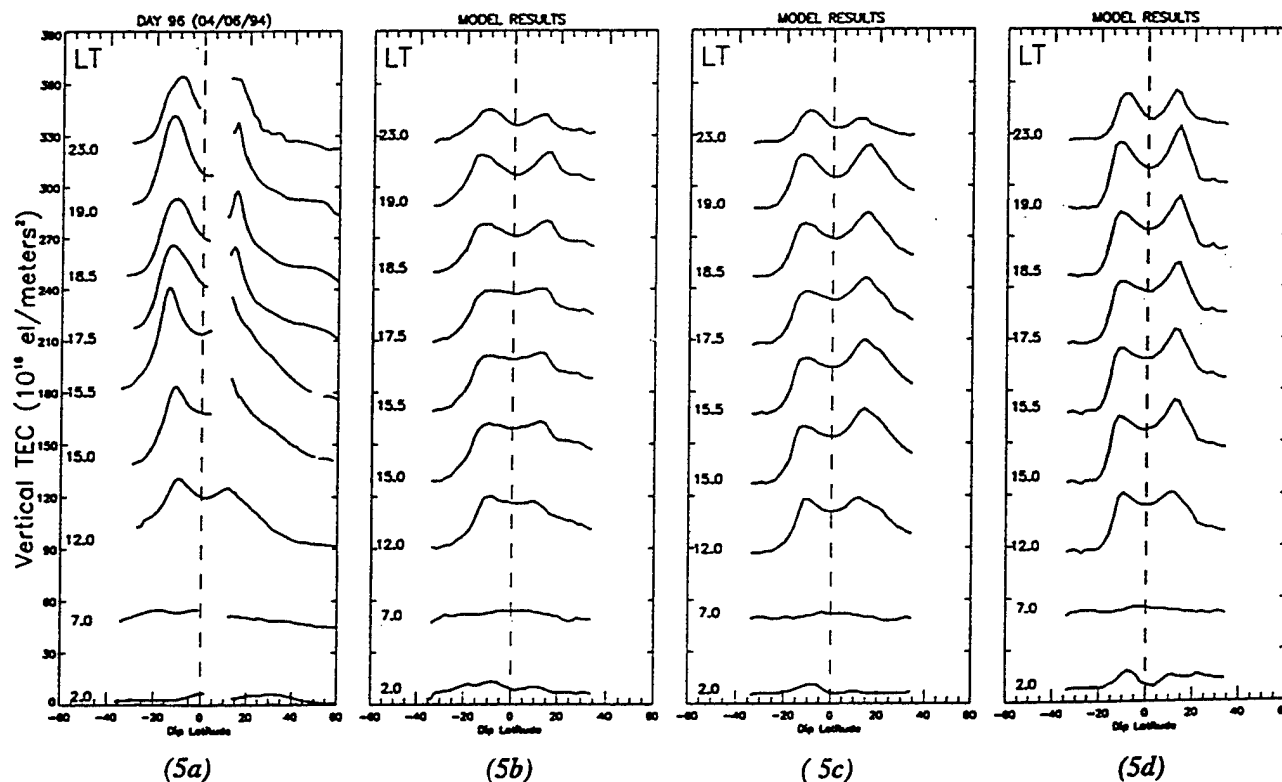


Figure 5a) Equivalent Vertical TEC measurements of 6 April 1994.

Figure 5b) Model calculations based on climatological $E \times B$ drift and original temperature model (see text).

Figure 5c) Model calculations with a more appropriate low latitude temperature model.

Figure 5d) Model calculations with a more appropriate low latitude temperature model and an $E \times B$ drift gradient.

These comparisons have illustrated the sensitivity of the equatorial anomaly to changes in ion and electron temperatures and $E \times B$ drift velocities. Additional calculations are in progress to investigate neutral wind effects and to refine the $E \times B$ drift gradient applied in the model. In this study, GTIM has shown the capability to reproduce some of the major features of measured data in the low-latitude region even under geomagnetically disturbed conditions.

Scintillation Observations

Measurements of scintillation activity were also detected during the campaign period. Ionospheric scintillation is caused by small scale irregularities in the electron density of the F2 region of the ionosphere. The most intense scintillation is found in the equatorial anomaly region. Prior studies have shown that scintillation observations have a distinct diurnal dependence. In the equatorial anomaly region, they are most likely to occur between sunset and midnight and may continue until dawn under disturbed conditions. Scintillation also has a clear longitudinal and seasonal dependence, where, in the American sector, scintillation is most likely to occur from September through March and is rarely experienced from May through August. These studies also show a clear dependence on solar activity, where occurrences of scintillation decrease with decreasing solar activity (Aarons and Basu, 1985, Basu et al., 1988, Wanniger, 1993, Aarons and Basu, 1994).

The GPS measurements made during the campaign to detect phase and amplitude scintillation conform to those earlier studies. Phase scintillation is generally a result of rapid large scale (1 km or greater) variations in TEC, therefore, it is possible to infer phase scintillation by observing rapid changes in TEC. In this study, the TEC calculations made with the dual frequency GPS data recorded at Arequipa and Santiago were utilized to infer the presence of phase scintillation activity. This was carried out by high pass filtering the 30 second values of slant TEC to remove the long term variations caused by diurnal changes and the changing elevation angle to the satellite. Relative changes in TEC over one minute periods then were computed to infer the strength of phase fluctuations observed from these two monitoring stations. Figure 6 summarizes these results for the Arequipa site on the 9th of April. In this figure, relative changes in TEC over one minute periods are plotted versus local time at the ionospheric pierce point for each of the GPS space vehicles noted in the left y-axis. The scale located in the lower right hand corner of the figure depicts the size of the fluctuations in TEC units. This figure illustrates that varying degrees of scintillation effects were observed between 0000 and 0200 hours local time by GPS space vehicles 5, 9, 13 and 20. Simultaneous measurements from GPS satellites 12 and 26 show no signs of scintillation. Results of this analysis for the entire campaign period show that occurrences of phase scintillation were detected from this site on seven nights during the campaign. On the nights of April 3rd and 4th, longer periods of phase scintillation were detected until dawn. Figure 7 displays the results during the same day for the Santiago station. Note that there are no measurements displaying rapid changes in TEC from this location. Analysis results for this station resulted in the detection of one period of mild phase scintillation effects in the early morning hours of April 4th.

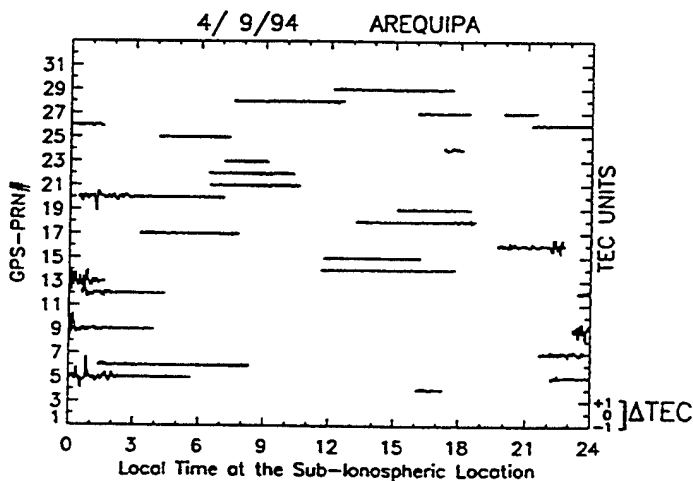


Figure 6) Changes in TEC over periods of one minute measured with GPS satellites from Arequipa on 9 April 1994.

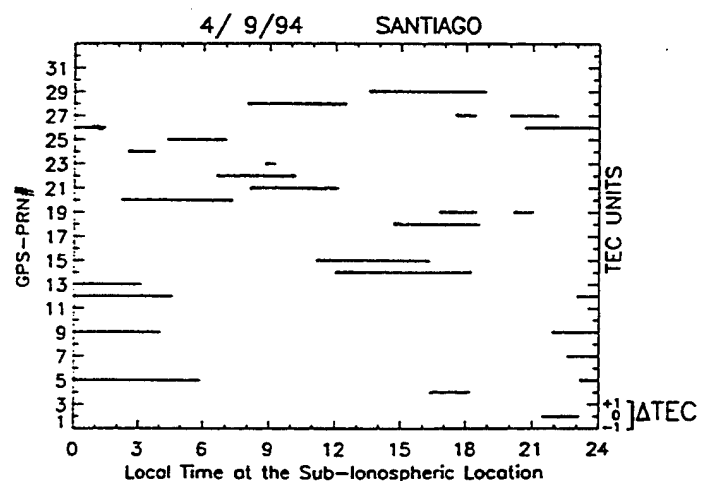


Figure 7) Changes in TEC over periods of one minute measured with GPS satellites from Santiago on 9 April 1994.

In addition to the phase scintillation that was inferred by the GPS measurements made at Arequipa and Santiago, amplitude scintillation measurements were made by GPS receivers that were co-located at the TRANSIT monitoring sites at Tucuman and Merida. The single frequency receiver at Tucuman was only able to measure amplitude scintillation, while the dual frequency receiver at Merida was used for both TEC and amplitude scintillation measurements. The GPS measurements made at Tucuman and Merida also agree with earlier studies on scintillation and complement the phase scintillation measurements made at Arequipa and Santiago. At the Tucuman station, evidence of low level amplitude

scintillation (2 to 3 dB fades peak-to-peak) was observed for one to three hours on six of the thirteen nights of operation. Two additional days, April 3rd and 4th, exhibited more intense scintillation effects (*Bishop and Basu, 1995*). The data recorded at Merida was carefully inspected for signs of amplitude scintillation by calculating the S_4 scintillation index during all the local nighttime hours. Values of S_4 were consistently below .2, indicating that scintillation was not observed from Merida during the entire campaign.

The primary reason for the differences in scintillation observed at these sites is illustrated in Figure 8. Equatorial scintillation is caused by the irregularities that originate in the F2 layer of the ionosphere over the equator. Near sunset, the layer is driven to higher altitudes over the equator by vertical $E \times B$ drift. At these higher altitudes, the layer, together with the embedded irregularities, diffuses down magnetic field lines producing scintillation effects at the height of the F2 layer at latitudes away from the equator. Figure 8 illustrates this scenario by showing magnetic field lines intersecting different heights over the magnetic equator. Also shown in this figure are slant ray paths from various GPS satellites to some of the stations used for scintillation measurements in the campaign. Assuming a mean height of 400 km for the peak of the F2 region, this figure indicates that the slant ray paths from the station located at Santiago, Chile can see up to 1000 km over the equator, as well as a height as low as 500 km over the equator. Due to its close proximity to the Santiago station, the ray paths from Tucuman were omitted from this figure. However, the slant ray paths from Tucuman indicate that the visibility over the magnetic equator ranged from approximately 400 km to 700 km. From the station at Arequipa, Peru, slant ray paths could see from the 400 km intersection over the magnetic equator to a height of nearly 600 km. The mountainous terrain surrounding the Merida, Venezuela station seriously limited the view toward the magnetic equator to 24° elevation. Therefore, slant ray paths from this location were only able to measure irregularities that occurred at heights in excess of 1000 km over the magnetic equator. Taking into account that scintillation effects were observed at Arequipa and Tucuman but not at Merida indicates that the height of irregularities over the magnetic equator during the campaign period was consistently below 1000 km. An interesting suggestion made by figure 8 is that with as few as three strategically located GPS monitoring stations, the vertical extent of the height of irregularities over the magnetic equator over the western portion of South America can be monitored in near real time.

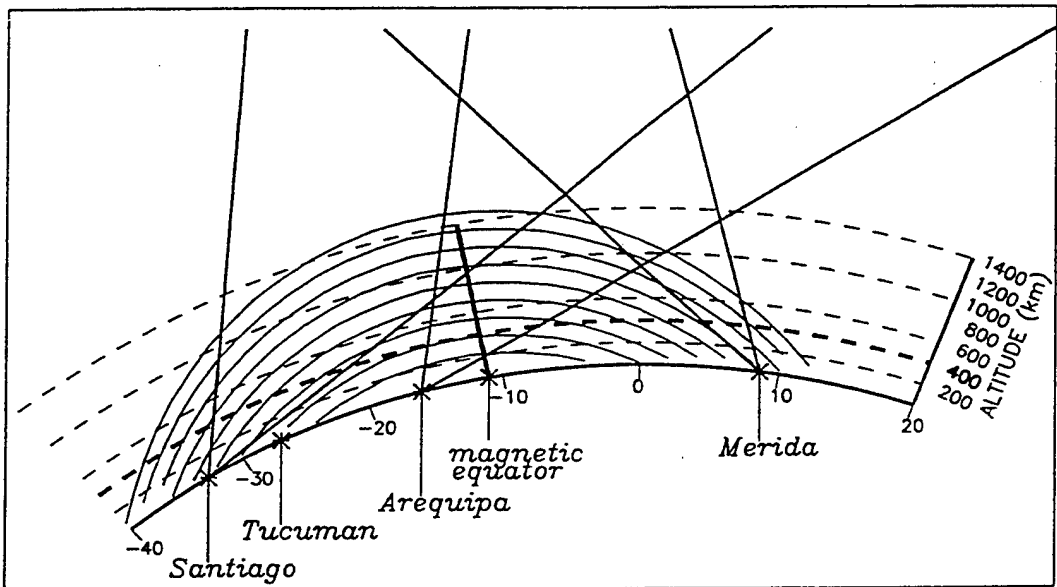


Figure 8) Magnetic field lines over the geomagnetic equator with slant ray paths from various GPS satellites to ground receiver sites.

Conclusions

The first attempt at measuring TEC over a large geographic latitude range has been successful. The data base collected illustrates the large day-to-day variability in the occurrence, location and amplitude of the equatorial anomaly. It is surprising that the TEC values are so low in the latitude range greater than $\pm 40^\circ$, and that the latitudinal gradients in TEC are steeper on the poleward edge of the southern anomaly peak than on the poleward edge of the northern anomaly peak. The multi-station data measurement technique has been validated by simultaneous measurements of TEC from dual

frequency GPS and dual frequency altimeter measurements from the TOPEX/POSEIDON satellite. Differences between these data sources is largely a factor of differences in slant to vertical conversion errors.

The GPS data recorded during the campaign was instrumental in defining the presence and magnitude of phase and amplitude scintillation. In addition, use of the GPS measurements have inferred a possible technique to determine the vertical extent of the height of irregularities over the magnetic equator in near real time.

Model comparisons have illustrated the sensitivity of the equatorial anomaly to changes in $E \times B$ vertical drift and have defined an apparent altitude dependence in the vertical drift measurements. Additional modeling work is required to investigate the neutral wind effects and to further test different drift gradients to determine how closely the model can fit the actual experimental data over a wide latitude range.

The prime purpose of the campaign was to develop an equatorial data base to be used in ionospheric tomography reconstructions. The absence of a station near the geomagnetic equator will hamper making continuous reconstructions of the equatorial ionosphere. Additional work is required to perform the actual tomographic reconstructions.

Acknowledgments. The authors would like to thank the many members of the Ionospheric Effects Division at Phillips Laboratory who participated in the campaign. Additional thanks are extended to Mr. Jay Spaulding at the U. S. Coast Guard Research and Development Center in Groton, Connecticut for the loan of the GPS Ashtech receiver that was used in Merida, Venezuela.

References

- Aarons, J. and S. Basu, "Scintillation on Trans-Ionospheric Radio Signals", Handbook on Geophysics and the Space Environment, A. S. Jursa, ed., Section 10.9, Air Force Geophysics Laboratory, 1985, NTIS accession number ADA 167000.
- Aarons, J. and S. Basu, "Ionospheric Amplitude and Phase Fluctuations at the GPS Frequencies", in Proceedings of ION GPS-94, The Institute of Navigation, Washington, D. C., September, 1994.
- Basu, S., E. Mackenzie and Su. Basu, "Ionospheric Constraints on VHF/UHF Communications Link During Solar Maximum and Minimum Periods", RADIO SCIENCE, Vol 23, No. 3, pp 363-378, May-June 1988.
- Bishop, G., and S. Basu, "Impacts of Ionospheric Fading on GPS Navigation Integrity", in Proceedings of the 1994 National Technical Meeting, The Institute of Navigation, Washington, D.C., January 1995.
- Brace, L. H., and R. F. Theis, "Global empirical models of ionospheric electron temperatures in the upper F region and plasmasphere based on in situ measurements for the Atmospheric Explorer-C, ISIS-1 and ISIS-2 Satellites", JATP, Vol. 43, No. 12, pp 1317-1343, 1981.
- Deshpande, M. R., R. G. Rastogi, H. O. Vats, J. A. Klobuchar, G. Sethia, "Effect of Electrojet on the Total Electron Content over the Indian Subcontinent", NATURE, V 267, pp 599-600, June 1977.
- IGS, "International GPS Service for Geodynamics", published by the International Association of Geodesy, Central Bureau, JPL, Pasadena, CA, May 1995.
- Klobuchar, J. A., "Ionospheric Effects on GPS", GPS WORLD, April 1991.
- Klobuchar, J. A., D. N. Anderson, and P. H. Doherty, "Model Studies of the Latitudinal Extent of the Equatorial Anomaly during Equinoctial Conditions", RADIO SCIENCE, Vol. 26, No. 4, pp 1025-1047, July-August 1991.

Leitinger, R., G. Schmidt, and A. Tauriainen, "An Evaluation Method Combining the Differential Doppler Measurements from Two Stations that Enables the Calculation of the Electron Content of the Ionosphere", *Journal of Geophysics*, Vol. 41, pp 201, 1975.

Preble, A. J., D. N. Anderson, B. G. Fejer, and P. H. Doherty, "Comparison between calculated and observed F region electron density profiles at Jicamarca, Peru", *Radio Science*, Vol. 29, No. 4, pp 857-866, July-August, 1994.

Rastogi, R. G., and J. A. Klobuchar, "Ionospheric Electron Content within the Equatorial F2 Layer Anomaly Belt", *J. Geophys. Res.*, Vol. 95, No. A11, pp 19,045-19,052, Nov. 1, 1990.

Tsedilina, E. E., O. V. Weitsman, and H. Soicher, "Time Delay of Transionospheric Radio Signals in a Horizontally Inhomogeneous Ionosphere", *RADIO SCIENCE*, Vol. 29, No. 3, pp 625-630, May-June 1994.

Wanniger, L., "Effects of the Equatorial Ionosphere on GPS", *GPS WORLD*, July 1993.

Winterbottom J., "WABS", Winterbottom, Allard, Beckham and Simpkins, data gap, private communication, 1994.

Solar Cycle Dependencies in Mid-Latitude Total Electron Content

Patricia H. Doherty
Institute for Space Research
Boston College
Newton, MA 02159-1164

John A. Klobuchar
Geophysics Directorate
Phillips Laboratory
Hanscom AFB, MA 01731-3010

Introduction

Total Electron Content data recorded at Hamilton, MA, over the last three solar cycles has been analyzed to illustrate short and long term effects of solar activity. In addition, statistics of TEC variability over an entire solar cycle have been generated to observe the average seasonal and solar cycle dependencies of this important parameter of the F2 region.

Information on the daily, seasonal and solar cycle variability in TEC is important to modern navigation and satellite ranging systems that must correct for time delay effects caused by the ionosphere.

Data base

The TEC data used in this study was recorded by the US Air Weather Service at Hamilton, MA (42.62°N, 70.8°W). TEC measurements at this mid-latitude location were made routinely from November 1967 through May 1992 by observing the Faraday rotation of linearly polarized VHF radio waves transmitted from available satellites. Standard processing of the data included converting the slant path measurements to equivalent vertical TEC at the ionospheric intersection (39°N, 70°W). In addition, efforts to eliminate n-pi ambiguity errors were made by using available foF2 values recorded at Wallops Island, VA (38°N, 75°W).

Variations in TEC are essentially controlled by the F2 region of the ionosphere, where electron densities and scale heights are the highest. The primary source of energy in the F region is the solar extreme ultraviolet (EUV) flux with wavelengths less than 1026 Angstroms. Since reliable time series of EUV are not readily available, we have relied upon the extensive, ground based series of 10.7 cm solar radio flux ($F_{10.7}$) measurements as an index of solar activity.

Short term response to solar activity

The short term fluctuations seen in solar flux are caused by the approximate 27 day rotation period of the sun. Work presented by Klobuchar and Doherty, 1992, showed that correlations between daily TEC and daily values of $F_{10.7}$ were inconsistent with some months showing a fair amount of positive correlation and other months showing poor or negative correlations. This study was completed for seven different geographic locations during a solar minimum and solar maximum year. In summary, the correlations were irregular, indicating that short term changes in TEC are not reflective of short term fluctuations in $F_{10.7}$.

Long term response to solar activity

Recent research has shown surprising evidence that TEC saturates at extremely high levels of 10.7 cm flux (Balan *et al.*, 1993, 1994). This research infers that the saturation in TEC is related to a similar saturation between 10.7 cm flux and solar EUV irradiances during intense solar activity. Work by Hedin, 1984, Donnelly, 1986 and Barth *et al.*, 1990 support this theory by showing a linear relationship between 10.7 cm flux and solar EUV on a long term basis with deviation at extreme levels of solar activity.

Figure 1 summarizes our effort to support or dispel TEC saturation at high levels of $F_{10.7}$. In this plot, TEC recorded over three solar cycles was used with the exception of days affected by geomagnetic activity. Sudden commencement storms cause an enhancement in daytime TEC that lasts for several hours. This enhancement is often followed by depletions in TEC that may last for a couple of days. In order to eliminate all storm effects from this study, we have excluded disturbed days ($A_p > 10$) and the day that follows a disturbed day. For the remaining data, daily averages of TEC between 11 and 17 hours local time

were calculated. The results are plotted versus daily $F_{10.7}$ for each of the three seasons, winter (November through February), summer (May through August) and equinox (March, April, September and October). This figure clearly illustrates the long term linear relationship between TEC and $F_{10.7}$. Although there is greater scatter in TEC with increasing values of 10.7 cm flux, strong signs of saturation are not apparent. Equinox displays subtle signs of saturation when $F_{10.7}$ exceeds 200. Further investigation of the equinox data found that many of the deviant points at flux values greater than 200 can be attributed to sets of consecutive days in early September 1980 and 1981. Early September is a period of transition from summer to equinox and this could account for the low measured values of TEC. It is important to note that all variations in TEC cannot be attributed to solar irradiance. Neutral winds, drifts, temperature and chemical composition also contribute to TEC variations.

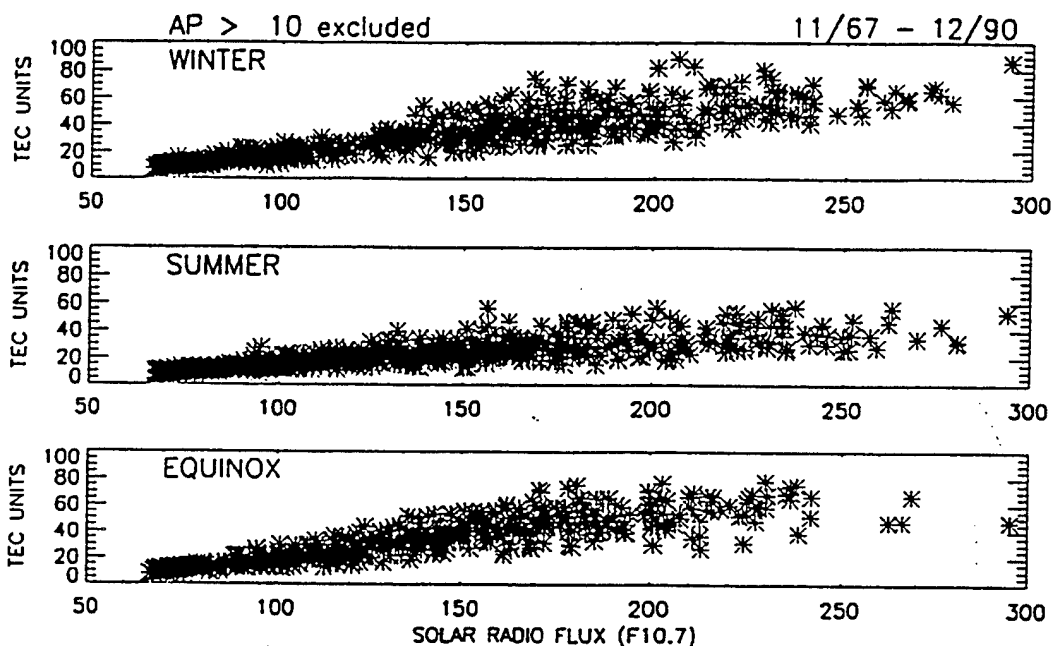


Figure 1) Mean daytime TEC versus daily $F_{10.7}$ for all geomagnetically quiet days from 11/67 through 12/90 measured at Hamilton, MA.

Statistics of Total Electron Content

The statistics of TEC measured at Hamilton, Ma have also been produced. They have been calculated separately for each of three seasons for three levels of solar activity: solar maximum represented by the year 1981, solar moderate by the year 1983 and solar minimum represented by 1986. Figure 2 presents the statistics of local daytime TEC in the form of arithmetic probability. In this type of display, TEC values are plotted versus their probability of occurrence. This plot format displays how closely the TEC for each season follows a normal distribution, and at what percentage it begins to deviate significantly from a normal distribution. This figure shows that the seasonal anomaly, where winter daytime is higher than summer daytime, is well developed at solar maximum but becomes less visible with declining solar activity.. It also shows that the data is normally distributed up to the 99th percentile where significant departures from normal behavior occur at all levels of solar activity.

Large departures from normal conditions are induced by geomagnetically disturbed conditions. If days with sudden commencement storms occurring during the early afternoon are removed from the calculations, these departures from a normal distribution disappear. Figure 3 illustrates this effect. All conditions are the same as in figure 2, however, all days with large positive phase enhancements from storm effects have been removed. These excluded days are few in number and are listed in the figures.

Figure 4 contains the results for nighttime conditions. The basic findings are that the summer nighttime TEC is higher than winter during solar maximum and moderate conditions. During solar minimum, nighttime TEC values for all seasons are about the same. The nighttime statistics illustrate that the data is approximately normally distributed, with no significant departures from normal behavior.

Conclusions

Short term changes in TEC are not well correlated with short term changes in $F_{10.7}$. Long term changes in TEC, however, are apparently correlated with solar cycle variations in $F_{10.7}$. The existence of saturation of TEC with high levels of solar flux is obscure, at least at this mid-latitude location.

The statistics of TEC measured at mid-latitude during all seasons, times of day and levels of solar activity are approximately normally distributed, at least over much of the distribution curve. Day to day and seasonal variability are much more apparent at higher levels of solar activity. Large departures from normal behavior are likely due to magnetic storm activity.

References

- Balan, N., G. J. Bailey, and B. Jayachandran, "Ionospheric evidence for a non-linear relationship between EUV and 10.7-cm fluxes during an intense solar cycle", *Planet. Space Sci.*, 41, 141, 1993.
- Balan, N. G. J. Bailey, B. Jenkins, P. B. Rao and R. J. Moffett, "Variations of ionospheric and related solar fluxes during an intense solar cycle", *J. Geophys. Res.*, 99, 2243-2253, 1994.
- Barth, C. A., W. K. Tobiska, G. J. Rothman, and O. R. White, "Comparison of 10.7-cm Radio Flux With SME Solar Lyman-alpha Flux", *Geophys. Res. Lett.*, 17, 571, 1990.
- Donnelly, R. F., H. E. Hinteregger, and D. F. Heath, "Temporal Variations of Solar EUV, UV, and 10.830 Angstrom Radiations", *J. Geophys. Res.*, 91, 5567, 1986.
- Hedin, A. E., "Correlation Between Thermospheric Density and Temperature, Solar EUV Flux, and 10.7-cm Flux Variations", *J. Geophys. Res.*, 89, 9828, 1984.
- Klobuchar, J. A., and P. H. Doherty, "The Correlation of Daily Solar Flux With Total Electron Content", *Proceedings of the International Beacon Satellite Symposium*, Cambridge, Ma, 1992.

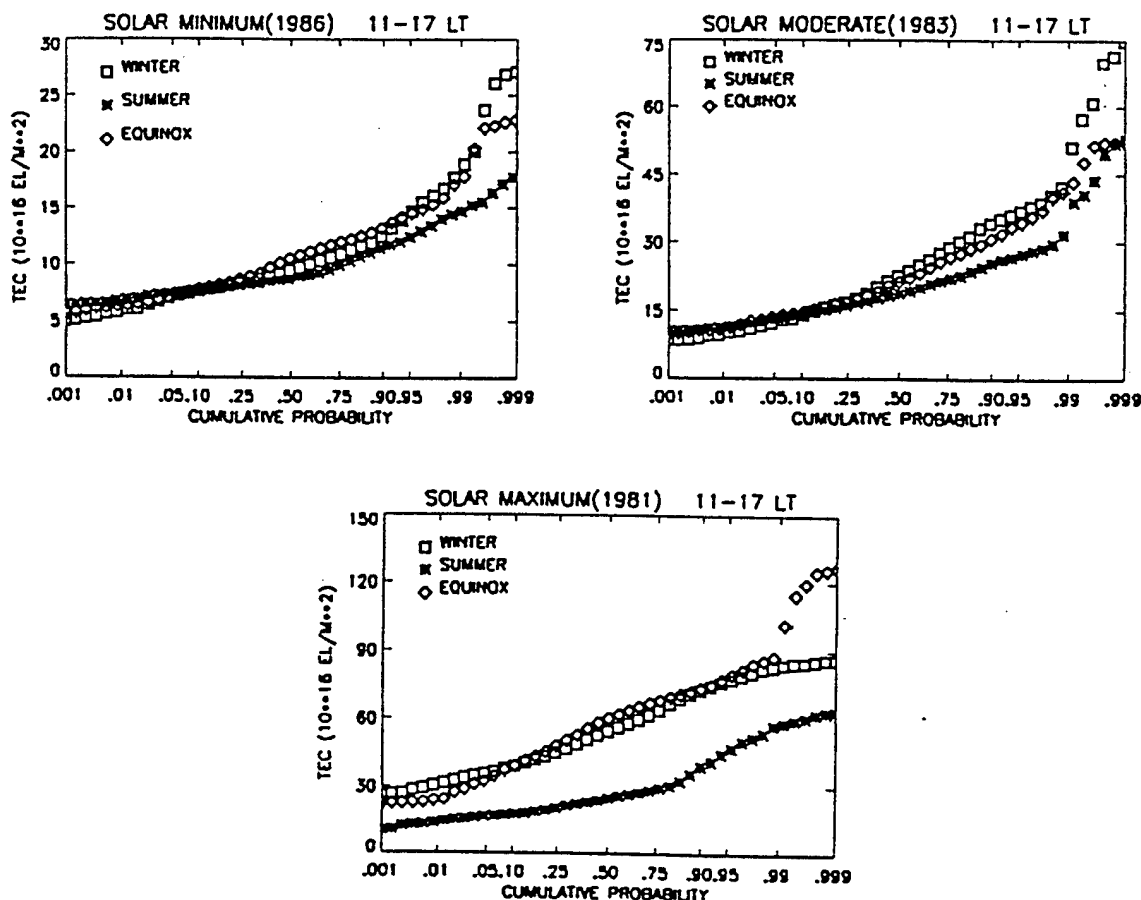


Figure 2) Statistics of local daytime TEC at Hamilton, MA for 3 levels of solar activity.

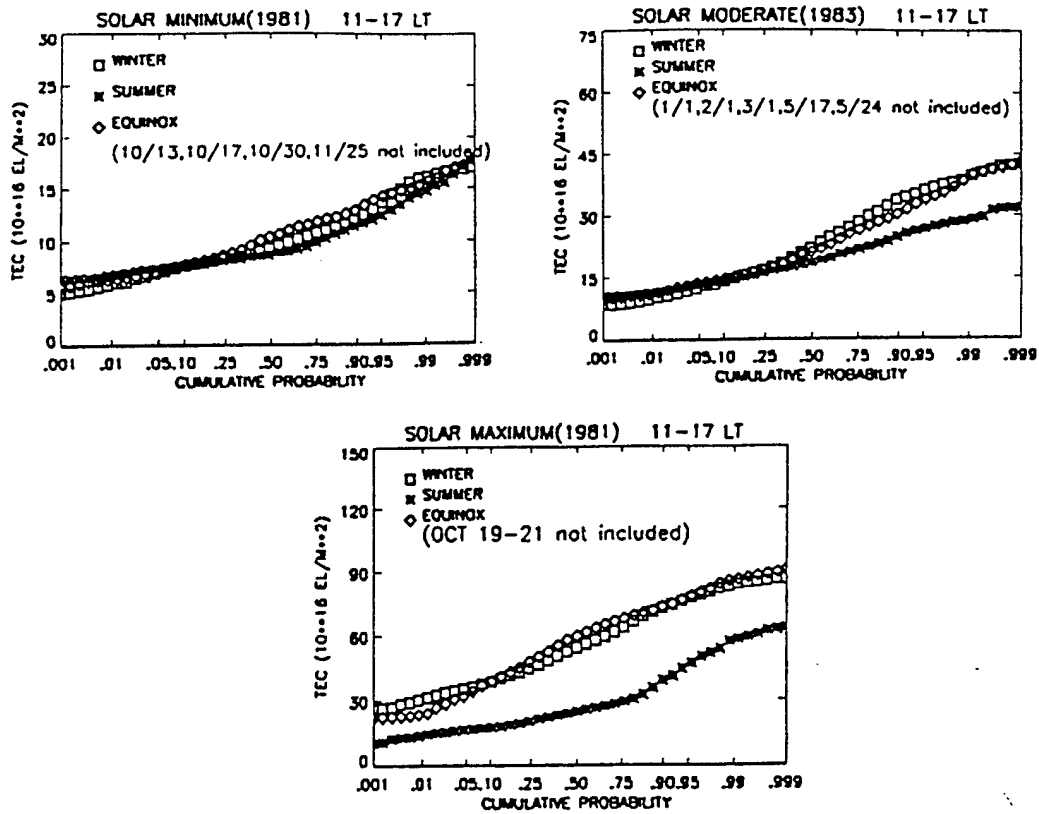


Figure 3) Statistics of local daytime TEC at Hamilton, MA for 3 levels of solar activity during magnetically quiet days.

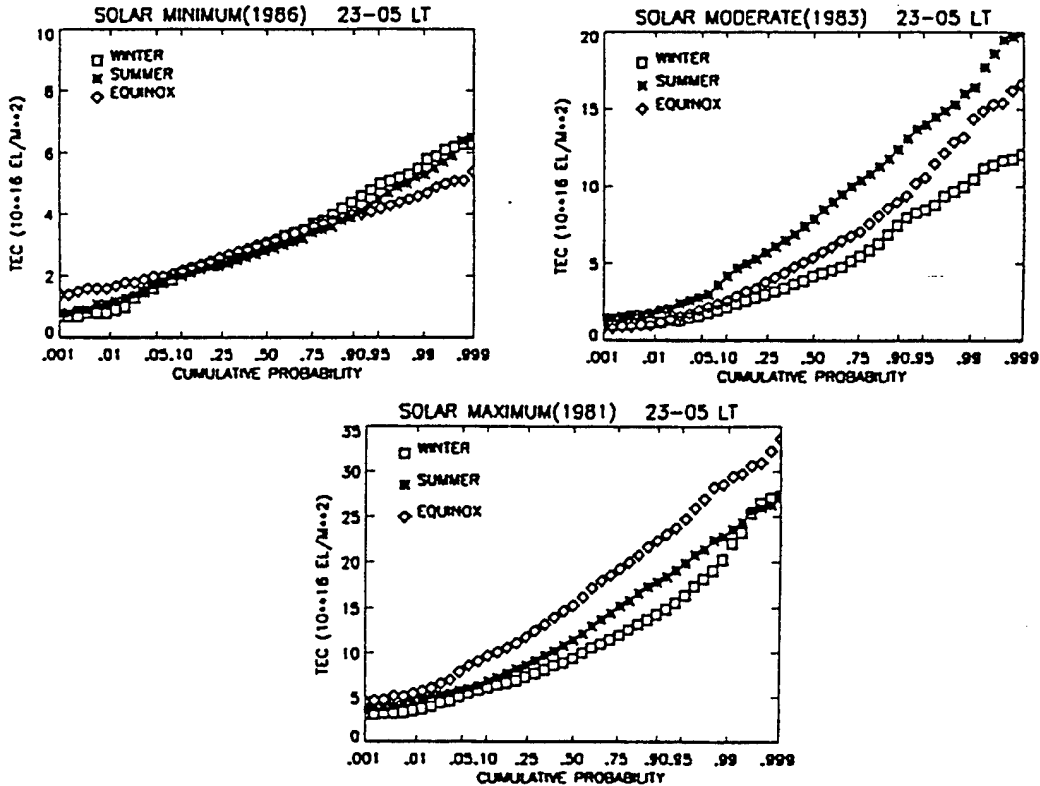


Figure 4) Statistics of local nighttime TEC at Hamilton, MA for 3 levels of solar activity.

IMPROVING IRI90 LOW LATITUDE IONOSPHERIC SPECIFICATION

Amanda J. Preble
HQUSAF/XOWX, Pentagon, Washington D.C.

Dwight T. Decker
Institute for Scientific Research, Boston College, Newton, MA

David N. Anderson
Ionospheric Effects Division, Phillips Laboratory, Hanscom AFB MA

ABSTRACT

At low latitudes a number of comparisons between the International Reference Ionosphere (IRI90) model of F-region electron density profiles with observed profiles measured by the Jicamarca incoherent scatter radar indicate that during the daytime, the observed profile shape is much broader in altitude than that specified by IRI90 while at night, just after sunset, observed F_2 -peak altitudes are significantly higher. This is especially true during periods of high solar activity. The theoretically-derived ionospheric parameters such as F_2 -peak density ($N_m F_2$), F_2 -peak altitude ($h_m F_2$), and profile shape which are contained in the Parameterized Ionospheric Model (PIM) have been shown to be in better agreement with Jicamarca observations. This paper describes an attempt to improve IRI90 at low latitudes by using five ionospheric parameters derived from PIM: the bottomside profile half thickness, $N_m F_2$, $h_m F_2$, and 2 parameters of a topside Chapman profile. The generation of electron density profiles using these five parameters will be presented as well as a description of how these expressions might be implemented into the IRI90 model.

INTRODUCTION

The International Reference Ionosphere Model (IRI90) is a global, climatological model which specifies ionospheric electron density profiles above 80 km representing monthly or "average" electron densities based on past ground-based, rocket and satellite observations[Bilitza, 1990]. The model, therefore, is only as good as the available observations. Because most of the data was obtained from ground based ionospheric sounders, there is a lack of observations from the low latitude region, from the high latitudes/polar cap and from the ocean areas. Given that most of the database comes from midlatitude stations, it is expected and reassuring to find that IRI90 does an excellent job of specifying this region's climatology. However, there is considerable evidence from past comparisons with both data and theoretical modeling results, that the low latitude portion of IRI90 is not very realistic in specifying the main ionospheric features. In this paper we propose an approach that uses theoretical modeling results to improve IRI90's specification of the low latitude ionosphere.

OBSERVATIONS

In Figure 1, we present an example of an electron density profile observed by the Jicamarca incoherent scatter radar which is located near the magnetic equator in Peru. Also included in the plot are IRI90 profiles. At 1200 local time the observed profile has a broad shape that is typical of the daytime profile shape seen in the equatorial region during solar maximum conditions. On the other hand, IRI90 has a shape more characteristic of midlatitudes and fails to reproduce this broad profile shape. Later in the day, at 1900 local time the observed layer has now been lifted to much higher altitudes due mostly to the enhanced post sunset $E \times B$ upward drift. This again is a characteristic feature of the equatorial region especially during solar maximum periods and again is a feature that we see is not reproduced by IRI90.

The broad shape of the daytime profiles and the post sunset lifting of the layer are not rare events. They occur regularly and can be seen in averaged data as is evident in Figure 2 which is adapted from Creamer

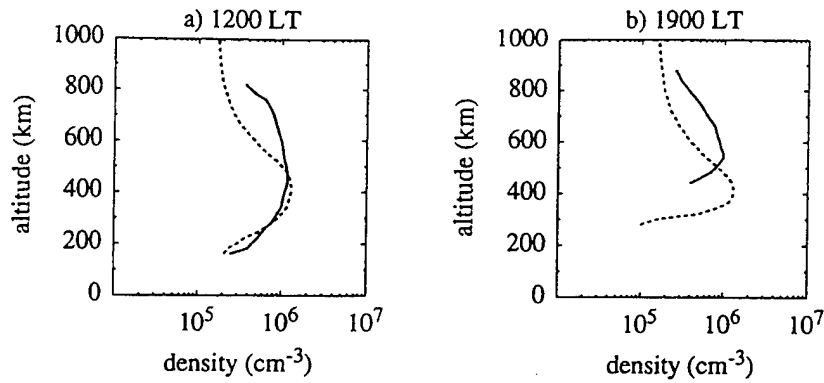


Figure 1: Comparison of measured profiles and IRI90 profiles for (a) 1200 and (b) 1900 LT. The solid curves are the observations and dashed curves are IRI90.

[1992]. In Figure 2, we show the hourly average data from several years of Jicamarca observations for maximum

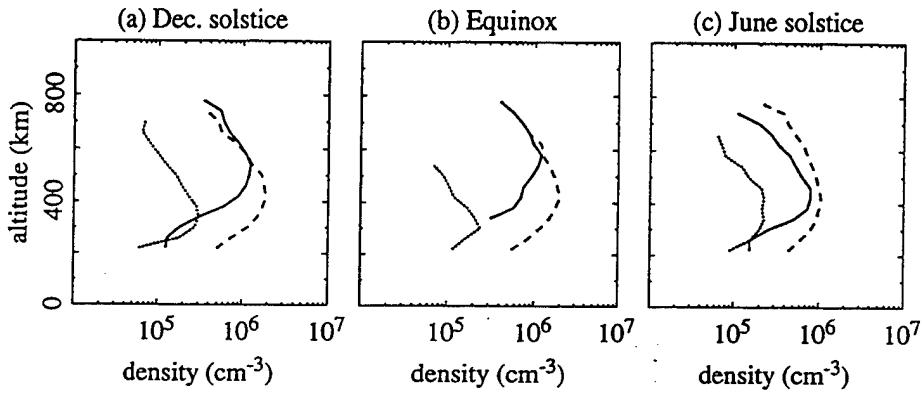


Figure 2: Hourly variations in measured electron density profiles for (a) December solstice, (b) equinox, and (c) June solstice, solar maximum conditions. The solid curve is 2000 LT, the long dashed curve is 1200 LT, and the short dashed curve is 0400 LT.

solar flux conditions. We see that the broad daytime profiles are evident in all three seasons, while the post sunset lifting appears just at December solstice and Equinox. Similar features are seen for moderate solar flux conditions but not for solar minimum conditions.

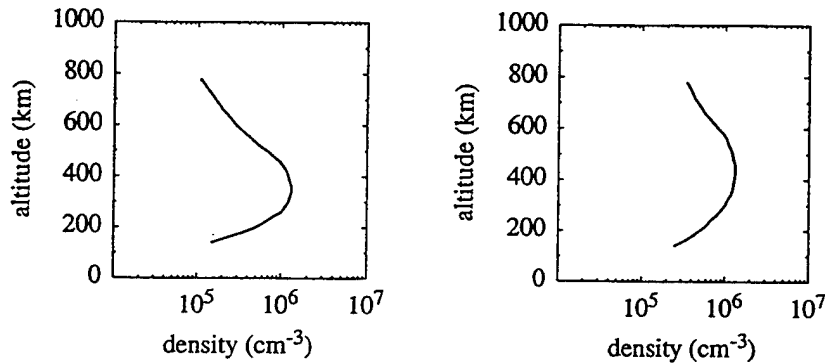


Figure 3: Electron density profiles observed by Kwajalein incoherent scatter radar.

Similar features are also evident in other longitude sectors. In Figure 3, we present profiles observed by the Kwajalein incoherent scatter radar located near the equator in the Pacific sector. On the left is an profile from the early morning before upward $\mathbf{E} \times \mathbf{B}$ drift has acted to broaden the peak, while on the right we see later in the day the characteristic broad layer of the low latitude daytime that results from the daytime upward $\mathbf{E} \times \mathbf{B}$ drift.

THEORETICAL MODELING

Over the last three decades, there have been many theoretical studies of the equatorial F_2 region and a number of computer models have been developed that reproduce the basic features of this region. Most recently, these models have evolved to the point that given realistic inputs for a particular day they are capable of reproducing the ionosphere of that day [Preble, *et al.*, 1994]. One such model is the Phillips Laboratory Global Theoretical Ionospheric Model (GTIM) which calculates electron density profiles as a function of location and time by solving ion continuity and momentum equations. In Figure 4, we present vertical profiles for 1200 and

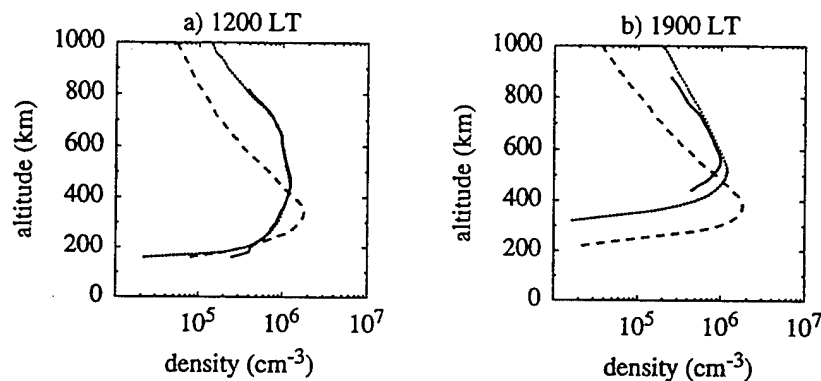


Figure 4: Comparisons of measured and calculated profiles for (a) 1200 and (b) 1900 LT. The solid curves are the observations, the short dashes are calculations that used observed drifts, and the long dashes are the calculations using zero drifts.

1900 LT from a GTIM simulation of October 1 and 2, 1970. We also include Jicamarca observations taken at those times. We see that when the observed upward $\mathbf{E} \times \mathbf{B}$ drift is used as an input to the model that the agreement between model and observation is excellent. Further we see that the model reproduces both the broad profile shape of the daytime and the lifting of the F_2 layer during the post sunset period. The additional curves illustrate the sensitivity of these characteristics to the magnitude of the $\mathbf{E} \times \mathbf{B}$ upward drift.

Recently, a computationally fast Parameterized Ionospheric Model (PIM) was developed at the Phillips Laboratory Geophysics Directorate as part of a global, real-time ionospheric specification model soon-to-be operational at the Air Force 50th Weather Squadron (50WS) in Colorado Springs [Daniell *et al.*, 1995]. PIM is based on many runs of several physical ionospheric models and as such is a global ionospheric model based on theoretical climatology rather than empirical climatology. For the low latitudes, GTIM was run under three solar cycle conditions (low, middle, and high F10.7 cm flux values) and three seasons (Fall/Spring equinox, summer and winter solstice periods) for four longitude sectors (American, Brazilian, Europe/Indian, and Pacific). Electron density profiles every 2° latitude and every hour local time were parameterized by 9 Empirical Orthonormal Functions (EOFs). At low and mid latitudes these EOFs were analytically fit in latitude and kept in tabular form over the 24 hour period. These tables and functions comprise the low latitude portion of PIM and reproduce very accurately the electron density profiles generated by GTIM.

Given the success of theoretical models in reproducing the basic features of low latitude we would expect that, in contrast to IRI90, PIM should likewise reproduce those features. In Figures 5-7 we illustrate the contrast between PIM and IRI90. In Figure 5, we directly compare PIM and IRI profiles at 1700 UT in the

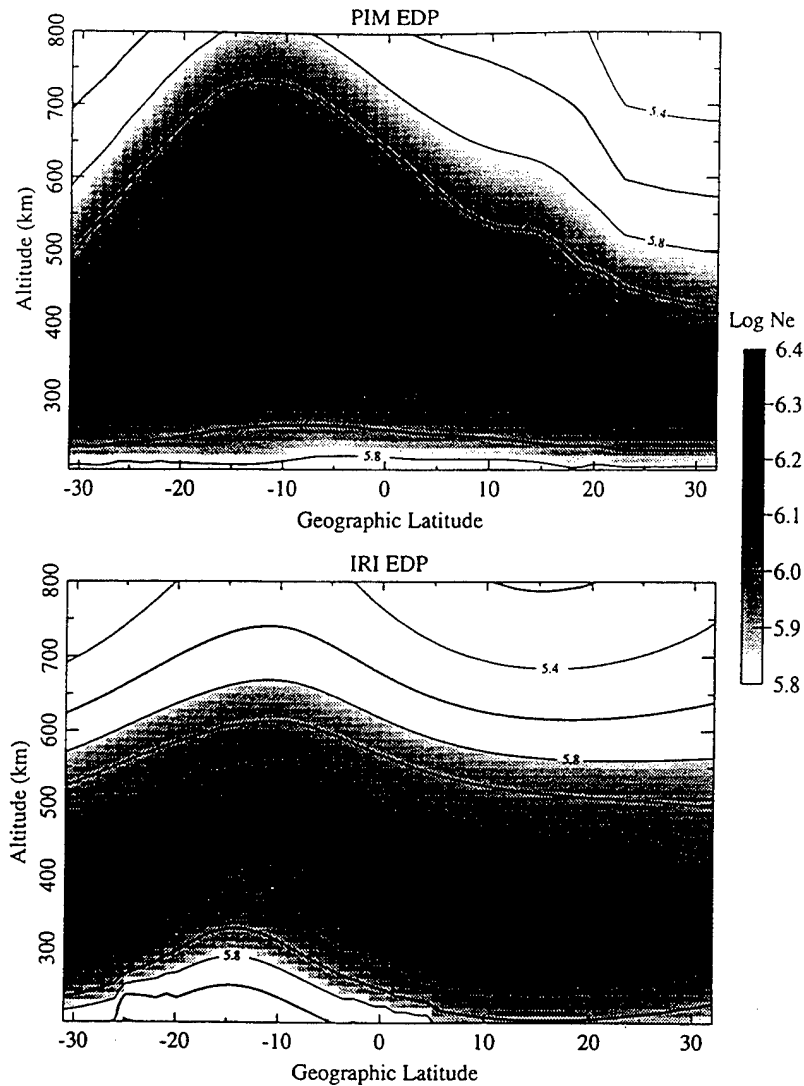


Figure 5: Electron density from PIM and IRI for 1700 UT (1200 LT) under solar maximum conditions on Day 100.

Jicamarca longitude meridian. The local time is around 1200 and we see that PIM produces a much broader F layer than does IRI90. The most dramatic differences are seen within about 10 degrees of the magnetic equator. In Figure 6, it is $h_m F_2$ that is compared over the entire globe at 0 UT and we see that largest differences between PIM and IRI90 are confined to the post sunset period near the magnetic equator. The topside half thicknesses are compared in Figure 7 and here a sizable difference is seen near the magnetic equator but extended over 180° in longitude. This also points out how the differences in thickness are not confined to just one longitude sector. In Figure 5, a clear difference in layer thickness was seen in the American sector at 1700 UT. At 1200 UT, this difference is seen in the Europe/Indian sector.

PROPOSED IMPROVEMENT TO IRI90: PIM OPTION

In describing the electron density profile (EDP) from 100 to 1000 km, IRI90 uses six subregions: the topside, the F_2 -bottomside, the F_1 layer, the intermediate region, the E-valley, the E-bottomside, and the D-region. The shortcomings described in this paper have involved the topside and F_2 -bottomside regions, and it is these

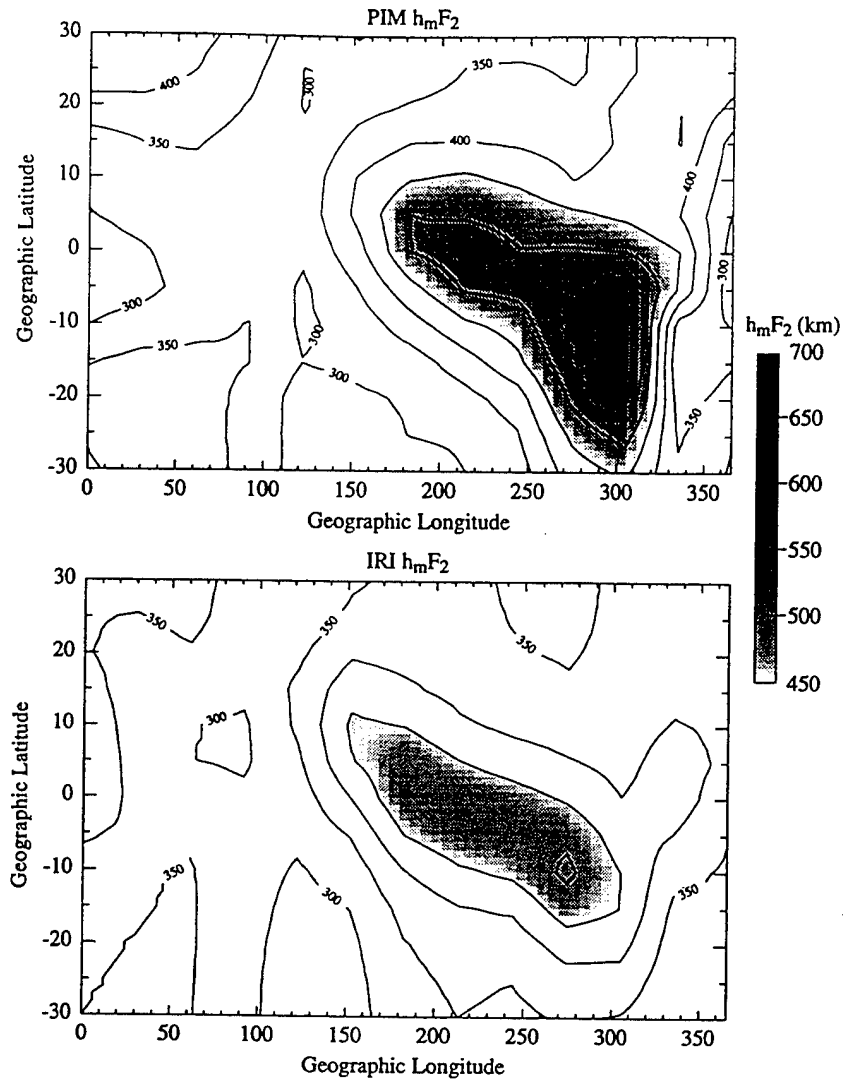


Figure 6: h_mF_2 from PIM and IRI for 0 UT under solar maximum conditions on Day 100.

regions we propose to improve by developing a PIM option to IRI. The present IRI90 normalizes both the topside and the F_2 -bottomside to the F_2 -peak density (N_mF_2) and altitude (h_mF_2). The F_2 peak density comes from either the CCIR or URSI coefficient sets that derive from Fourier and spherical expansions of ionosonde data. Likewise there are CCIR coefficients of $M(3000)$ which are used to infer h_mF_2 . The topside profile shape comes from analytic fits of the Bent sounder data [Llewellyn and Bent, 1973]. The fits are done using Epstein functions which can be used to define a Booker function. The Booker function used in IRI90 consists of 3 layers and it uses 8 parameters to define the profile. Five of the parameters are fixed and the other three are given as functions of geomagnetic latitude, solar flux, and f_0F_2 . (This profile can be described in terms of the LAY formalism [Bilitza and Rawer, 1990].) The bottomside is given by a fairly simple function which uses a thickness parameter. The present IRI90 either looks up this parameter or calculates from a half thickness from Gulyaeva. The PIM option would involve using PIM values for N_mF_2 , h_mF_2 and bottomside half thickness directly in IRI. To use the topside from PIM in IRI will require either fitting Booker functions to PIM profiles or fitting with some other function that would then have to be incorporated into IRI.

Presently, IRI90 allows the inputting of a N_mF_2 and h_mF_2 chosen by the user. To input a bottomside half

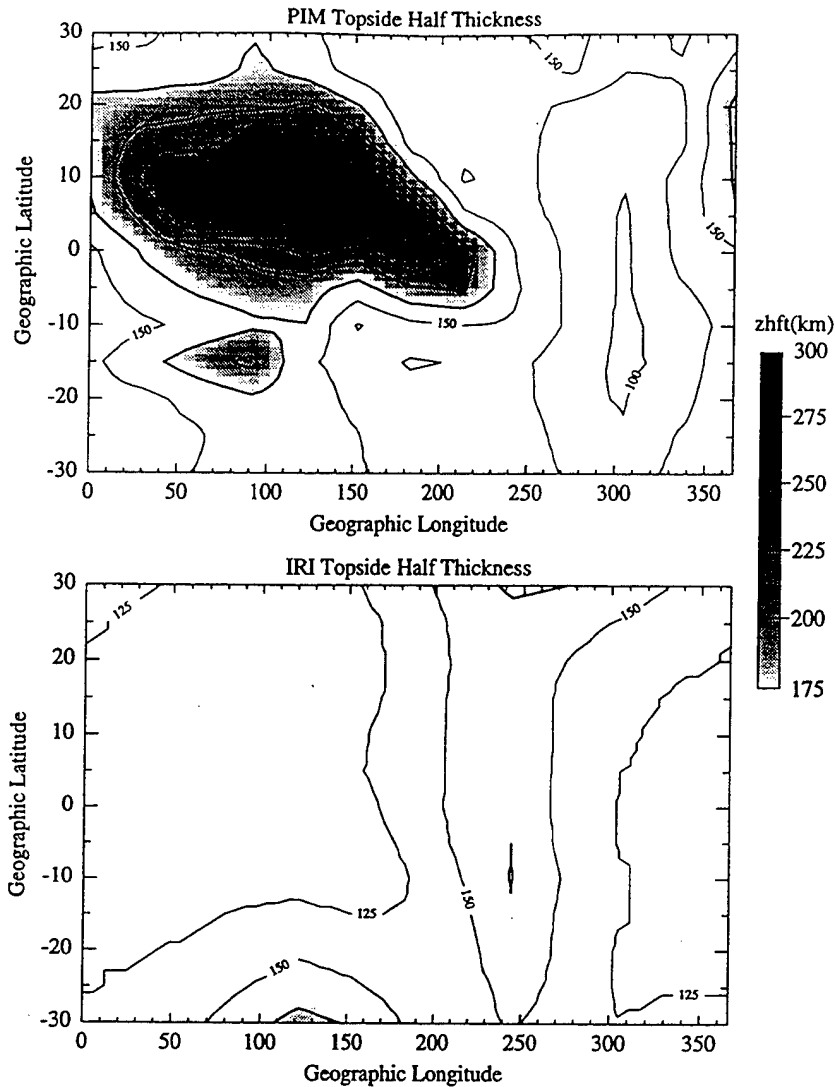


Figure 7: Topside half thickness from PIM and IRI for 1200 UT under solar maximum conditions on Day 100.

thickness chosen by the user requires modifications of the IRI driver routine such that a user-specified thickness can be accepted and substituted for the Gulyaeva thickness. For the topside, we have explored one possibility by fitting topside PIM profiles with 2-parameter Chapman profiles. The IRI driver was modified to accept these two parameters and a routine was added to IRI to calculate the topside profile using a Chapman profile rather than a Booker function. Overall, the examples in this paper required only 20 lines of new code to IRI90. Examples of how well IRI can reproduce PIM profiles using the 5 PIM parameters are given in Figures 8 - 11. In Figure 8a, we present the standard IRI90 (solid curve) and PIM(dotted curve) profiles for 1700 LT at the magnetic equator in the American sector for solar maximum conditions. We see a slight difference in the F_2 peak parameters and a dramatic difference in the profile shapes. Figure 8b shows PIM compared with IRI90 using $N_m F_2$ and $h_m F_2$ supplied by PIM. When the PIM bottomside half thickness is used by IRI90, we see in Figure 9a that IRI90 now reproduces well the lower F region of PIM. Finally in Figure 9b, the topside PIM profiles are also used by IRI90 and we see that the full PIM option does a reasonable job at reproducing the original PIM F region. Figures 10 and 11 demonstrate the same sequence but for 2000 LT when PIM has an F_2 layer up around 700 km. Again we see that supplying the five PIM parameters to IRI90 does a good job in

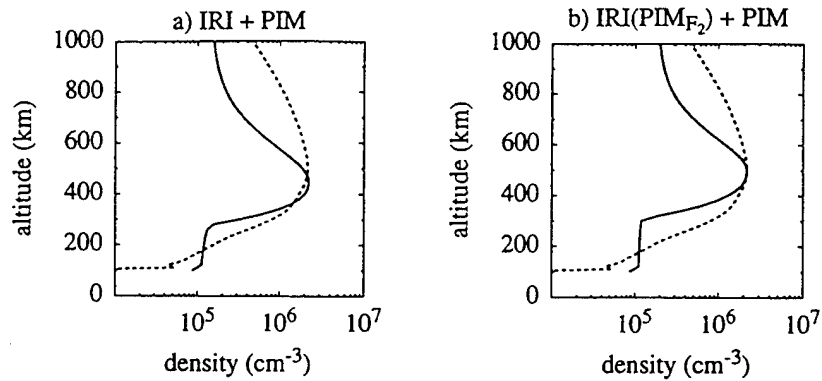


Figure 8: Comparisons at 1700 LT of IRI90 and PIM profiles for (a) standard IRI and (b) IRI using PIM F_2 peak parameters. Solid curves are IRI90 and dashed curves are PIM.

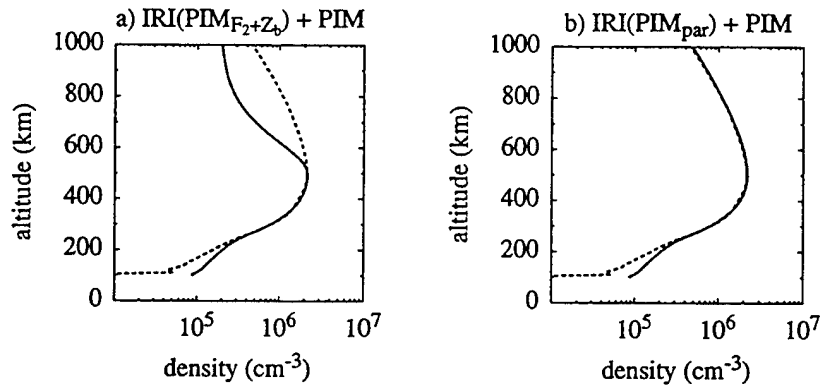


Figure 9: Comparisons at 1700 LT of IRI90 and PIM profiles for (a) IRI using PIM F_2 peak parameters and bottomside half thickness and (b) IRI using all five PIM parameters. Solid curves are IRI90 and dashed curves are PIM.

reproducing the original PIM F region profile.

The next step in developing a global PIM option will be to determine the 5 PIM parameters over the globe under various geophysical conditions. It is expected that the resultant database of parameters will then have to be condensed to a convenient size. One possibility would be to fit the 5 PIM parameters to analytic functions in the same way as was done with the F_2 peak parameters derived from ionosonde data (CCIR or URSI coefficients). Whether this is feasible approach will require further work. Finally, while the focus in this paper is on low latitudes, it would seem that given the fact that high latitude modifications are being considered for IRI it would be best to develop a global PIM option for IRI. This would avoid the problem of attempting to merge a PIM option in one region with standard IRI in other regions.

SUMMARY

At present, there are clear shortcomings in IRI90's description of the low latitude ionosphere. On the other hand, PIM contains many of the low latitude features that are not reproduced by IRI90. The present version of IRI90 is designed to accept $N_m F_2$ and $h_m F_2$ from outside sources. Thus it would be straightforward to develop a PIM option for these parameters in IRI90. Similarly, an external bottomside half thickness could easily be incorporated into IRI90 given the manner in which IRI90 presently defines its bottomside F region. Unfortunately, the parameter which is most in need of modification is the topside half thickness. Here there

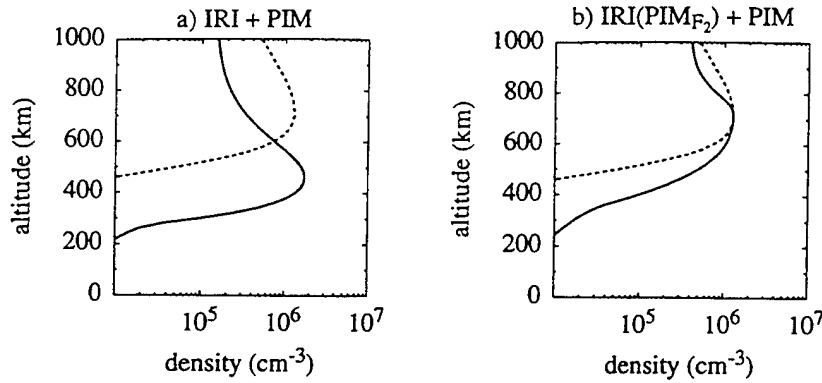


Figure 10: Comparisons at 2000 LT of IRI90 and PIM profiles for (a) standard IRI and (b) IRI using PIM F_2 peak parameters. Solid curves are IRI90 and dashed curves are PIM.

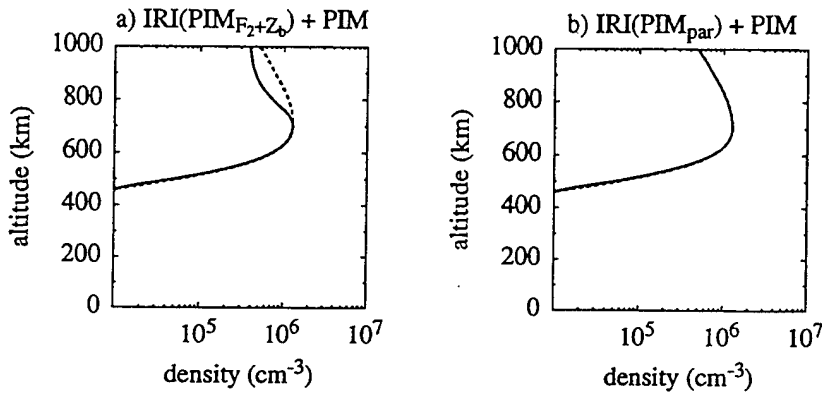


Figure 11: Comparisons at 2000 LT of IRI90 and PIM profiles for (a) IRI using PIM F_2 peak parameters and bottomside half thickness and (b) IRI using all five PIM parameters. Solid curves are IRI90 and dashed curves are PIM.

is no trivial way of incorporating a thickness from another source such as PIM into the present IRI. However, a fairly minor modification is possible that would use a 2 parameter Chapman profile rather than the Booker functions. If use of the Booker functions is desired then such functions would have to be fit to PIM profiles. Presently, we are pursuing the option that uses the Chapman profile and are developing representations of the 5 PIM parameters as functions of latitude, longitude, local time, solar cycle, season, and geomagnetic activity.

ACKNOWLEDGEMENTS

The work at Boston College was supported by Phillips Laboratory contract F19628-93-K0001.

REFERENCES

- Bilitza, D., International reference ionosphere 1990, NSSDC/WDC-A-R&S Report 90-22, Goddard Space Flight Center, Greenbelt, Maryland, 1990.
- Bilitza, D. and K. Rawer, New options for IRI electron density in the middle ionosphere, *Adv. Space Res.*, 10(11), 7-16, 1990.
- Creamer, A. P., Equatorial F-region electron densities over a solar cycle: Comparisons between observations and numerical models, M.S. thesis, 201pp., Utah State University, 1992.

- Daniell, Jr., R. E., L. D. Brown, D. N. Anderson, M. W. Fox, P. H. Doherty, D. T. Decker, J. J. Sojka, and R. W. Schunk, Parameterized ionospheric model: A global ionospheric parameterization based on first principles models, *Radio Sci.*, *30*, 1499- 1510, 1995.
- Preble, A. J., D. N. Anderson, B. G. Fejer, and P. H. Doherty, Comparison between calculated and observed F region electron density profiles at Jicamarca, Peru, *Radio Sci.*, *29*, 857-866, 1994.
- Llewellyn, S.K. and R. B. Bent, Documentation and description of the Bent ionospheric model, Air Force Geophysics Laboratory, Report AFCRL-TR-73-0657, Hanscom AFB, Massachusetts, 1973.

Potential Ionospheric Limitations to GPS Wide-Area Augmentation System (WAAS)

J. A. KLOBUCHAR

Air Force Phillips Laboratory, Hanscom AFB, Massachusetts

P. H. DOHERTY

Boston College, Newton, Massachusetts

M. BAKRY EL-ARINI

The MITRE Corporation, McLean, Virginia

ABSTRACT

Navigation and positioning using the FAA's GPS Wide-Area Augmentation System (WAAS) with single-frequency receivers suffers potentially from the unknown spatial variability of ionospheric range delays (e.g., spatial gradients in ionospheric delays) between ground locations where dual-frequency measurements from GPS satellites are being made. By deploying a sufficient number of dual-frequency GPS code and/or codeless reference receivers, it is possible to correct for most of the ionospheric range delay in a given large region using WAAS real-time prediction algorithms.

The statistics of differences in range delay over station separations from approximately 350 km to over 1,600 km are presented, using ionospheric data collected from a number of stations in North America. The results illustrate large ionospheric gradients during periods of high magnetic activity. Fortunately, these events are infrequent. For the midlatitudes, the accuracy goal is to keep ionospheric range delays to only a few meters for at least 99 percent of the time so that WAAS can be used in precision approaches. To illustrate the possibility of achieving this goal, statistics of estimation errors in ionospheric range delay using this data set are also presented.

INTRODUCTION

One of the potential limitations of the FAA's GPS Wide-Area Augmentation System (WAAS) is the differential ionospheric range delay over the area of visibility of various GPS satellites used in determining range and velocity (range-rate). There has been little previous work in determining the correlation distance of differences in ionospheric time delay, which is proportional to the total electron content (TEC) of the ionosphere. In [1], ionospheric range error is inferred from Faraday rotation measurements of VHF signals of opportunity transmitted from various geostationary satellites for determination of the correlation between pairs of stations located in the northern midlatitudes. The results in [1] show that the correlation coefficient between differences from

seasonal average daytime values at pairs of stations fell to a value of 0.7 for stations separated by approximately 1,800 km in the north-south direction, and approximately 3,000 km for stations located along the east-west direction. Little difference in the correlation distance was found with season. In [1] it is pointed out that a correlation value of 0.70 explains only 28 percent of the variability in the differences from mean conditions at one station with respect to the second station. The minimum distance used in [1] is approximately 1,000 km in the north-south direction and 1,600 km in the east-west direction. These results represent essentially all that was known on the statistical behavior of ionospheric range error between pairs of stations. Recently, the correlation coefficient was found between ionospheric pierce points when observing different pairs of GPS satellites from a single observing station during a 4 week period in 1989 [2]. This limited data set provides a correlation coefficient of 0.91 for a 1,000 km separation of ionospheric pierce points observed from a single station located in Austin, Texas. A lower correlation coefficient, similar to the results of [1] was found using equivalent ionospheric pierce points aligned with latitude, rather than longitude.

The results of [1] and [2] do not directly answer the pertinent question of ionospheric limitations on WAAS, namely: "Given a set of ionospheric range delays to various GPS satellites measured at a few stations, what are the corresponding ionospheric range delays for locations at varying distances from those observing stations?" Accordingly, in the late spring of 1992, the FAA, The MITRE Corporation (the Center for Advanced Aviation System Development [CAASD]), and Air Force Phillips Laboratory began a series of measurements of ionospheric range delay by monitoring both the dual-frequency differential group delay and the differential carrier phase of GPS satellites at a number of stations located on the East Coast of the United States. The objective was to determine the statistics of the differences in range error for station pairs having different separations. To further examine the ionospheric limitations to WAAS, statistics of errors in estimating ionospheric range delay were also computed. These estimation errors are the result of the differences between measured range delays and range delays that were estimated in a linear regression technique. Unfortunately, these GPS ionospheric range delay measurements were taken approximately one-half way down the current 11 year solar activity cycle. Absolute values of ionospheric range delays are known to vary with long-term solar cycle activity. Since GPS ionospheric range delay data during a period of solar maximum activity was not available, Faraday rotation data recorded during the 1981 solar maximum period was used to illustrate the same statistics during solar maximum. These solar maximum statistics illustrate worst-case ionospheric range delay conditions in the Continental United States (CONUS).

The final result of this overall ionospheric range delay estimation study will be the representation of the real-time ionospheric vertical delay over the extended CONUS region, specified at nodes of a 5×5 deg grid on the ionospheric sphere, updated continually by ionospheric measurements at various stations located in CONUS [3]. One of the major issues in WAAS is the number of ionospheric monitoring stations required to represent the ionospheric range delay between stations to within a specific error bound for a given percentage of time. Here, we present ionospheric range delay only. The conversion of range

delay to 3-D position error has been discussed in [4]. This paper reports the results of measurements designed to obtain the statistics on the required station spacing for real-time ionospheric measurements. The results of this paper are representative of a lower error bound on any real-time prediction algorithm for WAAS.

EXPERIMENTAL CONFIGURATION AND DATA REDUCTION

A number of dual-frequency GPS receivers were set up in the eastern United States to directly measure ionospheric range delay. The receivers used were the four-channel, dual-frequency Allen Osborne Associates Mini-Rogue Ionospheric calibration receiver and an eight-channel version of the same receiver. All of the receivers were internally calibrated prior to the experiment. The locations of the GPS receiving sites are given in Table 1, and the distances between station pairs discussed are shown in Table 2.

The 1981 solar maximum Faraday rotation data was taken by monitoring polarization changes in VHF transmissions from geostationary satellites of opportunity. For these observations, the important locations are the ionospheric pierce points looking towards the geostationary satellite. Those locations for the 1981 solar maximum study are shown in Table 3, and the distances between station pairs are given in Table 4.

Table 1—Locations of GPS Receiving Sites

Station	Latitude (deg, min)		Longitude (deg, min)	
Oldtown, ME	44°	57' North	68°	40' West
Hanscom AFB, MA	42°	27'	71°	16'
Atlantic City, NJ	39°	27'	74°	34'
Dayton Airport, OH	39°	54'	84°	13'
Georgetown, SC	33°	19'	79°	19'

Table 2—Distances Between Station Pairs

Station Pairs	Distance (km)
ME-MA	348
MA-NJ	434
NJ-E	782
NJ-C	805
NJ-OH	828
MA-OH	1,120
MA-SC	1,238
ME-OH	1,393
ME-SC	1,586

Table 3—Ionospheric Pierce Points for Faraday Measurements

Station	Latitude (deg, min)		Longitude (deg, min)	
Goose Bay, Labrador	47°	30' North	62°	12' West
Hamilton, MA	38°	42'	70°	42'
Kennedy Space Center, FL	26°	18'	79°	36'
Ramey, PR	17°	06'	67°	24'

Table 4—Distances Between Station Pairs

Station Pairs	Distance (km)
GB-HAM	1,197
HAM-KSC	1,612
KSC-RAMEY	1,623
HAM-RAMEY	2,426
GB-KSC	2,809
GB-RAMEY	3,417

The ionospheric pierce points of the Faraday rotation observations and the stations monitoring GPS signals are shown in Figure 1. The distances between the Faraday rotation pierce points are much too large for consideration for potential CONUS GPS ionospheric monitoring stations, but they probably do represent worst-case station spacing, and the fact that the data was already available for a period of very high solar activity made it worth including in the present study.

Absolute values of the slant ionospheric range delays were determined from the GPS measurements by using the standard technique initially suggested in [5], in which the absolute, but noisy, measurements of differential group delay are used only to fit precise relative differential carrier phase to an absolute range delay scale. This fitting procedure was done only over the higher-elevation portions of each GPS satellite pass from each station to minimize the potential effects of multipath on the absolute range delay determined from the

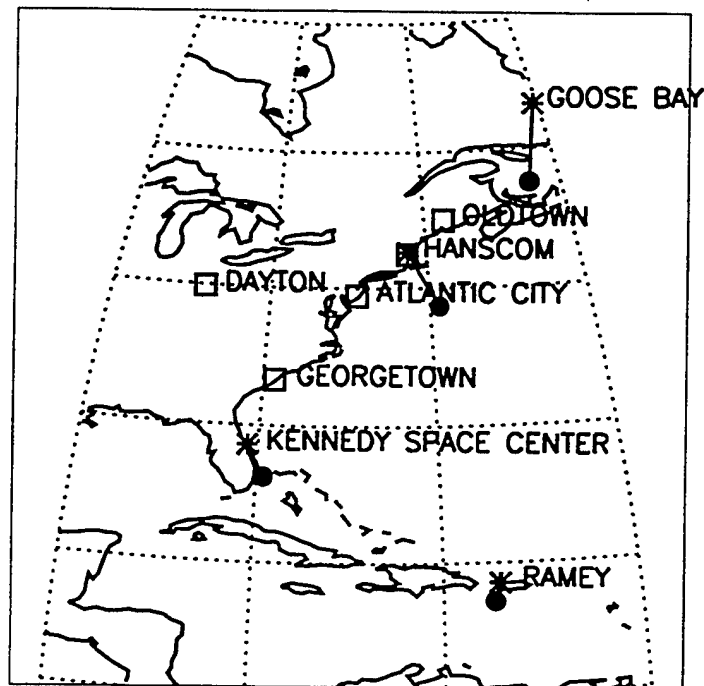


Fig. 1—Map of GPS Ionospheric Monitoring Stations and Ionospheric Pierce Points for Faraday Rotation Measurements

differential group delay. In practice, multipath is not a significant problem unless only the initial very-low-elevation-angle differential group delay data is used in this fitting procedure, and the multipath environment is poor.

Any potential errors in the differential group delay of each GPS satellite's 10.23 MHz P-code L1 and L2 transmissions (see [6] for a summary of those problems) could be neglected, as only differential range delays viewing the same GPS satellite at pairs of stations were used in the analysis, and each satellite bias was common to both stations.

DATA PRESENTATION METHOD

The statistics of ionospheric range delay presented in this paper were computed and plotted separately for each of three seasons: summer (May through August), winter (November through February), and the combined equinoxes (March, April, September, and October). The data was further separated into morning, daytime, evening, and nighttime hours local time. Only the daytime range delays are shown in this paper, as they represent higher absolute values than the nighttime data. The absolute ionospheric range delay values at a single station, as well as the differences between values at pairs of stations and errors in estimated range delays at individual stations, were then plotted against their cumulative probability. The resulting plots indicate the percentage of occurrences below and above certain probability values that can be seen easily.

The figures were plotted versus a probability scale on the x-axis, so that a straight line on the figure represents a Gaussian distribution. The slope of the line is then a measure of the standard deviation of the data. Departures from a straight line are simply departures from a "normal" or Gaussian distribution. This form of plot is an excellent method for examining the statistics of the distribution of this data set.

ABSOLUTE IONOSPHERIC RANGE DELAY AT A SINGLE STATION

Figure 2 shows the statistics of equivalent vertical ionospheric range delay for a single station during the daytime hours of the three seasons of the solar maximum year of 1981 for Hamilton, Massachusetts. Note that the equinox season shown in Figure 2 has a large departure from a normal curve above the approximate 99 percent probability point. Reasons for this are discussed below in the section on geomagnetic storm effects on the ionosphere.

Figure 2 shows that the median vertical ionospheric range delay is approximately 10 m for the winter and equinox seasons, but only 5 m for the summer season. For 99 percent of the time, the vertical delay is less than 15 m in the winter and equinox seasons. The 99 percent probability value is approximately 10 m for the summer season. For GPS satellites viewed at 5 deg elevation, the vertical delays shown in Figure 2 must be multiplied by a factor of approximately 3. Existing models can correct for the median ionospheric range delay to within $\approx \pm 10$ percent, but the day-to-day variability about the monthly median cannot be modeled. Thus, real-time ionospheric measurements must be made to correct for this unknown day-to-day ionospheric variability about the monthly median conditions.

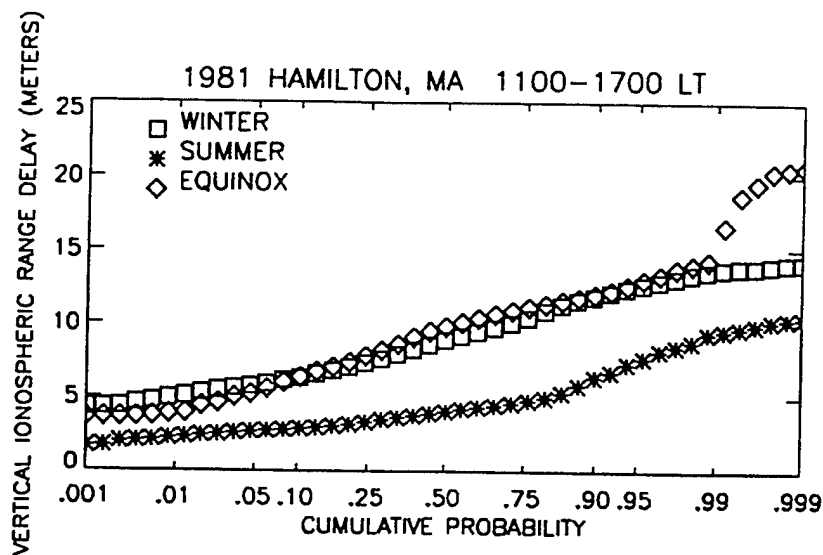


Fig. 2—Ionospheric Range Delay Statistics from Faraday Rotation Measurements Made at Hamilton, MA During the Solar Maximum Year 1981

Figure 3 shows similar ionospheric slant range delay statistics obtained by monitoring GPS satellites from Hanscom AFB during the 1992–93 time period. Since the GPS observations were obtained at all elevation angles from approximately 5 deg to overhead, the median, 1, 5, 95, and 99 percent probabilities are shown as a function of elevation angle. Note that the median delays at near-vertical elevation angles are smaller by an approximate factor of 2, as compared with those shown in Figure 2. This is due to the lower solar ultraviolet activity in 1992–93 as compared with 1981. The GPS data has not been converted to equivalent vertical range delays, nor have the individual GPS satellite group delay offsets been taken into account. The variation of range delay with elevation angle seen in Figure 3 follows approximately the secant of the zenith angle at an average ionospheric height of 350–400 km.

DATA COMPARISONS BETWEEN STATION PAIRS

The important parameter in this study is the difference in range delays as a function of distance. Thus, differences in the received absolute range delay from different stations viewing the same GPS satellites were computed. Pairs of pierce points using common GPS satellites were chosen in order to keep the distance between the ionospheric pierce points approximately the same as the station spacing, since the viewing angles to the satellites are nearly parallel for stations spaced within the region of our experimental work. For the Faraday rotation data, obtained from monitoring VHF signals of opportunity from geostationary satellites, the viewing directions were essentially constant, as was the distance between pairs of ionospheric pierce points.

The Faraday rotation data is of interest mainly because it is from a high solar activity period, and should represent near-worst-case midlatitude ionospheric range delay data for relatively large station separations. Figure 4 illustrates the

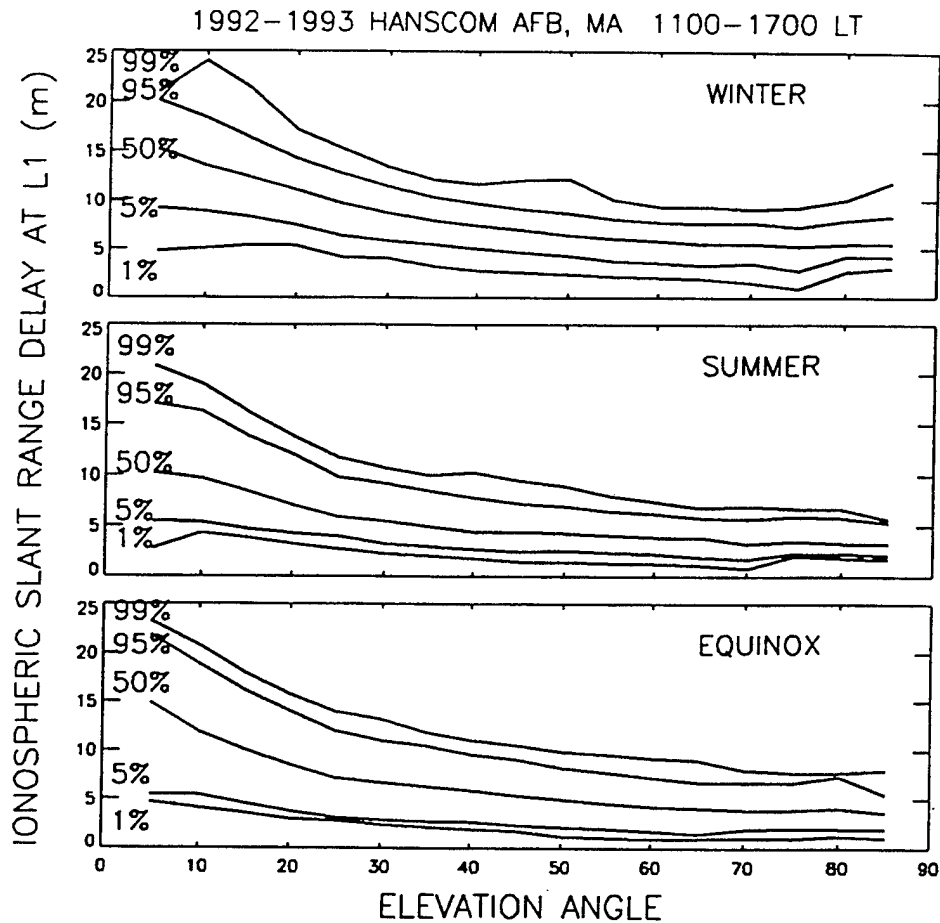


Fig. 3—Ionospheric Range Delay Statistics from GPS Measurements

residual equivalent vertical range delays between the Hamilton, Massachusetts ionospheric pierce point and the Goose Bay, Labrador ionospheric pierce point for the three seasons in 1981. The separation between these two ionospheric pierce points is approximately 1,200 km. Note that the median residual vertical range delay is less than 1 m for all three seasons of 1981. The ionospheric vertical range delay differences at the 1 percent cumulative probability point are less than -3 m for all seasons, but above the 99 percent point they are greater than +4 to +7 m, depending upon the season. At the 99.9 percent point, the differences are much greater for the 1981 equinox season. The reason for this large departure from a near-normal distribution above the 99 percent cumulative probability point is described below in the section on geomagnetic storm effects.

Figure 5 shows the cumulative probability of differences in vertical ionospheric range delay, in meters, for the Hamilton, Massachusetts and Kennedy Space Center, Florida pair of ionospheric pierce points. The distance between these two ionospheric pierce points is over 1,600 km. Note that the median difference is near zero for the winter season, yet it is less than -2 m for the

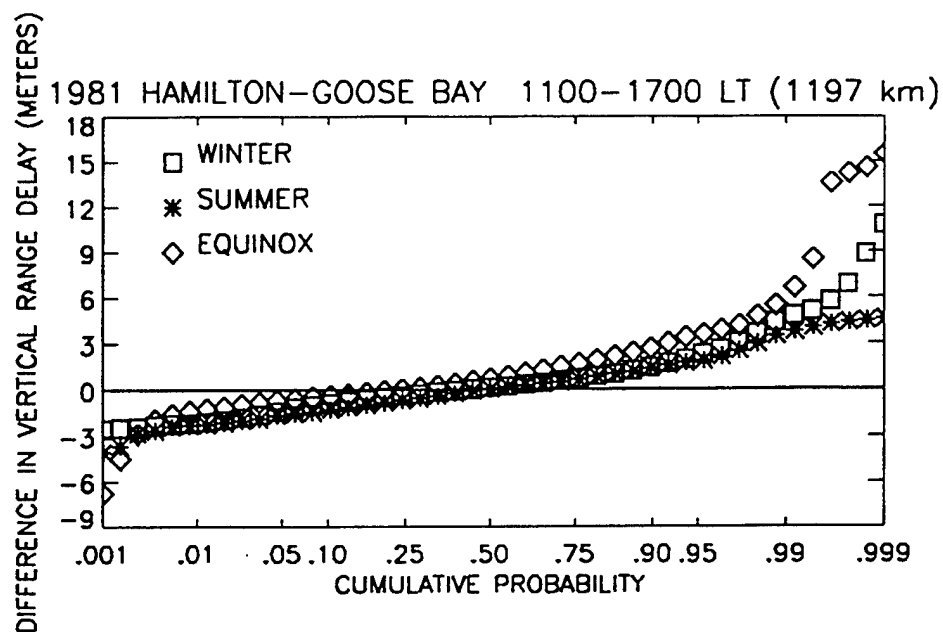


Fig. 4—Differences in Vertical Ionospheric Range Delays Observed Between Ionospheric Pierce Points Making Faraday Rotation Measurements from Hamilton, MA and Goose Bay, Labrador, for the Solar Maximum Year 1981

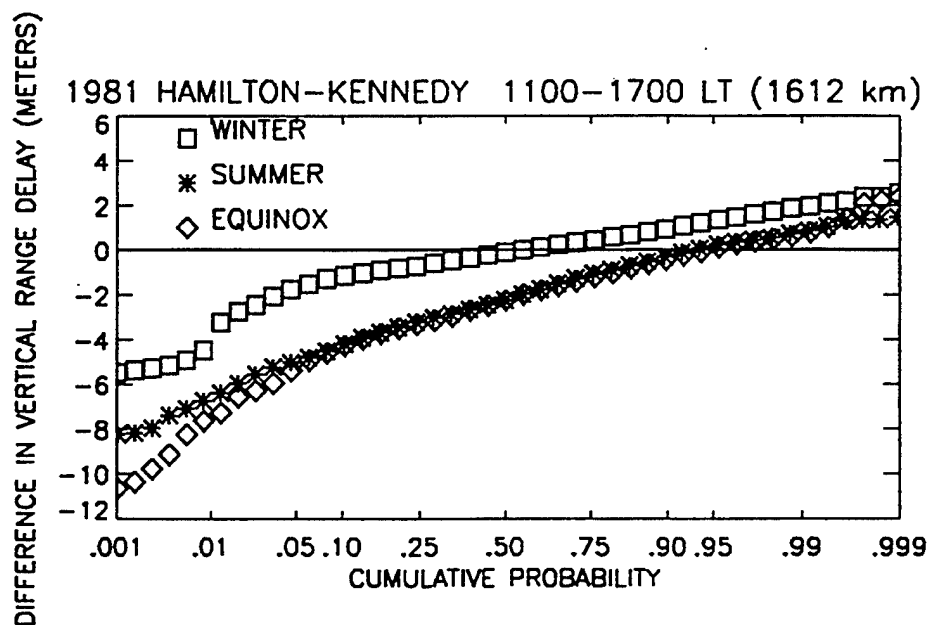


Fig. 5—Differences in Vertical Ionospheric Range Delays Observed Between Ionospheric Pierce Points Making Faraday Rotation Observations from Hamilton, MA and Kennedy Space Center, FL, for the Solar Maximum Year 1981

other two seasons. This difference may not be real given the unknown absolute calibration of the single-frequency Faraday rotation data, but in any case, median differences can be removed by existing ionospheric models. Thus for purposes of this work, differences in the delays between those at the median and those at other cumulative probability values are the important parameters. For the data illustrated in Figure 5, the relative vertical differential range errors from the median to the 5 percent and the 95 percent points vary from -2 to $+4$ m.

Figure 6 illustrates the cumulative probability of differences between solar maximum Faraday rotation data corresponding to the Kennedy Space Center, Florida and the Ramey, Puerto Rico ionospheric pierce points. For this station pair, the ionospheric pierce point separation is also approximately 1,600 km. Note that the absolute differences from the median difference values at both the 5 percent and 95 percent levels are approximately 2 m.

The Faraday range delay data obtained from the 1981 high solar maximum year was for rather large station spacings, but it was all the data available for high solar maximum conditions. When comparing the statistics from the Faraday data with those from the GPS data, it is important to recognize that the multistation GPS data collection began in April 1992, approximately one-half way down the current 11 year solar cycle. Also, shorter station spacings were used in the GPS experiment. Figure 7 illustrates the statistics of ionospheric slant range delay differences for the Hanscom AFB and Atlantic City Airport station pair for the three seasons, for daytime hours. For this station spacing of only 434 km, and for the lower solar activity conditions of 1992-93 as compared with 1981, the absolute differences from the median station differences at both the 5 percent and the 95 percent levels are approximately 1 m.

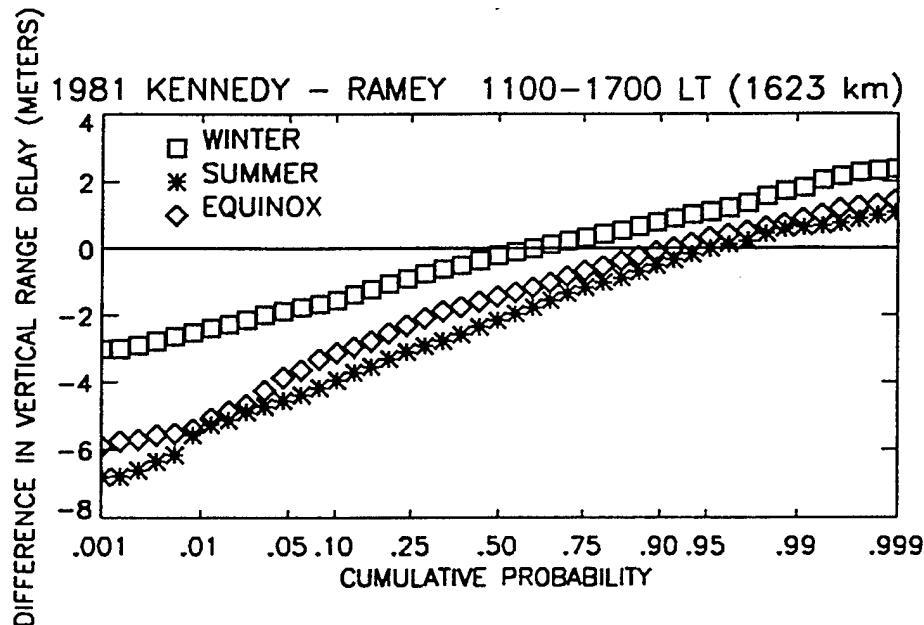


Fig. 6—Differences in Vertical Ionospheric Range Delays Observed Between Ionospheric Pierce Points Making Faraday Rotation Observations from Kennedy Space Center, FL and Ramey, PR, for the Solar Maximum Year 1981

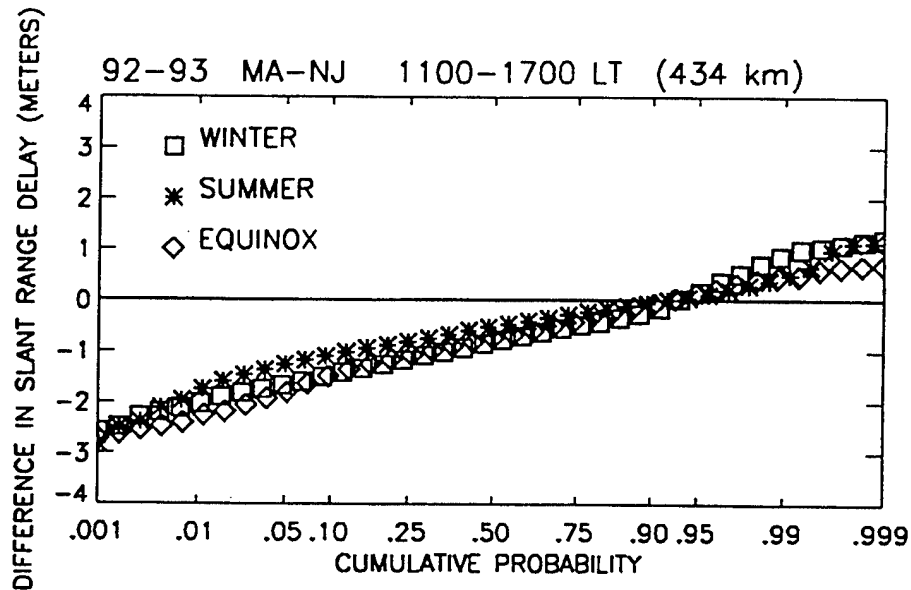


Fig. 7—Differences in Slant Ionospheric Range Delay Observed Between Stations Monitoring GPS Signals at Hanscom AFB, MA and Atlantic City, NJ in 1992-93

The larger station spacing of 1,120 km between Hanscom AFB and Dayton, Ohio had larger ionospheric range delay differences. These are illustrated in Figure 8, which shows departures from the median differences in the range of -3 m at the 5 percent level to ≈ 2 m at the 95 percent level. While these GPS

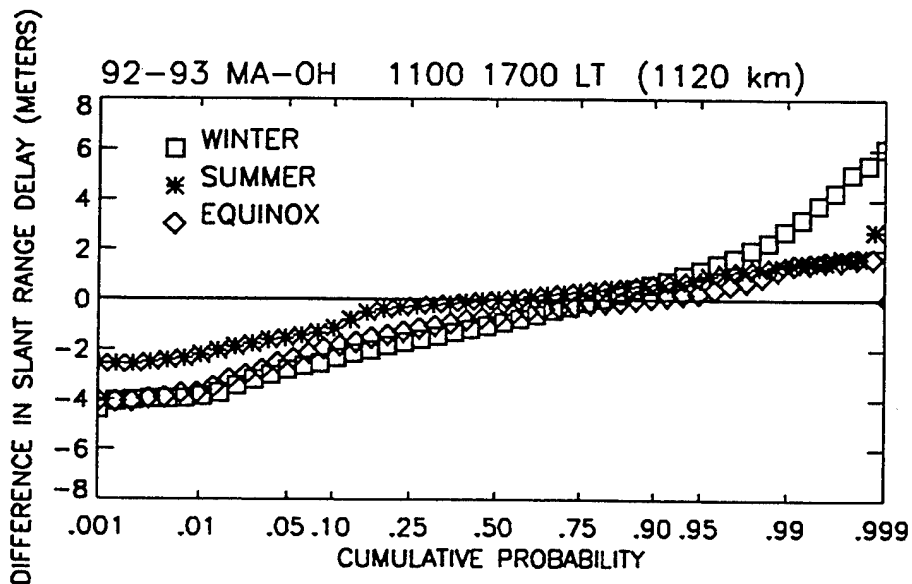


Fig. 8—Differences in Slant Ionospheric Range Delay Observed Between Stations Monitoring GPS Signals at Hanscom AFB, MA and Dayton, OH in 1992-93

observations were taken at many elevation angles, the median elevation angle was ≈ 45 deg, and a factor of approximately 2 should be used to convert those numbers to an assumed minimum GPS elevation angle of 5 deg.

SOLAR CYCLE DEPENDENCE OF IONOSPHERIC RANGE ERROR

The changing ultraviolet flux from the sun produces large differences in ionospheric range delay over the approximate 11 year solar cycle. The ionospheric range delays typically change by a factor of 3, or more, from solar minimum to solar maximum. Also, each solar cycle has different characteristics, and long-term future solar cycle behavior cannot be predicted with any great accuracy.

Unfortunately, the current portion of the present solar cycle during which our GPS measurements were taken was not a period of maximum solar activity, but was well down the descending phase of the current cycle of high activity. The solar maximum that occurred in 1989 was very similar to the solar flux value for the year 1981, for which the ionospheric range delays were available from the stations monitoring Faraday rotation. Figure 9 illustrates the last two solar cycles, indicating the periods during which the Faraday rotation and the GPS range error measurements were made. For a period of very high solar activity, such as during the solar cycle peak years of 1979–81 or 1989–91, the range delays, and the corresponding differences in range delays between pairs of stations, will be a factor of approximately 2 higher than those actually observed from the GPS satellites during the 1992–93 period. Thus to characterize high solar maximum conditions, the range delays and range delay differences given in Figures 3, 6, 7, and 8 should be multiplied by a factor of ≈ 2 .

GEOMAGNETIC STORM EFFECTS ON IONOSPHERIC RANGE DELAY

Referring to Figures 2 and 4, the large departures from a near-normal curve above the 99 percent cumulative probability for the equinox season of 1981

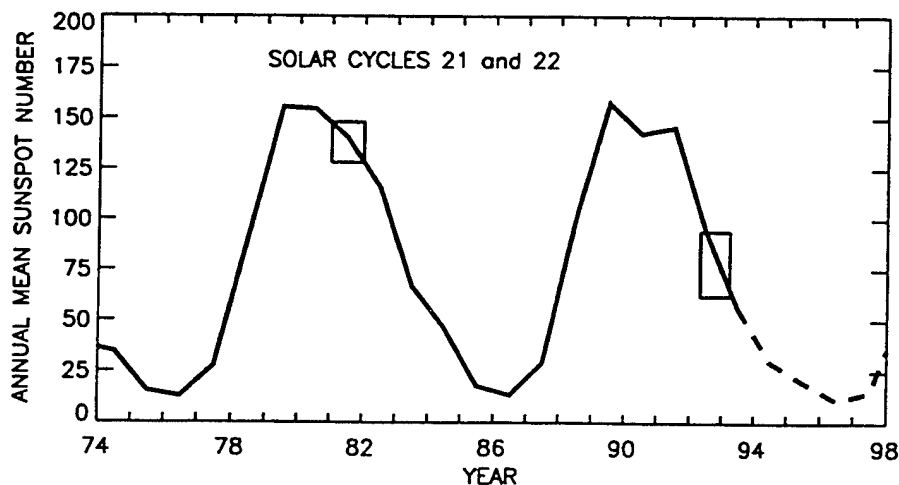


Fig. 9—Annual Mean Observed Sunspot Numbers for the Years 1974 Through 1993, with Predicted Values Through 1998

are due to the effects of one geomagnetic storm that occurred in October 1981. If only a few hours of the large, positive phase of this storm is removed from the equinox season, the positive departure in range delay for cumulative probabilities > 99 percent disappears. The October 1981 storm was by no means the largest storm that occurred during the measurement periods, but it was the one with the highest absolute departure from median ionospheric range delays and the largest geographic gradient.

Even though the effects of geomagnetic storms last for several days, the absolute ionospheric differential range delays are the important factor in WAAS, and these occur for only a relatively short period of time during a storm. If only a few major geomagnetic storms occur each year, and if the large ionospheric range delay gradients introduced by the storm effects occur for only the afternoon of the first day of each major storm period, that cumulative length of time is less than 1 percent of the entire year. Thus, the ionospheric range delay statistics will not be seriously affected, except below the 1 percent and above the 99 percent levels. Indeed, with the exception of the October 1981 storm, little evidence was found in the 1981 solar maximum Faraday rotation measurements, at any cumulative probability level, of major effects in the statistics of ionospheric range delay due to magnetic storms. During the approximately 1 year period of GPS range delay measurements in 1992-93, no evidence could be found of large magnetic storm effects on differential range delays. This is a hopeful sign for WAAS implementation.

In an operational WAAS, the ionospheric range delay will be continuously measured at a number of stations throughout the extended CONUS region. These real-time measurements can be used to determine what the ionospheric gradients are. If the gradients become too large to model successfully using the planned set of grid nodes, or if the real-time ionospheric range delay data becomes erratic or immeasurable because of the extremely rare occurrence of strong amplitude and phase scintillation effects in the CONUS region, then a simple warning message can be sent to users on a standard WAAS link, advising that the residual ionospheric error is not within the normal tolerances. Ionospheric delay gradients much larger than those normally observed in the CONUS region due to severe ionospheric disturbances are not expected to occur for more than a few days in each 11 year solar cycle.

ESTIMATION ERRORS IN IONOSPHERIC RANGE DELAY AT A SINGLE SITE

The objective of this paper is to obtain statistics on the required station spacing for the WAAS system. Results presented to this point summarize the statistics of measured ionospheric range delay at a single station, and differences in measured delays at pairs of stations with varying distances between them. To complement these results, the database was further used in a simple linear interpolation technique to determine potential errors in the estimation of ionospheric range delay. The technique used was simply to isolate the vertical delay measurement recorded at one station and fit the simultaneous vertical delay measurements recorded at the other three stations to a straight line, using a least-squares fit. The resultant least-squares line was then used to estimate the vertical delay at the isolated station. This estimated vertical delay

was compared with the measured vertical delay to determine an estimation error.

Figure 10 illustrates the results of this error estimation at the Hamilton pierce point using the 1981 solar maximum Faraday measurements from Goose Bay, Kennedy Space Center, and Ramey. Note that the closest stations to Hamilton are Goose Bay, which is 1,197 km north, and Kennedy Space Center, which is 1,612 km south. The results show median residual errors in vertical range delays with magnitudes of 0 to 1.5 m for all seasons. The largest absolute estimation errors of 3.3 m are visible at the 1 and 99 percent probability levels. The strong deviations below the 1 and above the 99 percent probability levels are attributable primarily to the geomagnetic storm effects discussed in the previous section. Results of the estimation process at the Kennedy Space Center are presented in a similar manner in Figure 11. The closest stations to the Kennedy site are Hamilton, which is 1,612 km north, and Ramey, which is 1,623 km south. The median residual errors are within 1 m for all seasons, and reach magnitudes similar to those at Hamilton for the 1 and 99 percent levels. The large geomagnetic storm effects are not as apparent at the Kennedy ionospheric pierce point as they are at the Hamilton pierce point.

A similar error estimation technique was applied to the GPS measurements of 1992–93. In this process, only data from the north-south station chain of Oldtown, Hanscom AFB, Atlantic City, and Georgetown was included. Simultaneous daytime slant delay measurements from these four stations viewing the same satellite were converted to equivalent vertical range delay at the ionospheric pierce point. Equivalent vertical delay measurements from three ionospheric pierce points were then used to estimate equivalent vertical delay at the fourth pierce point, which was compared with the measured equivalent vertical delay. Results of this error estimation process for the Hanscom AFB pierce points are presented in Figure 12. Note that the closest sites to Hanscom AFB are Oldtown, which is 348 km north, and Atlantic City, which is 434 km

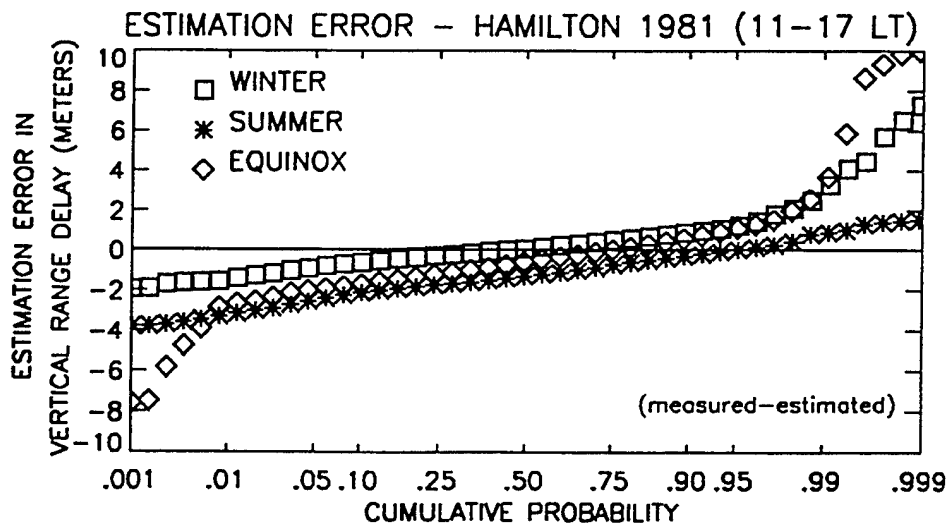


Fig. 10—Differences Between Faraday Rotation Measurements of Vertical Delay and Estimated Vertical Delay at the Ionospheric Pierce Point Viewed from Hamilton, MA

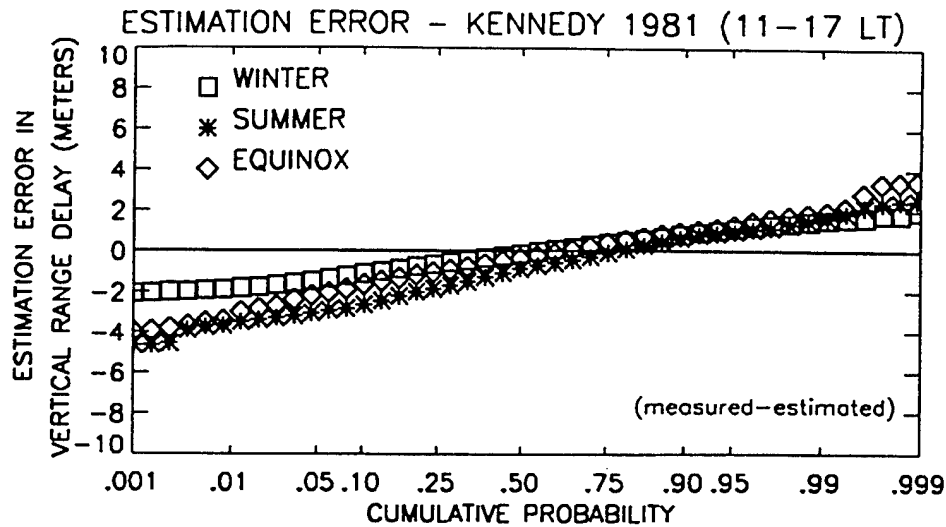


Fig. 11—Differences Between Faraday Measurements of Vertical Delay and Estimated Vertical Delay at the Ionospheric Pierce Point Viewed From Kennedy Space Center, FL

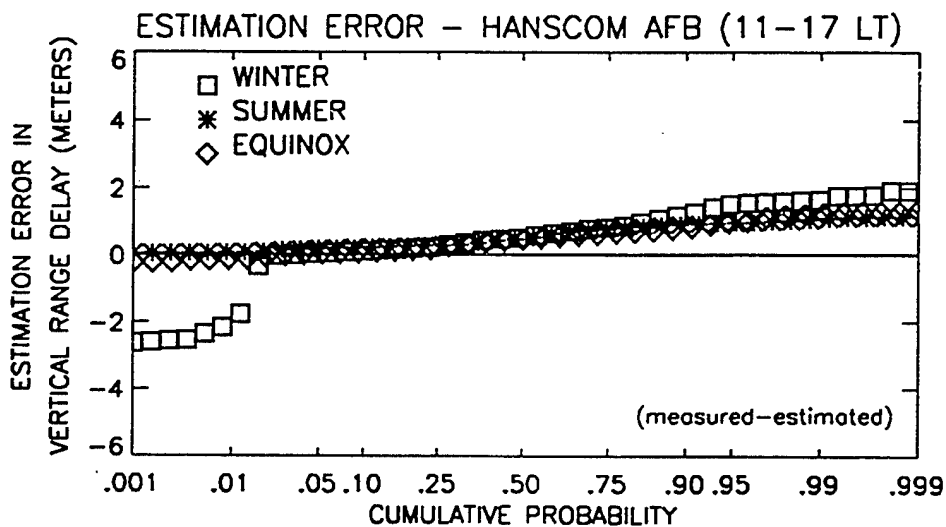


Fig. 12—Differences Between GPS Measurements of Vertical Delay and Estimated Vertical Delay at the Ionospheric Pierce Points Viewed from Hanscom AFB, MA

south. The overall estimation errors are much smaller than those found in the 1981 statistics, primarily because of the closer spacing between stations and the lower level of solar activity. Even at the 1 and 99 percent probability levels, the magnitude does not get larger than 1.8 m for any season. Figure 13 demonstrates similar results for measurements taken at Atlantic City. Here, the closest sites are Hanscom AFB, which is 434 km to the north, and Georgetown, which is 805 km south. Figure 13 shows that the overall estimation errors are within .5 m during the summer and reach magnitudes of

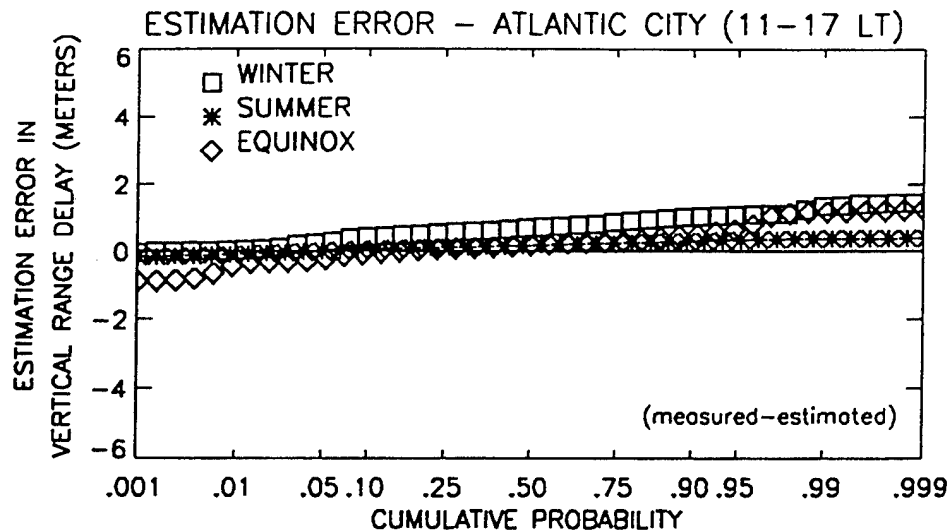


Fig. 13—Differences Between GPS Measurements of Vertical Delay and Estimated Vertical Delay at the Ionospheric Pierce Points Viewed from Atlantic City, NJ

only 1.4 m overall for the other two seasons. Table 5 summarizes the statistics of estimation errors in vertical range delay for two stations recording Faraday measurements—Hamilton and Kennedy Space Center—and the GPS measurement stations at Hanscom AFB and Atlantic City.

In this analysis, we were limited to using measurements from only three ionospheric pierce points to estimate ionospheric delay at a fourth pierce point. The WAAS ionospheric grid algorithm referenced in [3] basically uses measured ionospheric delays at the pierce points for each visible satellite from approximately 24 reference stations. These measured values are then used to estimate the vertical ionospheric delay for each node of an imaginary grid on the ionospheric sphere. The residual ionospheric delays in the WAAS system are expected to be smaller than those presented here since the grid algorithm uses all measurements available from all stations and visible satellites, and can

Table 5—Estimation Errors in Vertical Range Delay (m)

Station	Season	1%	5%	50%	95%	99%
Hamilton	winter	-1.49	-0.88	0.06	1.19	2.83
	summer	-3.24	-2.52	-1.33	-0.02	0.84
	equinox	-2.80	-2.00	-0.59	1.05	3.36
Kennedy	winter	-1.85	-1.45	-0.13	1.08	1.49
	summer	-3.60	-3.00	-0.85	0.93	1.55
	equinox	-3.23	-2.15	-0.35	1.23	1.88
Hanscom	winter	-1.80	0.03	0.53	1.52	1.67
	summer	0.06	0.18	0.48	0.96	1.08
	equinox	-0.13	0.04	0.46	0.97	1.24
Atlantic City	winter	0.03	0.27	0.71	1.08	1.35
	summer	-0.10	-0.01	0.18	0.34	0.37
	equinox	-0.40	-0.25	0.18	0.65	1.17

be made more sophisticated than the simple linear fit technique used in this analysis.

SUMMARY OF IONOSPHERIC DELAY DIFFERENCES AND CONCLUSIONS

Differences in GPS slant ionospheric range delays at the 1, 5, 95, and 99 percent cumulative probability levels, for daytime conditions for each station pair, and for each season, are given in Table 6. These values are summarized in Figure 14, which shows a steady increase in delay difference with station spacing for all the probability values. Most of the station pairs are aligned along an approximate north-south direction (e.g., Oldtown, Maine to Georgetown, South Carolina), but the Dayton, Ohio station is mainly west of the Atlantic coastal chain of the other stations. Data from the Dayton and Atlantic City station pair, the Hanscom AFB and Dayton station pair, and the Oldtown and Dayton station pair are shown as starred points in Figure 14. In most cases, they do not differ significantly from the lines drawn through the stations having a predominantly north-south spacing, indicating that there is little difference between the statistics of north-south and east-west ionospheric range delay differences, at least over this region in CONUS during the time of these observations.

Table 6—Difference in Slant Range Delays (m) Observed
for Stations Pairs vs Cumulative Probability

Distance (km)	Season	1%	5%	95%	99%
348 (ME-MA)	winter	-0.9	-0.5	1.4	2.6
	summer	-0.6	-0.6	0.5	0.7
	equinox	-1.1	-0.8	0.7	1.4
434 (MA-NJ)	winter	-1.3	-0.9	1.0	1.6
	summer	-1.3	-0.8	0.6	1.0
	equinox	-1.5	-1.0	0.9	1.3
782 (NJ-ME)	winter	-2.4	-1.5	1.5	2.5
	summer	-0.8	-0.6	0.7	1.1
	equinox	-3.2	-1.7	1.0	2.0
805 (NJ-SC)	winter	-2.3	-1.5	1.4	2.4
	summer	-1.2	-0.8	0.7	1.2
	equinox	-3.0	-1.8	1.2	1.9
828 (NJ-OH)	winter	-3.1	-2.2	1.9	2.7
	summer	-1.0	-0.8	0.9	1.8
	equinox	-2.5	-1.5	1.3	2.3
1,120 (MA-OH)	winter	-2.9	-1.8	2.1	4.0
	summer	-2.3	-1.5	0.9	1.4
	equinox	-2.9	-1.7	0.9	1.9
1,238 (ME-SC)	winter	-3.1	-1.8	1.6	2.8
	summer	-1.9	-1.0	1.0	1.7
	equinox	-4.8	-2.6	1.9	2.4
1,393 (ME-OH)	winter	-4.5	-2.9	3.0	5.2
	summer	-1.7	-1.3	1.4	2.0
	equinox	-3.7	-2.1	1.9	3.5
1,586 (ME-SC)	winter	-3.9	-2.9	2.7	4.4
	summer	-1.9	-1.2	1.4	2.1
	equinox	-5.1	-3.0	2.3	3.5

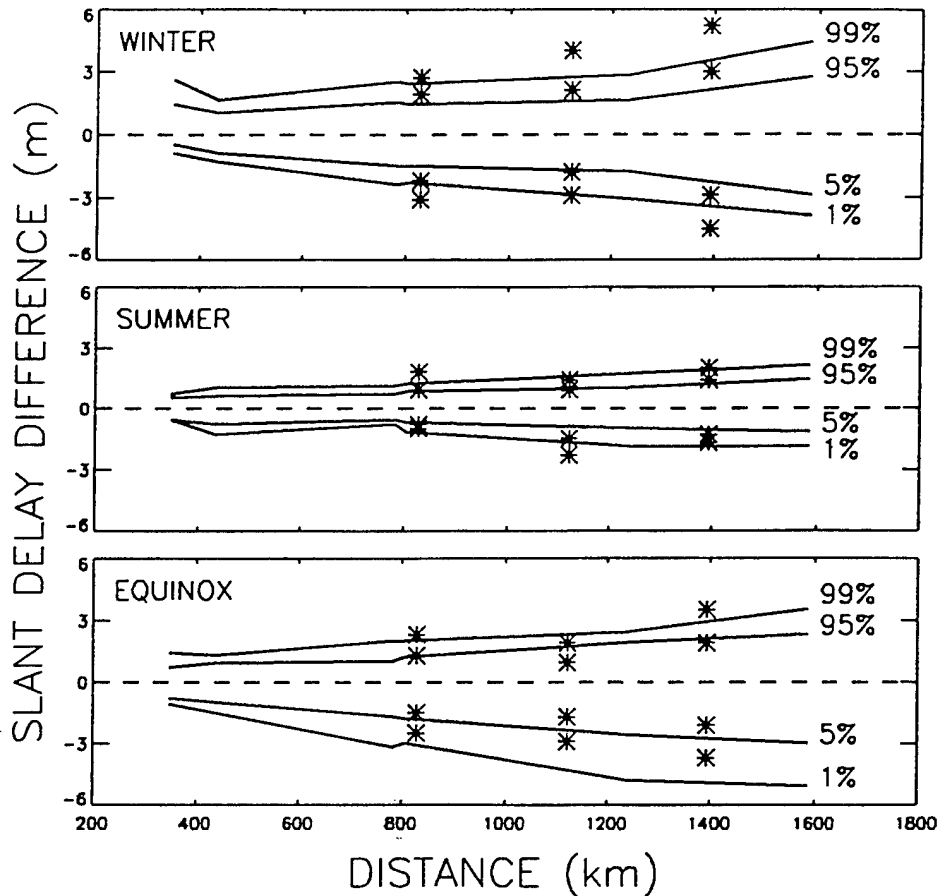


Fig. 14—Ionospheric Delay Differences Versus Station Spacing, for the Daytime Hours Only (data from station pairs with a major east-west direction component are indicated by an asterisk)

The results from the initial 1 year of measurements of GPS ionospheric range delays and 1 year of similar data from a high solar maximum year taken in and near the CONUS region show that differential slant range delays are approximately ± 2 m or less for station spacings of approximately 430 km for at least 99 percent of the time. Even for a pair of GPS stations spaced at over 1,100 km, the differential ionospheric range delays do not exceed approximately 5 m between the 5 and the 95 percent cumulative probability levels. Extrapolations to conditions of higher solar activity are not precise, but they indicate that a factor of 2 increase in range delays should be sufficient for even very high solar maximum conditions, as was the case for the last two solar maxima.

The results of this paper show that if a user is located ≈ 800 km from a monitoring station, the difference in slant ionospheric delays is within ≈ 2 m at the 5 and the 95 percent probability levels. During the peak of a high solar maximum period, this differential ionospheric range delay is approximately twice as large, e.g., 4 m. The spacing between WAAS reference stations in CONUS should be arranged to take these results into account. Since the results in this paper are based on actual measured data, they are representative of a

lower bound of any real-time prediction algorithm, which probably will not be able to fit better than the actual ionospheric measurements.

ACKNOWLEDGMENTS

This work was partially sponsored by the Satellite Program Office (AND-150) of the Federal Aviation Administration.

Based on a paper presented at The Institute of Navigation's 50th Annual Meeting, Colorado Springs, Colorado, 1994.

REFERENCES

1. Klobuchar, J. A. and Johanson, J. M., *Correlation Distance for Mean Daytime Electron Content*, Air Force Geophysics Laboratory TR-77-0185, ADA048117, 22 August 1977.
2. Gail, W. B., Prag, A. B., Coco, D. S. and Coker, C., *A Statistical Characterization of Local Mid-Latitude Total Electron Content*, Journal of Geophysical Research, Vol. 98, No. A9, pp. 15,717-27, September 1993.
3. El-Arini, M. B., Kellam, P., O'Donnell, P., Klobuchar, J. A., Wisser, T. C., and Doherty, P.H., *Ionospheric Experimentation for Wide Area Differential GPS (WADGPS) with Implications on Algorithm and System Design*, presented at the National Technical Meeting of The Institute of Navigation, San Francisco, CA, 20-22 January 1993.
4. Miliken, R. J. and Zoller, C. J., *Principles of Operation of NAVSTAR and System Characteristics*, Collection of Papers on GPS, Institute of Navigation, Washington, D. C. 1980, Vol. 1, pp. 3-14.
5. Jorgensen, P. S., *Ionospheric Measurements from NAVSTAR Satellites*, SAMSO-TR-79-29, AD A068809, December 1978, available from the Defense Technical Information Center, Cameron Station, Alexandria, VA.
6. Klobuchar, J. A., Basu, S. and Doherty, P. H., *Potential Limitations in Making Absolute Ionospheric Measurements Using Dual Frequency Radio Waves from GPS Satellites*, presented at the Ionospheric Effects Symposium, IES-93, May 1993. Available from NTIS, Springfield, VA.

Statistics of Time Rate of Change of Ionospheric Range Delay

Patricia H. Doherty
Institute for Space Research
Boston College
Newton, MA 02159

John A. Klobuchar
Ionospheric Effects Division
Phillips Laboratory
Hanscom AFB, MA

M. Bakry El-Arini
The MITRE Corporation
McLean, VA

ABSTRACT

The time rate of change of ionospheric range delay is a potential limitation to the Wide Area Augmentation System (WAAS) in precise positioning using radio waves from Global Positioning System, (GPS), satellites in the single frequency c/a mode. Dual frequency GPS users with access to the p-code automatically correct for the effects of both the ionospheric range delay and its rate of change. Single frequency GPS users can use a simple algorithm for ionospheric range delay to place an absolute scale on their measurements of c/a code minus carrier, to correct for the time rate of change of ionospheric range delay, but the inherent noisiness of the L1 code data can severely limit the single frequency ionospheric correction capability, especially in removing the effects of the rate of change of ionospheric range delay.

To investigate the statistics of ionospheric range-rate changes, dual frequency GPS data from stations in parts of the world representative of different ionospheric conditions was obtained from the International GPS Geodynamics Service, (IGS), network, managed by the Jet Propulsion Laboratory, (JPL). Values of dual frequency, differential carrier phase were computed at one minute intervals and then were high pass

filtered to remove long term changes. Relative ionospheric range delay changes over time intervals of 1, 2, 5, and 10 minutes duration were then computed and the statistics of these rates of change of ionospheric time delay were compiled for different times of day, viewing direction, and various conditions of magnetic activity. The largest rates of change of ionospheric range delay were observed in the auroral region during periods of high magnetic activity.

INTRODUCTION

One of the potential limitations to ionospheric corrections for the proposed Wide Area Augmentation System, (WAAS), (El-Arini, et. al., 1995) is in how rapidly ionospheric range delay corrections must be made in an operational WAAS. Large scale, slowly changing, ionospheric features can be removed by use of a network of dual frequency ionospheric monitoring stations, (El-Arini, et. al., 1993, 1994). However, rapidly changing ionospheric range delays are generally small scale, and are due to phase fluctuations which occur when the GPS signal passes through a region of irregularities in the ionosphere.

These irregularities produce short term phase fluctuations in the carrier of the radio waves which pass through them. The high rate of phase changes can potentially cause loss of phase lock of GPS receivers, especially when accompanied by amplitude fading. The amplitude of the radio wave also is subject to severe fading, which can be as deep as 25dB. There are also occasional signal enhancements, and the average signal power remains the same. These effects are commonly called phase and amplitude scintillations. Ionospheric irregularities most often occur in the auroral zone, that part of the high latitude region of the earth where charged particles coming from the sun directly impinge on the earth, causing visual aurora, and irregularities in the earth's ionosphere. The near-equatorial region, a belt of up to $\pm 30^\circ$ either side of the magnetic equator, produces the highest recorded scintillations, (Goodman and Aarons, 1990), but generally only during the local evening hours, and in patchy regions of the sky, unlike in the auroral region where the spatial and temporal extent of irregularities can be much greater.

Wanninger, (1992), used differences in GPS differential carrier phase over one minute time intervals to compute phase fluctuations of data collected from five stations in Brazil during a ten day period of observations in March 1992. His observations confirmed the well known temporal dependence of scintillations in the equatorial region, which begins shortly after local sunset and can extend until after local midnight, with periods of intermittent scintillation during this time interval. Wanninger, (1993), looked at the occurrence of GPS phase scintillation at the Kokee, Hawaii station, located somewhat north of the equatorial irregularity belt region. He found a significant occurrence of phase scintillation equatorwards of the Kokee station during the local nighttime hours, beginning about one hour after local sunset, and occasionally continuing until the following dawn period. Data from the Kokee station also was from 1992, on the declining phase of the current 11 year cycle of long term solar activity, but still a year having significant scintillation effects. The current solar minimum is expected to occur sometime in 1996. Though Wanninger's 1992 data was taken at least two years after the current sunspot cycle maximum, which occurred in 1989-1990, this maximum was abnormally large, and 1992 was a year having a mean sunspot number more representative of an average solar cycle maximum.

In this paper the emphasis is on GPS observations from the CONUS, and from the auroral region north of the CONUS, regions where the WAAS system likely will first be implemented, in order to quantify the magnitude of the short term changes in ionospheric range delay. Unfortunately, GPS data from these stations was only available online beginning in late 1993, and continuing through July 1994, well down the current solar cycle, not representative of solar cycle maximum conditions. Extrapolations to solar maximum conditions can be made, but with an uncertain degree of confidence. The dependence of phase fluctuations on the average location and extent of the auroral region, assumed to be a function of the magnetic K_p index, also are shown.

AVAILABLE GPS IONOSPHERIC DATA

In order to determine the statistics of ionospheric range-rate changes, dual frequency GPS data was obtained from the IGS network which provides an excellent opportunity to study the behavior of ionospheric

range delays and their rates of change over a wide range of latitudes. The potential use of this data base in ionospheric research is extensive and has been described by Wanniger, (1992 and 1993). The data base has already been utilized by Wilson, et. al., (1992) to generate global ionospheric maps. In addition, Wilson and Mannucci, (1993), used the IGS data base, (IGS, 1995), to estimate instrumental biases in the GPS receivers at the various IGS stations, as well as in individual GPS satellite transmitters. Sardon, et. al., (1994) also used data from several stations in the IGS network to estimate both GPS transmitter and receiver differential group delays. In this study, recent data from the IGS network has been obtained from a wide range of representative mid-latitude and auroral locations in the northern hemisphere, including Spitsbergen Island and Tromso, Norway, and several stations in the United States and in Canada.

The ionospheric data available from the IGS consists of 30 second values of carrier phase and group delay at both the GPS L_1 and the L_2 frequencies. From the available data it is possible to determine the statistics of these short term changes in delay. If time rates of change of ionospheric range delay are very large, and unpredictable, the residual range delays, even after correction, can still be unacceptable. On the other hand, if short term ionospheric range delay variations are found to be small, or if they change in an easily predictable manner over time, they will be easier to correct, and these predictable rates of change should not pose a problem in the correction process. Statistics of the percent occurrence of changes in ionospheric range delay are presented for different times of day, viewing direction and various levels of geomagnetic activity.

DATA PROCESSING PROCEDURE

The data used in this study was recorded from December 1993 through July 1994 at the IGS network locations illustrated in Figure 1 and listed below:

My Alesund, Svalbard Is.	78.8N, 11.8E
Tromso, Norway	69.7N, 18.9E
Fairbanks, AK	64.8N, 147.5W

Yellowknife, NW. Terr.	62.3N, 114.5W
Albert Head, B. C.	48.2N, 123.5W
St. John's, Newfoundland	47.4N, 52.7W
Westford, MA	42.4N, 71.5W
Goldstone, CA	35.1N, 116.9W
Richmond, FL	25.0N, 80.4W

All stations in the IGS network are equipped with GPS Rogue or Turborogue dual-frequency receivers which record both the differential carrier phase and the differential group delay from up to eight satellites simultaneously. To insure data compatibility, all stations in the network store the data in Receiver INdependent EXchange, (RINEX) format. In this study, absolute values of ionospheric range delay were not required, since only short term rates of change of ionospheric range delays were needed. In order to isolate short term range delay changes, the differential carrier phase measurements were filtered using a symmetrical finite impulse response filter with 51 weights having no attenuation at 15 minutes and 60 dB of attenuation at 60 minutes. This filter was designed to remove diurnal changes, any possible effects due to large amplitude, travelling ionospheric disturbances, which generally have periods longer than 15 minutes, and any changes induced by the changing satellite elevation angle which are relatively long term. These long term changes can be removed in an operational system either by modeling, or by the use of dual frequency codeless ionospheric measurements from the WAAS network of stations, (El-Arini, et. al., 1994). Short term changes in ionospheric range delay then were computed over time intervals of 1, 2, 5 and 10 minutes.

The Block II GPS satellites were switched to the a/s or anti-spoofing mode on February 1, 1994. Beginning at that time, the IGS receivers were operated in the codeless mode. Figure 2 shows examples of raw differential group delay and fitted slant ionospheric differential carrier phase data from Yellowknife, Northwest Territories, Canada for satellites operated in both a coded and a codeless mode. Note that the short term fluctuations in ionospheric range delay are seen readily on the differential carrier phase which is not significantly affected by multipath, or by a/s. Both in code and codeless operation it was possible to fit the differential carrier phase data to an absolute scale using the higher elevation portions of the differential group

delay data, though, in this study, since only rate of change values are used, absolute values of ionospheric range delay are not necessary.

STATISTICAL RESULTS

Monthly statistics of time rates of change of ionospheric range delay have been produced separately for 4 different time intervals of the day for each station used in this study. Times were converted to local time, (LT), at the receiver station and were grouped as follows: 05-11 hours LT, 11-17 LT, 17-23 LT, and 23-05 LT.

Figure 3 illustrates an example of the raw differential carrier phase, and the high pass filtered data obtained from one GPS satellite pass received at Yellowknife, Northwest Territories, Canada. Note that the short term fluctuations have peak to peak magnitudes of up to ± 0.3 meters. Figure 4 shows how these fluctuations are resolved over different time intervals. Note that the rates of change of ionospheric range delay computed over a one minute time interval, shown at the top of Figure 4, are the largest, followed in order, by those computed over 2 minute, 5 minute and 10 minute intervals. There are virtually no variations at 10 minute intervals, even though the high pass filter used to filter out long period variations had no attenuation for 10 minute periods, indicating that short-term fluctuations of differential carrier phase predominate in the data.

Figure 5 shows the statistics of the 1 minute and the 5 minute rates of change of ionospheric range delay. The results shown in Figure 5 are in the form of arithmetic probability plots. In this type of plot, changes in ionospheric range delay are plotted versus their probability of occurrence, in order to illustrate the shape of the distribution. A straight line indicates a "Gaussian" or normal distribution. The slope of the straight line is a measure of the standard deviation of changes about a mean value. Changes from a straight line are measures of the departures from a normal distribution, and usually occur near the very low and the very high probability regions of the plot. For all times of day at Yellowknife, the 1 minute rates of change of ionospheric range delay were higher than the 5 minute rates of change by a large factor, again clearly

showing that the changes observed are due to very short period fluctuations in the ionosphere.

In order to be certain that the ionospheric range delay variations seen at Yellowknife were due to short term, irregular changes in the ionosphere, and not to either diurnal or elevation angle changes which occur during a pass, a comparison of high pass filtered and raw, unfiltered ionospheric range delay change statistics was done. The results are shown in Figure 6. The statistics of the 15 minute changes shown in Figure 6 are for unfiltered data, while those for the 1 minute changes have been filtered using the filter described earlier. Note that the mid-latitude station at Westford, MA has a very small occurrence of 1 minute changes, while the Yellowknife station, located under the auroral region, shows very high 1 minute changes in ionospheric range delay. In both cases the changes over a 15 minute period are simply due to the diurnal and elevation angle effects which are slightly higher at the Westford station. Thus, it is reasonable to look only at the high pass filtered data to determine the statistics of the range delay variations which cannot be modeled.

Figure 7 shows a comparison of rates of change of ionospheric time delay that occurred over a 1 minute period during the local nighttime hours at Yellowknife, Fairbanks, Westford, Albert Head and Richmond during December 1993. It is evident that these changes occur most frequently at Yellowknife and at Fairbanks. Both of these stations are located under the auroral region. Figure 8 shows ionospheric range delay rates for a one minute interval for the same stations for the daytime hours of 11-17 local time. Even during the daytime hours the range delay changes are significant at both Yellowknife and Fairbanks. This is because of the irregularities in the auroral region.

The average location of the auroral region has been described by Feldstein in Holzworth and Meng, (1975), for various conditions of geomagnetic activity. The location of the auroral oval is depicted in Figure 9, for conditions of relatively high geomagnetic activity, using an auroral Q index of 6. Also illustrated in Figure 9 are the 400 km height intersections of rays from the Yellowknife station to GPS satellites. The 400 km height is taken as the mean height of the peak of the nighttime F2 region where most of the irregularities responsible for the scintillation effects occur. The auroral oval rotates in the geomagnetic latitude

coordinate system, which is centered at geomagnetic pole, located at 79.1° North, 288.9° East geographic latitude. For geomagnetically quiet conditions, indicated by an auroral Q index of zero, the auroral oval illustrated in Figure 9 would be narrower in width and would not extend as far equatorward, as is the case illustrated for a magnetic Q index of 6. As Figure 9 also illustrates, the Yellowknife station is under the aurora virtually all day long, and many GPS passes recorded at Fairbanks would also pass through the auroral zone. Measurements made at Albert Head and St. John's are not likely to be affected by the aurora during moderate magnetic conditions. During severe magnetic storms, however, the auroral oval expands both equatorwards and polewards, and effects can be seen down to the mid-latitudes. This effect can be seen in the data illustrated in Figure 10, where local daytime time rates of change of ionospheric range delay recorded at St. Johns have been sorted by different levels of magnetic activity, referenced by the magnetic K_p index.

SUMMARY OF RESULTS

Figure 11 summarizes the results for 1 minute time rates of change in ionospheric range delay for all locations, for 3 seasons, during the local nighttime hours. In this figure, the 1%, 5%, 50%, 95% and 99% cumulative probability levels of ionospheric range delay variations are plotted versus the geomagnetic latitude of each station. In all seasons phase scintillation effects become apparent in the auroral zone, at approximately 60° geomagnetic latitude. Figure 11 clearly showed virtually no short term scintillation effects from approximately 35° to 58° North geomagnetic latitude, corresponding to 25° to 48° geographic latitude, during this portion of the current solar cycle.

Several months of range delay change statistics were computed from data taken at the Kokee, Hawaii station, located slightly northward of the equatorial anomaly region of peak occurrence of ionospheric irregularities. At the 1994 near-minimum in long term solar cycle activity the occurrence statistics of ionospheric range delay variations in the equatorial region are much lower than those in the auroral region. More study is required to determine why this is the case, but irregularities in the equatorial region generally occur only

in the post-sunset to local midnight time period, and have a patchy nature even during those time periods, while the auroral region has a greater temporal and spatial occurrence. The differences in temporal and spatial extent likely significantly affect the differences in overall occurrence statistics between the two regions.

CONCLUSIONS

The data set made available by the IGS network is an important asset to the ionospheric research community. During the time period from late 1993 through July 1994, which is well down in the current 11 year solar activity cycle, only small effects were seen in short term rates of change on ionospheric range delays, not exceeding 0.3 meters per minute, even at the 1% and the 99% statistical points, during the nighttime hours of maximum activity. During years of high solar activity, the background electron densities and the irregularities which produce scintillation effects are expected to be approximately three times larger than those during the period of measurements available for this paper. During solar maximum conditions the anticipated rates of change of range delay should be approximately three times larger, but, even then, likely will exceed 1 meter per minute, only below the 1 percentile, and above the 99 percentile.

Fortunately, these rates of change are not cumulative over time, that is, they do not represent larger absolute changes over longer periods, but can be characterized as random fluctuations superimposed upon the normal large scale background variations which are adequately corrected by the planned constellation of dual frequency codeless WAAS ionospheric monitoring stations.

These results indicate that the largest short term changes in ionospheric range delays occur in the auroral zone during the nighttime hours. The largest changes occur within 1 minute, indicating that they are related to auroral phase scintillations. The CONUS region is free of significant, short term changes in ionospheric range delay during this period of low solar activity, even at the 1% and the 99% statistical levels.

ACKNOWLEDGEMENTS

This work was partially sponsored by the Satellite Program Office, (AND-510) of the Federal Aviation Administration.

REFERENCES

- El-Arini, M. B., P. Kellam, P. O'Donnell, J. A. Klobuchar, T. C. Wisser, P. H. Doherty, "The FAA Ionospheric Experiment for Wide-Area Differential GPS (WADGPS)", presented at the ION meeting, San Francisco, CA, 20-22 Jan 1993.
- El-Arini, M. B., C. J. Hagarty, J. P. Fernow, J. A. Klobuchar, "Development of an Error Budget for a GPS Wide-Area Augmentation System (WAAS)", The ION National Technical Meeting, San Diego, CA 24-26 January 1994.
- El-Arini, M. B., R. S. Conker, T. W. Albertson, J. K. Reagan, J. A. Klobuchar, and P. H. Doherty, "Comparison of Real-Time Ionospheric Algorithms for a GPS Wide-Area Augmentation System (WAAS)", NAVIGATION: Journal of The Institute of Navigation, Vol. 41, No. 4, pp 393 - 413, Winter 1994-1995.
- Goodman, J. M., and J. Aarons, "Ionospheric Effects on Modern Electronic Systems", Proc. IEEE, Vol. 78, pp 512-528, March 1990.
- Holzworth, R. H. and C. I. Meng, "Mathematical Representation of the Auroral Oval", Geophysical Research Letters, Vol. 2, No. 9, Sept. 1975.
- IGS, "International GPS Service for Geodynamics", published by the International Association of Geodesy, Central Bureau, JPL, Pasadena, CA, May 1995.

Jorgensen, P. S., "Ionospheric Measurements from NAVSTAR Satellites", SAMSO-TR-79-29, AD A068809, December 1978. Available from the Defense Technical Information Center, Cameron Station, Alexandria, VA 22304

Sardon, E., A. Rius, and N. Zarraoa, "Estimation of the Transmitter and Receiver Differential Biases and the Ionospheric Total Electron Content from Global Positioning System Observations", RADIO SCIENCE, Vol. 29, No. 3, pp 577-586, May-June 1994.

Wanninger, L., G. Seeber and M. A. Campos, "Limitations of GPS in Central and South America due to the Ionosphere", presented at the International Conference "Cartography-Geodesy", Maracaibo, Veneuela, Nov. 24 - Dec. 4, 1992.

Wanninger, L. "Ionospheric Monitoring Using IGS Data", presented at the 1993 Berne IGS Workshop, Berne, March 25-26, 1993.

Wilson, B. D., A. J. Mannucci, C. D. Edwards, and T. Roth, "Global Ionospheric Maps Using a Global Network of GPS Receivers", Proceedings of the International Beacon Satellite Symposium, Cambridge, MA, 1992.

Wilson, B. D. and A. J. Mannucci, "Instrumental Biases in Ionospheric Measurements Derived from GPS Data", Proceedings of the 1993 ION-GPS Meeting, Salt Lake City, Utah, 1993.

FIGURE CAPTIONS

Figure 1. Map of station locations used in rate of change of ionospheric range delay study.

Figure 2. Differential group delay and differential carrier phase under code and codeless conditions.

Figure 3. Ionospheric delay variations, before and after removal of low frequency spectral components.

Figure 4. Ionospheric delay variations over the time intervals indicated.

Figure 5. Statistics of ionospheric delay variations over 1 minute and 5 minute periods for different times of day.

Figure 6. Statistics of ionospheric range delay changes for satellite passes from Westford and Yellowknife for which the long period variations were not filtered out.

Figure 7. Statistics of ionospheric delay variations for nighttime hours for the stations indicated.

Figure 8. Statistics of ionospheric delay variations for daytime hours for the stations indicated.

Figure 9. Map of station locations, GPS 400 km height intersections and the auroral region.

Figure 10. Statistics of daytime ionospheric delay variations for St Johns, Newfoundland for different conditions of magnetic activity.

Figure 11. Summary of statistics of nighttime ionospheric delay variations for different seasons versus geomagnetic latitude.

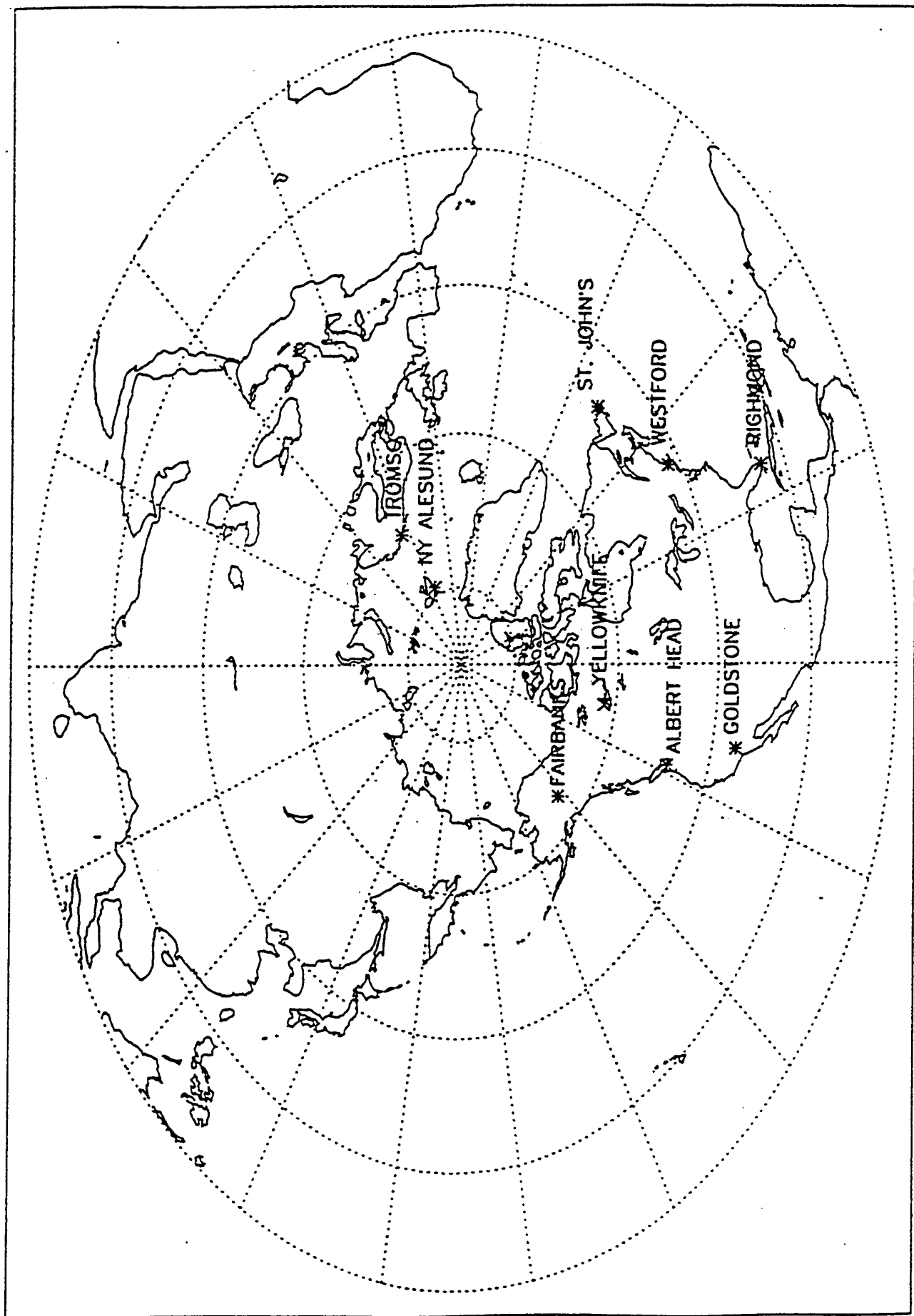


FIGURE 1

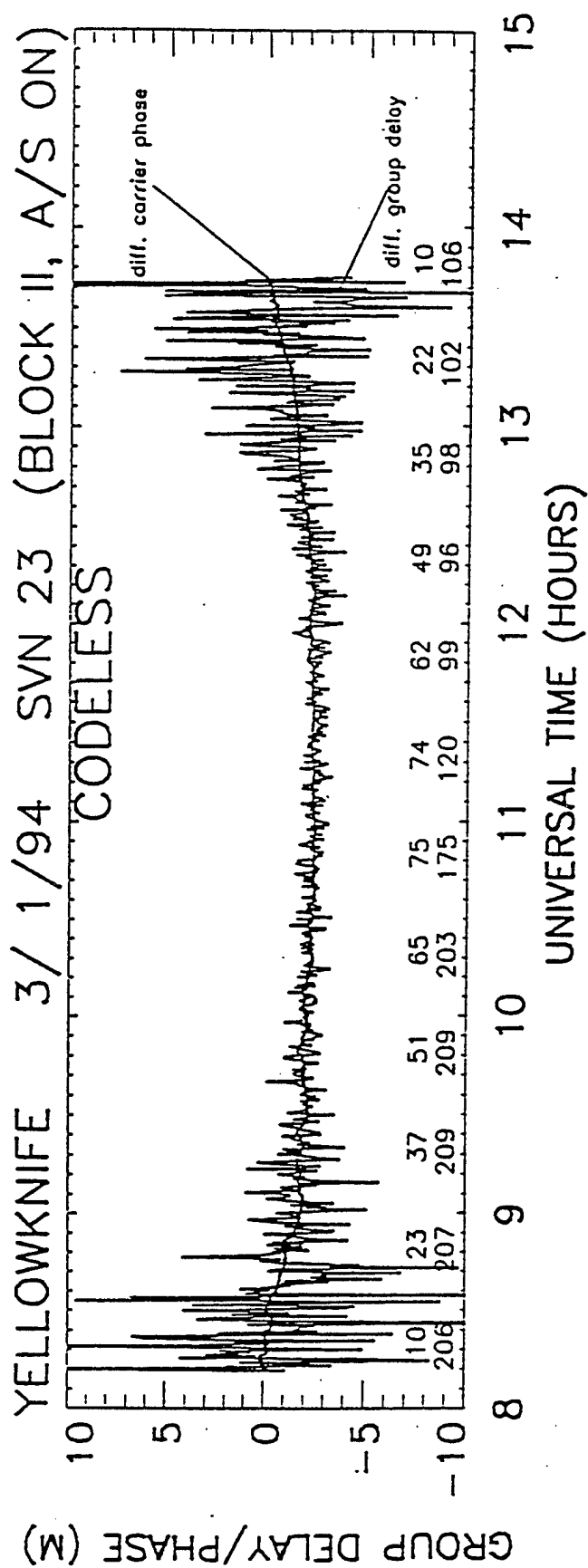
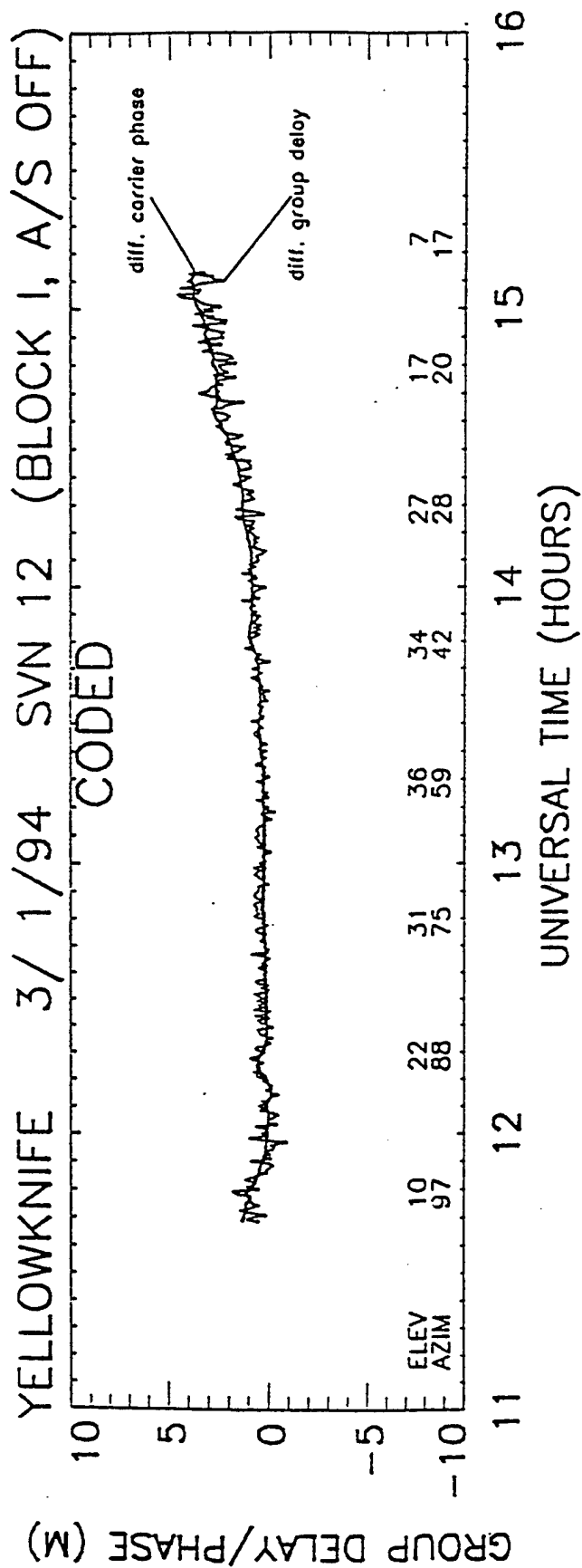


FIGURE 2

YELLOWKNIFE 3/01/94 SVN 23

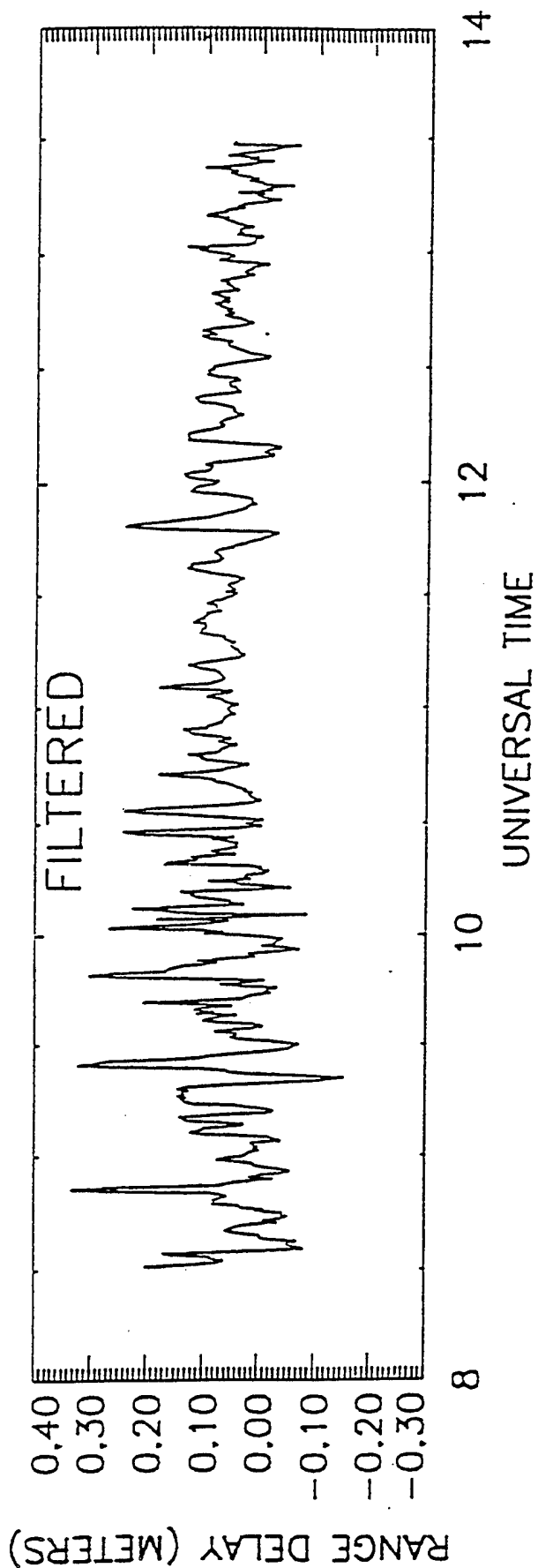
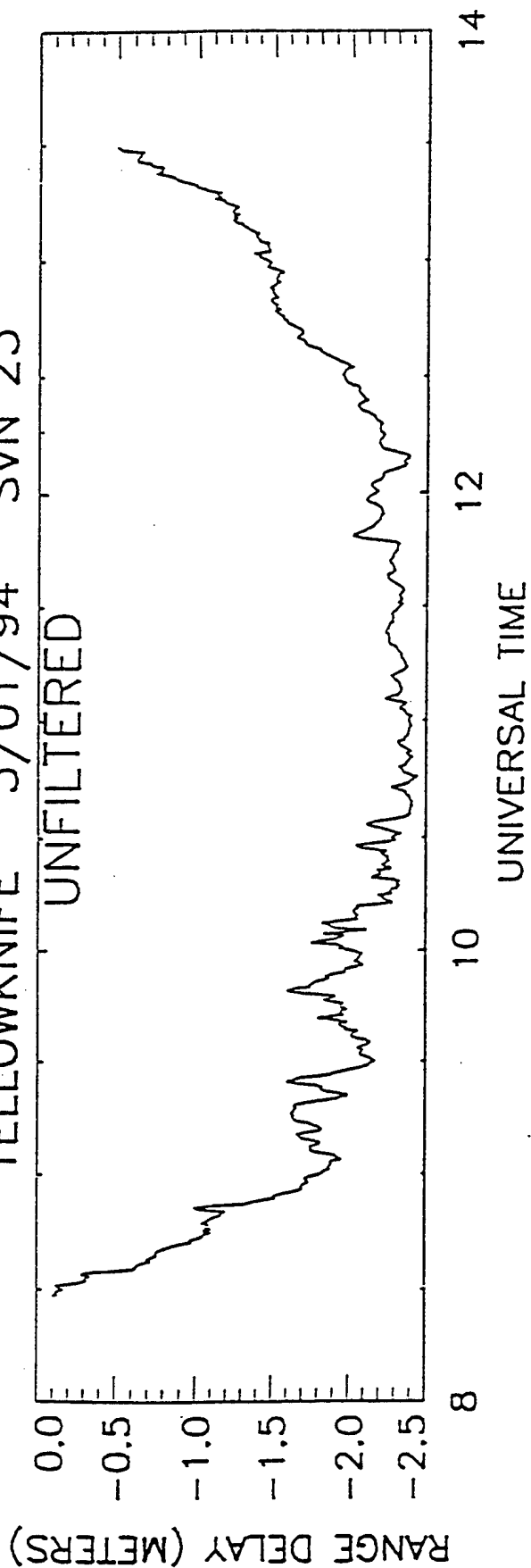


FIGURE 3

RATE OF CHANGE OF RANGE DELAY (M/MIN)

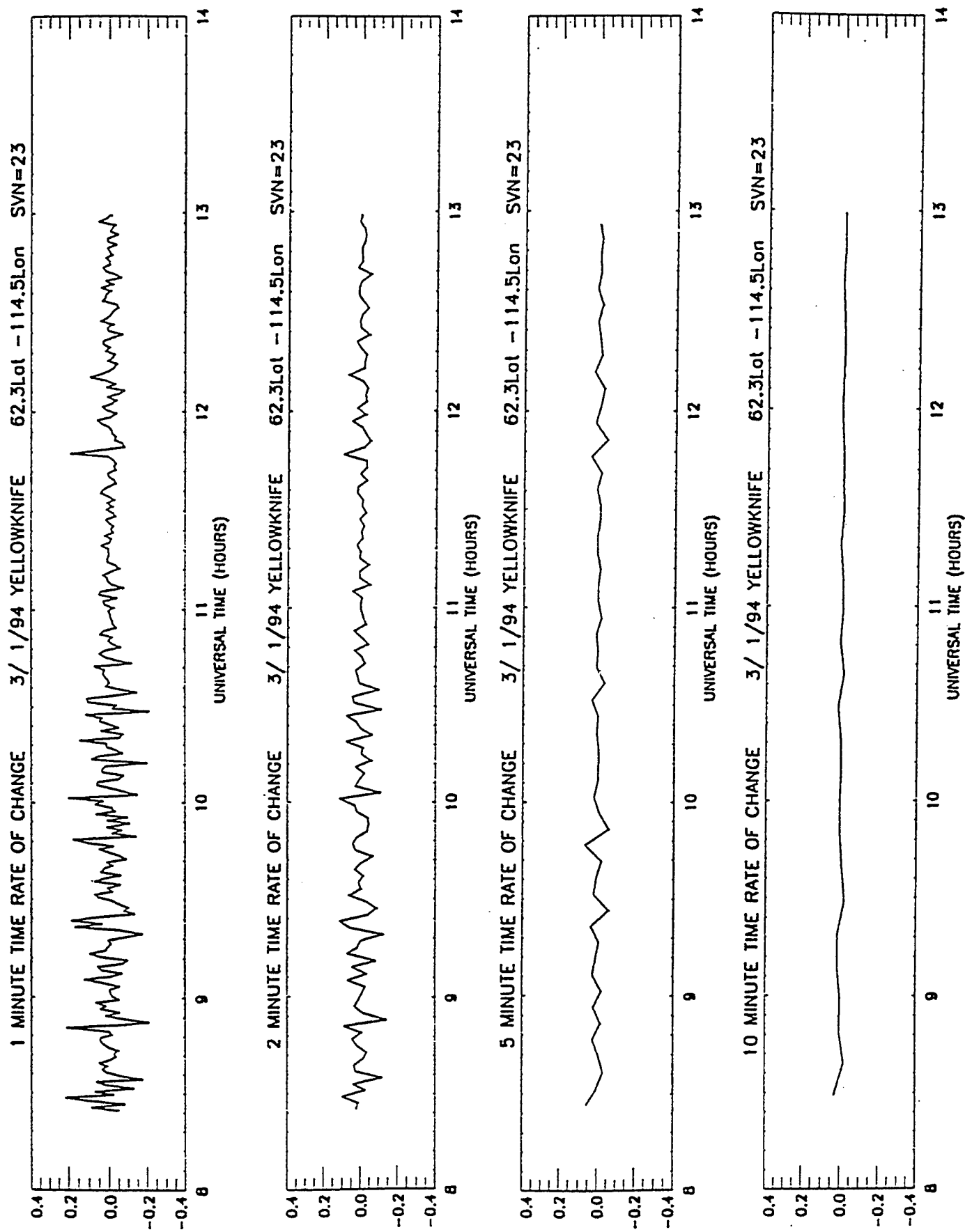
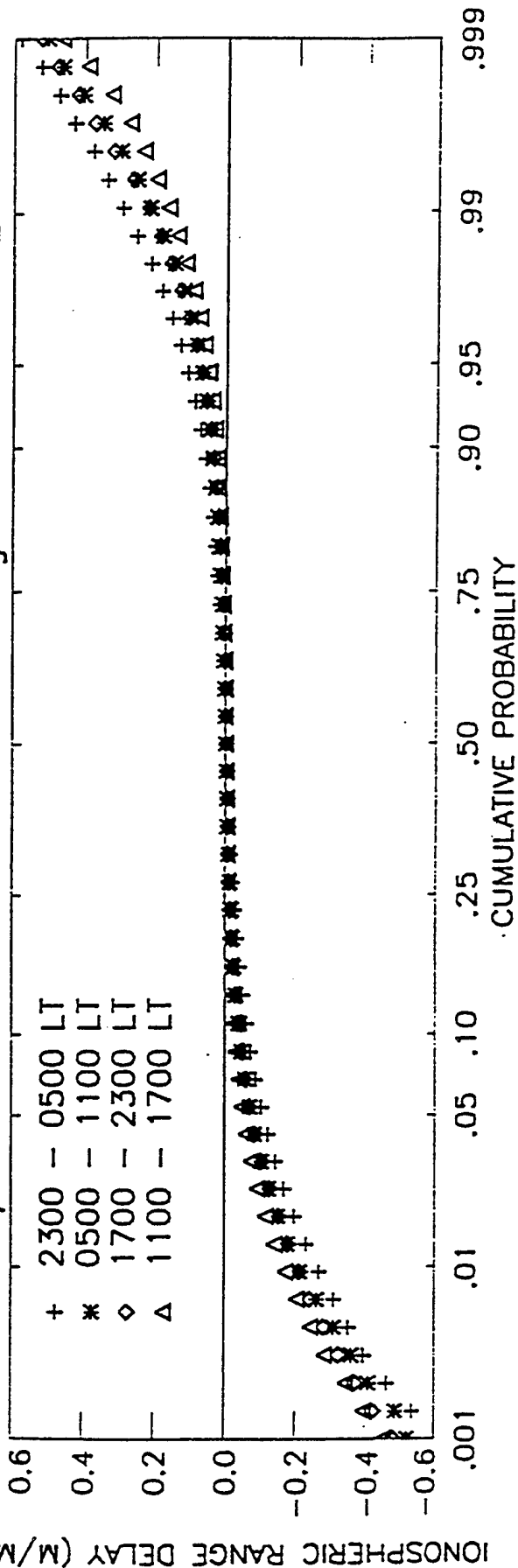


FIGURE 4

12/93 1 Minute Time Rate of Change YELLOWKNIFE



12/93 5 Minute Time Rate of Change YELLOWKNIFE

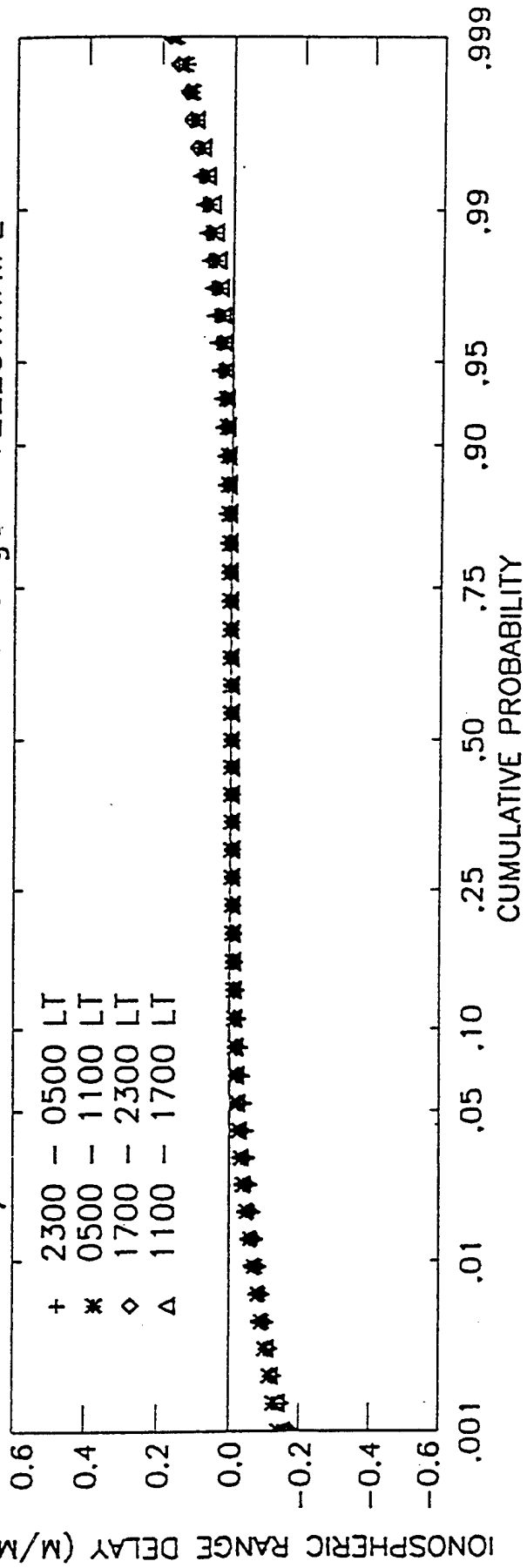


FIGURE 5

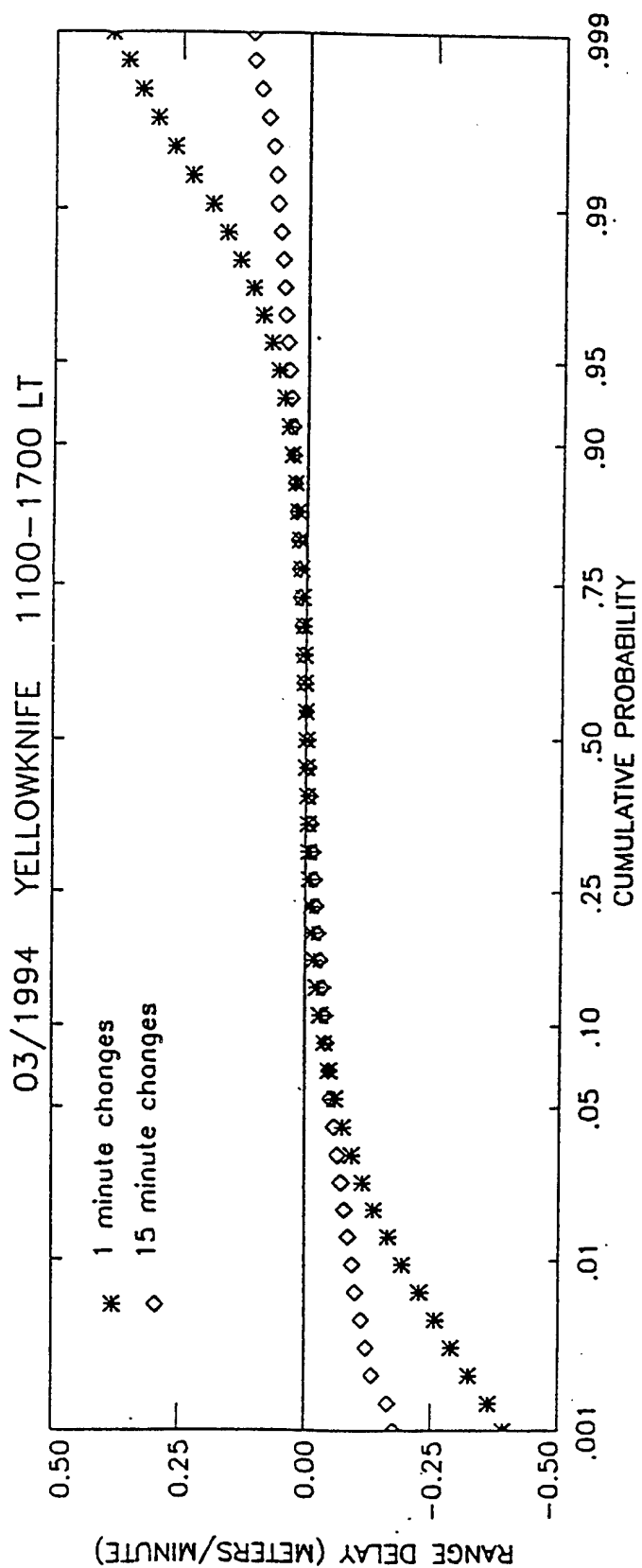
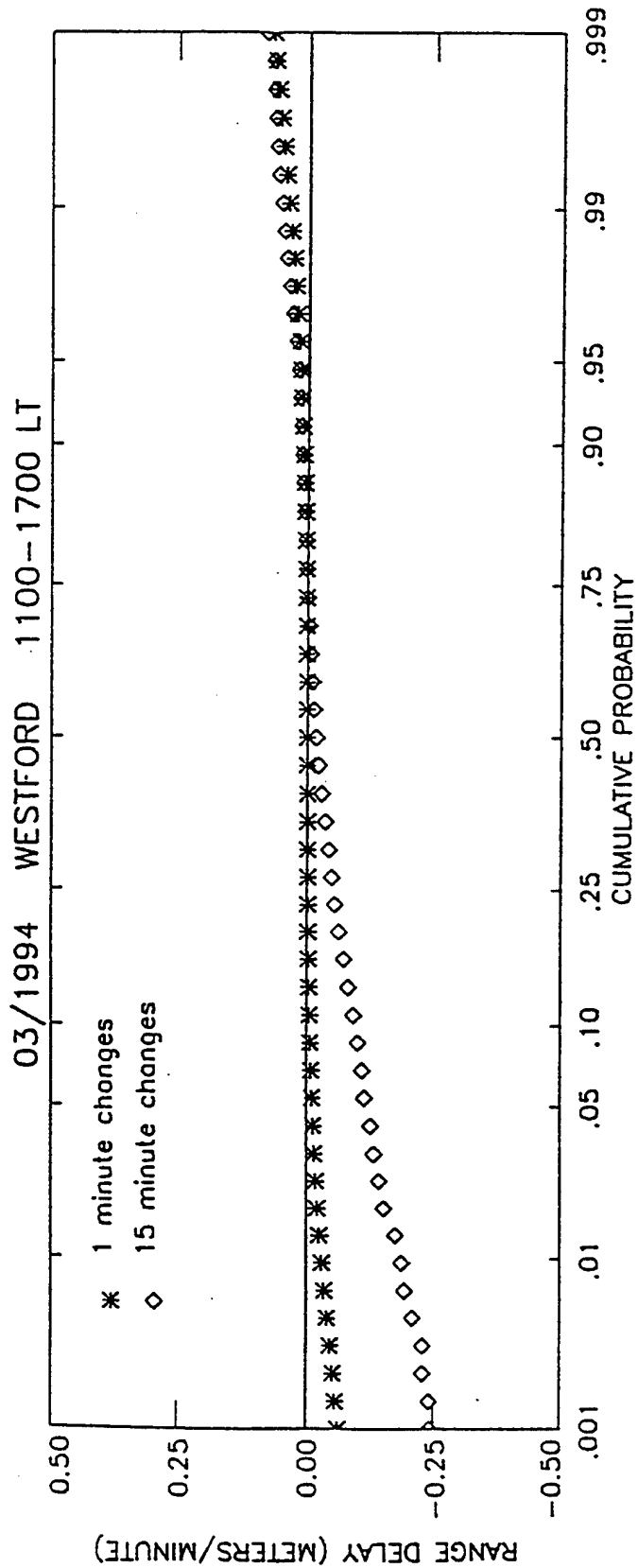


FIGURE 6

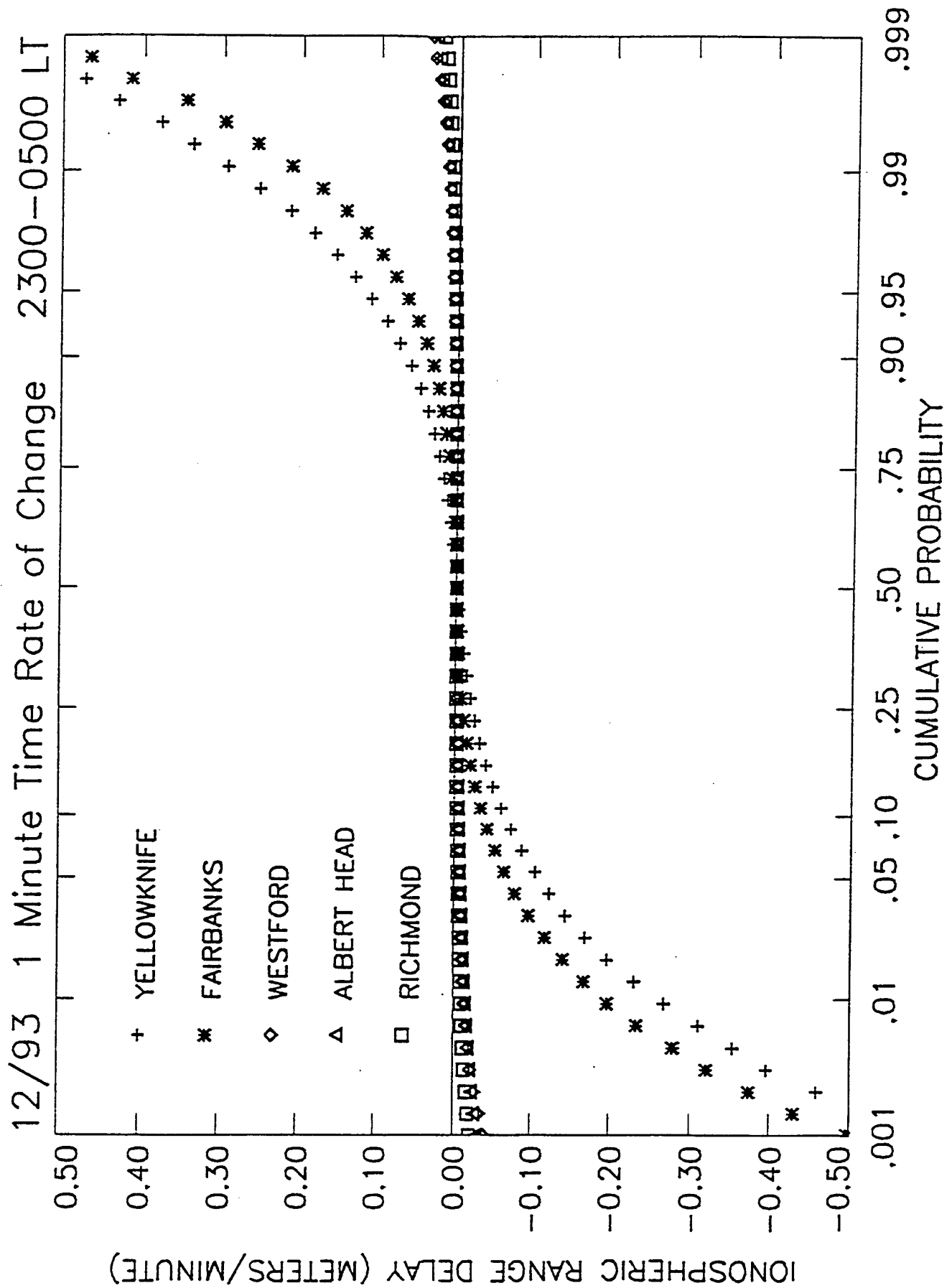


FIGURE 7

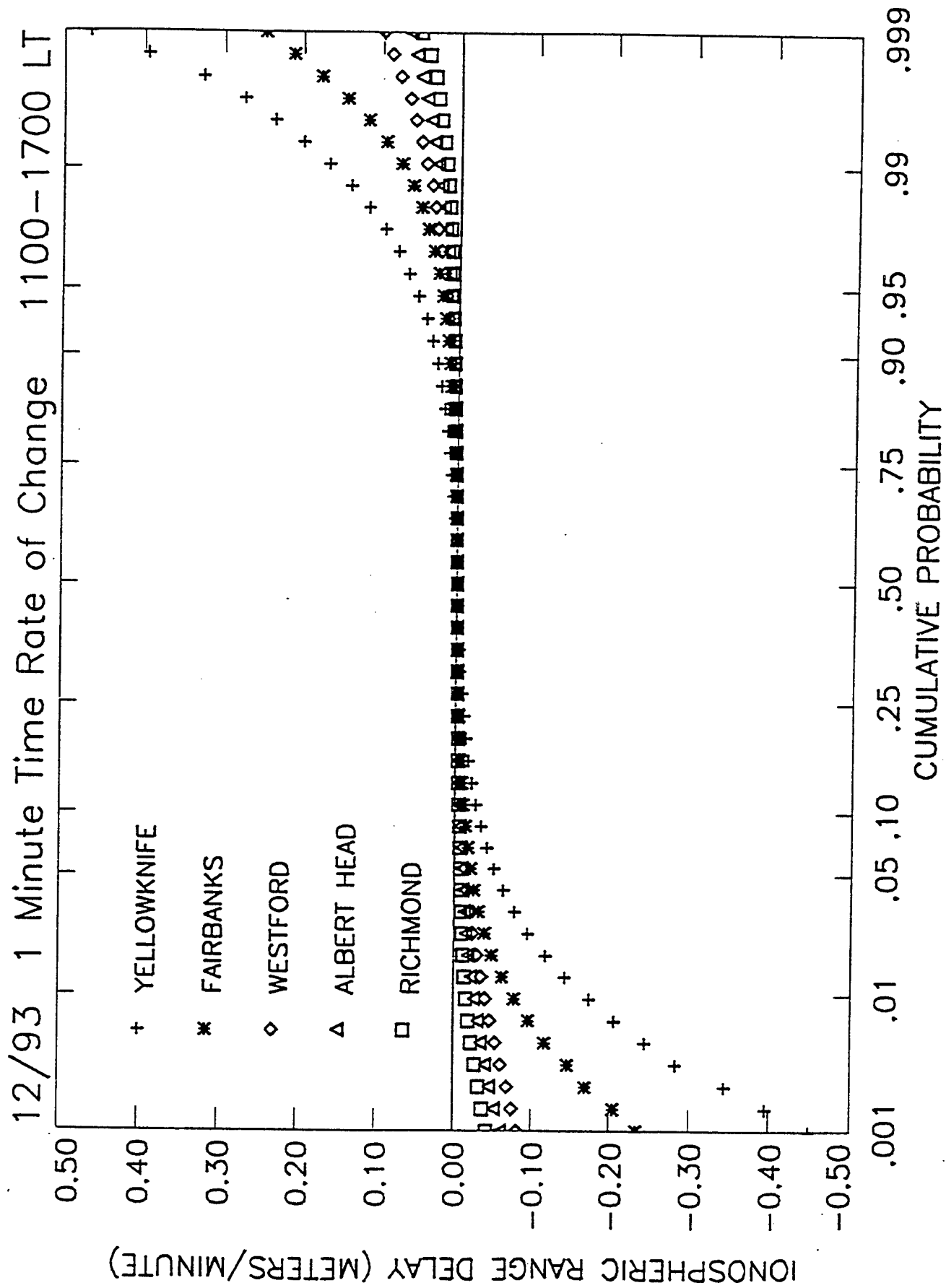


FIGURE 8

Q = 6 CGLT = 0.00 YELLOWKNIFE LT = 2200

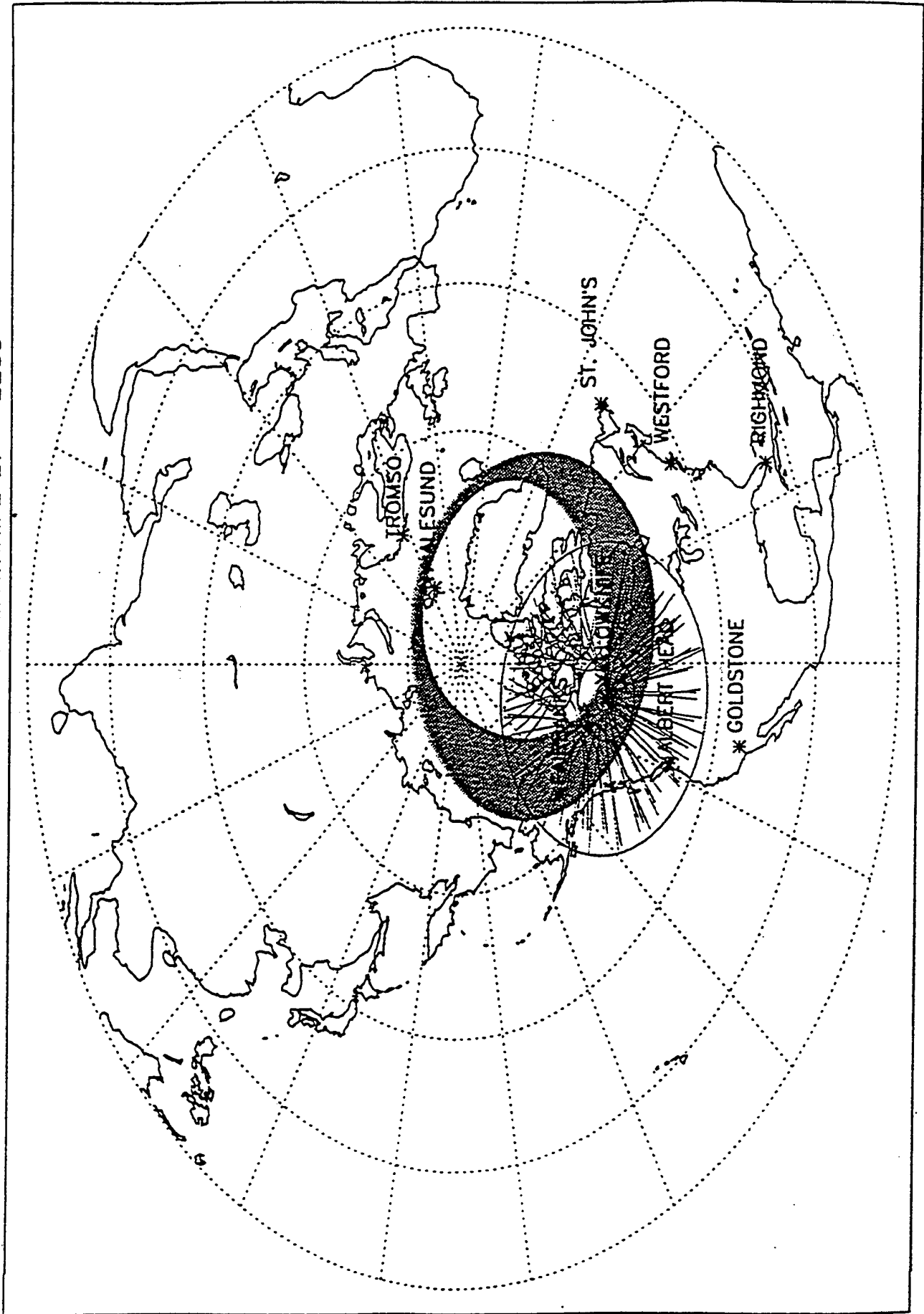


FIGURE 9

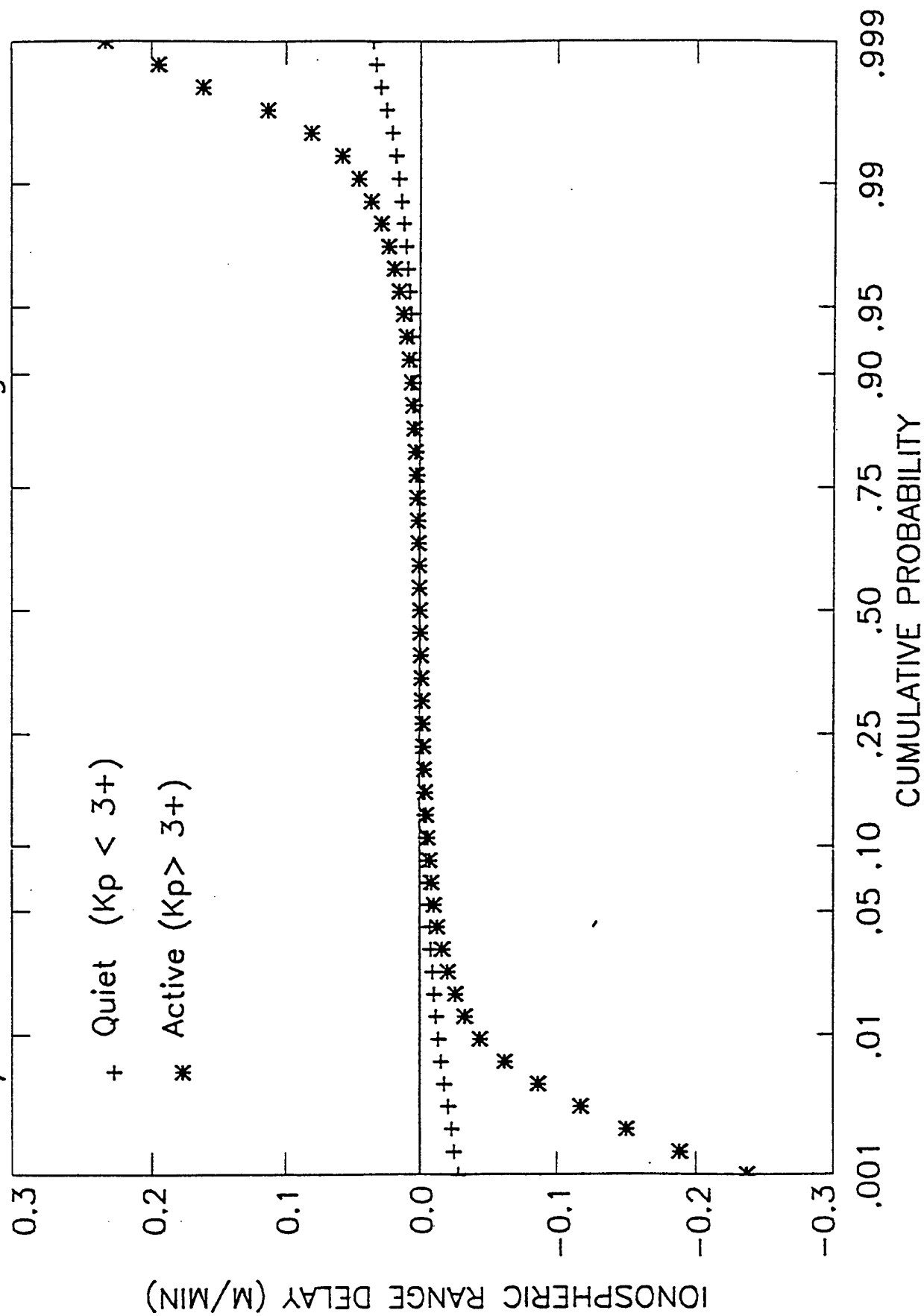


FIGURE 10

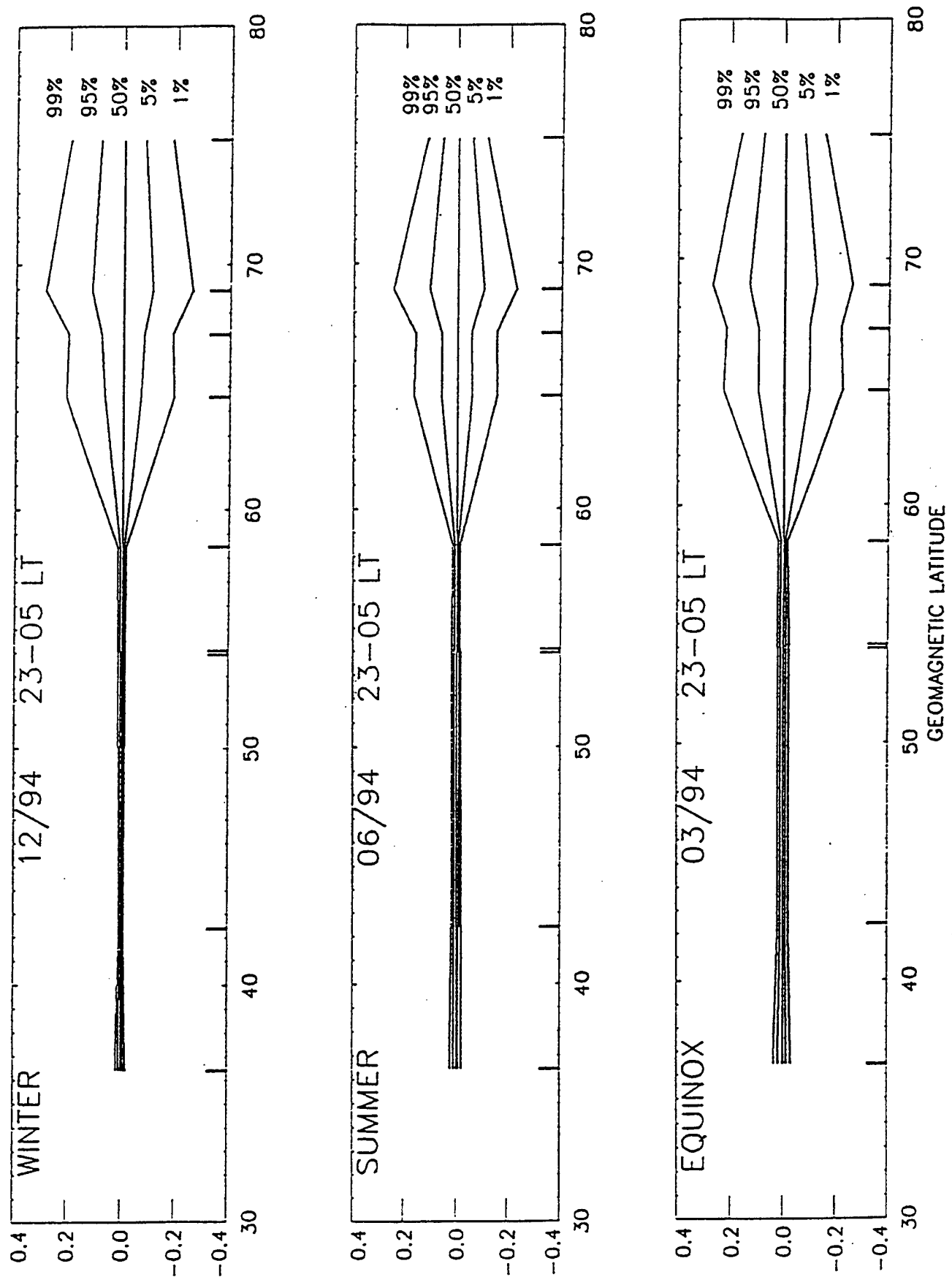


FIGURE 11

The U.S. Government is authorized to reproduce and sell this report.
Permission for further reproduction by others must be obtained from
the copyright owner.

Upgoing electrons produced in an electron-proton-hydrogen atom aurora

Dwight T. Decker,¹ B. Basu,² J. R. Jasperse,^{3,4} D. J. Strickland,⁵
J. R. Sharber,⁶ and J. D. Winningham⁶

Abstract. The first test of a self-consistent theory for the combined electron-proton-hydrogen (H) atom aurora is presented. Specifically, the upgoing differential electron flux that results from precipitating protons and electrons is modeled and compared to observations. The observations are from the Low Altitude Plasma Instrument (LAPI) on board the Dynamics Explorer 2 satellite. Excellent agreement between data and theory is produced when a kappa distribution is used to extrapolate the observed proton spectra to energies beyond the instrument's energy cutoff (27 keV). More definitive tests of the model will require more comprehensive observations as well as improvements in available proton-H atom cross sections. However, it is concluded that data clearly supports the theoretical prediction that the secondary electron spectra due to precipitating protons and H atoms is much softer than that produced by precipitating electrons. Also, the implication that the incoming proton spectra have a high-energy power law tail raises the possibility that previous determinations of the total ion energy flux are too low.

1. Introduction

Recently, a self-consistent model for the combined electron-proton-hydrogen atom aurora has been developed [Basu *et al.*, 1993; Strickland *et al.*, 1993]. The primary feature of this model involves numerically solving three coupled linear transport equations for the electron, proton, and hydrogen (H) atom differential fluxes as functions of altitude, energy, and pitch angle. To date, the portion of the model that solves just the electron transport equation has been tested against a variety of data [Meier *et al.*, 1980; Strickland, 1981; Meier *et al.*, 1982; Strickland *et al.*, 1984; Meier *et al.*, 1989; Winningham *et al.*, 1989]. On the other hand, the solutions of the two coupled equations for the proton and H atom fluxes have had only one type of comparison with data. That is, calculations of the ionization produced by specific proton aurora have been in good to fair agreement with the ionization observed by incoherent scatter radar [Basu *et al.*, 1987; Senior *et al.*, 1987]. For the newest feature of the three-component model, that is the coupling between the electrons and the protons-H atoms, there has been no comparisons with observations.

The purpose of this paper is to present the first test of the fully coupled three-component transport model. Specifically, we model the upgoing electrons that result from downgoing

electrons and protons incident at the top of the ionosphere. Measurements from the Low Altitude Plasma Instrument (LAPI) [Winningham *et al.*, 1981] on board the Dynamics Explorer 2 (DE 2) satellite provide both the needed boundary conditions (incident electron and proton fluxes) and the resultant upgoing electron fluxes with which the model results are compared.

The plan of the paper is as follows. The basic elements of the theoretical model are described in section 2. In section 3, we discuss the model predictions concerning upgoing (or backscattered) electrons. The LAPI observations are introduced in section 4 followed by comparisons with theory in section 5. The paper concludes with a discussion and summary in section 6.

2. Theoretical model

The fundamental feature of this three-component auroral model is the use of transport theoretic methods to solve a set of three coupled Boltzmann equations for the electron, proton, and H atom differential fluxes. In solving these equations, we assume steady state conditions, no electric fields, a uniform geomagnetic field (no magnetic mirroring), and azimuthal symmetry about the geomagnetic field line. The collisional processes included are the various types of collisions between the energetic precipitating particles and the neutral constituents of the ionosphere. Also included is the process where energetic electrons undergo "frictional" energy loss due to Coulomb collisions with the thermal electrons.

The protons and H atoms are coupled to each other by charge-changing collisions with neutrals (charge exchange and stripping). The electrons in turn are coupled to the protons and H atoms, because secondary electrons are produced from ionizing collisions between neutrals and protons and H atoms. The new feature of this model over previous work is that the secondary electrons produced by the primary protons and H atoms are included in the solution of

¹Institute for Scientific Research, Boston College, Newton, Massachusetts.

²Phillips Laboratory, Hanscom Air Force Base, Massachusetts.

³Centre de Recherche en Physique de l'Environnement, Saint-Maur-des-Fossés, France.

⁴Permanently at Phillips Laboratory, Hanscom Air Force Base, Massachusetts.

⁵Computational Physics, Inc., Fairfax, Virginia.

⁶Southwest Research Institute, San Antonio, Texas.

the electron transport equation. The three transport equations, discussions of the various collision processes, and the numerical methods for solving the equations can be found in the work by *Basu et al.* [1993] and will not be given here.

Besides calculating the differential fluxes, the auroral model also uses those fluxes to calculate emission and ionization yields that result from the precipitating particles. To illustrate how all these various components fit together, we give in Figure 1 a flow diagram of the model. For the case of a pure electron aurora, let us focus our attention on the left side of the diagram. We begin with a precipitating electron flux (Φ_e) at the top of the atmosphere at some altitude z_0 . This flux serves as the boundary condition for solving the electron transport equation to obtain the electron differential flux for altitudes below z_0 . These fluxes are then used to calculate profiles of optical emissions and ion densities. The sequence of computer models represented by this portion of the diagram has been developed over the last couple of decades by Strickland and coworkers [Strickland et al., 1976, 1983, 1989].

Turning to the right side of the diagram, we consider the case of a proton-H atom aurora. Here we imagine a flux of precipitating protons at some altitude z_0 , and again we want to calculate the differential flux at altitudes below z_0 . An additional complication, as compared to the electron transport problem, is that as protons penetrate into the atmosphere, some are converted into energetic H atoms through charge exchange collisions with neutrals. These energetic H atoms in turn can be converted back into protons by charge-stripping collisions. The result is that a flux of protons will be converted into a flux of protons and H atoms. Thus if we are interested in the flux of either specie, we need to determine both by solving two coupled transport equations. As in the electron case, these differential fluxes can then be used to calculate the optical emissions and ion densities that arise directly from the precipitating protons and H atoms. The computer model that solves for the proton and H atom fluxes has been developed over the last decade by J. Jasperse, B.

Basu, and coworkers [Jasperse and Basu, 1982; Basu et al., 1987, 1990].

The description given above of the proton-H atom aurora model is missing an important element. That element is the production of secondary electrons by collisions between atmospheric neutrals and energetic protons and H atoms [Basu et al., 1993; Strickland et al., 1993]. This coupling of the protons and H atoms to the electrons is the new feature of the current model and is represented in our flow diagram by the box in the middle. The fact that this coupling is one way means that we first start on the right side of the diagram and solve for the proton and H atom fluxes. Moving to the left in the diagram, these fluxes are then used to calculate a secondary electron source. This source in turn becomes an input in solving for the resulting electron flux. Having obtained all the necessary fluxes, they can then be used to calculate the optical emissions and ion densities that are produced in a proton-H atom aurora. Furthermore, by including both precipitating electrons and protons at altitude z_0 , the model can treat the mixed case of an electron-proton-H atom aurora.

As mentioned in the introduction, the solution for the pure electron aurora case has been tested against a variety of data. This includes comparisons with measured differential fluxes, optical emissions, and ion densities. On the other hand, for the proton-H atom aurora the only previous comparison with data has involved the resultant ion density, not including the additional ionization produced by secondary electrons. To date, no detailed comparisons have been made with observed proton or H atom differential fluxes or the resultant electron fluxes. The original plan for this work was to make a comparison between the theory for and the observations of the electron fluxes that are produced in a "pure" proton-H atom aurora. In particular, we planned on studying the upgoing electron fluxes that result from the proton-H atom-produced secondary electrons. We chose to focus on upgoing electrons rather than the proton and H atom fluxes for two reasons: (1) these electrons are calculated by the newest and

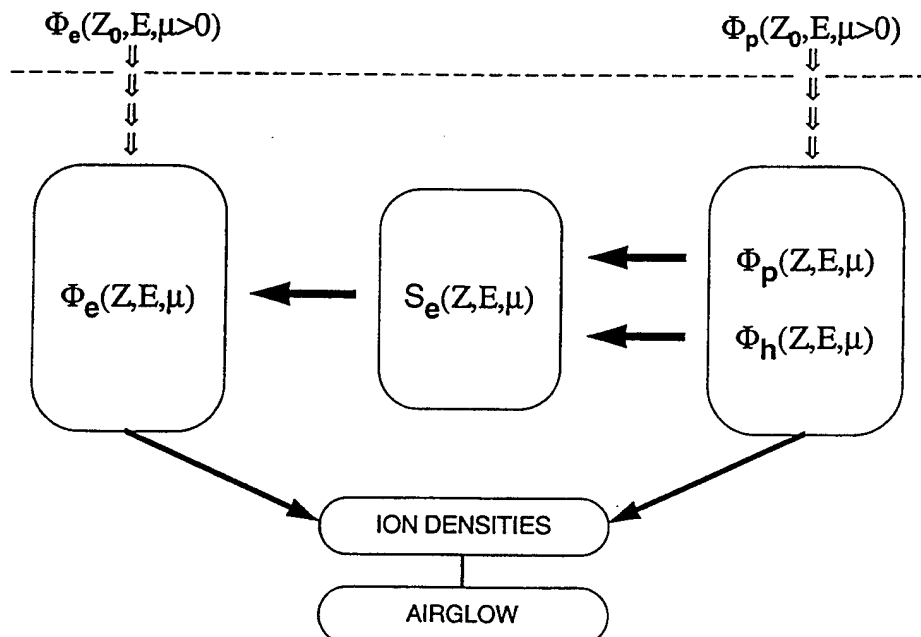


Figure 1. A flow diagram of the electron-proton-H atom auroral model.

least-tested part of the model, and (2) we believed observations of such electron fluxes were available with which to make the comparisons. However, when we began searching for observations of proton precipitation, we found no cases of a truly pure proton-H atom aurora. Rather, all the cases of proton precipitation that we examined included some electron precipitation. Thus we realized that we had to deal with the more general situation of a mixture of precipitating protons, H atoms, and electrons. However, our primary interest was in assessing our modeling of upgoing electrons produced by protons and H atoms, and thus an understanding of the relative roles of precipitating electrons, protons, and H atoms became crucial for selecting the data to use and making our assessment. With this in mind, we decided to perform several calculations to help us develop that understanding. These calculations, which involved both electron and proton precipitation, are discussed in the next section.

Finally, since we are going to focus on upgoing electrons, a few comments about their production are appropriate. In the model, the only coupling between different pitch angles comes from electron-neutral elastic scattering and secondary electron production. These then are the only sources of upgoing electrons in the model. Forward scattering is assumed for all other collision processes and, as mentioned,

magnetic mirroring is neglected. Hence the model produces no upgoing protons and H atoms as well as no mirrored electron population. In the future, we hope to assess the accuracy of these approximations by comparing to Monte Carlo solutions to the problem [Kozelov and Ivanov, 1992; Kozelov, 1993; Sergienko and Ivanov, 1992].

3. Upgoing electrons

As stated above, we needed to contrast the upgoing electrons produced by precipitating protons and H atoms to those produced by precipitating electrons. For our pure electron precipitation case, we used an isotropic incident electron flux that had a Maxwellian energy distribution along with a low-energy tail. The Maxwellian had a characteristic energy of 1 keV and the total incident energy flux, including the low-energy tail, was $1 \text{ erg cm}^{-2} \text{ s}^{-1}$. A description of the low-energy tail is given by Strickland *et al.* [1993]. For the pure proton-H atom case, we used an isotropic incident proton flux that was also a Maxwellian with an energy flux of $1 \text{ erg cm}^{-2} \text{ s}^{-1}$ but had a characteristic energy of 9 keV. This difference of characteristic energies was chosen such that peak altitude for the ionization rates would be about the same in the two cases [Jasperse and Basu, 1982]. In Figure 2, we

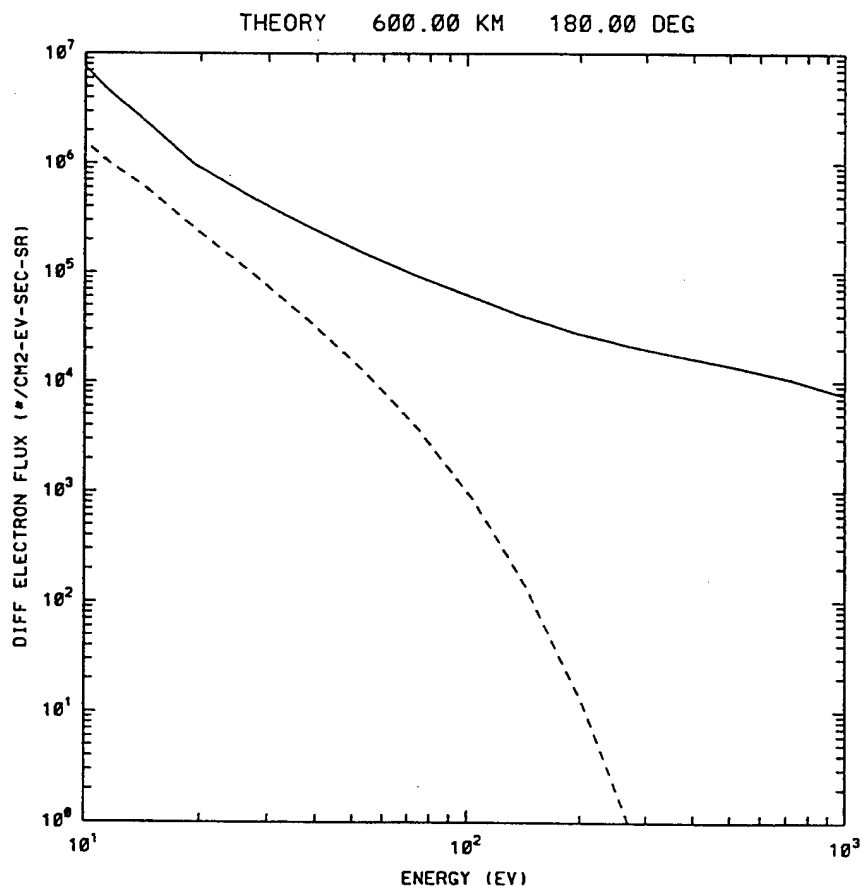


Figure 2. Theoretical differential electron number flux at a pitch angle of 180.0° (upward flux) and an altitude of 600 km versus energy. The solid curve is for a pure electron aurora with an incident Maxwellian distribution and a low energy tail. The characteristic energy is 1 keV and the total incident flux is $1 \text{ erg cm}^{-2} \text{ s}^{-1}$. The low-energy tail is described by Strickland *et al.* [1993]. The dashed curve is for a pure proton-H atom aurora with an incident Maxwellian distribution of protons. The characteristic energy is 9 keV and the total incident energy is $1 \text{ erg cm}^{-2} \text{ s}^{-1}$.

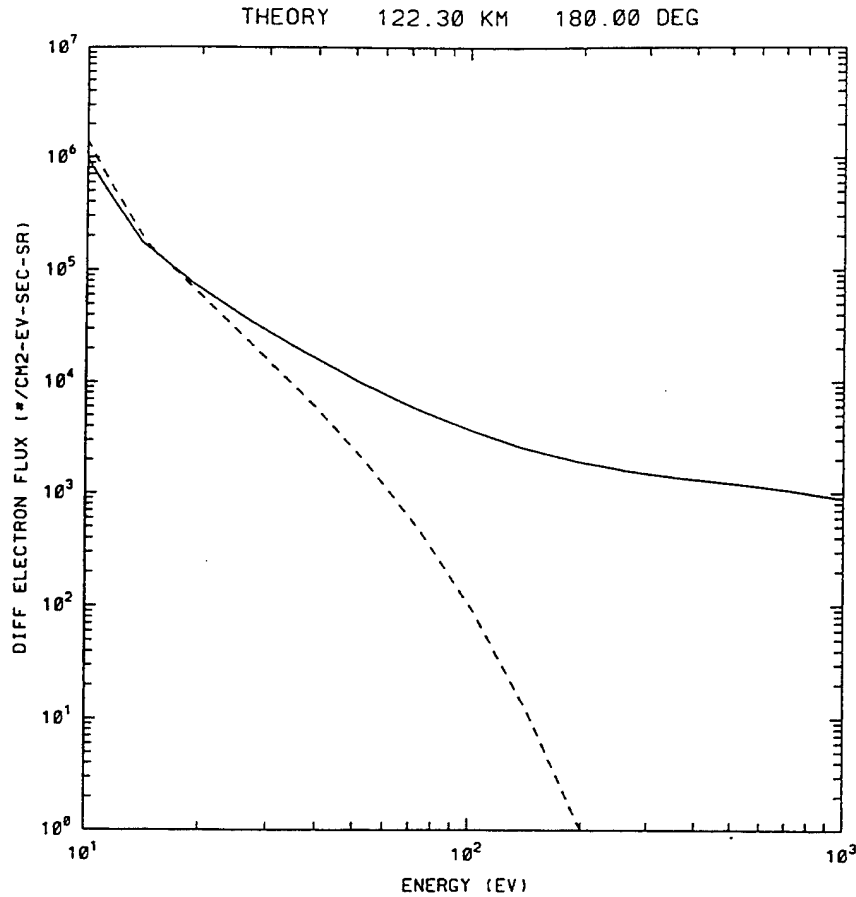


Figure 3. The same as Figure 2 except that the theoretical differential electron number flux is at an altitude of around 120 km.

show the resultant upflowing electron flux at 600 km as a function of energy from 10 to 1000 eV (pitch angle = 180.0°) for both the electron precipitation (solid curve) and proton precipitation (dashed curve) cases. We see that there is a dramatic difference between the proton-H atom-produced electron spectrum and that produced from electron precipitation. The proton-H atom-produced electrons are much softer as compared to the electron precipitation case, the electron flux varying from about a factor of 3 less at 10 eV to around 4 orders of magnitude less at above 200 eV. In Figure 3, a similar comparison is made for a lower altitude (~ 120 km). We see that while the electron spectrum produced by protons and H atoms (dashed curve) still has a characteristic softness, at low energies it is now comparable to that produced by electron precipitation.

One reason for these differences is that in the precipitating electron case most of the higher-energy upgoing electrons are degraded primary electrons, and thus by definition the precipitating proton-H atom case is missing this source. Another important reason for this difference is that at lower energies, secondary electron production becomes the dominant source of upgoing electrons and the secondary electron source function produced by protons and H atoms is much softer than the one produced by precipitating electrons. This difference, as explained by Basu *et al.* [1993] and Strickland *et al.* [1993], is due to the fact that (for energies of auroral interest) cross sections for secondary electron

production by proton and H atom impact decrease exponentially with increasing secondary electron energy, whereas the cross sections for electron impact decrease as an inverse power law with increasing secondary energy.

The difference predicted by the model for the upgoing electrons in a proton-H atom aurora versus an electron aurora represents both an opportunity and a problem. The opportunity is that this dramatic difference can be looked for in the data and in principle gives an easy way to qualitatively check this aspect of the model. The problem with having such a difference is a twofold one. First, given the magnitude of the predicted upgoing electrons produced by protons and H atoms, along with the sensitivity of LAPI, any comparisons between data and theory will be limited to energies from 10 to around 200 eV. Second, the large difference between the two types of precipitation puts very rigid requirements on what we choose as a "nearly pure" proton-H atom aurora. Since electron precipitation produces so many upgoing electrons compared to the proton-H atom precipitation, it takes very little precipitating electron flux in a so-called pure proton aurora to overwhelm those electrons produced from the protons and H atoms. Furthermore, since the focus of our comparison will be concentrated on the 10-200 eV range, any precipitating electrons above 10 eV can have an effect. This means that if we are searching for a pure proton-H atom aurora and find a case where keV-precipitating protons are present, it is not sufficient to check that there are no keV-

DYNAMICS EXPLORER

YR/DAY: 81/289

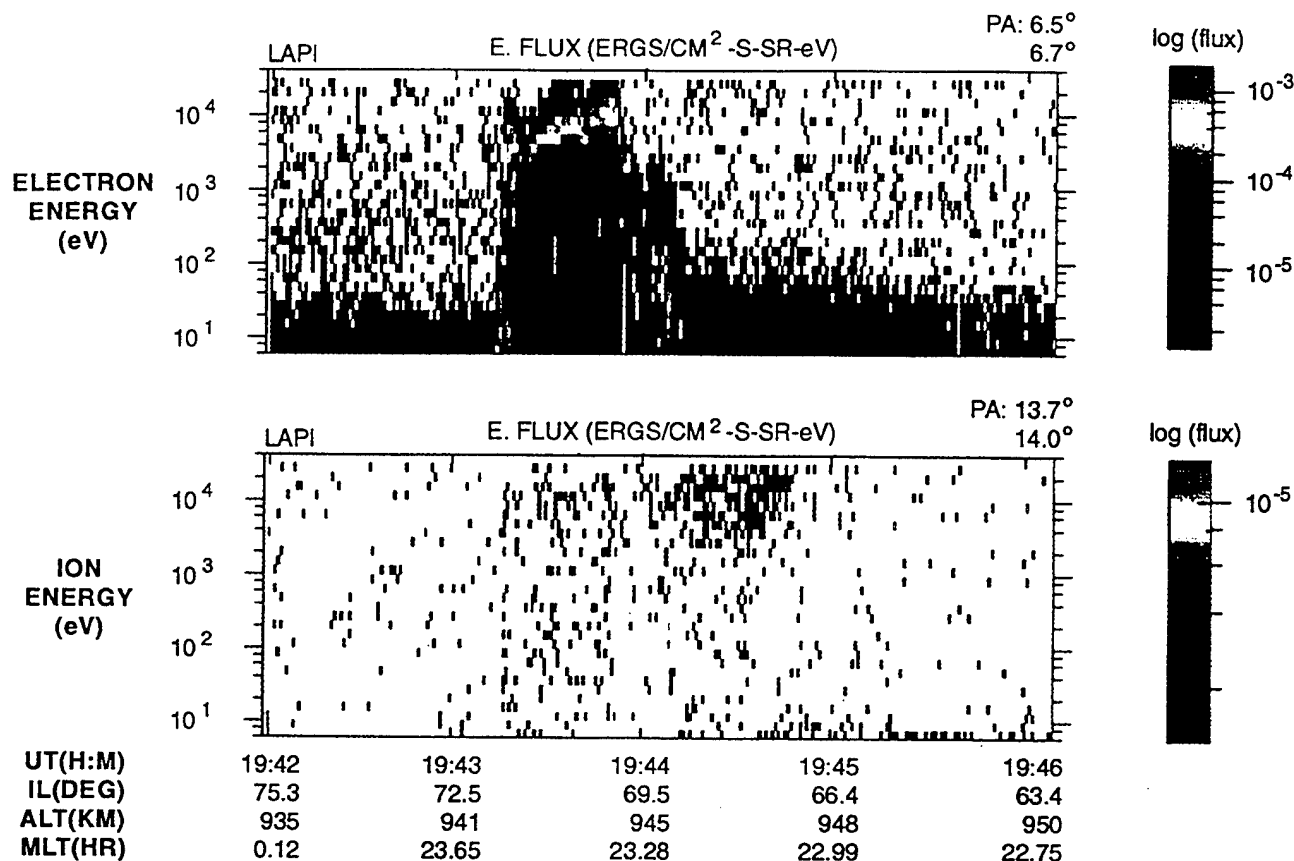


Plate 1. An energy-time spectrogram for electron and ion energy fluxes from the low altitude plasma instrument (LAPI) on the Dynamics Explorer 2 satellite on day 289 of 1981 from 1942 to 1946 UT. (top) Data are for electrons at $\sim 6.6^\circ$ pitch angle. (bottom) Data are for ions at $\sim 13.85^\circ$ pitch angle. A pitch angle of 0° is defined as particles moving downward toward the Earth. The color bars on the right give the z axis scale for the data in units of log differential energy flux ($\text{ergs cm}^{-2} \text{s}^{-1} \text{sr}^{-1} \text{eV}^{-1}$). The universal time (UT), invariant latitude (IL), altitude (ALT), and magnetic local time (MLT) are provided at the bottom of the graph.

precipitating electrons. Rather, we also have to take into account the precipitating electrons with energies of tens to hundreds of eVs. Another source of these low-energy electrons that should be minimized is photoelectron production below the satellite. Photoproduction above the satellite is no problem as it is accounted for by the boundary conditions.

4. Observations and Qualitative Comparison

The LAPI flown on the DE 2 consisted of 15 individual parabolic electrostatic analyzers designed and mounted to obtain detailed pitch angle distributions of ions and electrons as a function of energy. During the period of observation utilized for this paper, data from eleven analyzers comprising ten electron and six ion spectra were available every 1s. Six of the electron spectra and two of the ion spectra were for downgoing pitch angles (0° to 90°). The remaining four electron and four ion spectra were for upgoing pitch angles (90° to 180°). The energy range of the measurements was from 5 eV to 27 keV with an energy resolution of 32%.

The observations that we have chosen to focus on come from one pass on day 289 in 1981 when DE 2 passed through both an electron aurora and then through a fairly pure proton aurora. This can be seen in Plate 1, which is an energy-time spectrogram from this pass for the time period 1942 to 1946 UT. The top panel is a spectrogram of the electron energy flux at a pitch angle of $\sim 6.6^\circ$. The lower panel gives the ion energy flux at a pitch angle of $\sim 13.85^\circ$. The calibration bar for the color scale is given to the right of each panel. Examining first the ion (lower) panel, we see the ion precipitation is concentrated between 19:44 and 19:45 UT. Turning to the electron (top) panel, the onset of energetic precipitating electrons is observed at around 19:43:12 UT. At around 19:43:52, a fairly dramatic softening of the electron spectra is seen when the peak above 2 keV disappears. This is followed at around 19:44:10 by a further softening such that for the remainder of the panel the bulk of the electron energy flux resides below 100 eV. A comparison of the two panels shows that between 19:44 and 19:45, when the ion precipitation is observed, only a very weak electron precipitation is present. To date, this is the best case of a pure

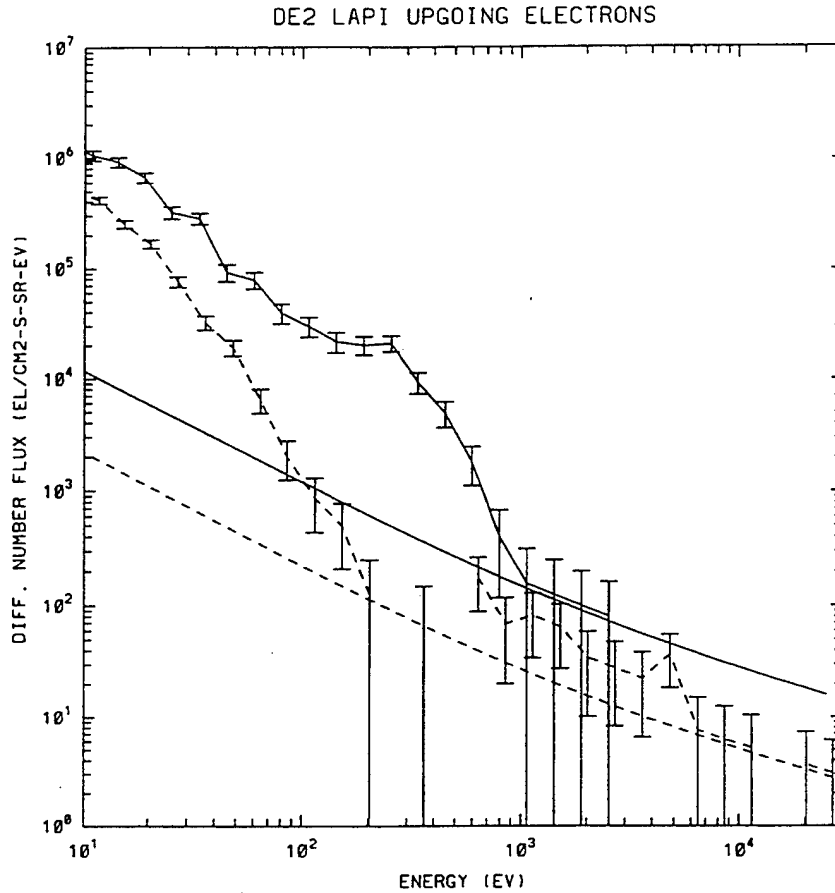


Figure 4. The observed differential number flux of electrons at a pitch angle of $\sim 163^\circ$ (upward flux) versus energy. The solid curve is a 4-s average for a period beginning at 1943:56 UT on day 289 of 1981. The dashed curve is a 23-s average for a period beginning at 1944:19 UT on the same day. The diagonal straight lines are the two-count instrument sensitivity levels.

proton-H atom aurora that we have found. Note, in our analysis we assume that all detected ions are protons.

Before turning to our detailed modeling, let us examine the observed upgoing electrons produced by just precipitating electrons and those produced by our so called pure ion precipitation. In Figure 4, we present the observed upgoing electron flux at a pitch angle of $\sim 163.6^\circ$. The solid curve is the average of 4 spectra taken around 19:43:56 UT, while the dashed curve is the average of 23 spectra taken over 23 seconds starting at 19:44:19 UT. The diagonal lines are the respective sensitivity curves (1 count) and the error bars are the one sigma standard deviation calculated from the number of counts. These times were chosen because the energy flux ($\sim 0.2 \text{ ergs cm}^{-2} \text{ s}^{-1}$) in the precipitating electrons at 19:43:56 is about the same as the energy flux in the precipitating protons at around 19:44:19 UT. The idea is to see how the observations in Figure 4 compare qualitatively with the calculations shown in Figure 2. We see that the precipitating electrons produce many more upgoing electrons than the precipitating protons. At 10 eV, we see around a factor of 2 difference, but at 200 eV the difference has grown to around 2 orders of magnitude. Qualitatively, this is similar to the difference predicted by the model (see Figure 2) except that the model predicts a 3 to 4 order of magnitude difference at 200 eV. The observations show a smaller difference because we don't have truly pure proton precipitation. In Figure 5, we show the observed downgoing electron fluxes for these two

times. A comparison of Figures 4 and 5 shows that the 2 orders of magnitude difference seen in the upgoing electron fluxes simply reflects a similar difference in the downgoing electron fluxes. Thus, as we will verify in the next section, even the small amount of precipitating electron flux that accompanies the ion precipitation in our case study will act to "muddy the waters" when we attempt to examine the upgoing electrons that result from ion precipitation.

5. Quantitative Comparison

In this section, we turn to the details of modeling the observations between 19:44:19 and 19:44:41 UT, where the nearly pure proton aurora occurs. We begin by discussing the specific inputs used for this case. The neutral atmosphere used comes from MSIS-86 (mass spectrometer/incoherent scatter) [Hedin, 1987] using the parameters appropriate for the day of the observations. To include the effects of collisions between energetic and thermal electrons, an ambient electron density is required. For this case, that density is given by a profile that has an F_2 peak density of $4.18 \times 10^5 \text{ cm}^{-3}$, has a peak height of 380 km, and is constrained to agree with the DE 2 observed electron density at 950 km. These values of the F_2 peak parameters fall well within the range of observations for the auroral region during periods of solar maximum. The most critical inputs are the

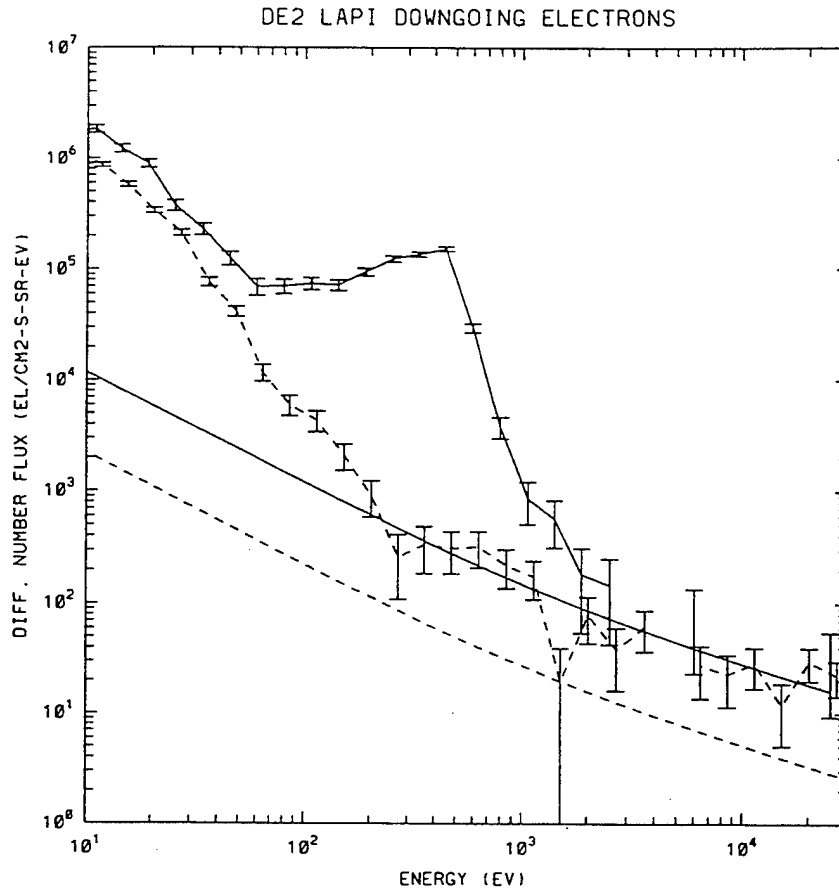


Figure 5. The same as Figure 4 except that the differential electron number flux is at a pitch angle of $\sim 6^\circ$ (downward flux).

incoming proton and electron fluxes used as boundary conditions at the satellite altitude, and they are discussed next.

As indicated in the previous section, ion data were available at two downgoing pitch angles. Since the data were essentially the same at the two pitch angles, we assumed the incoming ion flux was isotropic over the lower hemisphere. As can be noted in the spectrogram, the ion event had fairly low count rates, and it was necessary to sum over all the sweeps (23) that contained significant ion precipitation. In Figure 6, we give the average of the 23 sweeps (solid curve) and include error bars that are again the one-sigma standard deviation calculated from the counting statistics. The solid diagonal curve is the one-count instrument sensitivity level. The dashed curves are two different fits that are discussed below.

As can be seen in Figure 6, the data ends at 27 keV, but we have extrapolated our fits out to 150 keV. The reason for this is that we have found that the model results for upgoing electron flux are sensitive to the assumed incident proton flux above 27 keV. In this case, extrapolating with a Maxwellian (long-dashed line) versus a kappa distribution (short-dashed line) results in a factor of 3 difference in the inferred incident energy flux. A number flux given by a kappa distribution has the functional form of $E[1 + E/\kappa E_0]^{-\kappa-1}$ where E_0 is the characteristic energy, and the index κ is a constant. For $E < \kappa E_0$, this gives a Maxwellian flux and for $E \gg \kappa E_0$, a power law flux. Hence the smaller the κ the larger is the flux at high energies. The value $\kappa = 3.0$ chosen for the fit was the

smallest value reported from fits of observed ion energy spectra in the plasma sheet [Christon *et al.*, 1989]. In both extrapolations, a characteristic energy of 8 keV was used. We also fit the low-energy part of the spectrum, but we have found that the upgoing electron flux is insensitive to this portion of the proton flux.

For the electron data, five downgoing pitch angles were usable. These measurements were interpolated onto the energy grid required by the model and then averaged over pitch angle. We also averaged the electron data over the same 23 sweeps as for the ion data.

As mentioned in the previous section, a possible source of low-energy electrons is photoproduction below the satellite. During the observations, the solar zenith angle was from 113.6° to 114.4° . This puts the terminator between 680 and 724 km, giving a potential photoelectron source region from around 700 km to the satellite altitude of around 950 km. Calculations, including a photoelectron source at these altitudes, show that they contribute less than a percent to the upgoing electron flux.

An additional complication is that the data were taken at an altitude from 935 to 950 km. At this height, the precipitating particles still have to descend several hundred kilometers before any significant interaction occurs between the precipitating particles and the neutrals. The one collisional process that still can have some effect at these altitudes is that of low-energy electrons (< 30 eV) undergoing energy loss through Coulomb collisions with the thermal electrons. Thus

over this altitude region, the energetic precipitating particles are primarily undergoing adiabatic motion in a nonuniform magnetic field (magnetic mirroring), a process that is neglected in the model. To reduce the impact of this effect, we have restricted our comparisons with data to pitch angles near 180 deg. We should note that while this may minimize the effect of mirroring, it does not eliminate it altogether. A study of the entire pitch angle distribution of the observed electrons will require that the effects of magnetic mirroring be included in the model.

The final issue to discuss before presenting the results is that of proton beam spreading. As noted by *Jasperse and Basu* [1982], at high altitudes (typically above 300 km) a correction is needed for the transverse beam-spreading effect. This can be estimated on the basis of the work of *Iglesias and Vondrak* [1974]. In our case, the latitudinal width of the proton precipitation is around 160 km, which leads to a correction factor of .65. But this factor describes the net reduction of the flux at arc center at altitudes below the region where spreading occurs. On the other hand, we are interested in the upgoing electron flux at 950 km and thus are interested in the reduction of the flux all through the region where spreading occurs. This means that ignoring the spreading should overestimate the upgoing electron flux and using the 0.65 factor should underestimate the upgoing electron flux. Since a spreading factor will simply linearly scale the contribution due to protons and H atoms, we can do the calculation using a factor of 1 and then after the fact examine the impact of this spreading uncertainty on our results.

In Figure 7, we show a comparison between the observed upward electron flux and two calculations from the electron-proton-H atom transport model. The solid curve is an average of 23 s of data at a pitch angle of 163.8°. The vertical error bars are again the standard deviations based on the number of counts. The horizontal error bars give the energy resolution at each energy. The short-dashed curve gives model results when the kappa distribution was used in the high-energy extrapolation of the proton flux, and the long-dashed curve is for the Maxwellian extrapolation. Clearly, our results are sensitive to the assumed extrapolation. The calculation using the kappa distribution does an excellent job reproducing the observed data, with the modeled electron flux passing within the error bars for 10 out of 11 data points. The Maxwellian gives a reasonable shape but does fall somewhat below the data. The model results are shown at 153.5°, which is the closest angle on the calculational pitch angle grid to 163.8°. Since no significant difference is predicted by the model between 153.5° and 180.0°, an interpolation to 163.8° would produce similar results.

Since we had to use a case that included both electron and proton precipitation, it is of interest to see how many of the upgoing electrons are due to protons and H atoms and how many are due to electrons. Figure 8 shows the resultant upgoing electron flux from a calculation with only precipitating protons (dashed curve) and one with only precipitating electrons (solid curve). Note, the proton-only calculation used the kappa distribution extrapolation. We see that from 10 to around 100 eV, the two types of precipitation produce comparable amounts of upgoing electrons. Recall that above 100 eV, as seen previously in Figure 2, the upgoing electron flux is essentially entirely caused by the precipitating electrons. These calculations also allow us to

assess the effect of using a 0.65 spreading factor in the calculation. For those energies where a little less than half of the upgoing flux is due to protons and H atoms, the upgoing flux would be reduced by 15%.

6. Discussion and Summary

In this paper, we have presented the first comparisons between observations and the results of a fully coupled three-component auroral transport model. This model solves for the electron, proton, and H atom differential fluxes as functions of altitude, energy, and pitch angle. Using observed incoming electron and ion fluxes as boundary conditions, we have calculated the resulting upgoing electron flux. In Figure 7, the calculated flux is compared to the observed upgoing flux, and they are in excellent agreement. However, our ability to produce such agreement was dependent on extrapolating the observed incoming proton flux from 30 to 150 keV using a kappa distribution with $\kappa = 3.0$ and $E_0 = 8.0$ keV. This raises two questions: (1) is the kappa extrapolation reasonable?, and (2) what other uncertainties should we consider in assessing the reliability of the agreement?

In considering which extrapolation to use, we first considered where the observations were made. These are auroral observations made as the satellite is moving equatorward in the premidnight sector. Examining the electron data in Plate 1, we see prior to 19:43:52 energetic electron spectra that are indicative of precipitation from the boundary plasma sheet. The subsequent softening of the electron spectra and the fact that the satellite is moving equatorward in the premidnight sector suggest that the proton precipitation is coming from the inner regions of the central plasma sheet (CPS). While we have few examples of ionospheric observations of proton spectra at energies above 30 keV, there have been studies of ion populations in the CPS [*Christon et al.*, 1988, 1989, 1991] which have included such energies. Their findings have been that at high energies ($E >$ characteristic or peak energy) there is a nonthermal power law tail which can be fitted using a kappa distribution. With kappa distributions being normally observed in the plasma sheet, the critical question for us is whether they are still present when the ions reach ionospheric altitudes. As noted above, we have found little ionospheric proton data at energies above 30 keV. In one paper however, data from various instruments were combined to show that proton distributions at ionospheric altitudes have high-energy tails and are the same as those seen for Earthward streaming protons in the outer boundary of the plasma sheet [*Lyons and Evans*, 1984]. Another example of the proton differential flux at ionospheric heights over the energies of interest comes from the Particle Environment Monitor (PEM) experiment on board the Upper Atmosphere Research Satellite (UARS) [*Sharber et al.*, 1993]. The spectra that are shown in their Figure 4 were observed in the auroral zone at an altitude of 585 km and the broadly peaked spectra are characteristic of precipitation from the CPS. The observations were made during a magnetic storm and an examination of this ionospheric ion spectrum shows a high-energy power law tail similar to that described by *Christon et al.* [1991] as typical of CPS ion populations. While neither of the two cases we have just described precisely fits our situation (that is, ion precipitation from the CPS during periods of magnetically

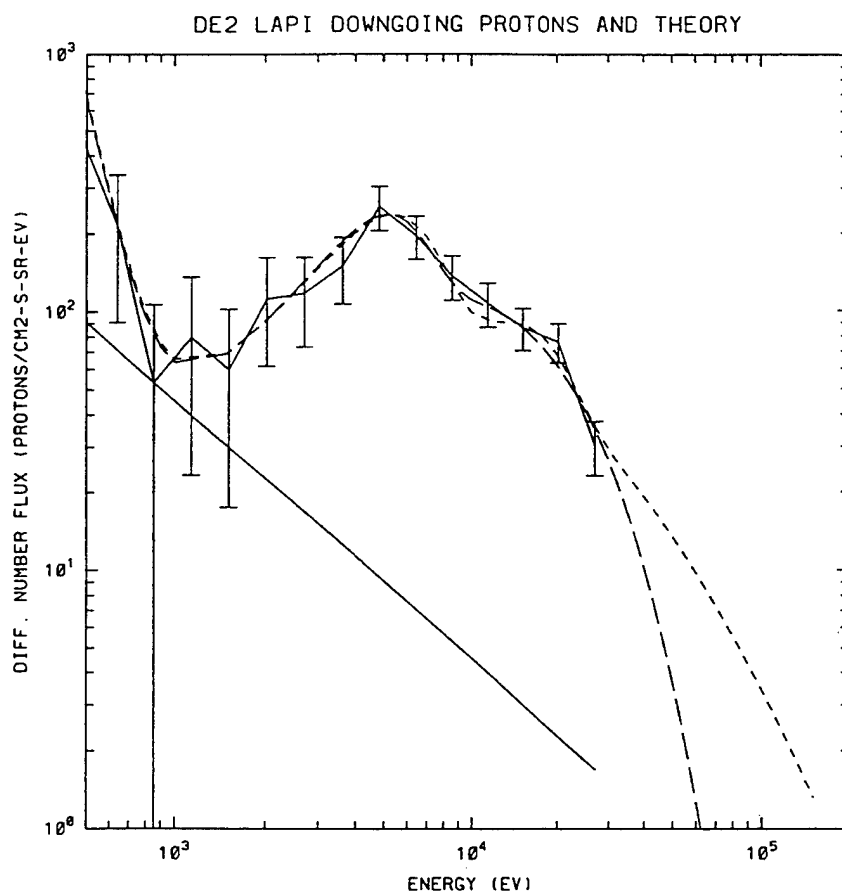


Figure 6. The differential number flux of ions at a pitch angle of $\sim 14^\circ$ (downward flux) and an altitude of around 950 km versus energy. The points on the solid curve are the observed 23-s averages for a period beginning at 1944:19 UT on day 289 of 1981. The dashed curves are fits to the data that were used as inputs to the model. Extrapolations to higher energies were used to provide high-energy tails for the incident flux. The short-dashed curve used a kappa distribution for the extrapolation, and the long-dashed curve used a Maxwellian.

quiet conditions), they indicate that the use of a kappa distribution to extrapolate above 30 keV is perhaps reasonable.

Is the value of $\kappa = 3$ that we have used reasonable? Again, turning to *Christon et al.* [1989], they report that during undisturbed periods κ ranges from 3 to 9.5. We have shown that using $\kappa = 3$ gives excellent agreement with the data. If we use $\kappa = 9.5$, the model underestimates the data but does a better job than that with the Maxwellian. While we have used a κ at one extreme of the observed range, we need to remember that the κ one determines depends critically on how the fitting is done. In the work by *Christon et al.* [1989], they were attempting to fit particle spectra over three decades in energy. On the other hand, we extrapolated from around 30 to 150 keV. When we tried fitting a kappa function to the ion spectrum given by *Sharber et al.* [1993], we found that if we wanted to fit from 74 to 500 keV, a $\kappa = 6.5$ does a reasonable job. However, if we fit from 40 to 150 keV, a κ range of 3.5 to 4.5 gives reasonable results. Thus given the data currently available, we conclude that a $\kappa = 3$ is certainly a possibility, but questions concerning its probability will have to wait until more observations are available.

We now discuss the other uncertainties we have to deal with. At the top of the list is the question of cross sections.

In particular, those cross sections for collisions between energetic protons-H atoms and the neutral species of the atmosphere. We focus on proton-H atom cross sections because typically the various electron cross sections are much better known. In general, the cross sections for proton-H atom collisions with N_2 and O_2 are measured and the quoted accuracies are typically ± 20 -30%. On the other hand, the collisions involving atomic oxygen are not measured, and one has to resort to "estimates" based on other cross sections. The one exception is for charge-changing collisions for which measurements have been made with quoted accuracies of 25%, but at present there are still factors of 2 disagreement between some of these measurements. We have not performed a systematic sensitivity study involving all the cross sections. However, we have looked at the effect of changing the atomic oxygen ionization cross section. The reason for this is that we have found that for energies less than 100 eV, over 90% of the upgoing electron flux at 950 km originates from above 200 km. Hence collisions with oxygen are playing a dominant role in producing the upgoing electron flux. The variation we considered was to use our O_2 ionization cross section for the O ionization cross section. In the past, various O cross sections have sometimes been estimated to be some fraction of the O_2 cross section, and we

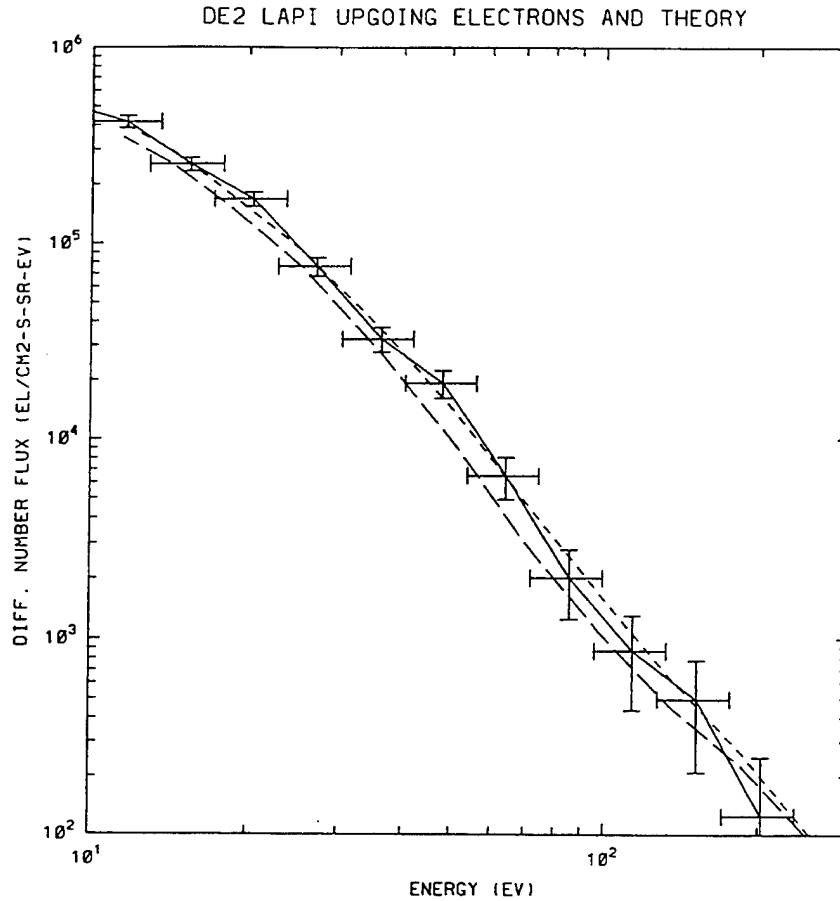


Figure 7. The differential number flux of electrons at an altitude of 950 km versus energy. The points on the solid curve are the observed 23-s averages at a pitch angle of $\sim 163.8^\circ$ for a period beginning at 1944:19 UT on day 289 of 1981. The dashed curves are theoretical fluxes at a pitch angle of 153.5° . The short-dashed curve used a kappa distribution to extrapolate the incident proton flux and the long-dashed curve used a Maxwellian.

feel that using the total O_2 cross section represents a maximum upper bound for the O cross section. In the case of ionization of O by proton or H atoms, this represents an increase of around a factor of 2 near the peak (~ 60 keV) of the cross section. The effect of this change in the $\kappa = 3$ calculation was to increase the upgoing electron flux below 100 eV by up to 25%. Between 100 and 200 eV, the effect drops to less than a percent as the upgoing electron flux becomes dominated by the electron precipitation. Since the protons are responsible for a little less than half of the upgoing flux, this means the upgoing flux produced by protons and H atoms increased by up to 60%. Using the enhanced O cross section in the Maxwellian calculation produces a smaller effect of a 12% increase. It is smaller in this case, because with the Maxwellian extrapolation the protons contribute only around 20% of the total upgoing electrons. What this then says is that by using a range of O cross sections between our present cross section and our upper bound cross section, a range of kappas could be found to fit the data. On the other hand, even using the upper bound cross section is not sufficient to bring the Maxwellian case into agreement with the data.

Two other uncertainties have already been discussed in the previous section: proton beam spreading and mirroring. As discussed, beam spreading would tend to lower the calculated

fluxes and would make agreement worse for those extrapolations that already lead to underestimates of the data. For the extrapolation presented here, we estimated its maximum effect might be to cause a 15% reduction in the upgoing flux. The effect of mirroring is much less clear cut. Monte Carlo calculations [Kozelov, 1993] have shown that mirroring of the protons tends to reduce the downward proton and H atom flux by something like 5-20% but creates an upward flux above 200 km that can be up to 10% of the downgoing flux. Without doing a calculation that includes mirroring, it is difficult to determine whether mirroring creates a net increase or decrease to the upgoing electron flux. We would expect that whatever the effect, it will be less than 10%.

In Figure 8, we showed that from 10 to 100 eV a little more than half of the upgoing flux is due to electron precipitation with the remainder being produced by the proton- H atom precipitation. This means that any uncertainty in the electron transport calculation is as important as that in the proton- H atom transport calculation. While there have been many more opportunities to test electron transport calculations, we have found few examples where the upgoing electrons due to electron precipitation have been modeled and compared to data. In calculations we have made involving photoelectrons and the polar rain [Decker *et al.*, 1990], we

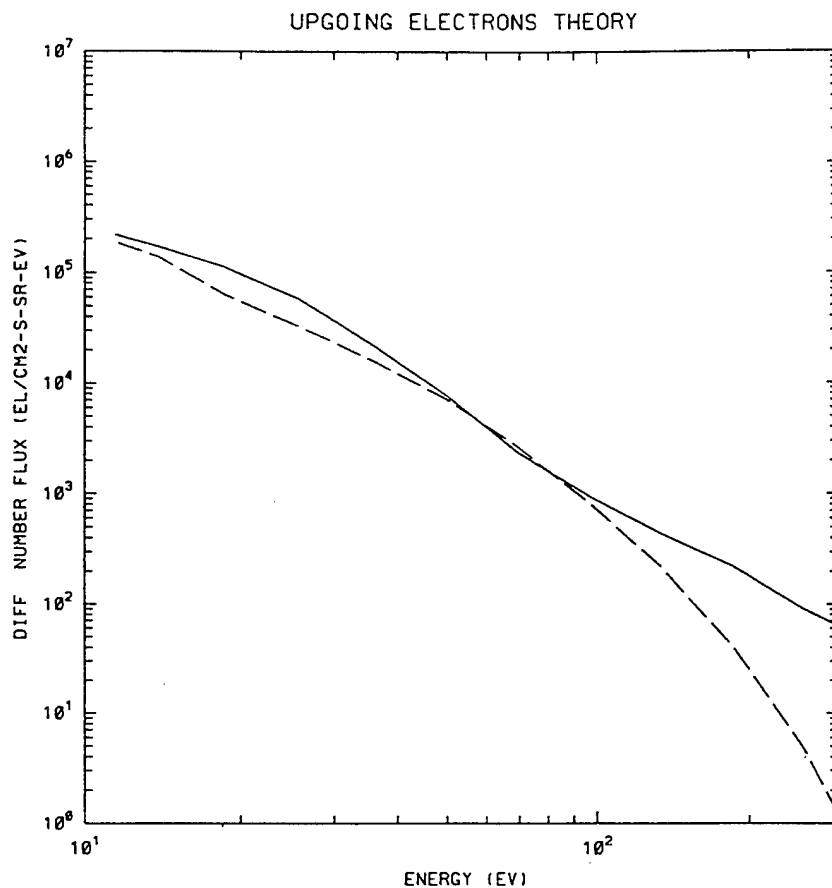


Figure 8. Theoretical differential electron number flux at a pitch angle of 153.5° and an altitude of 950 km versus energy. The solid curve is from the calculation using only the observed incident electron flux as the incident flux. The dashed curve is for the case where only the observed incident ion flux is used as the incident flux.

found the low-energy upgoing electrons (< 80 eV) were about 25% below LAPI observations. A topic for future study will be to perform a study on upgoing electrons in a pure electron aurora. One issue we have been able to explore is that of the role of electron-electron collisions in determining the low-energy upgoing electrons. The electron density profile used was selected precisely to give the fit seen in Figure 7 for the $\kappa = 3$ case. We found that turning off the electron-electron collisions had a significant effect at energies below 30 eV. For example, at 11.5 eV the upgoing flux increased by over a factor of 2 when the Coulomb collisions were turned off. Thus, at energies below 30 eV the assumed electron density profile is as critical as the assumed extrapolation for the high-energy protons in determining the upgoing electrons.

The final uncertainty we wish to discuss is in the LAPI measurements themselves. Laboratory calibrations give a relative instrumental uncertainty of the LAPI analyzers of $\pm 23\%$. It is the relative calibration rather than the absolute that is critical in this case because both the inputs to (downgoing electrons and protons) and the outputs from (upgoing electrons) the linear transport model are measured by LAPI. Hence any absolute uncertainty would shift both the inputs and the outputs but not effect the quality of our agreement between model and data. The observations used in this paper were taken within the first few months of the DE 2 flight and

there was no evidence of any degradation nor was any anticipated at that point in the life of the instrument.

The effect of all the above uncertainties is that there is a range of κ that could produce excellent fits to the data both in shape and magnitude. On the other hand, to produce an equally good fit to the data using a Maxwellian extrapolation, while not impossible, would require taking full advantage of the relative uncertainties of the instrument as well as judicious choice of adjusted cross sections.

Clearly, more definitive tests of the model will require better-known cross sections, as well as more comprehensive observations. While PEM on UARS holds some promise for providing ion data over a larger energy range, for the foreseeable future validating proton/H atom transport models will continue to be a difficult task. However, two conclusions regarding the proton aurora can be derived from the present study. First, the observations presented do support the prediction of the model (as discussed in sections 3 and 4) that the secondary spectra due to protons and H atoms is much softer than that produced by precipitating electrons. This is shown in Figure 4, where we can see that an electron aurora of the same energy flux as a proton aurora produces significantly more upgoing electrons over the energy range of 10 to 1000 eV. The other conclusion of this study is that the incoming proton differential flux at ionospheric altitudes most

likely has a power law behavior at high energies. If this is the typical situation, it implies that determinations of total energy flux from instruments with low-energy cutoffs by assuming a Maxwellian distribution [Hardy *et al.*, 1989] may seriously underestimate the flux. For example, in the case discussed in this paper when we fitted with the Maxwellian, we estimated a total energy flux of $\sim 0.21 \text{ ergs cm}^{-2} \text{ s}^{-1}$ whereas when fitted with a kappa distribution with $\kappa = 3$ the total energy flux was $\sim 0.63 \text{ ergs cm}^{-2} \text{ s}^{-1}$. A similar point for the plasma sheet is discussed in Christon *et al.* [1991]. Since various ionospheric effects of the proton aurora have been previously calculated [Strickland *et al.*, 1993] by assuming a Maxwellian distribution, these calculations should be repeated using kappa distributions in order to fully assess the impact of these high-energy power law tails.

Acknowledgments. One of us (JRJ) should like to acknowledge important discussions with C. Senior. The work by DTD was supported by Air Force contracts F19628-88-K-0008 and F19628-93-K-0001 with Boston College. The work by BB and JRJ at the Phillips Laboratory was supported by the Air Force Office of Scientific Research (AFOSR). The work by DJS was supported by various Phillips Laboratory contracts with CPI. The work at Southwest Research Institute was supported by NASA contract NAS5-33031.

The Editor thanks G. Khazanov and another referee for their assistance in evaluating this paper.

References

- Basu, B., J. R. Jasperse, R. M. Robinson, R. R. Vondrak, and D. S. Evans, Linear transport theory of auroral proton precipitation: A comparison with observations, *J. Geophys. Res.*, **92**, 5920, 1987.
- Basu, B., J. R. Jasperse, and N. J. Grossbard, A numerical solution of the coupled proton-H atom transport equations for the proton aurora, *J. Geophys. Res.*, **95**, 19069, 1990.
- Basu, B., J. R. Jasperse, D. J. Strickland, and R. E. Daniell Jr., Transport-theoretic model for the electron-proton-hydrogen atom aurora, *1, Theory*, *J. Geophys. Res.*, **98**, 21517, 1993.
- Christon, S. P., D. G. Mitchell, D. J. Williams, L. A. Frank, C. Y. Huang, and T. E. Eastman, Energy spectra of plasma sheet ions and electrons from $\sim 50 \text{ eV/e}$ to $\sim 1 \text{ MeV}$ during plasma temperature transitions, *J. Geophys. Res.*, **93**, 2562, 1988.
- Christon, S. P., D. J. Williams, D. G. Mitchell, L. A. Frank, and C. Y. Huang, Spectral characteristics of plasma sheet ion and electron populations during undisturbed geomagnetic conditions, *J. Geophys. Res.*, **94**, 13409, 1989.
- Christon, S. P., D. J. Williams, D. G. Mitchell, C. Y. Huang, and L. A. Frank, Spectral characteristics of plasma sheet ion and electron populations during disturbed geomagnetic conditions, *J. Geophys. Res.*, **96**, 1, 1991.
- Decker, D. T., J. R. Jasperse, and J. D. Winningham, Energetic photoelectrons and the polar rain, in *Physics of Space Plasmas (1989)*, SPI Conference Proceedings and Reprint Series, Vol. 9, edited by T. Chang, G. B. Crew, and J. R. Jasperse, pp. 15-28, Scientific, Cambridge, Mass., 1990.
- Hardy, D. A., M. S. Gussenhoven, and D. Brautigam, A statistical model of auroral ion precipitation, *J. Geophys. Res.*, **94**, 370, 1989.
- Hedin, A. E., MSIS-86 thermospheric model, *J. Geophys. Res.*, **92**, 4649, 1987.
- Iglesias, G. E., and R. R. Vondrak, Atmospheric spreading of protons in auroral arcs, *J. Geophys. Res.*, **79**, 280, 1974.
- Jasperse, J. R., and B. Basu, Transport theoretic solutions for auroral proton and H atom fluxes and related quantities, *J. Geophys. Res.*, **87**, 811, 1982.
- Kozelov, B. V., Influence of the dipolar field on transport of proton-H atom fluxes in the atmosphere, *Ann. Geophys.*, **11**, 697, 1993.
- Kozelov, B. V., and V. E. Ivanov, Monte Carlo calculation of proton-hydrogen atom transport in N_2 , *Planet. Space Sci.*, **40**, 1503, 1992.
- Lyons, L. R., and D. S. Evans, An association between discrete aurora and energetic particle boundaries, *J. Geophys. Res.*, **89**, 2395, 1984.
- Meier, R. R., D. J. Strickland, P. D. Feldman, and E. P. Gentieu, The ultraviolet dayglow, 1, Far UV emissions of N and N_2 , *J. Geophys. Res.*, **85**, 2177, 1980.
- Meier, R. R., R. R. Conway, P. D. Feldmann, D. J. Strickland, and E. P. Gentieu, Analysis of nitrogen and oxygen far ultraviolet auroral emissions, *J. Geophys. Res.*, **87**, 2444, 1982.
- Meier, R. R., D. J. Strickland, J. H. Hecht, and A. B. Christensen, Deducing composition and incident electron spectra from ground-based auroral optical measurements: A study of auroral red line processes, *J. Geophys. Res.*, **94**, 13541, 1989.
- Senior, C., J. R. Sharber, O. de la Beaujardière, R. A. Heelis, D. S. Evans, J. D. Winningham, M. Sugiura, and W. R. Hoegy, E and F region study of the evening sector auroral oval: A Chatanika/Dynamics Explorer 2/NOAA 6 comparison, *J. Geophys. Res.*, **92**, 2477, 1987.
- Sergienko, T. I., and V. E. Ivanov, A new approach to calculate the production rates of the ionosphere species excited by auroral electrons, *Proc. 19th Annual European Meeting on Atmospheric Studies by Optical Methods*, IRF Sci. Rep. 209, p. 495, Inst. for Rymdfysik, Kiruna, 1992.
- Sharber, J. R., R. A. Frahm, J. D. Winningham, J. C. Biard, D. Lummerzheim, M. H. Rees, D. L. Chenette, E. E. Gaines, R. W. Nightingale, and W. L. Imhof, Observations of the UARS particle environment monitor and computation of ionization rates in the middle and upper atmosphere during a geomagnetic storm, *Geophys. Res. Lett.*, **20**, 1319, 1993.
- Strickland, D. J., Electron transport, chemistry and optical emissions in the auroral E-layer, *Rep. AFGL-TR-81-0042*, Air Force Geophys. Lab., Bedford, Mass., 1981.
- Strickland, D. J., D. L. Book, T. P. Coffey, and J. A. Fedder, Transport equation techniques for the deposition of auroral electrons, *J. Geophys. Res.*, **81**, 2755, 1976.
- Strickland, D. J., J. R. Jasperse, and J. A. Whalen, Dependence of auroral FUV emissions on the incident electron spectrum and neutral atmosphere, *J. Geophys. Res.*, **88**, 8051, 1983.
- Strickland, D. J., R. E. Daniell Jr., D. Decker, J. R. Jasperse, and H. C. Carlson, Determination of ionospheric electron density profiles from satellite UV emission measurements, *Rep. AFGL-TR-84-0140*, Air Force Geophys. Lab., Bedford, Mass., 1984.
- Strickland, D. J., R. R. Meier, J. H. Hecht, and A. B. Christensen, Deducing composition and incident electron spectra from ground based auroral optical measurements: Theory and model results, *J. Geophys. Res.*, **94**, 13527, 1989.
- Strickland, D. J., R. E. Daniell Jr., J. R. Jasperse, and B. Basu, Transport-theoretic model for the electron proton-hydrogen atom aurora, 2, Model results, *J. Geophys. Res.*, **98**, 21533, 1993.
- Winningham, J. D., J. L. Burch, N. Eaker, V. A. Blevins, and R. A. Hoffman, The Low Altitude Plasma Instrument (LAPI), *Space Sci. Instrum.*, **5**, 465, 1981.
- Winningham, J. D., D. T. Decker, J. U. Kozyra, J. R. Jasperse, and A. F. Nagy, Energetic ($>60 \text{ eV}$) atmospheric photoelectrons, *J. Geophys. Res.*, **94**, 15335, 1989.
- B. Basu, Phillips Laboratory, Geophysics Directorate (GPIM), 29 Randolph Rd., Hanscom AFB, MA 01731-3010. (email: basub@plh.af.mil)
- D. T. Decker, Institute for Scientific Research, Boston College, 885 Centre St., Newton, MA 02159. (email: decker@plh.af.mil)
- J. R. Jasperse, Centre de Recherches en Physique de l'Environnement, 4 Avenue de Neptune, 94107 Saint-Maur-des Fossés, France. Permanently at Phillips Laboratory, Geophysics Directorate (GPIM), 29 Randolph Rd., Hanscom AFB, MA 01731-3010.
- J. R. Sharber and J. D. Winningham, Southwest Research Institute, Postal Drawer 28510, San Antonio, TX 78228-0510. (e-mail: sharber@swri.space.swri.edu; david@dewsl.space.swri.edu)
- D. J. Strickland, Computational Physics, Inc., 2750 Prosperity Ave, Suite 600, Fairfax, VA 22031. (e-mail: dstrick@euler.cpi.com)

(Received August 2, 1994; revised May 15, 1995; accepted May 18, 1995.)

Collisional Degradation of the Proton-H Atom Fluxes in the Atmosphere: A Comparison of Theoretical Techniques

Dwight T. Decker¹

Boris. V. Kozelov²

B. Basu³ and J. R. Jasperse³

V. E. Ivanov²

Received _____; accepted _____

Short title: COMPARISON OF PROTON TRANSPORT CALCULATIONS

¹Institute for Scientific Research, Boston College, Newton, Massachusetts.

²Polar Geophysical Institute, Apatity, Russia.

³Phillips Laboratory, Hanscom Air Force Base, Massachusetts.

Abstract. Three methods for calculating the transport of energetic protons and hydrogen atoms within the earth's atmosphere are compared. The methods are (1) a Monte Carlo (MC) simulation, (2) a discrete energy loss solution to the linear transport equations, and (3) a continuous slowing down approximation (CSDA). In the calculations performed, all three models use the same cross sections, three component (N_2 , O_2 , O) neutral atmosphere, and incident isotropic Maxwellian proton fluxes of various characteristic energies (1–20 keV). A variety of quantities are calculated and compared including energy deposition rates, eV/ion pair, hemispherically averaged differential fluxes of protons and H atoms, energy integrated differential fluxes and total proton and H atom fluxes. The agreement between all three models is excellent except at the lowest altitudes. Apart from these altitudes, the differences that do exist are small compared to the errors that generally result from poorly known inputs and compared to the typical errors quoted for geophysical observations. The altitudes where the results do differ significantly are where the proton and H atom fluxes are severely attenuated and are below the altitudes where the bulk of the energy deposition and ionization takes place.

1. Introduction

It is well established that an essentially permanent feature of the Earth's high latitude atmosphere is the presence of auroral particle fluxes. It is also well known that these precipitating fluxes from the magnetosphere consist of mostly electrons and protons with a small admixture of other ions. Early ground-based optical observations [Romick and Elvey, 1958; Galperin, 1959] indicated that electron and proton aurora could have separated latitudinal distributions. Later satellite observations of the precipitating particles established that statistically the electron and protons precipitate within two ovals that are not co-located [Sharber, 1981; Hardy et al., 1989]. Further, an examination of the the Hardy statistical models [Hardy et al., 1987, 1991] reveals that in the afternoon and evening sectors the ions at the lower auroral latitudes can carry a significant portion of the incoming energy flux. Thus in order to study the dissipation of auroral energy within the earths atmosphere, it is necessary to study not just the transport and collisional degradation of energetic electrons but also those of protons.

The transport of energetic protons within matter is a problem that has been studied for a variety of physical situations. In the case of transport of auroral protons within the atmosphere there are several features that add to the difficulty of the problem. Some of those features are (1) auroral proton energies can be less than the energy of the maximum of the ionization cross section, (2) there is a large gradient of the atmospheric density with respect to altitude, and (3) the Earth's magnetic field is present. The first feature requires detailed knowledge of cross sections since simple estimations (Born approximation) of cross sections are not valid. Further, at auroral energies the charge changing processes have to be included and this introduces energetic hydrogen (H) atoms into the problem. The effect of the large gradient in the atmosphere is to create a strong altitude dependence in the mean free path of the protons and H atoms. Hence the behavior of the particle flux is highly dependent on altitude. The presence of the Earth's magnetic field acts to cause the protons to follow fieldlines into the ionosphere.

However, the H atoms are not constrained by the magnetic field. This coupled with the altitude dependent mean-free path results in a lateral spreading of the p-H flux at high altitudes but essentially no spreading at low altitudes. Finally, a feature that can be a useful simplification in any modeling is that all the collision processes involving protons and H atoms are strongly peaked in the forward direction. However at very low energies ($E < 1\text{keV}$) energy loss due to elastic collisions does become significant.

There have been several treatments of p-H transport that have appeared in the literature. They can be generally categorized as range theoretic, continuous slowing down, linear transport theoretic, and Monte-Carlo. The range theoretic method is based on laboratory measurements of range energy relations for protons in air or its theoretical approximations and has been used in the works of *Eather* [1966, 1967, 1970], *Isaev and Pudovkin* [1972], *Henriksen* [1979], and *Rees* [1982]. The continuous slowing down approximation (CSDA) uses more detailed information about scattering processes and was used for the auroral proton problem in *Edgar et al.* [1973, 1975]. Work on analytic estimations of lateral spreading of p-H flux [*Johnstone*, 1974; *Iglesias and Vondrak*, 1974] also can be classified as using the CSDA.

In more recent years, linear transport (LT) theory has been used to solve for the auroral proton and H atom fluxes. In *Jasperse and Basu* [1982] the coupled transport equations based on the Boltzmann equation were solved analytically and in a follow on paper [*Basu et al.*, 1987] theoretically calculated electron density profiles due to incident protons were found in good agreement with Chatanika radar data. This in turn was followed by the development of a fully numerical code for solving the linear transport equations [*Basu et al.*, 1990].

The Monte-Carlo (MC) method has been applied to the auroral proton problem by *Davidson* [1965], *Ponomarev* [1976], *Galperin et al.* [1976], and *Kozelov and Ivanov* [1992]. Most recently, *Kozelov* [1993] has implemented the method using a full three species neutral atmosphere and the influence of the Earth's magnetic field. While

computationally intensive the Monte-Carlo method does have the advantage of including processes, such as beam spreading or mirroring, that are difficult to treat in the other approaches.

Assessing the validity of any approach usually involves either 'back of the envelope' estimates of neglected processes, a posteriori calculations of those processes, comparisons to observations, or comparisons to alternative approaches. The difficulty in comparing approaches is that when comparing to results of other authors there are often differences in cross sections, boundary conditions, and geophysical conditions that confuse the issue of comparing methods. MC and CSDA models with the same input parameters were compared by *Porter and Green* [1975], but the comparison was only for homogeneous molecular nitrogen and the initial proton flux was taken as isotropic and monoenergetic with initial energy 1 keV. More extensive comparisons for a N_2 atmosphere were made in *Kozelov and Ivanov* [1992]. They considered initial energies from 1 keV to 1 MeV. For initial energies less than 10 keV, differences were found near the high altitude boundary and at lowest altitudes of penetration.

The purpose of this paper is to compare three methods for calculating the transport and collisional degradation of energetic protons and H atoms in the earth's ionosphere using identical cross sections, boundary conditions, and geophysical conditions. We will show that for several quantities the differences between the three methods are reasonably small compared to the model uncertainties that arise from uncertainties in the required inputs (cross sections, neutral densities, and boundary conditions) and the uncertainties in the available observations (particle fluxes, optical emissions, and ion densities). The three methods considered are the CSDA, LT, and MC. In section 2 we briefly describe the three models used. A more detailed discussion of the relationship between the CSDA and LT models is given in an appendix. After a discussion in section 3 concerning the physical processes and input parameters included in all three models, we present in section 4 the comparison of the various results from the models. The

paper concludes with a discussion and summary in section 5.

2. Description of theoretical models

2.1 Continuous slowing-down approximation (CSDA)

The CSDA describes the degradation of the energetic particle's energy in terms of loss functions. For a mono-energetic mono-directional p-H flux the equation for energy loss is given by

$$-\mu \frac{dE}{dz} = \frac{\sum_{\alpha} n_{\alpha}(z) \left[L_{\alpha,P}(E) \Phi_P(z, E, \mu) + L_{\alpha,H}(E) \Phi_H(z, E, \mu) \right]}{\Phi_P(z, E, \mu) + \Phi_H(z, E, \mu)} \quad (1)$$

where Φ 's are the energetic particle fluxes, z is the altitude, μ is cosine of the pitch angle, and $n_{\alpha}(z)$ are the densities for neutral specie α . $L_{\alpha,P}(E)$ and $L_{\alpha,H}(E)$ are the loss functions for the protons and H atoms due to collisions with neutral gases and are given by

$$L_{\alpha,P}(E) = \sum_j W_{\alpha,P}^j(E) \sigma_{\alpha,P}^j(E) \quad (2)$$

$$L_{\alpha,H}(E) = \sum_j W_{\alpha,H}^j(E) \sigma_{\alpha,H}^j(E) \quad (3)$$

where $\sigma_{\alpha,P}^j(E)$ is the cross section for a type j collision between a proton and a neutral specie α and $W_{\alpha,P}^j(E)$ is the corresponding energy loss. Similarly, $\sigma_{\alpha,H}^j(E)$ and $W_{\alpha,H}^j(E)$ are the cross sections and the energy loss for collisions involving H atoms.

Usually the loss function is defined for a charge state equilibrium flux [Porter and Green, 1975]. Here, in an implementation developed by Kozelov, the loss function is defined using the nonequilibrium flux that describes the modification of the flux charge state composition. The nonequilibrium flux is calculated using the following equations

$$\mu \frac{d\Phi_P(z, E, \mu)}{dz} = \Phi_H(z, E, \mu) \sum_{\alpha} n_{\alpha}(z) \sigma_{\alpha}^{01}(E) - \Phi_P(z, E, \mu) \sum_{\alpha} n_{\alpha}(z) \sigma_{\alpha}^{10}(E) \quad (4)$$

$$\frac{d\Phi_H(z, E, \mu)}{dz} = -\frac{d\Phi_P(z, E, \mu)}{dz} \quad (5)$$

where σ^{10} and σ^{01} are the total cross sections for charge exchange and stripping respectively. The calculational procedure consists of solving equations (1), (4) and (5) on a altitude, energy and pitch angle grid with the incoming flux at the high altitude boundary being approximated by a set of mono-energetic mono-directional particle streams. A more detailed discussion of the CSDA can be found in the Appendix.

2.2 Linear Transport (LT) model

The fundamental feature of the LT model is the use of transport theoretic methods to solve two coupled Boltzmann equations for the proton and H atom differential fluxes. In solving these equations, we assume steady-state conditions, no electric fields, a uniform geomagnetic field (no magnetic mirroring), and azimuthal symmetry about the geomagnetic field line. The collisional processes included are the various types of collisions between the energetic precipitating particles and the neutral constituents of the ionosphere. The protons and H atoms are coupled to each other by charge-changing collisions with neutrals (charge exchange and stripping). The two transport equations, discussions of the various collision processes, and the numerical methods for solving the equations can be found in *Basu et al.* [1993] and will not be given here. A discussion of the relationship between the linear transport theory and the CSDA can be found in the Appendix.

2.3 Monte Carlo model (MC)

The MC model uses a 'collision-by-collision' algorithm which is based on simulating the individual trajectories of a large number of protons and H atoms. The 'history' of each particle is represented as a series of collisions that are separated by segments of free streaming within a magnetic field. The selection of the path length between collisions and the collisional parameters is made by mapping into a random number, ξ , generated uniformly in the range 0-1.

The altitude of the particle after the $(i + 1)^{st}$ path length is determined from the formula

$$-\ln \xi = \int_{z_i}^{z_{i+1}} \frac{dz}{\mu} \sum_{\alpha} n_{\alpha}(z) \sigma_{\alpha,\beta}^{tot}(E_i), \quad (6)$$

where z_i is the altitude before the $(i + 1)^{st}$ path length, $\sigma_{\alpha,\beta}^{tot}(E_i)$ is the total cross section of the particle in gas α , E_i is the particle's energy after the i^{th} collision, β is the charge state of the particle (p or H). The neutral species with which the $(i + 1)^{st}$ collision occurred are determined by random sampling using the probabilities $n_{\alpha}(z) / \sum_{\alpha} n_{\alpha}(z)$, where α is N_2 , O_2 , or O . The type of collision is also selected by random sampling using probabilities $\sigma^j(E_i) / \sigma^{tot}(E_i)$, where j is the type of collision. When a collision occurs the energy of the particle is decreased based on the type of collision used. In the case of charge exchange or stripping collisions the charge state of the particle is modified. To simulate an initial Maxwellian energy distribution at the high altitude boundary we divide the full energy range into 10-12 energy channels and place within each channel 8000 to 24000 protons. The cosine of the initial pitch angle for each particle is determined from the expression $\mu = \cos \theta = \sqrt{\xi}$, where ξ is a random number generated uniformly in the range 0-1. During the simulation of a particle's trajectory its location is stored along with the various quantities needed for determining such quantities as the particle fluxes, energy deposition, ionization rates, etc. The results of the simulation are processed by statistical methods. If we have N realizations of a random variable x , then the average value is taken as $\bar{x} = \frac{1}{N} \sum_{i=1}^N x_i$. The statistical error, Δx , is estimated from expressions

$$\Delta x = C\sqrt{Dx}, \quad Dx \approx \frac{1}{N} \sum_{i=1}^N (x_i - \bar{x})^2,$$

where x is the random value, x_i is the i^{th} realization of the value, Dx is the dispersion. If $C \approx 1.4$, then the probability that the value $x \in [\bar{x} - \Delta x, \bar{x} + \Delta x]$ is equal to 0.7.

3. Inputs

In order to facilitate our comparison, we wanted to make the geophysical inputs, the microscopic parameters, and the physical processes included in the three models as identical as possible. Considering the physical processes, we find that all three models include the transport and degradation of protons and neutral hydrogen atoms as they collide with the neutral species of the ionosphere. The CSDA and LT assume a uniform magnetic field(no mirroring) and a plane parallel geometry (no spreading), on the other hand the MC method can handle the effects of magnetic mirroring as well as lateral spreading of the energetic particles. For these comparisons, magnetic mirroring and lateral spreading were turned off in the MC calculations. Similarly, both CSDA and LT assume forward scattering while MC can include angular scattering. Again we simplify the MC model and use the forward scattering approximation in all calculations for this paper.

By microscopic parameter we are referring to the various cross sections and energy losses that are needed by the models. The MC and CSDA use a more extensive set than is used by the LT model. While what cross sections are used can have serious impact when comparing to observations, the critical point here is to have all three models use the same set. We chose to use the simpler LT set as described in *Basu et al.* [1993]. The one exception is that for the average energy of the ejected electron in the stripping process we use the same expression as is used for the ionization process. This was done simply as a convenience for making the comparison between the three models.

Finally let us turn to what we call the geophysical conditions, that is the neutral atmosphere and the incoming particle flux. The neutral atmospheric densities (N_2 , O_2 , and O) and the neutral temperature as a function of altitude are obtained from the mass spectrometer/incoherent scatter (MSIS-86) neutral atmosphere model [*Hedin*, 1987]. The MSIS-86 parameters used were an F10.7 and a 81 day averaged F10.7 value of 150, a daily A_p of 20, a geographic latitude of 65° north, a longitude of 35° east, a local

solar time of 24, and a date of December 16, 1993. All calculations have a boundary altitude at 700 km and an incident isotropic proton flux that has a Maxwellian energy distribution.

4. Results

Calculations were made using the models for a range of Maxwellian characteristic energies (1-20 keV) and an incident energy flux of $0.5 \text{ ergs cm}^{-2}\text{sec}^{-1}$. The results in all cases were similar so we will present detailed comparisons for just one case: a characteristic energy of 8 keV and a minimum energy of 500 eV. In Figures 1a-1f, we show the hemispherically averaged differential flux for the protons and H atoms at several selected altitudes. In this and in the following figures, the CSDA results are given by the dotted curves, the LT by the dashed curves and the MC by either squares or error bars. The statistical error in the MC results is either indicated by the error bars or is smaller than the size of the square symbols used in the plots. At 550 km, 150 km below the boundary altitude, we see that the proton energy distributions from all three models are in excellent agreement. Likewise the H atom plot shows excellent agreement, though the MC simulation is a bit "noisy" due to the lack of particles as the H atom flux builds up from a starting value of zero at the boundary. At 250 km (Fig. 1b) the agreement remains excellent between all three models. While the shape of the spectra are little changed, the H atom flux has continued to increase at the expense of the proton flux. Descending further to 152 km (Fig. 1c), we see that the low energy part of the spectra have filled in as particles cascade down from higher energies. The MC shows a little more noise at the lowest energies, but the agreement remains fairly good between all models. Dropping to lower altitudes, the low energy portion of the spectra continue to increase and with the three models still in reasonable agreement reach a maximum around 118 km (Fig. 1d). Though we do see a clear separation between the CSDA and LT results at lower energies. At 110 km (Fig. 1e), the magnitude of the

spectra at all energies have decreased and the CSDA and LT continue to show a clear separation. Finally just 4 km lower at 106 km (Fig. 1f), the CSDA and LT are showing larger differences and the error in the MC results have grown to the point that it is difficult to decide if it agrees more with the CSDA or the LT model.

Having considered the energy distribution of the fluxes averaged over pitch angle, let us now turn to plots (Figures 2a-2g) of the differential flux integrated over energy versus the cosine of the pitch angle. At 670 km (Fig. 2a), we see an isotropic proton flux with all three models in excellent agreement and a much smaller H atom flux that has had only 30 km to build up from zero flux at the boundary. The H atom flux is largest near 90° pitch angle where the protons have undergone the greatest number of collisions. Figures 2b and 2c illustrate the build up of the H atom flux at lower altitudes. At 550 km, we see the build up is still largest at pitch angles near 90°, though by 250 km the pitch angle distributions for both protons and H atoms are isotropic. Through this range of altitudes the models have remained in excellent agreement. At 250 km the MC proton result is low compared to the CSDA and LT for the pitch angle nearest to 90° ($\cosine = -.05$). This difference is apparently from a slight numerical oscillation in the altitude dependence of the MC results for this particular pitch angle. Down at 152 km (Fig. 2d), the fluxes remain isotropic and the models remain in good agreement except near 90° where significant fall off of the flux is observed. The CSDA shows the largest decrease followed by the LT and then the MC results. By 118 km (Fig. 2e), the results at pitch angles closer to 90° are showing large decreases in the fluxes as well as some separation between the models. On the other hand, nearer to 180°, the fluxes are still large and all three models remain in good agreement. As was seen earlier, when there is a significant reduction in the flux, it is the CSDA which shows the greatest decrease. At any particular pitch angle, the LT and MC models remain in reasonable agreement until the flux has decreased about three orders of magnitude from what it was at higher altitudes. At 110 km (Fig. 2f), some separation between models is occurring at all pitch

angles and by 106 km (Fig. 2g) both the CSDA and MC results are clearly falling below those of the LT model.

In Figures 3a and 3b, we show the energy integrated differential flux at one pitch angle ($\cosine = -.95$) as a function of altitude. As before, we see that all three models are in excellent agreement until they reach the lowest altitudes where the fluxes are severely attenuated. Similar plots for other pitch angles show the same trend with the altitude of severe flux attenuation moving higher as a pitch angle of 90° is approached. As seen above, at all pitch angles except one the LT model penetrates slightly deeper into the atmosphere than the CSDA and MC models. The one exception is the angle nearest 90° ($\cosine = -.05$) where the MC penetrates deeper than the CSDA and LT.

Given the excellent agreement between the differential fluxes, similar agreement is expected between various integrals over the fluxes. In Figure 4 we show the hemispherically averaged total flux from all three models and again see excellent agreement. Figures 5a and 5b show the energy deposition rates where the LT and CSDA models agree to within 5% and both generally fall within the MC errors. Again at the lowest altitudes (below the peak of the deposition) we see that the LT model penetrates slightly deeper (less than 1 km) into the atmosphere than does the CSDA or MC model. Finally in Figure 6, we show the eV/ion pair for various characteristic energies and see excellent agreement (within 1.5%) between all three models.

5. Discussion and Summary

We have shown that except at the lowest altitudes three models for proton-H atom transport are in excellent agreement. The differences between the models are generally smaller than the errors that can arise from poorly known cross sections and/or the errors typically quoted for geophysical observations. For example, the measured cross sections for proton/H atom collisions with N_2 and O_2 have quoted accuracies of typically $\pm 20 - 30\%$. For most collisions involving atomic oxygen, there are no measurements

and one resorts to "estimates" based on other cross sections. One exception is for charge changing collisions for which measurements have been made with quoted accuracies of 25%, but at present there are still factors of 2 disagreement between some of these measurements. Such uncertainties can lead to errors of comparable magnitude in the model results[*Decker et al.*, 1995]. Likewise, measurements of proton fluxes typically involve low count rates and instrumental errors in the 10 to 30% range. Optical measurements of proton auroras typically quote errors larger than 10%. Thus for the purposes of comparing to observations all three models are effectively identical. Further, the quality of the agreement between models gives us some confidence that there are no major errors in the three computer codes.

The one exception to the otherwise excellent agreement between the models is at the lowest altitudes,(see Figs. 1f, 2g, and 3b), where the proton and H atom fluxes are severely attenuated. While the differences between the models are apparent in all the altitude dependent quantities examined, their fundamental source is the differences between the differential fluxes. In Figures 2a-2g it is evident that the altitudes at which these differences occur depend on the pitch angle of the flux. However, if we consider the fluxes not as a function of altitude but rather as a function of a pitch angle dependent collision or scattering depth such as

$$\tau_P(z, E, \mu) = - \sum_{\alpha} \sigma_{\alpha, P}(E) \int_z^{z_b} \frac{dz'}{\mu} n_{\alpha}(z'), \quad (7)$$

we find that the differences between models occur at around the same collision depth essentially independent of the particular pitch angle. It is the dependence of the collision depth on the cosine of the pitch angle that causes the differences between models to appear at different altitudes for different pitch angles. We thus find that the model differences arising at low altitudes occur at large collision depths where the collisional mean free paths are small compared to the scale heights of the neutral constituents and the altitude step sizes that are typically used in transport calculations. One consequence

of this is that the algorithms designed to solve the transport problem often have difficulties at these altitudes and can be very sensitive to the details of their numerical implementation. For the LT model, we have found that it is particularly sensitive to the altitude grid used in this region. In our initial calculations of the energy integrated proton differential flux using a nonuniform grid of 77 altitudes, the LT results near a pitch angle of 180° and at 106 km were over a factor of 2 larger than the MC results. The calculations shown here (Fig. 2g and 3b) used 353 altitudes and the LT results are within 20% of the MC results. The general observed tendency was that when too few grid points were used the LT model penetrated deeper into the atmosphere than did the MC model and as the grid resolution was improved the LT model approached the MC model. Fortunately, these differences have little effect on such issues as where energy is deposited in the atmosphere or where the bulk of the ionization takes place. Likewise, predictions of the typical observables: particle fluxes, ion densities, ion and neutral temperatures, and optical emissions are little affected by these differences. Thus for most aeronomical purposes these differences deep in the atmosphere are of no consequence.

It is interesting that when the LT calculations were made with a grid of 77 altitudes, the particle and energy conservation was quite good. Over most altitudes, particle and energy conservation was better than 1% and at the lowest altitudes both particles and energy were conserved to within a few percent. When the calculations were made with 353 altitudes, the conservation properties were little changed. For example, at some lower altitudes the particle conservation was a little better by a couple of percent and at others a little worse by a couple of percent. However, if we examine the energy integrated differential flux near a pitch angle of 180° and at 106 km a modest change in particle conservation is accompanied by over an 80% change in the flux. This can be understood by recalling that what is normally done when testing the particle and energy conservation is to first sum the total number of particles and total energy coming

into the system at the top of the atmosphere. One then calculates at each altitude the total number of particles and total energy arriving at that altitude along with what has been lost from the system at all higher altitudes. In this way a check is made whether any particles or energy are lost or created due to the numerical methods being used. However, once the lowest altitudes have been reached and the fluxes are orders of magnitude below their original values most of the particles and energy have left the system. The number of particles that are left contribute very little to the total conservation and thus there can be significant errors in the fluxes yet no strong indication of this in the conservation tests. This implies that checking the overall particle and energy conservation is a necessary but not a sufficient test of the accuracy of a particle transport model. On the other hand, one can test particle and energy conservation at a particular altitude relative to an altitude that is fairly close. In that case, it is possible to get some measure of the quality of the solution even when most of the particles have left the system. For example, if we test particle conservation at a particular altitude relative to the altitude one grid point higher, we find for the LT calculation using 77 altitudes that near a pitch angle 180° between 109 and 104 km the conservation degrades from 1% to 26%. Thus we do have some indication that with this particular altitude grid there are problems with the solution of at the very low altitudes.

While the models have been brought into good agreement, we should note that differences can be seen between the models as they are used in different studies. This is perhaps most obvious when Monte Carlo runs are made that include mirroring and beam spreading. *Kozelov* [1993] has shown that these effects have an impact on the albedo, the charge fractions, and the energy deposition. Clearly if these effects are important for a particular study, neither the CSDA nor the present LT model will be appropriate. Further differences can arise between the models due to differences in the collisional processes, cross sections, and energy losses that are used. To obtain the level of agreement presented in this paper, we had to take great care in making sure that all

these factors were the same in all three models. In particular, we found that the eV/ion pair is very sensitive to any such differences. This is consistent with the discussions in *Edgar et al.*, [1973] and *Strickland et al.*, [1993] where it is pointed out that the shape of the eV/ion pair versus characteristic energy depends on the behavior of the cross sections and energy losses. For example, in Figure 6 we have included some additional calculations of the eV/ion pair. The symbol 'E' labels MC calculations that used the cross section set used for this study but also included energy loss due to elastic collisions and extended the minimum energy down to 100 eV. Here we see how including another channel for energy loss (momentum transfer in elastic scattering) leaves less energy available for ionization and hence acts to increase the eV/ion pair. The solid curve gives the results of MC calculations of Kozelov and Ivanov using their standard cross section set. Here the dramatic difference comes in large part from larger low energy excitation cross sections in the Kozelov and Ivanov cross section set. Again the effect is to raise the eV/ion pair at low energies as other collisional processes compete with ionization to degrade the energy of the protons and H atoms. The differences between cross section sets arise because of the lack of necessary cross section measurements and thus the need to make estimates and extrapolations in order to assemble a complete set. The focus of this paper has been on comparing three models and not the issue of what cross sections to use nor how well the models compare to observations. However the success of the comparisons does suggest that our ability to model actual observations is presently limited by uncertainties in cross sections and the lack of suitable observations rather than our ability to solve the equations that describe the known physics of proton/H atom transport.

Acknowledgments. The work by DTD was supported by Air Force contracts F19628-93-K-0001 with Boston College. The work by BB and JRJ at the Phillips Laboratory was supported by the Air Force Office of Scientific Research (AFOSR). The work of BVK and VEI was supported by the Russian Foundation of Fundamental Investigations (RFFI).

Appendix

The purpose of this appendix is to derive an implementation of the continuous slowing-down approximation (CSDA) from linear transport theory. We begin with the linear transport equations for protons(*P*) and hydrogen atoms(*H*) as given in *Basu et al.* [1990]

$$\begin{aligned} \left[\mu \frac{\partial}{\partial z} + \sum_{\alpha} n_{\alpha}(z) \sigma_{\alpha,P}(E) \right] \Phi_P(z, E, \mu) = \\ \sum_{\alpha} n_{\alpha}(z) \int dE' d\mu' \left[\sum_k \sigma_{\alpha,P}^k(E', \mu' \rightarrow E, \mu) \Phi_P(z, E', \mu') \right. \\ \left. + \sigma_{\alpha}^{01}(E', \mu' \rightarrow E, \mu) \Phi_H(z, E', \mu') \right] \end{aligned} \quad (A1)$$

$$\begin{aligned} \left[\mu \frac{\partial}{\partial z} + \sum_{\alpha} n_{\alpha}(z) \sigma_{\alpha,H}(E) \right] \Phi_H(z, E, \mu) = \\ \sum_{\alpha} n_{\alpha}(z) \int dE' d\mu' \left[\sum_k \sigma_{\alpha,H}^k(E', \mu' \rightarrow E, \mu) \Phi_H(z, E', \mu') \right. \\ \left. + \sigma_{\alpha}^{10}(E', \mu' \rightarrow E, \mu) \Phi_P(z, E', \mu') \right] \end{aligned} \quad (A2)$$

where $\Phi_{\beta}(z, E, \mu)$ is the differential flux of particles (in units of $cm^{-2}s^{-1}eV^{-1}sr^{-1}$) of type $\beta(=P, H)$ as a function of altitude(*z*), energy(*E*), and cosine of the angle between the particle velocity and the *z* axis (μ); the *z* axis is antiparallel (parallel) to the geomagnetic field line in the northern (southern) hemisphere; and n_{α} is the concentration of the neutral species α . The cross sections for the various collisional processes are $\sigma_{\alpha,\beta}^j(E)$ (in units of cm^{-2}) where *j* ($=k, 10, 01$) labels the type of collision. The index *k* refers only to excitation and ionization type collisions and 10 and 01 refer to charge exchange and stripping collisions respectively. The total cross section summed over types of collisions is given by $\sigma_{\alpha,\beta}(E)$. For the differential cross sections, we make the forward-scattering approximation to the angular dependence and assume

$$\sigma_{\alpha,\beta}^j(E', \mu' \rightarrow E, \mu) = \sigma_{\alpha,\beta}^j(E') \delta(E' - W_{\alpha,\beta}^j(E') - E) \delta(\mu' - \mu) \quad (A3)$$

where E' is the incident particle energy, E is the final energy, and $W_{\alpha,\beta}^j(E)$ is the energy loss associated with collision type *j*.

Our first step in developing a CSDA implementation is to break the calculation into two pieces. On the one hand, we calculate the relative charge state composition of the flux by

neglecting energy loss and only considering the conversion of protons into H atoms and H atoms back into protons. This is done by setting $W_{\alpha,\beta}^j(E) = 0$ and using (A3) in performing the μ' and E' integrations to obtain

$$\left[\mu \frac{\partial}{\partial z} + \sum_{\alpha} n_{\alpha}(z) \sigma_{\alpha}^{10}(E) \right] \Phi_P(z, E, \mu) = \sum_{\alpha} n_{\alpha}(z) \sigma_{\alpha}^{01}(E) \Phi_H(z, E, \mu) \quad (\text{A4})$$

$$\left[\mu \frac{\partial}{\partial z} + \sum_{\alpha} n_{\alpha}(z) \sigma_{\alpha}^{01}(E) \right] \Phi_H(z, E, \mu) = \sum_{\alpha} n_{\alpha}(z) \sigma_{\alpha}^{10}(E) \Phi_P(z, E, \mu) \quad (\text{A5})$$

which are (in a slightly different form) equations (4) and (5) that are used in calculating the charge state composition of the flux. These equations are identical to equations (17) and (18) in *Basu et al.* [1990] and were originally derived for use at high altitudes. While the particle fluxes that are predicted from these equations are reasonable only for high altitudes, it was found that the calculated flux fractions are accurate at all altitudes.

On the other hand, we also need a method to calculate the effects of energy degradation on the fluxes. This is done by assuming the flux fractions are known and calculating an "average" energy loss for protons and H atoms together. To develop the needed equation, we multiply (A1) and (A2) by E , integrate over μ and E , and add the resulting equations to obtain

$$\begin{aligned} \frac{\partial}{\partial z} \int dE d\mu \mu E \Phi_T(z, E, \mu) = \\ - \sum_{\alpha} n_{\alpha}(z) \int dE d\mu \left[L_{\alpha,P}(E) f_P(z, E, \mu) + L_{\alpha,H}(E) f_H(z, E, \mu) \right] \Phi_T(z, E, \mu) \end{aligned} \quad (\text{A6})$$

where $\Phi_T = \Phi_P + \Phi_H$, $f_{\beta} = \Phi_{\beta}/\Phi_T$, and

$$L_{\alpha,\beta}(E) = \sum_j W_{\alpha,\beta}^j(E) \sigma_{\alpha,\beta}^j(E). \quad (\text{A7})$$

Note that these are the loss functions given in section 2 as equations (2) and (3). At this point, we make the continuous slowing-down approximation. That is we assume that the energy of a particle is a continuous function of altitude, $E(z)$. This means that the stochastic nature of the collisional degradation of the protons and H atoms is neglected and all particles starting with the same energy will lose the same amount of energy as they pass through the same range of altitudes. Thus if we divide Φ_T into mono-energetic, mono-directional streams at the top of the atmosphere, they will maintain their independent identity as they penetrate down through

the atmosphere. Thus the CSDA allows us to write Φ_T in the following form,

$$\Phi_T(z, E, \mu) = \sum_S I_S(z) \delta(E - E_S) \delta(\mu - \mu_S). \quad (\text{A8})$$

For each stream, denoted by S we can use (A8) in evaluating (A6) giving

$$\begin{aligned} \frac{\partial}{\partial z} \left[\mu_S E_S I_S(z) \right] = \\ - \sum_{\alpha} n_{\alpha}(z) I_S(z) \left[L_{\alpha,P}(E_S) f_P(z, E_S, \mu_S) + L_{\alpha,H}(E_S) f_H(z, E_S, \mu_S) \right] \end{aligned} \quad (\text{A9})$$

We next return to (A1) and (A2), integrate over μ and E , add the resulting equations and obtain the statement of particle conservation that follows from the transport equations, namely,

$$\frac{\partial}{\partial z} \int dE d\mu \mu \Phi_T(z, e, \mu) = 0. \quad (\text{A10})$$

This gives for each stream,

$$\frac{\partial}{\partial z} \left[\mu_S I_S(z) \right] = 0. \quad (\text{A11})$$

Combining (A9) and (A11) gives

$$\frac{dE_S}{dz} = - \frac{1}{\mu_S} \sum_{\alpha} n_{\alpha}(z) \left[L_{\alpha,P}(E_S) f_P(z, E_S, \mu_S) + L_{\alpha,H}(E_S) f_H(z, E_S, \mu_S) \right] \quad (\text{A12})$$

which in section 2 is given as equation 1. This then gives us an ordinary differential equation to solve for the energy (E) as a function of altitude (z).

In the implementation used in this paper, we begin with a flux of downgoing protons at some boundary altitude. As mentioned, the energy and pitch angle distribution of the protons is represented by a set of mono-energetic, mono-directional protons stream. The atmosphere is divided into a series of horizontal layers and equations (A4), (A5), and (A12) are applied to each stream. The equations are integrated from altitude to altitude using an explicit Euler method with (A4) and (A5) being solved assuming the energy of the stream is unchanged within a layer and (A12) being solved assuming the flux fractions are unchanged within a layer. At each succeeding altitude, the flux fractions and stream energy are updated for use in integrating down to the next altitude. In this way, the energy degradation and changing composition of each stream are calculated as the protons and H atoms penetrate down from the top of the atmosphere.

References

- Basu, B., J.R. Jasperse and N.J. Grossbard, A numerical solution of the coupled proton-H atom transport equations for the proton aurora, *J. Geophys. Res.*, **95**, 19069, 1990.
- Basu, B., J.R. Jasperse, R.M. Robinson, R.R. Vondrak and D.S. Evans, Linear transport theory of auroral proton precipitation. A comparison with observations, *J. Geophys. Res.*, **92**, 5920, 1987.
- Basu, B., J.R. Jasperse, D.J. Strickland and R.E.Jr. Daniell, Transport-theoretic model for the electron-proton-hydrogen atom aurora. 1. theory, *J. Geophys. Res.*, **98**, 21517, 1993.
- Davidson, G.T., Expected spatial distribution of low-energy proton precipitated in the auroral zones, *J. Geophys. Res.*, **70**, 1061, 1965.
- Decker, D. T., B. Basu, J. R. Jasperse, D. J. Strickland, J. R. Sharber, and J. D. Winningham, Upgoing electrons produced in an electron-proton- hydrogen atom aurora, *J. Geophys. Res.*, **100**, 21409, 1995.
- Eather, R.H., Auroral proton precipitation and hydrogen emissions, *Rev. Geophys.*, **5**, 207, 1967.
- Eather, R.H., Ionization produced by auroral proton precipitation, *Ann. Geophysic.*, **26**, 609, 1970.
- Eather, R.H. and K.M. Burrows, Excitation and ionization by auroral protons, *Aust. J. Phys.*, **19**, 309, 1966.
- Edgar, B.C., W.T. Miles and A.E.S. Green, Energy deposition of protons in molecular nitrogen and applications to proton auroral phenomena, *J. Geophys. Res.*, **78**, 6595, 1973.
- Edgar, B.C., H.S. Porter and A.E.S. Green, Proton energy deposition in molecular and atomic oxygen and applications to the polar cap, *Planet. Space Sci.*, **23**, 787, 1975.
- Galperin, Yu.I., Hydrogen emission and two types of auroral spectra, *Planet. Space Sci.*, **1**, 57, 1959.
- Galperin, Yu.I., R.A. Kovrazhkin, Yu.N. Ponomarev, J. Crasnier and J.A. Sadaud, Pitch angle distributions of auroral protons, *Ann. Geophysic.*, **32**, 109, 1976.
- Hardy, D.A., M.S. Gussenhoven and D. Brautigam, A statistical model of auroral ion

- precipitation, *J. Geophys. Res.*, **94**, 370, 1989.
- Hardy, D.A., M.S. Gussenhoven, R. Raistrick and W.J. McNeil, Statistical and functional representations of the pattern of auroral energy flux, number flux, and conductivity, *J. Geophys. Res.*, **92**, 12275, 1987.
- Hardy, D.A., W.J. McNeil, M.S. Gussenhoven and D. Brautigam, A statistical model of auroral ion precipitation, 2. Functional representation of the average patterns, *J. Geophys. Res.*, **96**, 5539, 1991.
- Henriksen, K., Variations of proton energy and pitch angle spectra in the upper atmosphere, *J. Atmos. Terr. Phys.*, **41**, 633, 1979.
- Hildebrand, F. B., *Advanced Calculus for Applications*, 2nd ed., 733pp., Prentice-Hall, Englewood Cliffs, New Jersey, 1976.
- Iglesias, G.E. and R.R. Vondrak, Atmospheric spreading of protons in auroral arcs, *J. Geophys. Res.*, **79**, 280, 1974.
- Isaev, S.I. and Pudovkin, M.I. *Aurora and the processes in the Earth's magnetosphere*, Nauka, Moscow, 1972.
- Jasperse, J.R. and B. Basu, Transport theoretic solutions for auroral proton and H atom fluxes and related quantities, *J. Geophys. Res.*, **81**, 811, 1982.
- Johnstone, A.D., The spreading of a proton beam by the atmosphere, *Planet. Space Sci.*, **20**, 292, 1972.
- Kozelov, B.V., Monte Carlo calculation of proton-hydrogen atom transport in N_2 , *Planet. Space Sci.*, **11**, 1503, 1992.
- Kozelov, B.V., Influence of the dipolar magnetic field on transport of proton-H atom fluxes in the atmosphere, *Ann. Geophysic.*, **11**, 697, 1993.
- Kozelov, B.V. and V.E. Ivanov, Effective energy loss per electron-ion pair in proton aurora, *Ann. Geophysic.*, **12**, 1071, 1994.
- Ponomarev, Yu.N., Intrusion of the monoenergetic monodirectional beams of protons into the polar high atmosphere, *Kosmicheskie issledovaniya (in Russian)*, **14**, 144, 1976.
- Porter, H.S. and A.E.S. Green, Comparison of Monte Carlo and continuous slowing-down approximation treatments of 1-keV proton energy deposition on N_2 , *J. Appl. Phys.*, **46**,

5030, 1975.

Rees, M.H., On the interaction of auroral protons with the earth's atmosphere, *Planet. Space Sci.*, 30, 463, 1982.

Romick, G.J. and C.T. Elvey, Variations in the intensity of the hydrogen emission line H β during auroral activity, *J. Atmos. Terr. Phys.*, 12, 283, 1958.

Sharber, J.R. The continuous (diffuse) aurora and auroral-E ionization. in *Physics of Space Plasmas*, vol.4, edited by T.S.Chang, B.Coppi and J.R.Jasperse, p.115, Scientific Publishers, Cambridge, Mass., 1981,

Figure Captions

Fig. 1a. Hemispherically averaged proton (left panel) and hydrogen atom (right panel) fluxes versus energy at an altitude of 550 km. The error bars are the Monte Carlo results, the long dashes are the linear transport results, and the dotted curves are the results from the continuous slowing down approximation. The incident proton flux is a Maxwellian with a characteristic energy of 8 keV and a total incident energy flux of $.5 \text{ ergs cm}^{-2} \text{ sec}^{-1}$.

Fig. 1b. Same as Figure 1a for an altitude of 250 km.

Fig. 1c. Same as Figure 1a for an altitude of 152 km.

Fig. 1d. Same as Figure 1a for an altitude of 118 km.

Fig. 1e. Same as Figure 1a for an altitude of 110 km.

Fig. 1f. Same as Figure 1a for an altitude of 106 km.

Fig. 2a. The differential flux integrated over energy versus the cosine of the pitch angle for protons (left panel) and hydrogen atoms (right panel) at an altitude of 670 km. The error bars are the Monte Carlo results, the long dashes are the linear transport results, and the dotted curves are the results from the continuous slowing down approximation. The incident proton flux is a Maxwellian with a characteristic energy of 8 keV and a total incident energy flux of $.5 \text{ ergs cm}^{-2} \text{ sec}^{-1}$.

Fig. 2b. Same as Figure 2a for an altitude of 550 km.

Fig. 2c. Same as Figure 2a for an altitude of 250 km.

Fig. 2d. Same as Figure 2a for an altitude of 152 km.

Fig. 2e. Same as Figure 2a for an altitude of 118 km.

Fig. 2f. Same as Figure 2a for an altitude of 110 km.

Fig. 2g. Same as Figure 2a for an altitude of 106 km.

Fig. 3a. The differential flux integrated over energy versus altitude for protons (H^+) and hydrogen atoms (H) at a pitch angle of 161.8° ($\cosine = -.95$). The error bars are the Monte Carlo results, the long dashes are the linear transport results, and the dotted curves are the results from the continuous slowing down approximation. The incident proton flux is a Maxwellian with a characteristic energy of 8 keV and a total incident energy flux of $.5 \text{ ergs cm}^{-2} \text{ sec}^{-1}$.

Fig. 3b. Same as Figure 3a with expanded scale at lower altitudes.

Fig. 4. Hemispherically averaged total flux versus altitude for protons (H^+) and hydrogen atoms (H). The incident proton flux is a Maxwellian with a characteristic energy of 8 keV and a total incident energy flux of $.5 \text{ ergs cm}^{-2} \text{ sec}^{-1}$.

Fig. 5a. Energy deposition rate versus altitude. The boxes are the Monte Carlo results, the long dashes are the linear transport results, and the dotted curves are the results from the continuous slowing down approximation. The incident proton flux is a Maxwellian with a characteristic energy of 8 keV and a total incident energy flux of $.5 \text{ ergs cm}^{-2} \text{ sec}^{-1}$.

Fig. 5b. Same as Figure 5a with expanded scale at lower altitudes.

Fig. 6. The quantity 'eV per electron-ion pair' versus characteristic energy of incident protons given by Maxwellian distributions. The boxes are the Monte Carlo results, the 'pluses' are the linear transport results, the 'X's are the results from the continuous slowing down approximation, the 'E's are results from Monte Carlo calculations that include momentum transfer in elastic collisions and have a minimum energy of 100 eV. The solid curve shows results from Monte Carlo calculations that used the original cross section set of Kozelov and Ivanov.

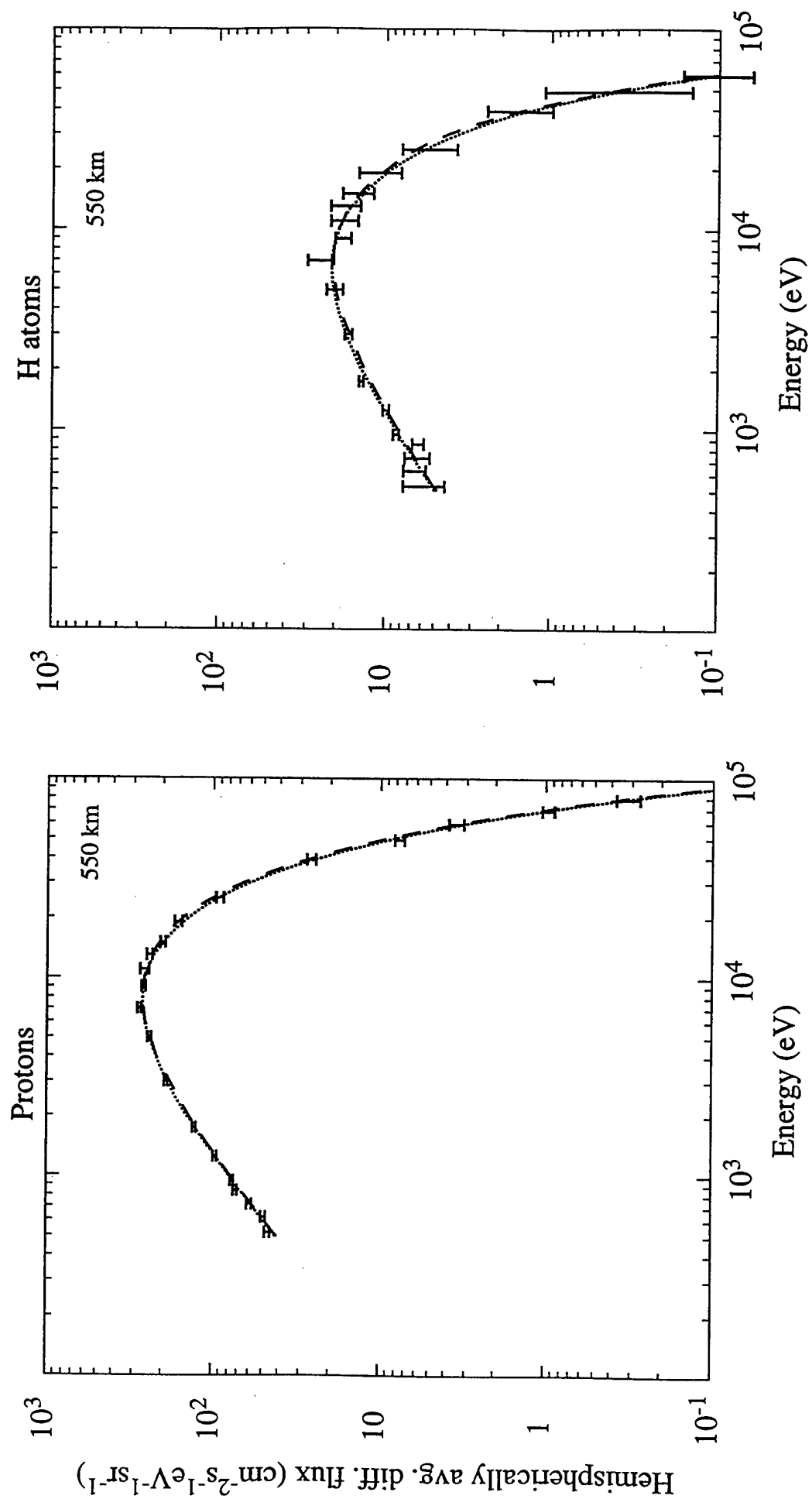


FIGURE 1a

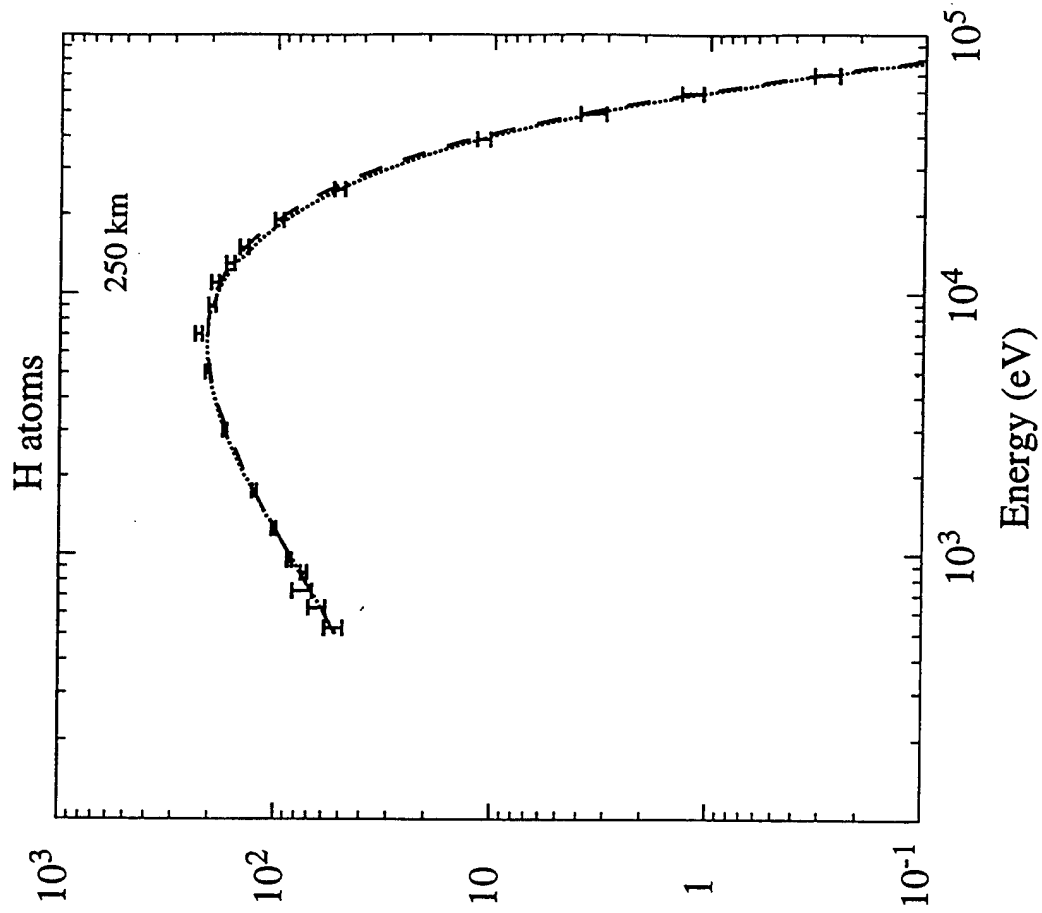
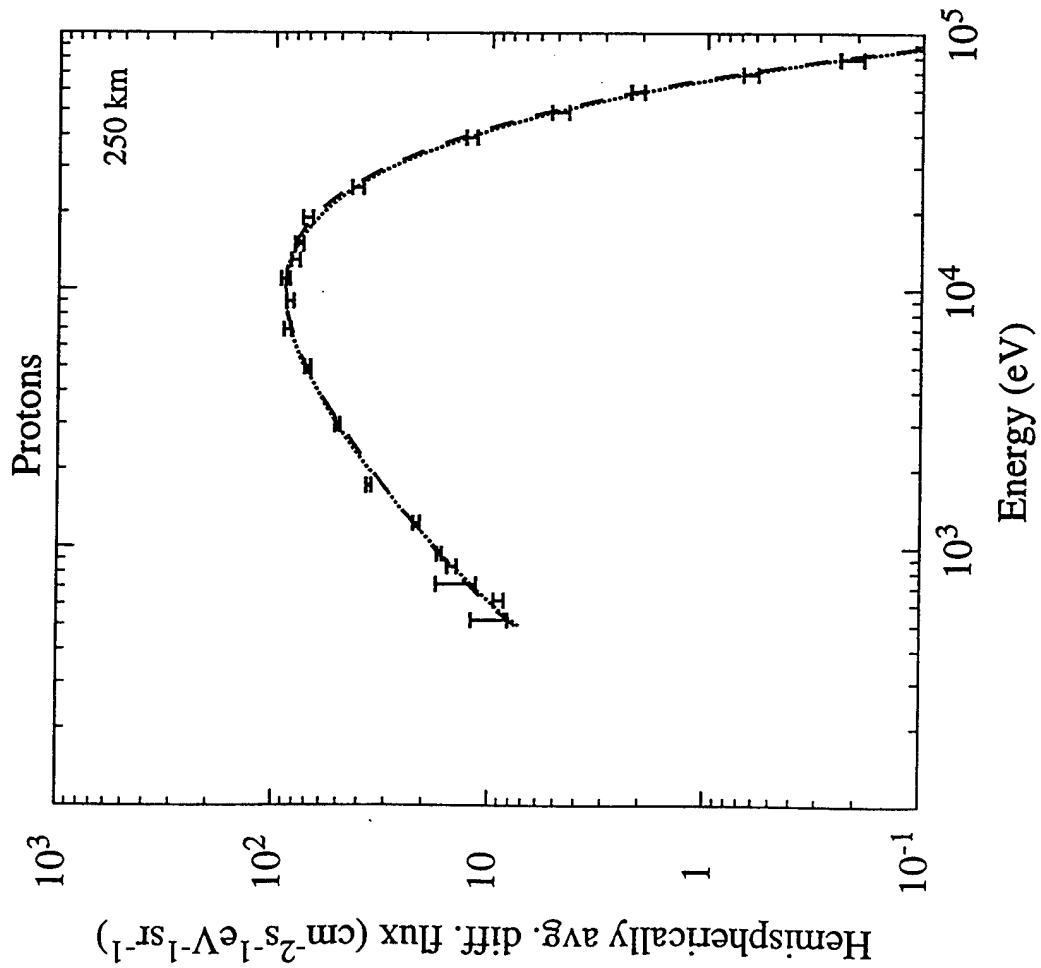


FIGURE 1b

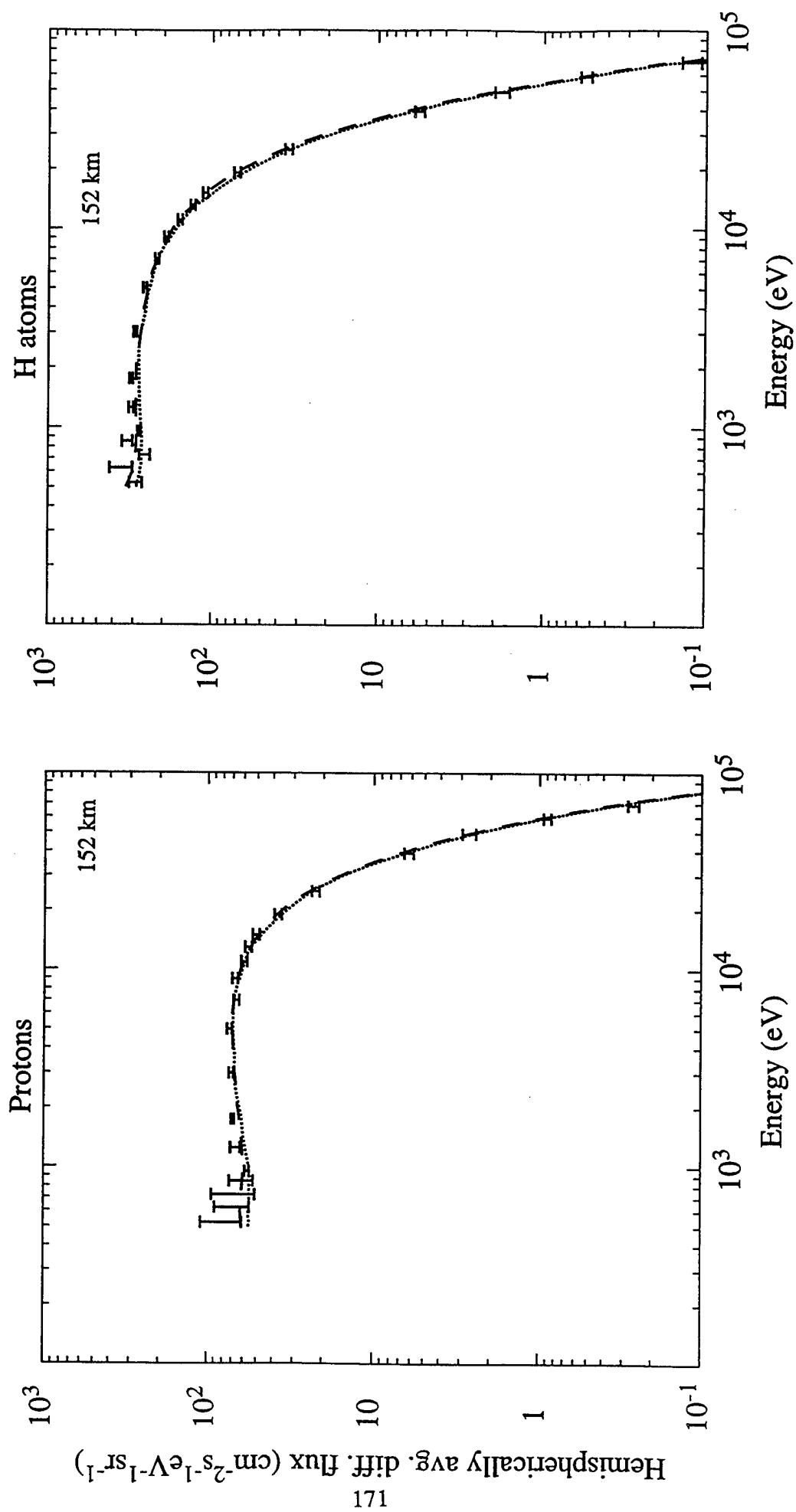


FIGURE 1c

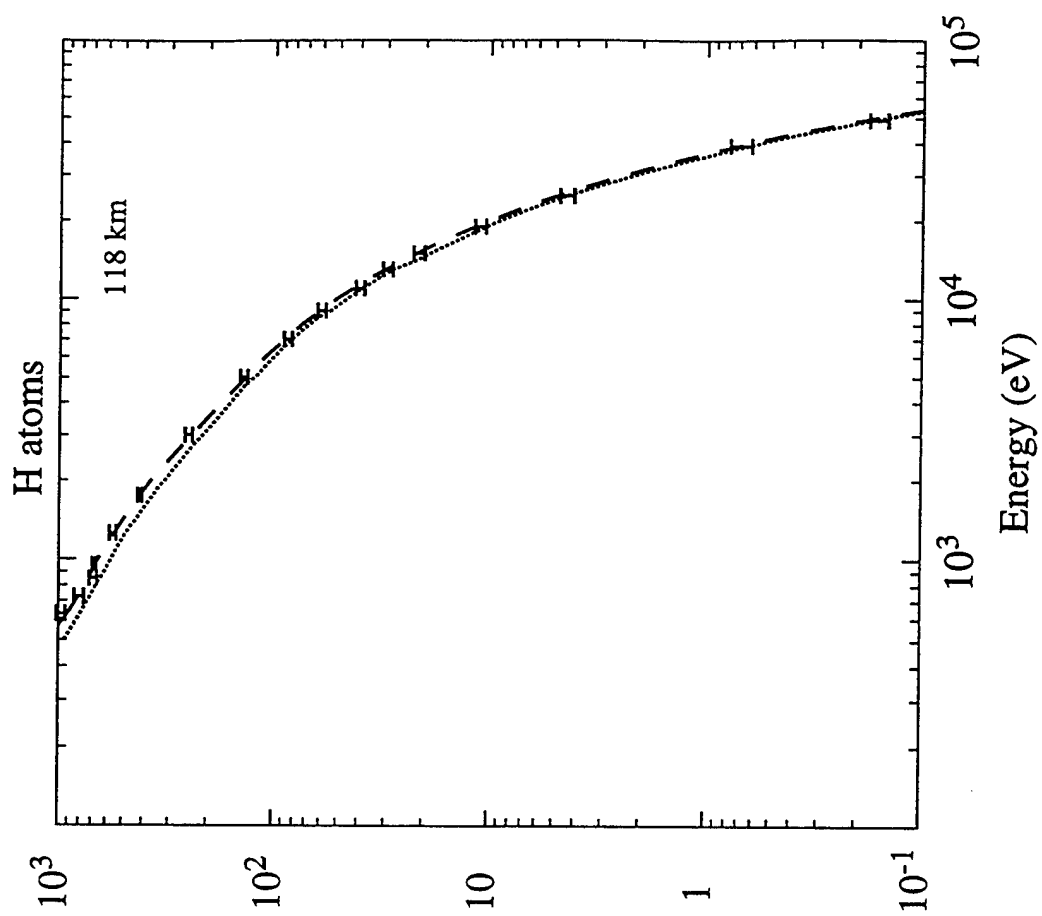
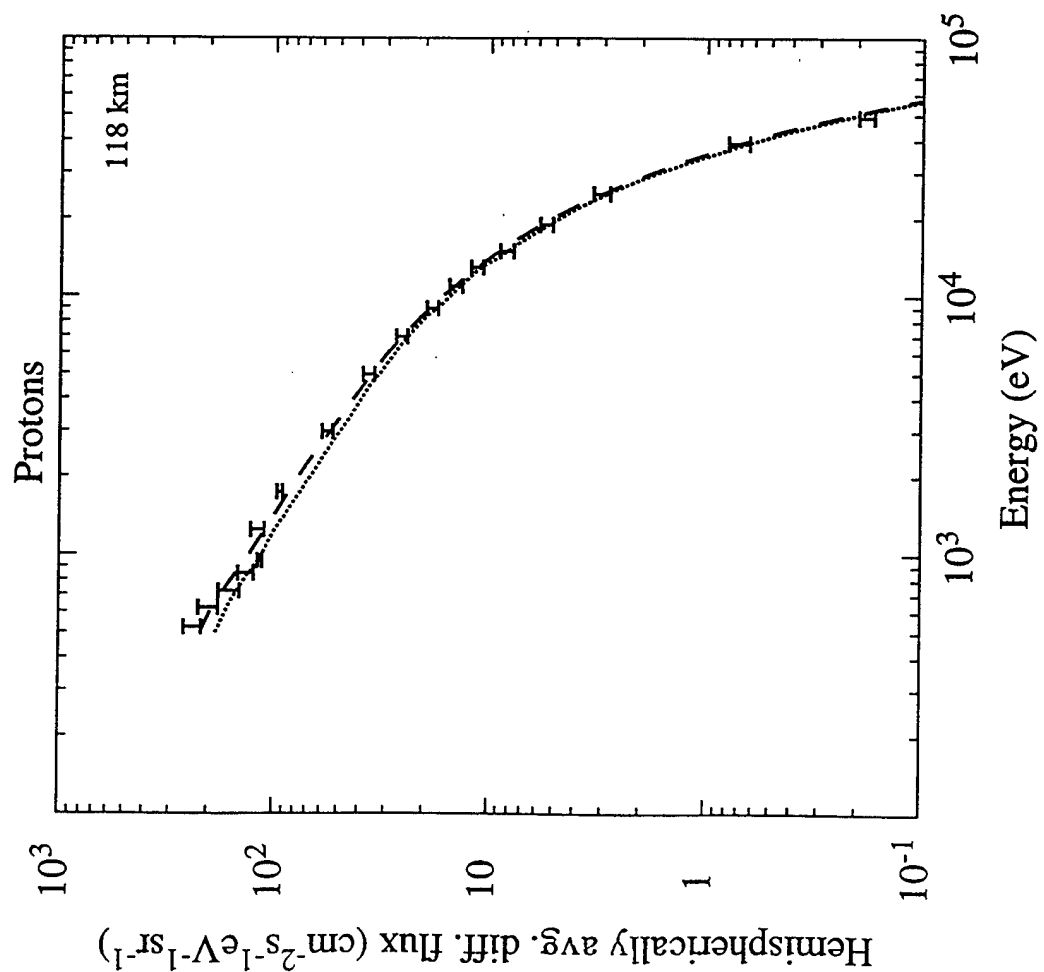


FIGURE 1d

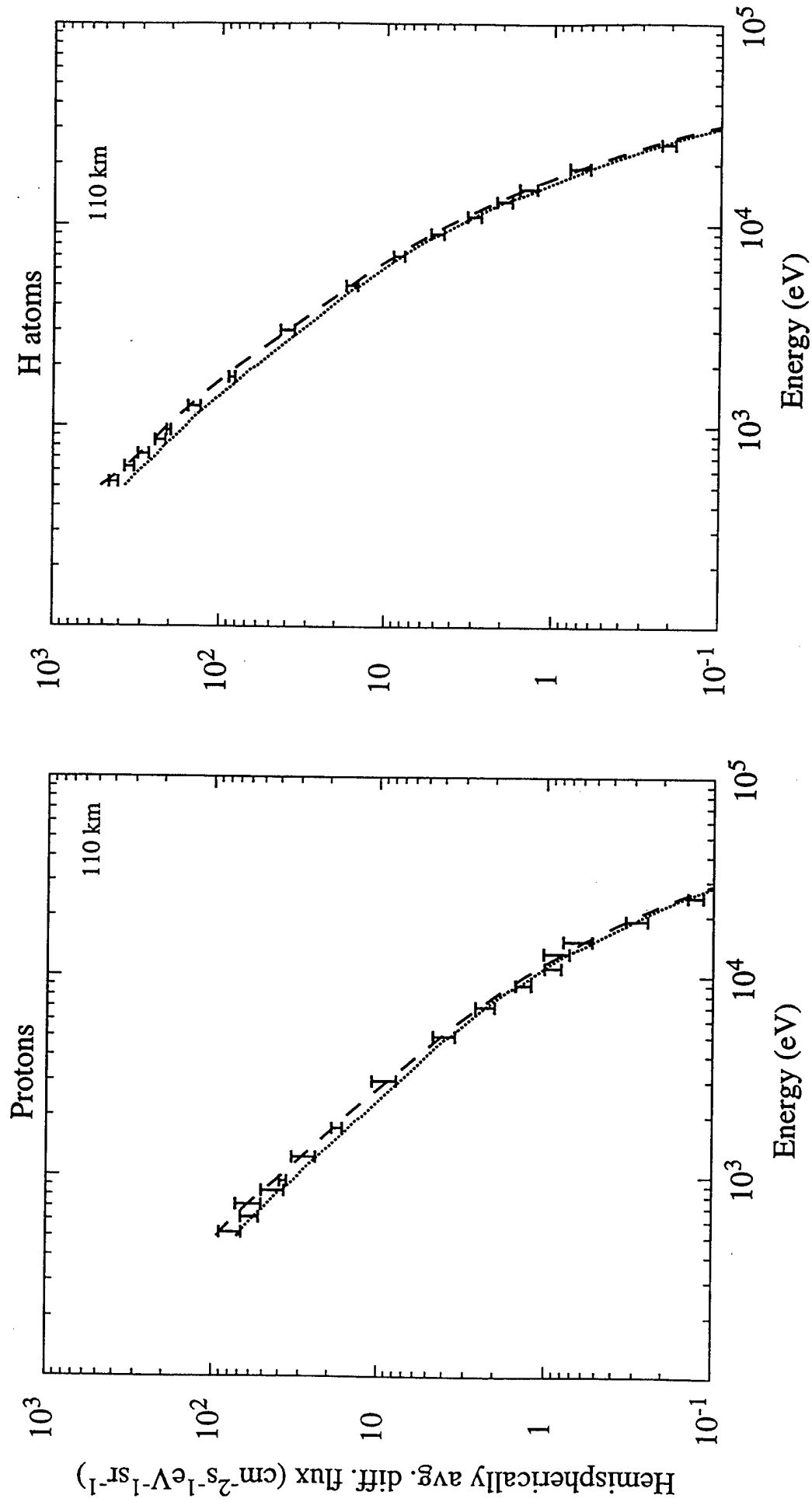


FIGURE 1e

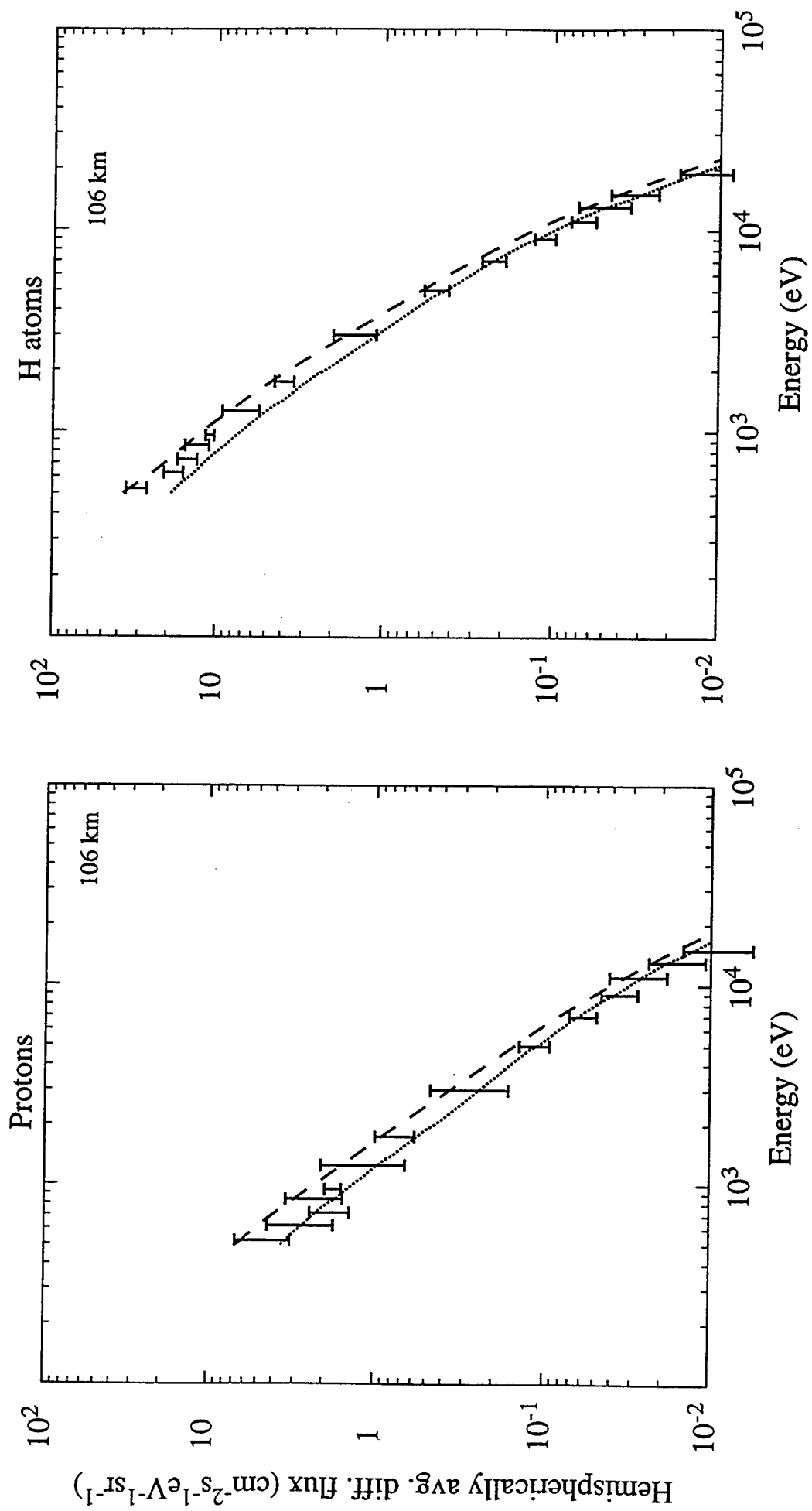


FIGURE 1f

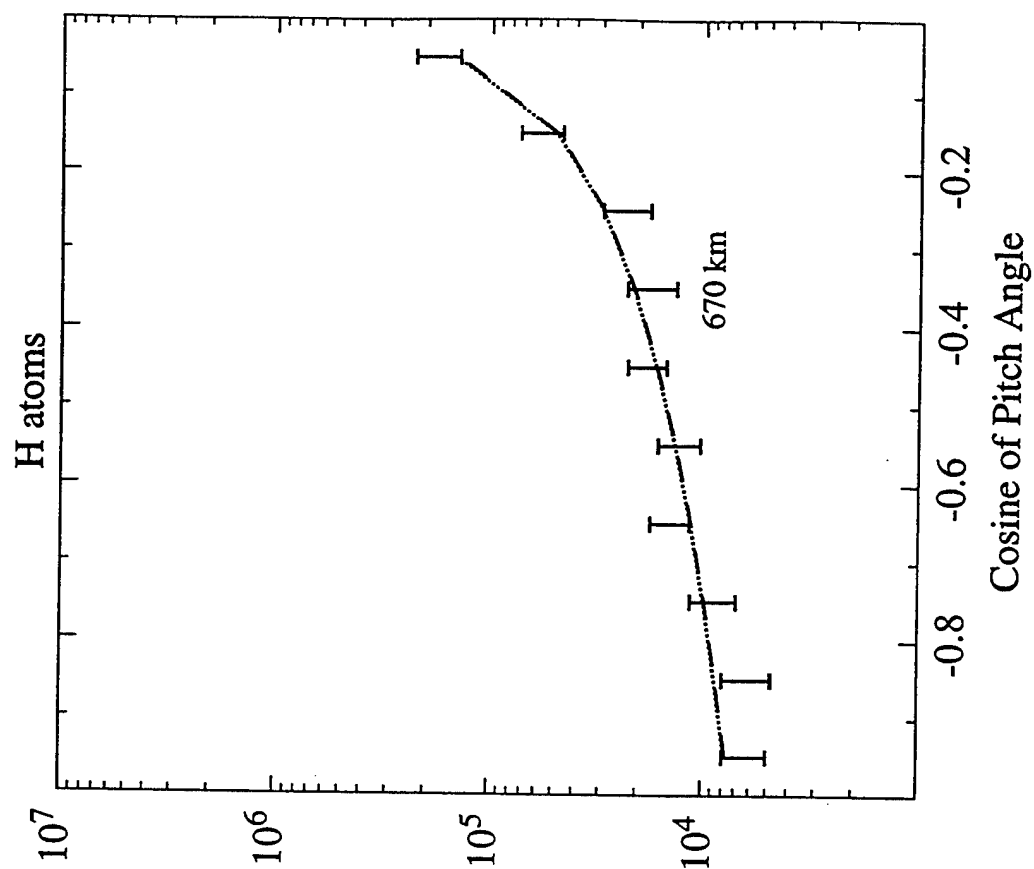
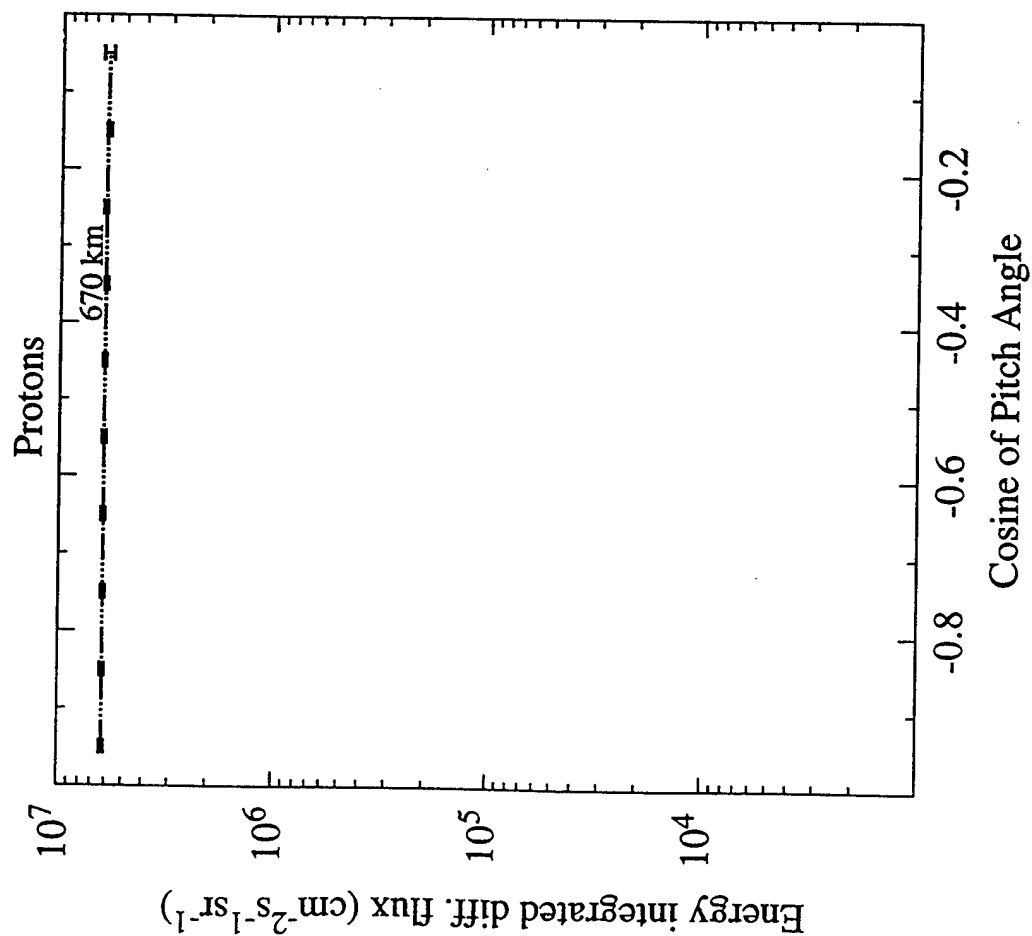


FIGURE 2a

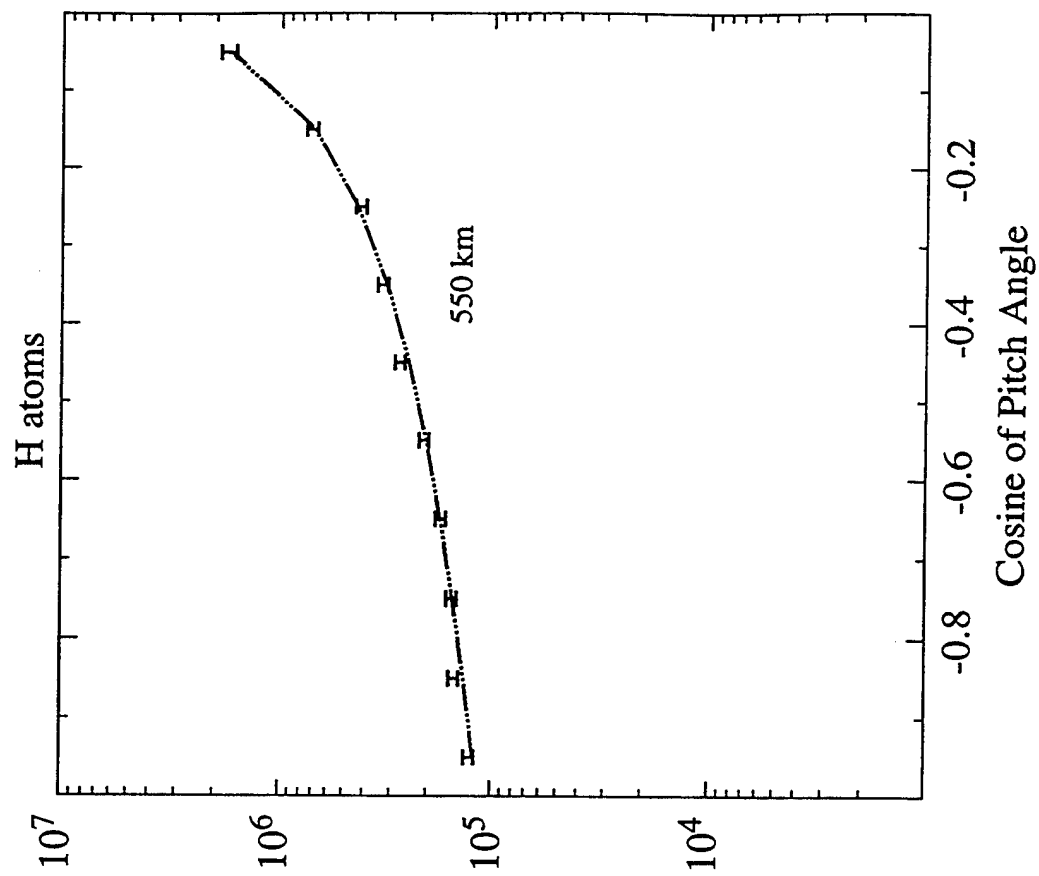
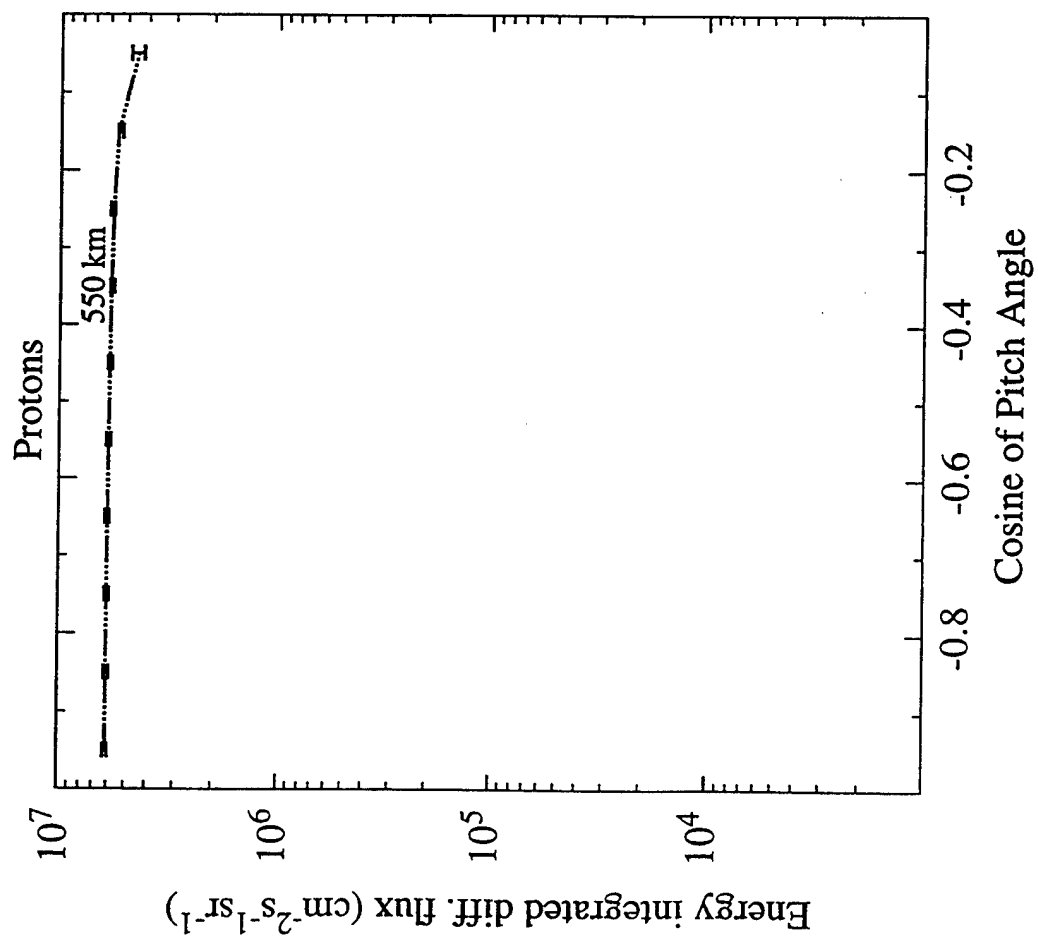


FIGURE 2b

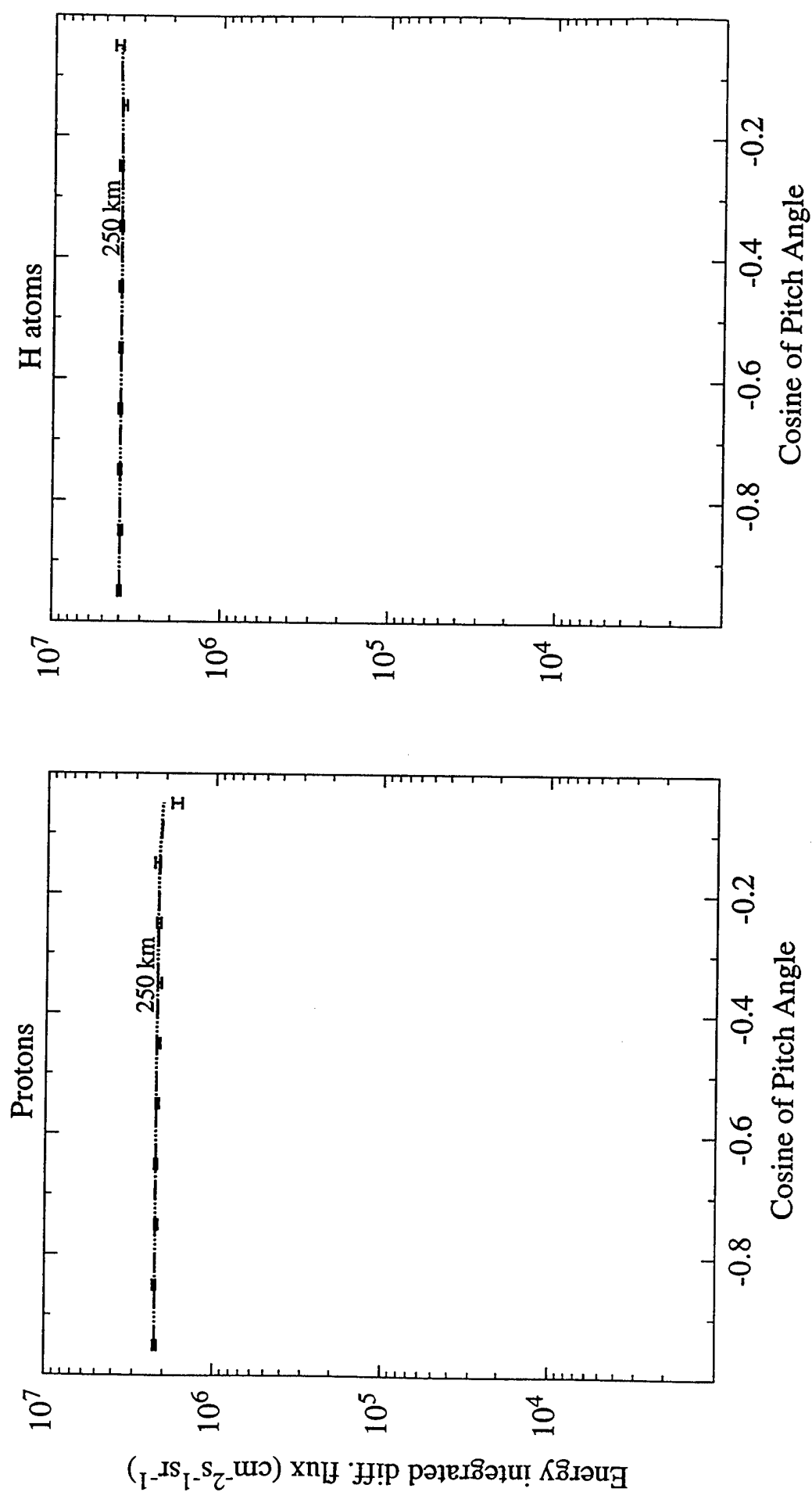


FIGURE 2c

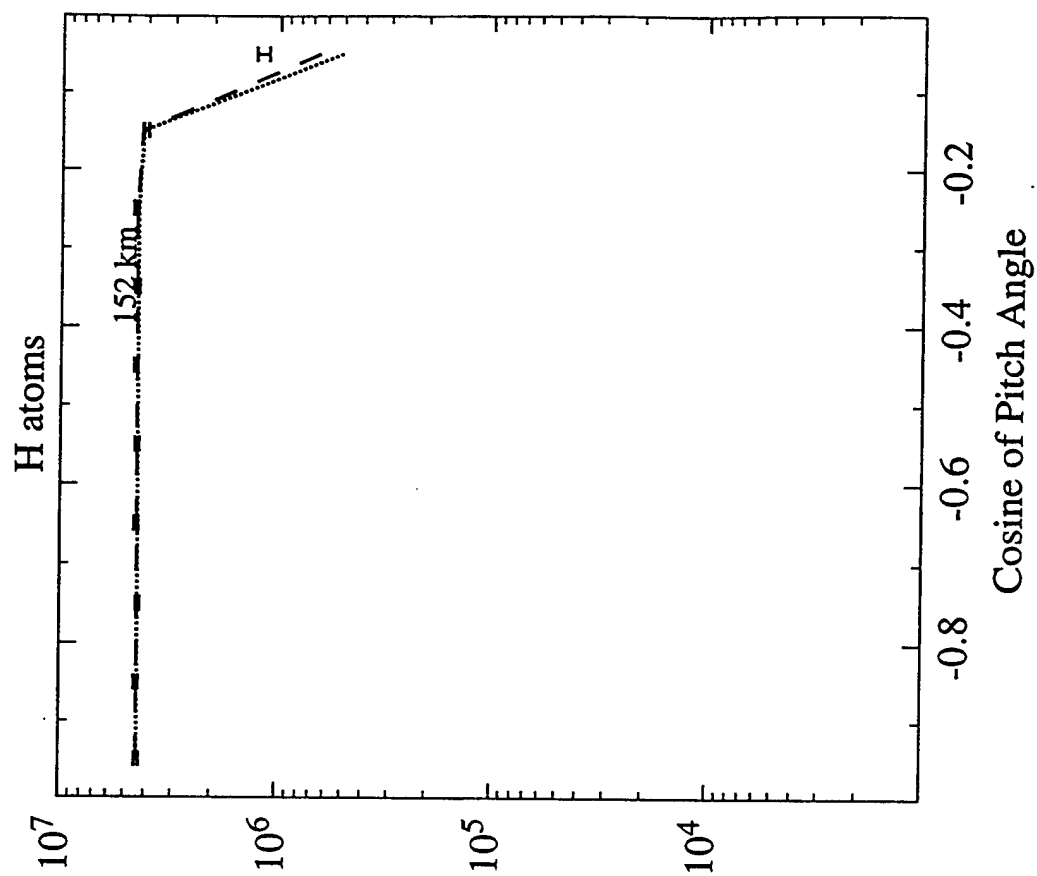
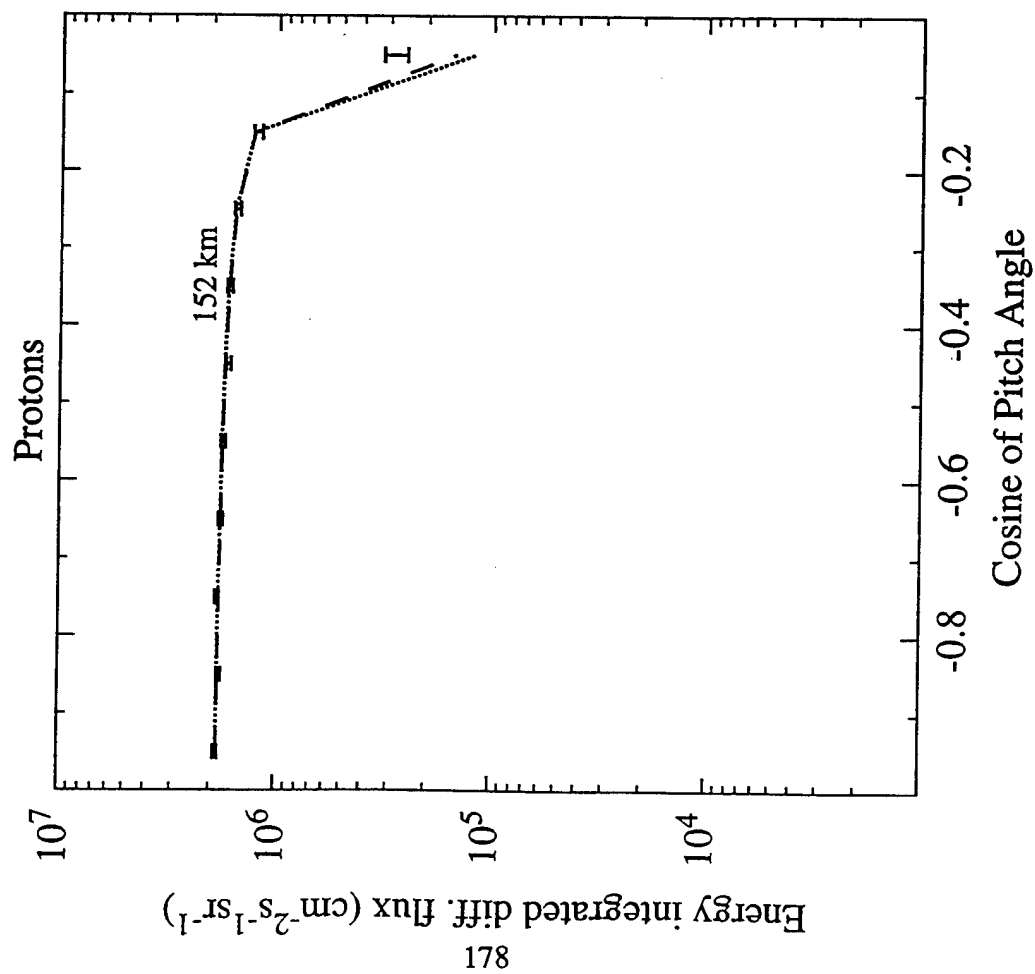


FIGURE 2d

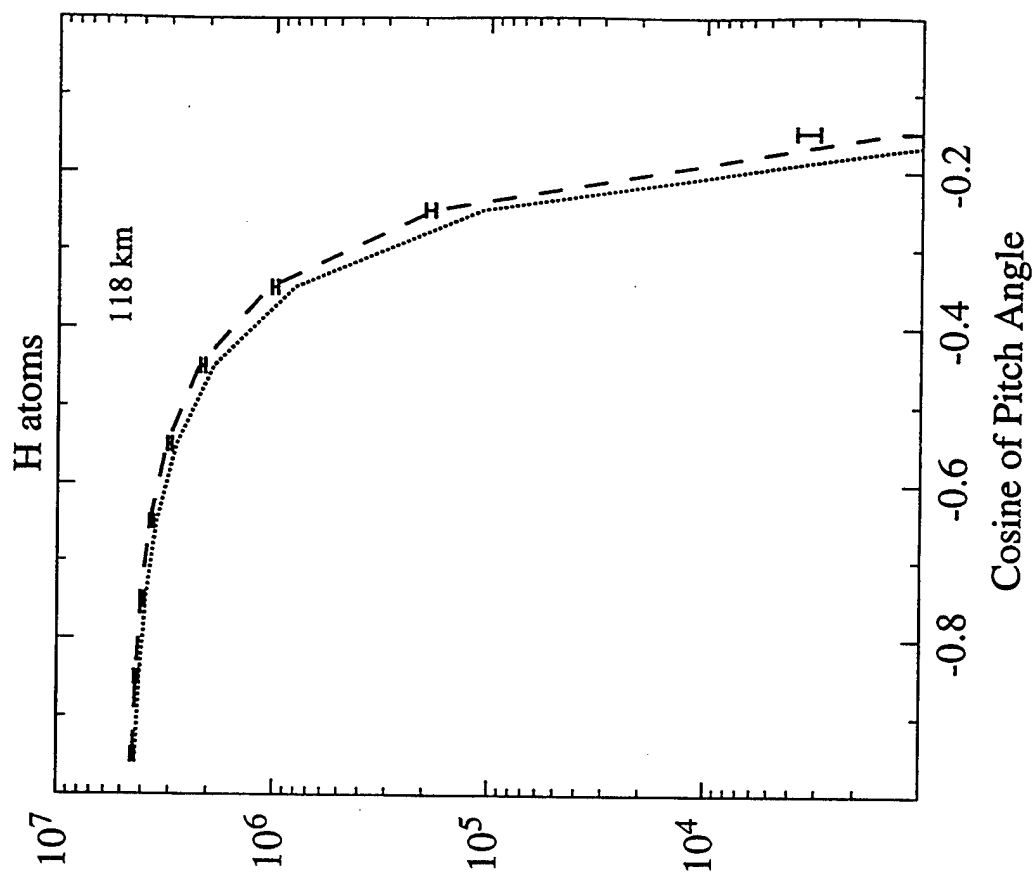
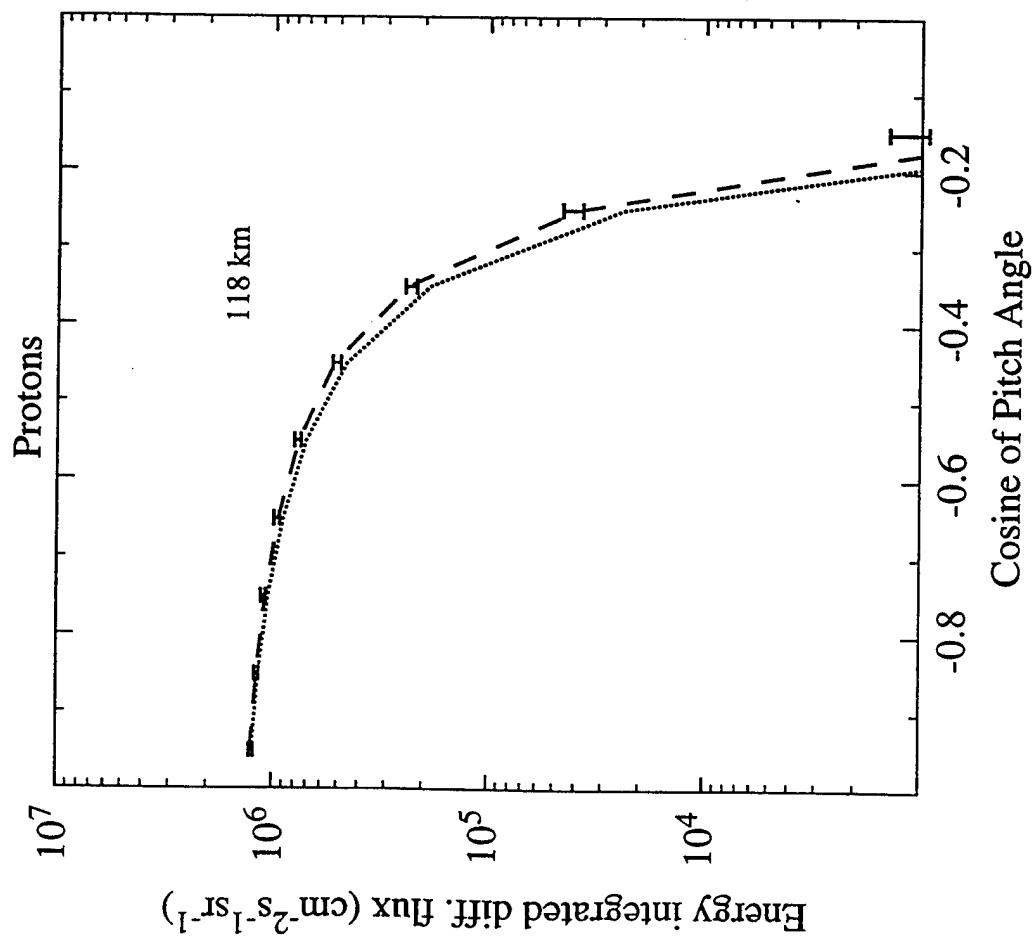


FIGURE 2e

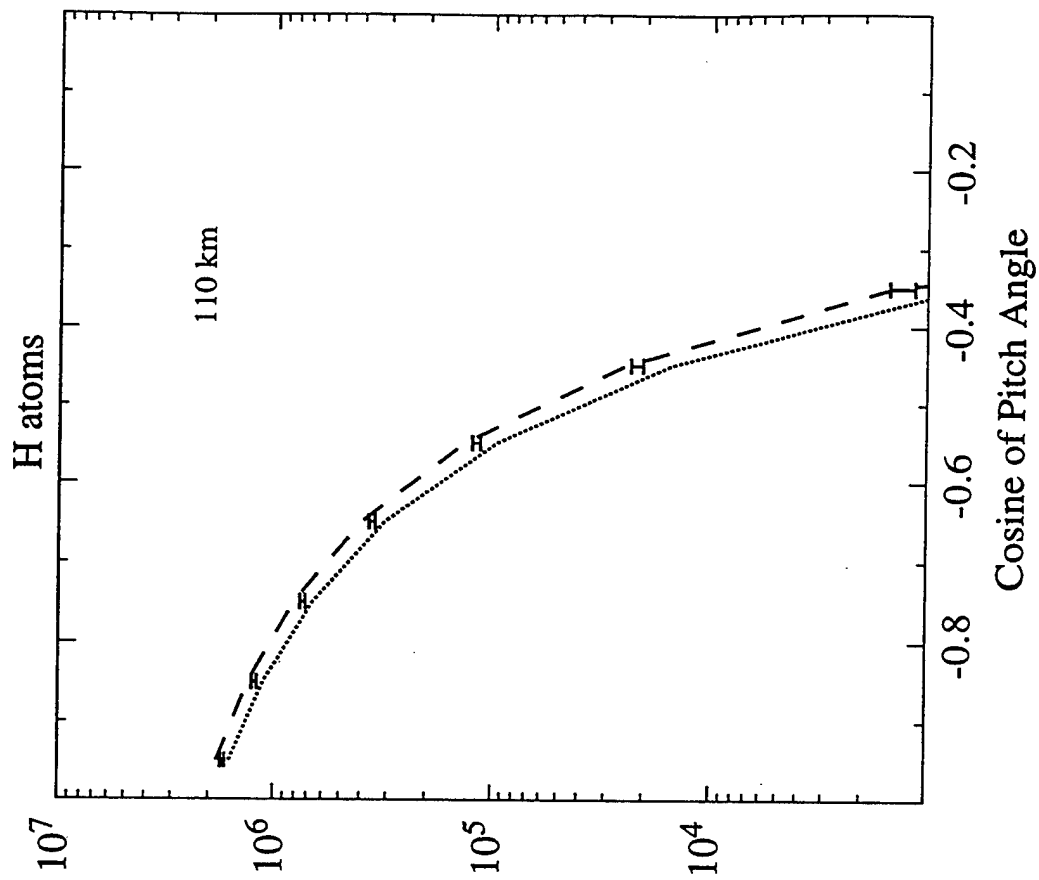
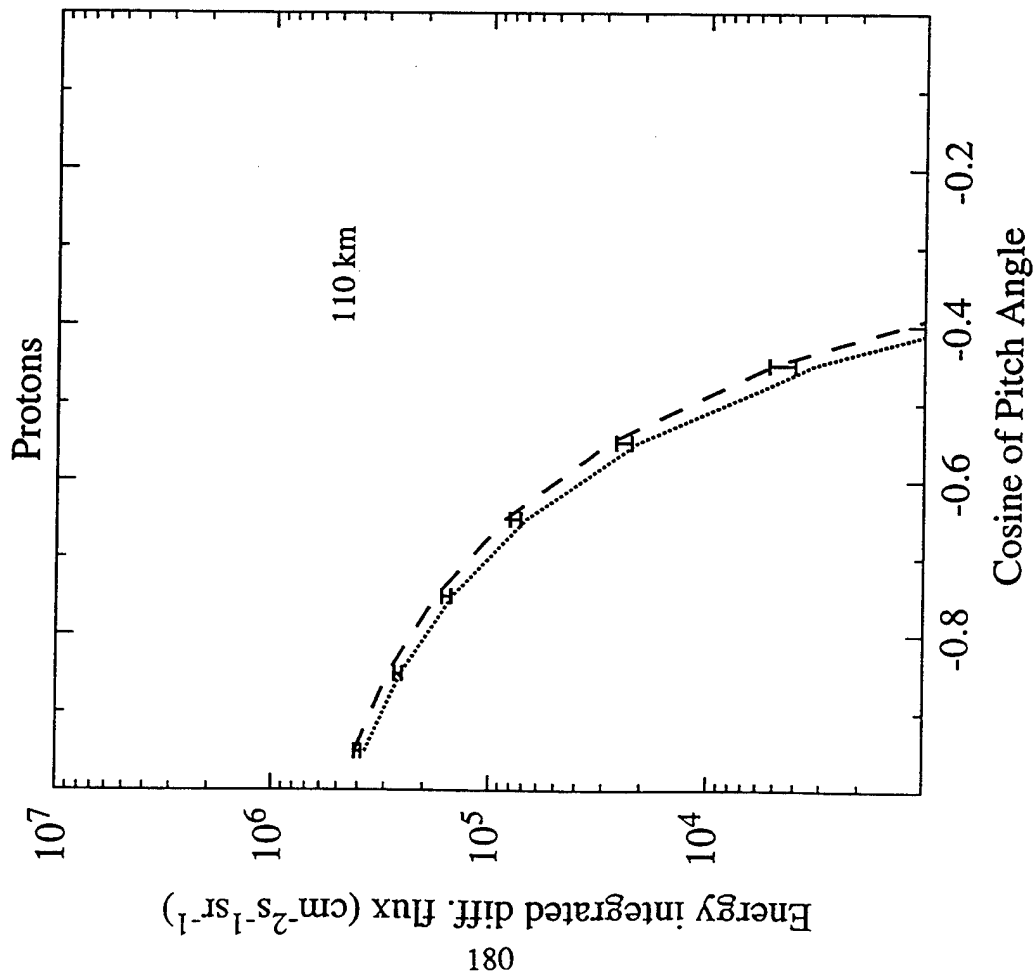


FIGURE 2f

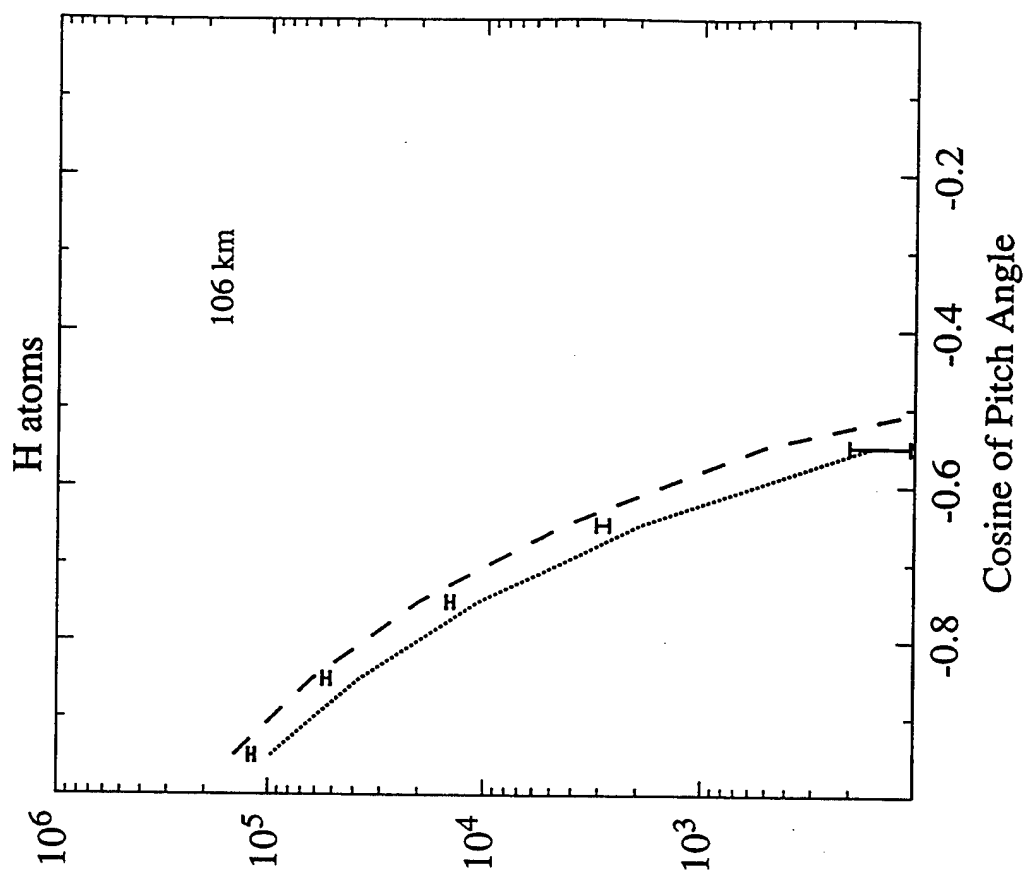
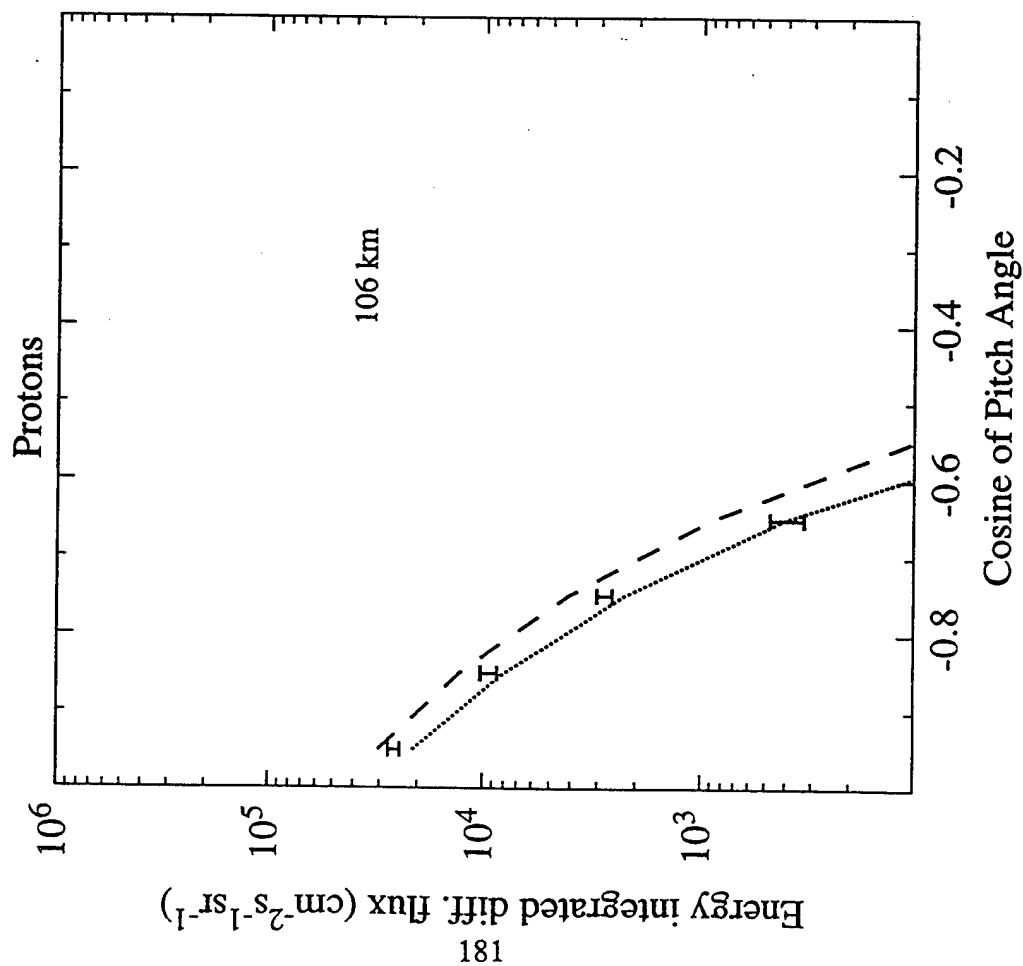


FIGURE 2g

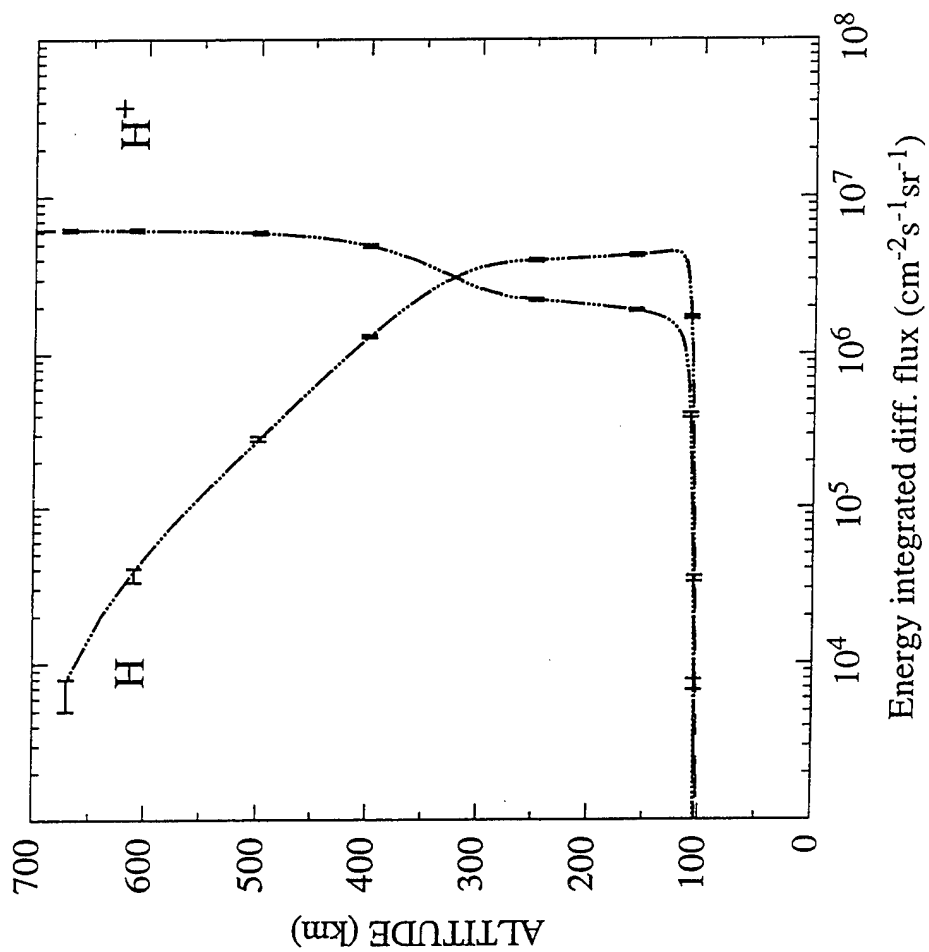


FIGURE 3a

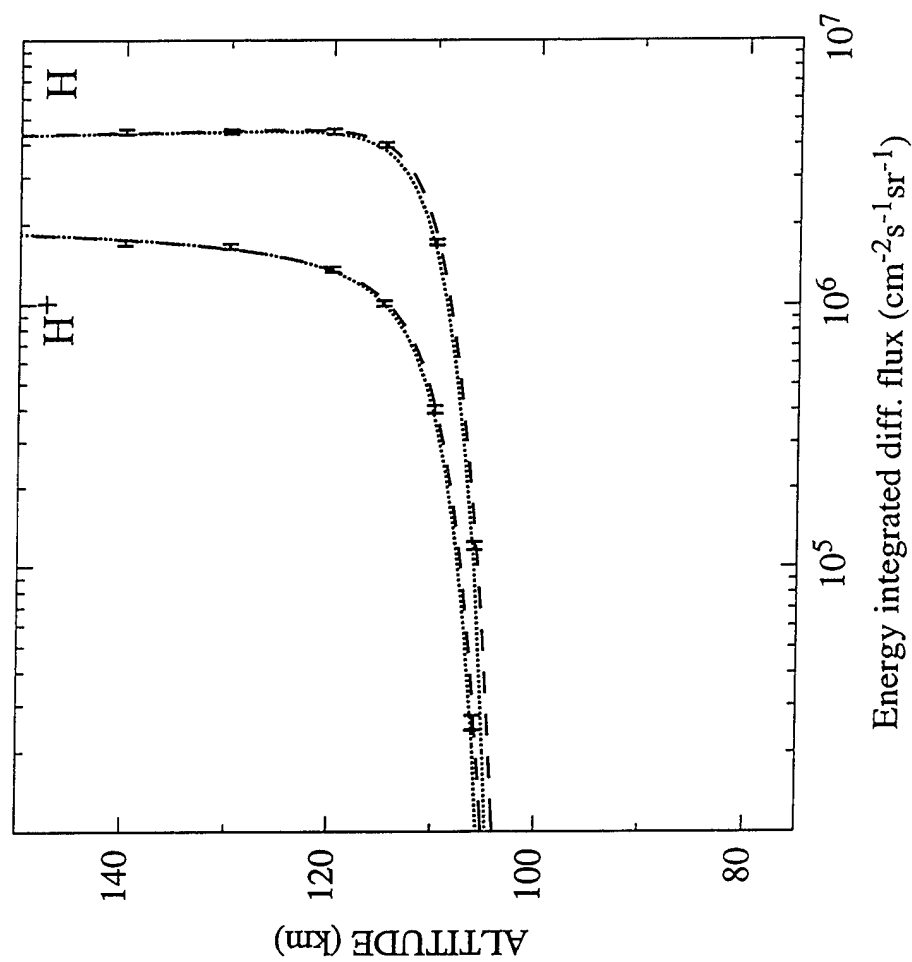


FIGURE 3b

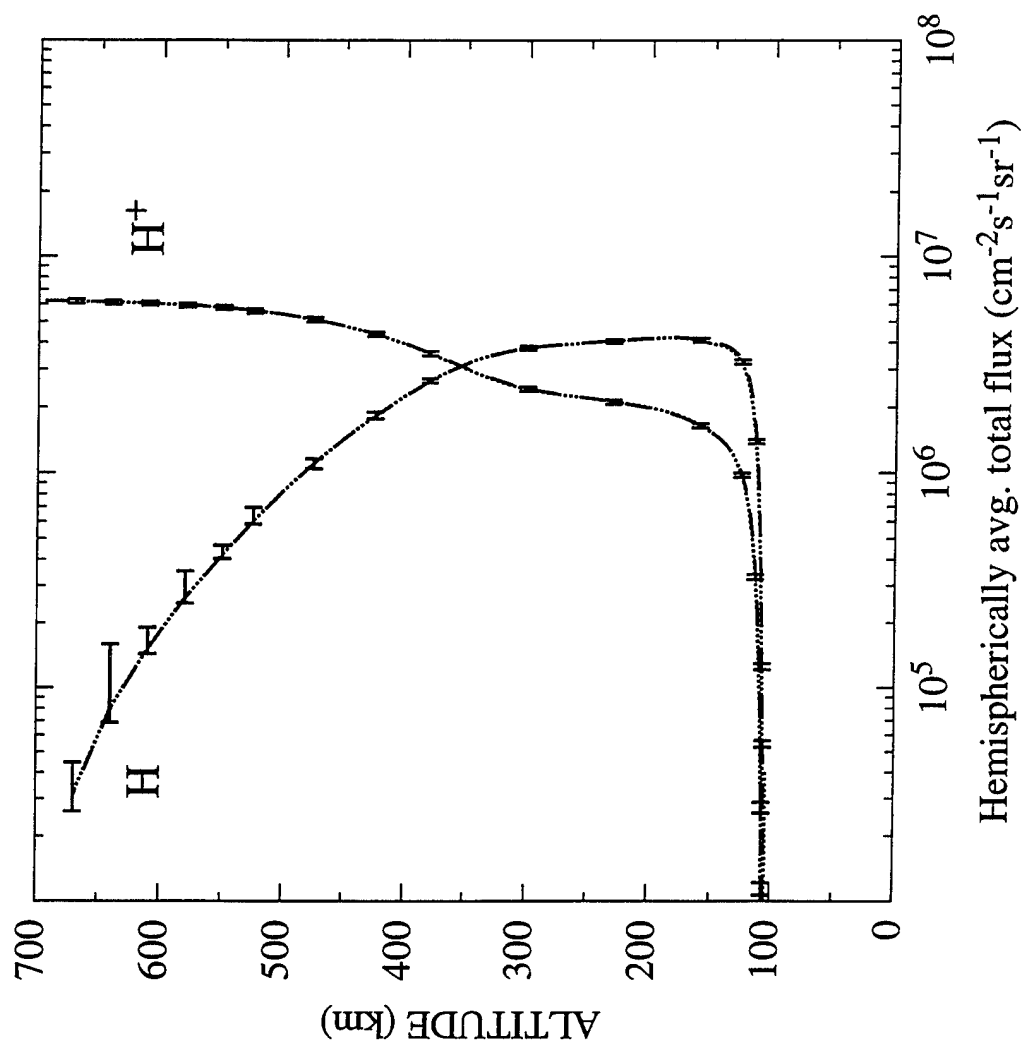


FIGURE 4

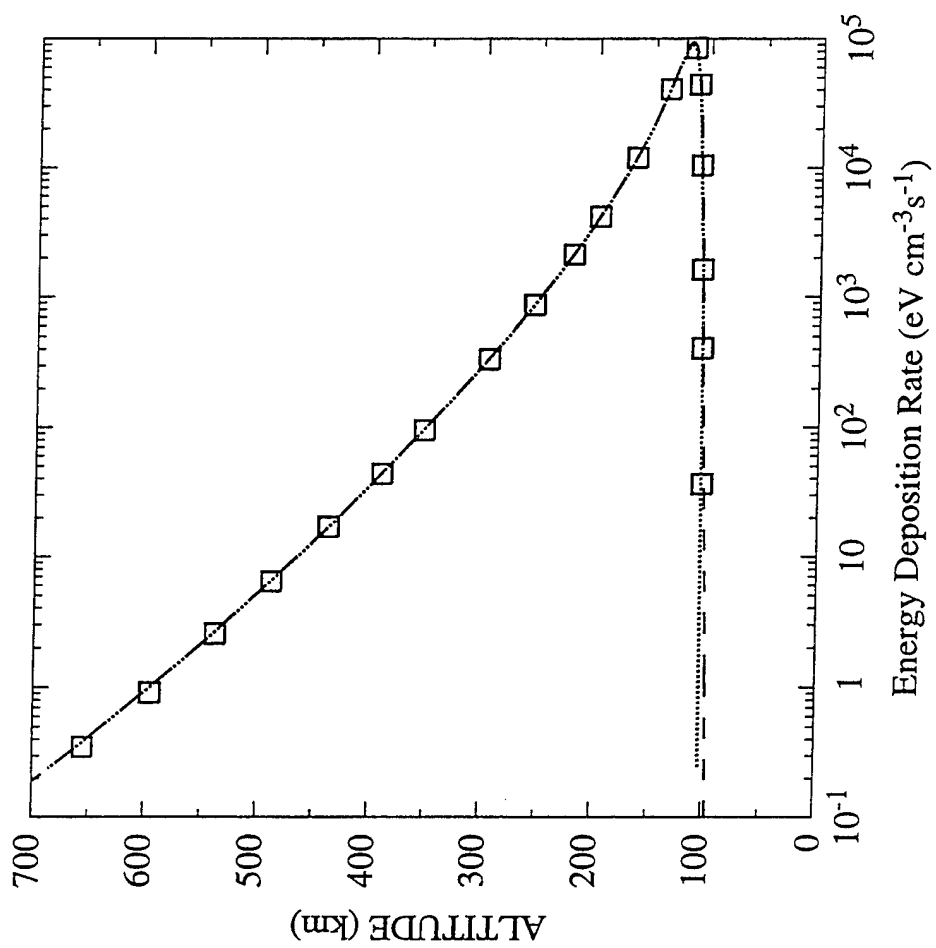


FIGURE 5a

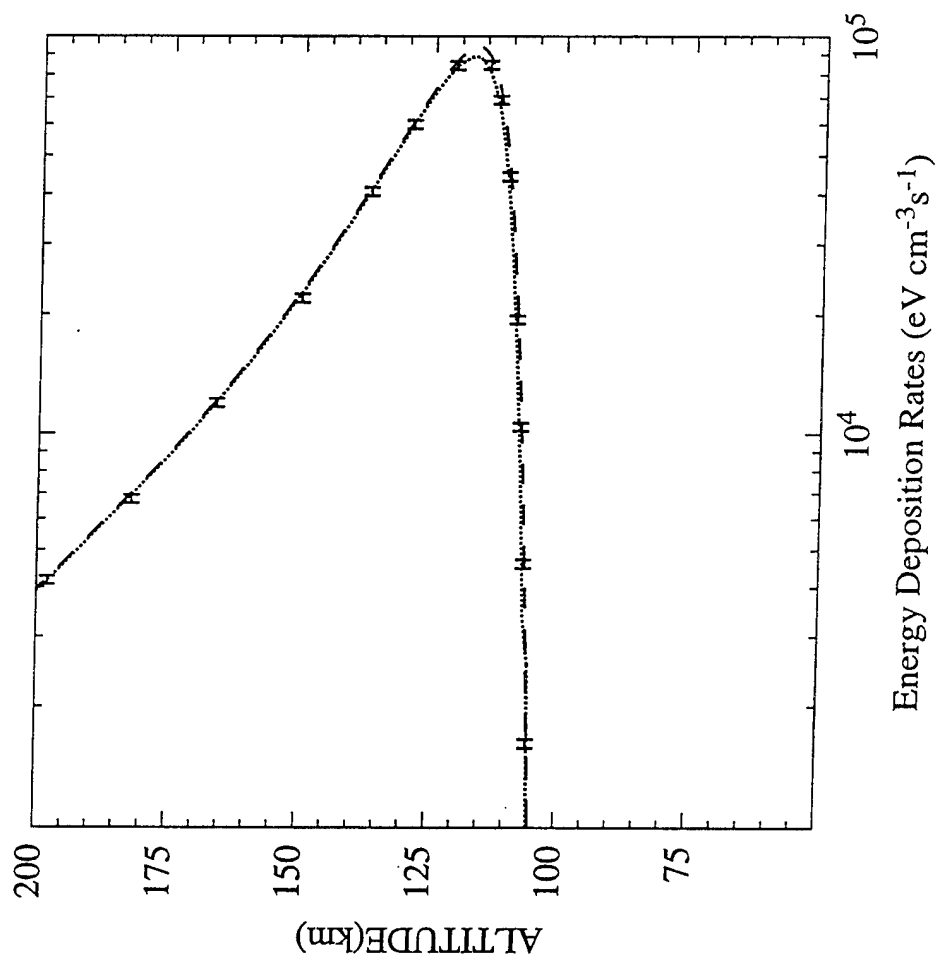


FIGURE 5b

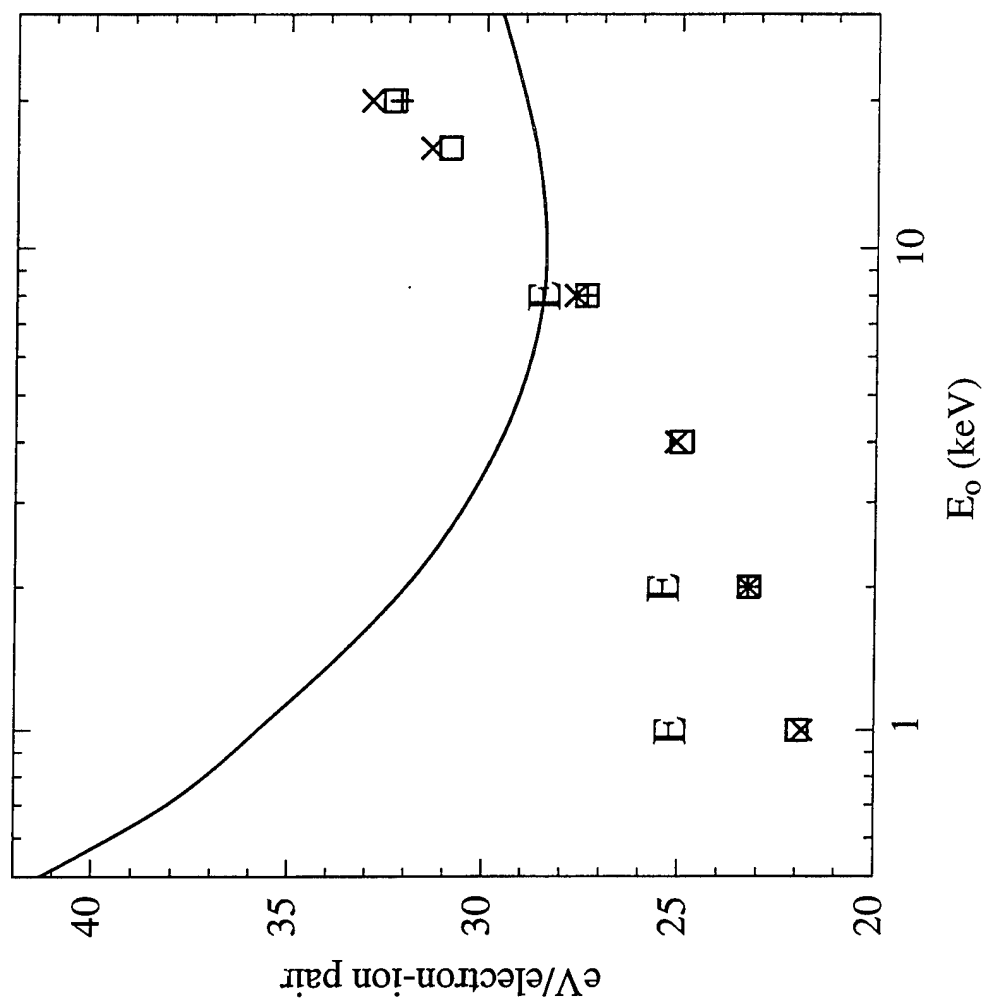


FIGURE 6

INCIDENT PROTON SPECTRA: IONOSPHERIC EFFECTS OF HIGH-ENERGY POWER LAW TAILS

Bamandas Basu

Ionospheric Effects Division, Phillips Laboratory, Hanscom AFB MA

Dwight T. Decker

Institute for Scientific Research, Boston College, Newton, MA

John R. Jasperse

Ionospheric Effects Division, Phillips Laboratory, Hanscom AFB MA

ABSTRACT

Studies of ion populations in the central plasma sheet (CPS) [Christon *et al.*, 1988, 1989, 1991] have found that at high energies ($E >$ characteristic or peak energy) there is a nonthermal power law tail which can be fitted using a kappa distribution. While similar studies for ionospheric altitudes are fewer, Lyons and Evans [1984] combined data from various instruments to show that proton distributions at ionospheric altitudes do have high-energy tails and are similar to those seen for earthward streaming protons in the outer boundary of the plasma sheet. More recently, the Particle Environment Monitor (PEM) experiment on board the Upper Atmosphere Research Satellite (UARS) has observed ionospheric ion spectra with a high-energy power law tail [Sharber *et al.*, 1993] similar to that described by Christon *et al.* [1991] as typical of CPS ion populations. However, all previous theoretical calculations of proton-hydrogen atom transport have assumed a Maxwellian distribution for the incident proton spectra [Strickland *et al.*, 1993]. In this paper, we present the impact that high-energy power law tails have on calculations of the ionospheric effects of precipitating protons.

INTRODUCTION

It is now well established that the precipitating high energy particle fluxes in the earth's auroral atmosphere consist of mostly electrons and protons with a small admixture of heavier ions. Earlier ground-based optical observations [Romick and Elvey, 1958; Galperin, 1959] and later satellite observations [Sharber, 1981; Hardy *et al.*, 1989] of the particle fluxes have established the fact that statistically the electrons and protons precipitate within two ovals that are not co-located. Further statistical studies by Hardy *et al.* [1987, 1991] have revealed that in the afternoon and evening sectors of the auroral oval, the protons at lower latitudes can carry a significant portion of the incoming energy flux. On the eveningside and near the equatorward edge of the oval, in particular, the energy flux of the protons can equal or exceed that of the electrons. Thus in order to study the dissipation of energy as well as the resultant ionization and excitation of optical emissions within the auroral atmosphere, it is necessary to study not just the transport and collisional degradation of the energetic electrons but also those of the energetic protons.

The most critical input in any theoretical model that calculates the energy deposition, ionization, etc. by the energetic particles is the incident particle flux. In-situ measurements by the particle detectors on board the satellites can provide this needed input data. Unfortunately, most of the known satellite proton data, with few exceptions, do not cover energies beyond 30 keV; whereas, for accurate modeling of the proton aurora, depending on the energy at which the peak value of the incident flux occurs, particle spectrum extending up to the energy of 100 keV or more is needed for proper accounting of the integral particle and energy fluxes. This deficiency in the proton data is usually overcome by extrapolating the data to high energies. The question that arises then is whether to extrapolate by using a Maxwellian or by some power law distribution. This is an important question because if a Maxwellian is used to extrapolate the proton data to high energies while the incident proton spectrum actually has a power law high energy tail, the incident energy flux carried by the

protons will be underestimated and, more important, the calculated altitude profiles of ionization rate, electron density and various optical emission rates will also be erroneous.

While we have few proton spectra at ionospheric altitudes with energies beyond 30 keV, there have been studies of ion populations in the CPS [Christon *et al.*, 1988, 1989, 1991] that included higher energies. These studies have shown that at high energies ($E >$ characteristic or peak energy) the ions have a nonthermal power law tail which can be fitted using a kappa distribution. Lyons and Evans [1984] combined data from various instruments to show that proton energy distributions at ionospheric altitudes also have high-energy tails and are the same as those seen for earthward streaming protons in the outer boundary of the plasma sheet. Recently, the Particle Environment Monitor (PEM) on board the Upper Atmosphere Research Satellite (UARS) [Sharber *et al.*, 1993] has observed ion spectra at ionospheric altitudes with high-energy power law tails similar to those described by Christon *et al.* [1991] as typical of CPS ion populations. More recently, Decker *et al.* [1995] have shown that an excellent agreement between the upgoing electron fluxes measured by the Low Altitude Plasma Instrument (LAPI) on board the Dynamics Explorer 2 (DE 2) satellite and those predicted theoretically can be achieved only when a kappa distribution is used to extrapolate the observed incident proton spectra to energies beyond the instrument's cut-off energy (27 keV). It is reasonable to infer from all these that the incident proton spectra at ionospheric altitudes do indeed have non-Maxwellian high-energy tails albeit under certain magnetospheric conditions.

In previous calculations of proton aurora-related quantities [Strickland *et al.*, 1993], only Maxwellians have been used for the incident spectra. In this paper we present results for a Maxwellian with a power-law tail (modelled by a kappa distribution) beyond 30 keV and compare these results with those for a pure Maxwellian incident proton spectrum. Specifically, we show the differences in the altitude profiles of the hemispherically averaged particle fluxes and the ionization rate. Differences in the altitude profiles of various optical emission rates will be shown elsewhere in future.

THEORETICAL MODEL AND RESULTS

The theoretical model consists of a coupled set of transport equations for the proton and the hydrogen atom fluxes [Jasperse and Basu, 1982]. These equations, numerical method of solving them, and the input quantities (cross sections for various collision processes and the model neutral atmosphere) have been described in Basu *et al.* [1990, 1993]. The numerical code solves the equations for a given incident proton flux (the incident hydrogen atom flux is taken to be zero) to obtain the particle fluxes as a function of altitude, energy and pitch angle and then calculates the ionization rates and optical emission rates due to precipitating protons and hydrogen atoms. The contributions from the secondary electrons to these rates can be calculated by solving the electron transport equation in which the secondary electrons produced by the protons and hydrogen atoms are used as source functions [see Basu *et al.*, 1993 and Strickland *et al.*, 1993]. In this paper we shall deal only with the primary ionization rates.

Results are shown for two types of incident proton spectra: (1) a pure Maxwellian with a characteristic energy $E_0 = 8$ keV and an energy flux $Q_0 = 1 \text{ erg cm}^{-2} \text{ s}^{-1}$; and (2) the same Maxwellian up to 30 keV and a power law tail above 30 keV modelled by a kappa ($= 4$) distribution where the kappa distribution has the functional form of $E[1 + E/\kappa E_0]^{-\kappa-1}$. Figure 1 shows the two types of incident spectra. In contrast to the energy flux of $1 \text{ erg cm}^{-2} \text{ s}^{-1}$ being carried by the pure Maxwellian spectrum, the type 2 spectrum has about $2 \text{ ergs cm}^{-2} \text{ s}^{-1}$. In all the figures, the type 1 spectrum and the results associated with it are shown in solid lines and those for the type 2 are shown in dashed lines. In Figs. 2a-2c, we show the hemispherically averaged proton fluxes (integrated over all pitch angles and divided by 2π) for the two incident spectra as a function of energy and at three selected altitudes. Similar functional behavior of the hemispherically averaged hydrogen atom fluxes are shown in Figs. 3a-3c. In Figure 2a, we see that at 500 km the H^+ flux has decreased somewhat but with little change in shape. In Figure 3a, we see that the H atom flux has reached significant levels due to the various charge changing processes between the energetic particles (H^+ and H) and the neutral constituents of the atmosphere. However for both H^+ and H, the particles that originated from the high energy tail at 600

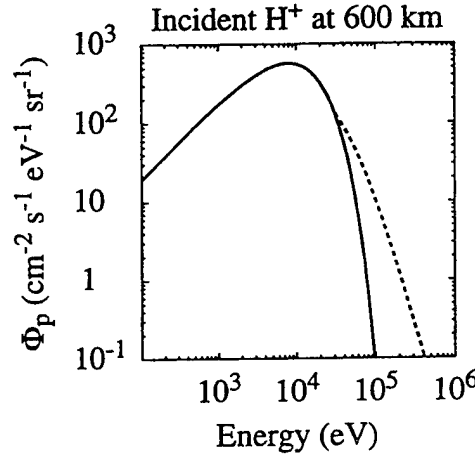


Figure 1: Incident proton fluxes versus energy used in the calculations presented in this paper. The solid curve is pure 8 keV Maxwellian with an incident energy flux of $1 \text{ erg cm}^{-2} \text{ s}^{-1}$. The dashed curve is the power law tail above 30 keV modeled by a kappa ($=4$) distribution.

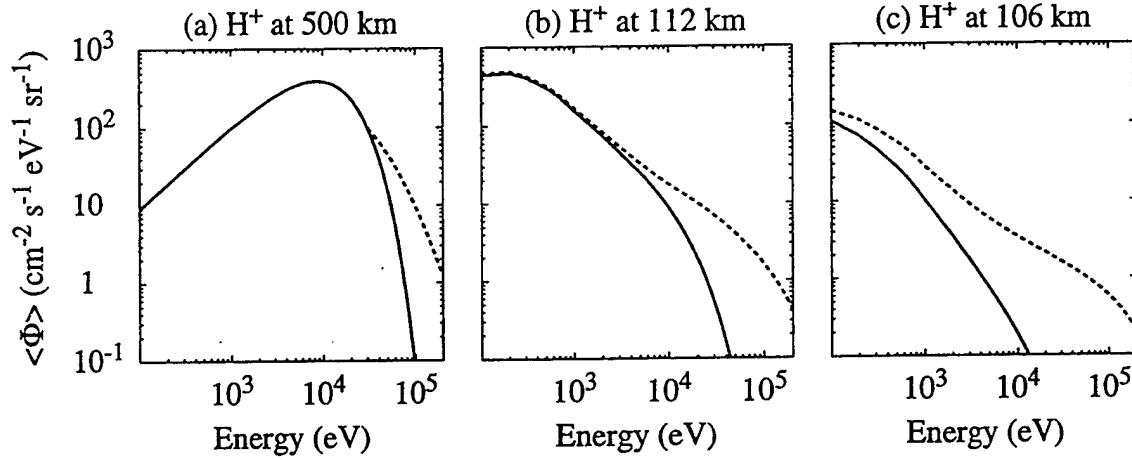


Figure 2: Hemispherically averaged proton fluxes versus energy. The solid curves are from the pure Maxwellian case and the dashed curves are from the power law tail case. (a) altitude = 500 km; (b) altitude = 112 km; (3) altitude = 106 km.

km have lost little energy and are still above 30 keV. In Figures 2b and 3b, we see that at 112 km the shape of both the H^+ and H atoms spectra have changed as particles cascade down in energy and increase the low energy portion of the energy distributions. As a result, some of the particles that originated as part of the power law tail above 30 keV have now cascaded to below 10 keV. Finally at 106 km, we see that the degradation of the spectra continue and particles that started above 30 keV can now be found at all energies. In Fig. 4 we show the volume ionization rates resulting from the two types of incident spectra. We point out that the peak value of the ionization rate for the type 2 spectrum is $\sim 1.32 \times 10^4 \text{ cm}^{-3} \text{ s}^{-1}$ and it occurs at 112.5 km, while that for the type 1 spectrum is $\sim 7.7 \times 10^3 \text{ cm}^{-3} \text{ s}^{-1}$ occurring at 115 km. We can see that the region around the peaks of the profiles is a transition region where the rates go from being moderately different (20% apart) above the peaks to significantly different (over an order of magnitude apart) along the bottomside of the profiles. These differences between the two profiles may be explained in terms of the differences in the incident energy flux and the differences in the particle fluxes (as shown in Figs. 2 and 3) by also taking into account the energy dependence of the relevant ionization cross sections.

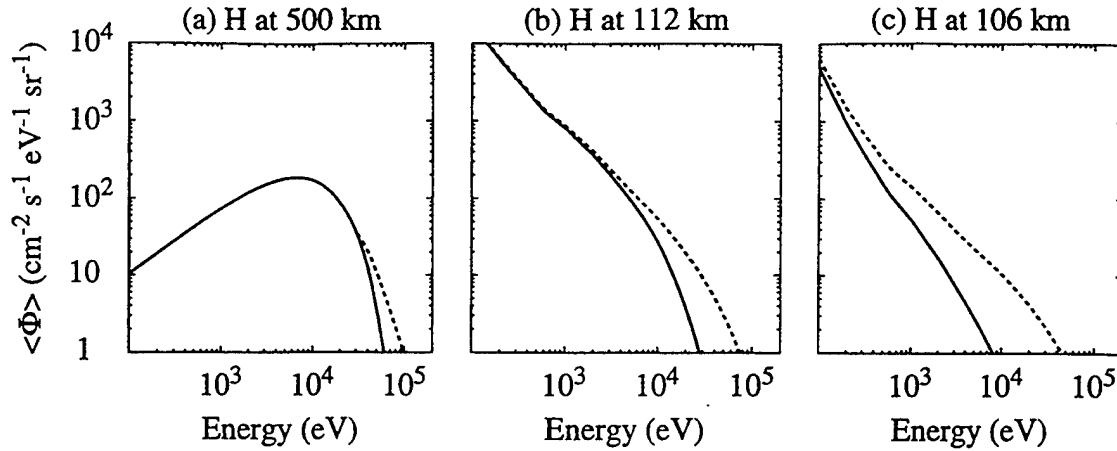


Figure 3: Hemispherically averaged H atom fluxes versus energy. The solid curves are from the pure Maxwellian case and the dashed curves are from the power law tail case. (a) altitude = 500 km; (b) altitude = 112 km; (c) altitude = 106 km.

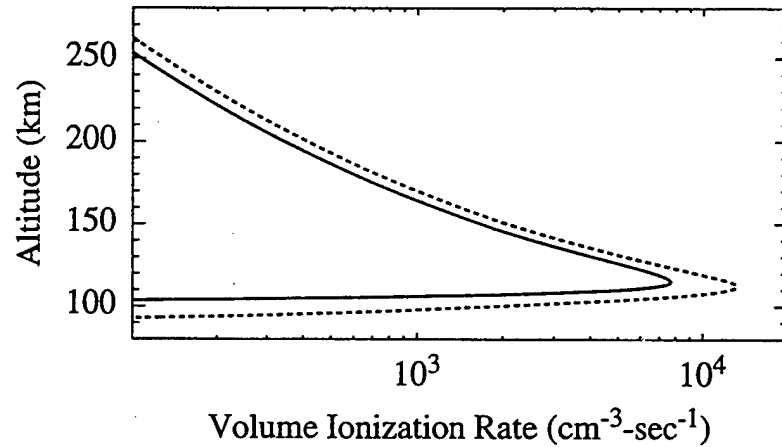


Figure 4: Volume ionization rates versus altitude for two types of incident proton spectra. The solid curve is for the pure Maxwellian case and the dashed curve is for the power law tail case.

DISCUSSION

We have shown the effects of the two types of extrapolations of proton data to high energies and have pointed out that the differences can be attributed to the differences in the particle fluxes, which are the fundamental quantities. In this short paper we have concentrated only on the hemispherically averaged differential fluxes and the volume ionization rates. It is expected that qualitatively similar results will also be obtained for the various optical emission features associated with the proton aurora.

The first point we wish to emphasize is that if the energy distributions of incident proton fluxes are measured out to around 30 keV and it is assumed that a Maxwellian describes the spectra above 30 keV, then the total incident energy flux will most likely be underestimated. This follows from the observations in the magnetosphere and ionosphere of power law tails in the ion distributions. In particular, *Christon et al.* [1989] reported that during undisturbed periods ion distributions could be fit with kappa distributions where κ ranges from 3 to 9.5. In this paper, we found that using $\kappa = 4$ and a characteristic energy of 8 keV gave an incident energy flux twice that of the pure Maxwellian case. Similarly, in *Decker et al.* [1995] it was found that fitting ion

observations from LAPI using a $\kappa = 3$ gave three times the incident energy flux deduced from fitting with a pure Maxwellian. Further, for characteristic energies higher than 8 keV the differences, for a given κ , between the Maxwellian and the power law tail will be even more pronounced. On the other hand, for characteristic energies less than 8 keV the differences will be less. Given the observed ranges of characteristic energies and the observed range of κ , there is clearly great uncertainty in the incident ion energy flux deduced from such instruments as LAPI.

The impact of the power law tail in the incident proton flux on the differential flux and the ionization rate is evident in Figures 2–4. The major impact is seen to occur in the lower E region where the particles that originated above 30 keV come to play a significant role in both the particle spectra and the ionization rate. It also follows that the electron density profiles resulting from the ionization will be different for the two types of extrapolations and so care should be taken in choosing the extrapolation scheme when the electron density profiles are to be theoretically predicted. In this case, the approximately 70% difference between the ionization peaks would mean around a 30% difference at this altitude in the electron density. By 106 km, a factor of 9 difference in the ionization leads to a factor of 3 difference in the electron density. Also we note that the effect is not to simply scale the ionization rate but to shift the location of the peak and to modify the shape of the ionization profile. Conversely, if we want to infer the incident proton spectra from observed electron density profiles and if we assume that the spectra are Maxwellians, then we may predict proton spectra with characteristic energy and energy flux which are substantially different from what actually they should be.

Observationally, if an instrument such as PEM which measures protons between 1 eV to 150 MeV were available for monitoring the proton aurora then the uncertainties discussed above could be avoided. However, given the observed range of ion characteristic energies within the auroral region such a large range is not strictly necessary for the purposes of simply monitoring the proton aurora. Using observations from the central plasma sheet as a guide, we find that if the goal is to measure 90% of the incident energy flux then an instrument that goes up to 1 MeV would appear to be adequate. If the goal is to simply go high enough in energy to determine if the distribution is kappa like rather than Maxwellian, an instrument going up to 100 keV should be adequate. Though we should note that under very active conditions the observed magnetospheric spectra can not be represented by a single functional form and an instrument going to 1 MeV might still be necessary to confidently characterize the proton spectra. If such monitors are not available, then the next option is to develop an empirical model of the power law tail based on available data. The PEM instrument on UARS would be ideal for this except for the fact that UARS is not a polar orbiting satellite and does not routinely sample the auroral region. Thus the data coverage may turn out to be far from adequate. On the theoretical side, our transport model will be exercised over a range of characteristic energies and κ in order to fully quantify the impact of high-energy power law tails. As mentioned earlier, such calculations will also be expanded to include various optical emissions that arise in a proton aurora.

ACKNOWLEDGEMENTS

This work was supported in part by the Air Force Office of Scientific Research. The work at Boston College was supported by Phillips Laboratory contract F19628-93-K0001.

REFERENCES

- Basu, B., J. R. Jasperse, and N. J. Grossbard, A numerical solution of the coupled proton- H atom transport equations for the proton aurora, *J. Geophys. Res.*, *95*, 19069, 1990.
- Basu, B., J. R. Jasperse, D. J. Strickland, and R. E. Daniell, Transport-theoretic model for the electron-proton-hydrogen atom aurora. 1. Theory, *J. Geophys. Res.*, *98*, 21517, 1993.
- Christon, S. P., D. G. Mitchell, D. J. Williams, L. A. Frank, C. Y. Huang, and T. E. Eastman, Energy spectra of plasma sheet ions and electrons from 50 eV/e to 1 MeV during plasma temperature transitions, *J. Geophys. Res.*, *93*, 2562, 1988.
- Christon, S. P., D. J. Williams, D. G. Mitchell, L. A. Frank, and C. Y. Huang, Spectral characteristics of

- plasma sheet ion and electron populations during undisturbed geomagnetic conditions, *J. Geophys. Res.*, **94**, 13409, 1989.
- Christon, S. P., D. J. Williams, D. G. Mitchell, C. Y. Huang, and L. A. Frank, Spectral characteristics of plasma sheet ion and electron populations during disturbed geomagnetic conditions, *J. Geophys. Res.*, **96**, 1, 1991.
- Decker, D. T., B. Basu, J. R. Jasperse, D. J. Strickland, J. R. Sharber, and D. Winningham, Upgoing electrons produced in an electron-proton-hydrogen atom aurora, *J. Geophys. Res.*, **100**, 21409, 1995.
- Galperin, Yu. I., Hydrogen emission and two types of auroral spectra, *Planet. Space Sci.*, **1**, 57, 1959.
- Hardy, D. A., M. S. Gussenhoven, R. Raistrick and W. J. McNeil, Statistical and functional representations of the pattern of auroral energy flux, number flux and conductivity, *J. Geophys. Res.*, **92**, 12275, 1987.
- Hardy, D. A., M. S. Gussenhoven and D. Brautigam, A statistical model of auroral ion precipitation, *J. Geophys. Res.*, **94**, 370, 1989.
- Hardy, D. A., W. J. McNeil, M. S. Gussenhoven and D. Brautigam, A statistical model of ion precipitation, 2. Functional representation of the average patterns, *J. Geophys. Res.*, **96**, 5539, 1991.
- Jasperse, J. R. and B. Basu, Transport theoretic solutions for auroral proton and H atom fluxes and related quantities, *J. Geophys. Res.*, **87**, 811, 1982.
- Lyons, L. R. and D. S. Evans, An association between discrete aurora and energetic particle boundaries, *J. Geophys. Res.*, **89**, 2395, 1984.
- Sharber, J. R., The continuous (diffuse) aurora and auroral-E ionization, in *Physics of Space Plasmas*, vol.4, edited by T. S. Chang, B. Coppi and J. R. Jasperse, p.115, Scientific Publishers, Cambridge, Mass., 1981.
- Sharber, J. R., R. A. Frahm, J. D. Winningham, J. C. Biard, D. Lummerzheim, M. H. Rees, D. L. Chenette, E. E. Gaines, R. W. Nightingale, and W. L. Imhof, Observations of the UARS particle environment monitor and computation of ionization rates in the middle and upper atmosphere during a geomagnetic storm, *Geophys. Res. Lett.*, **20**, 1319, 1993.
- Strickland, D. J., R. E. Daniell, Jr., J. R. Jasperse, and B. Basu, Transport-theoretic model for the electron proton-hydrogen atom aurora: 2. Model results, *J. Geophys. Res.*, **98**, 21533, 1993.

MODELING POLAR CAP *F*-REGION PATCHES USING TIME VARYING CONVECTION

J. J. Sojka¹, M. D. Bowline¹, R. W. Schunk¹, D. T. Decker²,
C. E. Valladares², R. Sheehan², D. N. Anderson³, and R. A. Heelis⁴

Abstract. Creation of polar cap *F*-region patches are simulated for the first time using two independent physical models of the high latitude ionosphere. The patch formation is achieved by temporally varying the magnetospheric electric field (ionospheric convection) input to the models. The imposed convection variations are comparable to changes in the convection that result from changes in the B_y IMF component for southward interplanetary magnetic field (IMF). Solar maximum-winter simulations show that simple changes in the convection pattern lead to significant changes in the polar cap plasma structuring. Specifically, in winter, as enhanced dayside plasma convects into the polar cap to form the classic tongue-of-ionization (TOI) the convection changes produce density structures that are indistinguishable from the observed patches.

1. Introduction

Over the last decade, observations have established that, during periods of southward IMF, patches of enhanced ionization drift across the polar cap in an antisunward direction [Buchau *et al.*, 1983; Weber *et al.*, 1984]. These patches, although strongest in winter, occur at all seasons and levels of solar and geomagnetic activity. Their horizontal dimensions range from hundreds to several thousand kilometers. Patches also possess small scale structuring from meters to tens of kilometers. As they convect across the polar cap, the patch shape can change [Robinson *et al.*, 1985]. Several models of convection dynamics have been proposed to explain patch formation. Anderson *et al.* [1988] proposed that polar cap expansion in response to K_p changes brings high density plasma into the cusp region while Lockwood and Carlson [1992] argued that flux transfer event (FTE) signatures in the cusp cause short-lived enhanced flows that transport plasma into the polar cap. Indeed, Pinnock *et al.* [1993] have presented an example of one such event. In this study, two physical models of the high-latitude ionosphere were used to simulate patch formation caused by time varying convection that responds to IMF B_y changes.

2. TDIM and PL Ionospheric Models

The Utah State University Time-Dependent Ionospheric Model (TDIM) and the Phillips Laboratory (PL) *F*-region

model were used in independent studies of polar cap *F*-region patch formation. Both simulations used the same patch formation scenario and discovered the same consequences of "realistically" varying the magnetospheric electric field on the polar cap electron density distribution.

The USU TDIM is a multi-species (O_2^+ , N_2^+ , NO^+ , O^+ , N^+ , and He^+) global model of the ionosphere that is based upon solutions of the continuity, momentum, and energy equations in the collision-dominated 13-moment transport formulation. The development of this model is described by Schunk [1988], while the model predictions and comparisons with observations are described by Sojka [1989]. The PL *F*-region model is a single species (O^+) global model of the ionosphere that is based upon solutions of the continuity and momentum equations. Its development involved generalizing the theoretical low latitude *F*-region model of Anderson [1973].

3. Patch Simulation

Two sets of results are presented to highlight the sensitivity of the polar cap plasma to the structuring that results from the time varying convection electric fields; in particular, a time dependence driven by a time varying B_y IMF component. In the PL simulation, the semi-empirical convection model of Hairston and Heelis [1990] is used to simulate time varying southward IMF patterns. The TDIM simulation used two Heppner and Maynard [1987] convection patterns to do likewise.

3.1. PL *F*-Region Patch Simulation.

Figure 1 shows the plasma drift trajectories for the two IMF conditions used in the PL simulations. Both convection patterns are for southward IMF and a cross-polar cap potential of 80 kV. They differ in that the left and right patterns

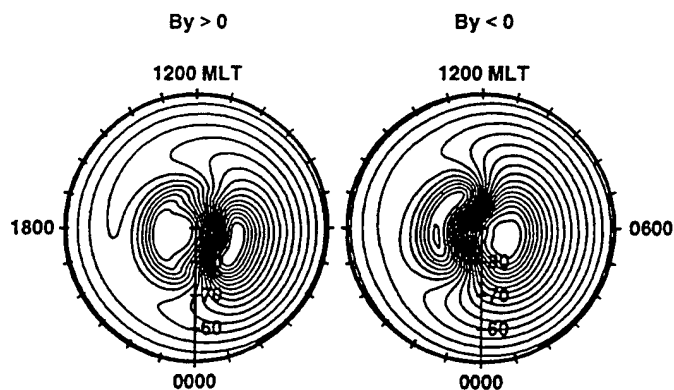


Fig. 1. Hairston and Heelis [1990] convection patterns with corotation added for southward IMF, where IMF $B_y = 8$ gamma (left panel) and IMF $B_y = -8$ gamma (right panel). The cross polar cap potential is 80 kV and the polar cap radius is 12 degrees.

¹ Center for Atmospheric and Space Science, Utah State University

² Institute for Space Research, Boston College

³ Geophysics Directorate, Phillips Laboratories

⁴ University of Texas, Dallas

correspond to IMF B_y values of 8 and -8 gamma, respectively. The patterns are from the *Hairston and Heelis* [1990] semi-empirical electric field model with a corotational potential field added. Note that the plasma enters the polar cap in the vicinity of the cusp region, pre-noon, and then convects antisunward across the polar cap. For B_y negative, the flow is across the dusk-side of the polar cap (right panel, Figure 1), while for B_y positive this flow is on the dawn-side (left panel, Figure 1). This IMF B_y control of the ionospheric polar cap plasma convection is well known [Heppner and Maynard, 1987] but its full significance in the formation of polar cap patches has not been recognized. Since the details of how a given ionospheric convection pattern changes into a new pattern are largely unknown at this time, we adopted a rather simplistic procedure for changing from one convection pattern to the next. For this simulation, the convection pattern is maintained for 17 hours and then, at 1700 UT, is changed to the pattern in the right panel, and again at 1830 UT, is changed back to the first pattern.

For this simulation and that of the TDIM, winter solstice and solar maximum conditions were adopted with an F10.7 of 190 and a K_p of 4. The auroral precipitation model of *Hardy et al.* [1985] for a K_p of 4 was used, and was kept constant during the entire simulation. O^+ profiles were generated at 5-minute time steps for the 17 hours prior to the 1700 UT first convection change and through to 2100 UT. Snapshots of the F_2 peak density ($N_m F_2$) at 1700, 1830, 2000, and 2100 UT are shown in Plate 1. At 1700 UT, a well-defined TOI feature in the polar cap shows how the plasma transport associated with the Figure 1 left-panel convection brings high-density plasma into the dawn-side of the polar cap. The peak density in the TOI is around $1 \times 10^6 \text{ cm}^{-3}$. In the remainder of the polar cap, the density drops to values as low as $1 \times 10^5 \text{ cm}^{-3}$.

The effect of changing the convection pattern at 1700 UT

can be seen in the $N_m F_2$ snapshot at 1830 UT. A new TOI begins to form on the dusk-side of the polar cap and structuring of the high-latitude plasma also begins as the old dawn-side tongue is caught up in the circulation of the dawn convection cell. At 1830 UT, the convection changes back to its initial pattern and further structuring occurs in the high-latitude plasma at 2000 and 2100 UT (see Plate 1). In particular, after 2000 UT a TOI forms back in the dawn-side of the polar cap. It is the remnants of what was the dusk-side TOI, which are deformed and striated due to differing trajectories of the dusk convection cell. In the next section, results of a TDIM simulation will illustrate further details of how plasma structuring occurs.

3.2. TDIM F-Region Patch Simulation

The TDIM simulation followed the same methodology described for the PL simulation. The *Heppner and Maynard* [1987] empirical convection model was used. Specifically, the A and DE patterns, which correspond to southward IMF for B_y slightly negative and B_y strongly negative, respectively, were used. Plate 2 shows these two convection patterns within the TDIM simulation region. This region is centered on the magnetic pole and extends from 70° invariant latitude on the noon meridian to 70° invariant latitude on the midnight meridian, with noon at the top. The dawn-dusk latitudinal extent is somewhat smaller, i.e., from 76° invariant latitude at dawn to 76° invariant latitude at dusk. Each trajectory was followed for 24 hours prior to the snapshot. Each arrow in the convection patterns represents a 20-minute trajectory taken from within the simulation region. The A pattern convection is fairly uniform over the polar region at about 500 m/s. In contrast, the DE pattern has a dusk sector flow speed of 1000 m/s and a slow dawn sector flow of $< 200 \text{ m/s}$.

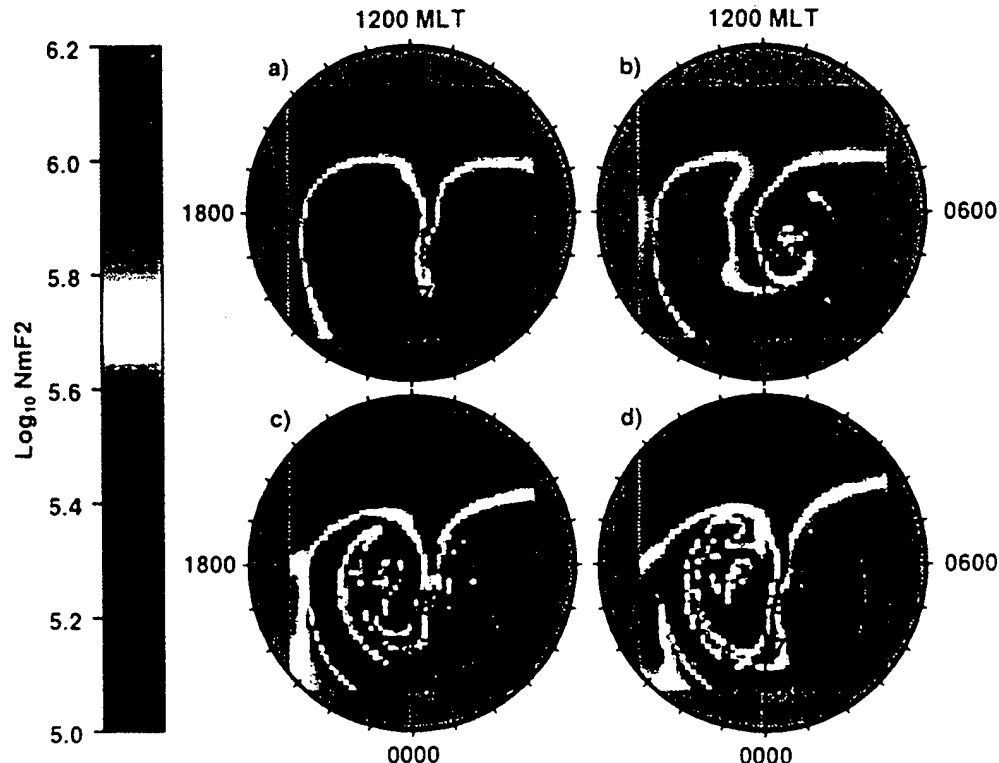


Plate 1. Four color-coded $N_m F_2$ snapshots from the PL simulation. Each snapshot uses the same color coding of densities. The UT of each snapshot is as follows: (a) 1700 UT; (b) 1830 UT; (c) 2000 UT; and (d) 2100 UT.

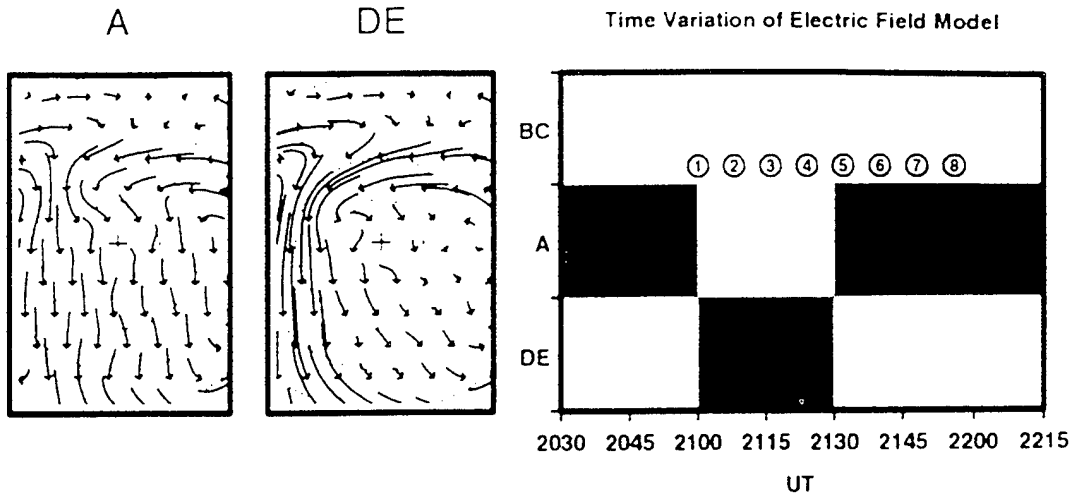


Plate 2. The A and DE convection patterns within the TDIM simulation region (left panels). The dotted red circles represent constant invariant latitudes at 5° intervals from the magnetic pole (red cross). Noon is at the top. The right panel shows the time history of the TDIM simulation as well as times of density snapshots (circled numbers) shown below.

The TDIM simulation is schematically shown in Plate 2 as a time-line plot at the top next to the two convection panels. Numbers are circled and placed along the time axis. These numbers identify the times of the TDIM $N_m F_2$ snapshots shown in Plate 3. These are at eight minute time intervals beginning at 2100 UT when the first change in the convection pattern occurs. A well defined TOI is present in the first snapshot. Panel 3, sixteen minutes after the change to DE, already shows well defined changes in the TOI. However,

this only occurs near the throat; everywhere else the convection associated with the TOI has slowed down, but maintains the same flow direction. This differential flow trend is maintained until 2130 UT. Each panel up to this time shows that the distortion of the tongue increases. Indeed, by 2130 UT, Panel 5, the density structuring is too complex to be referred to as a single TOI. At 2130 UT, the convection reverts back to the A pattern and the ensuing snapshots show how the plasma entering the polar cap at the cusp begins to

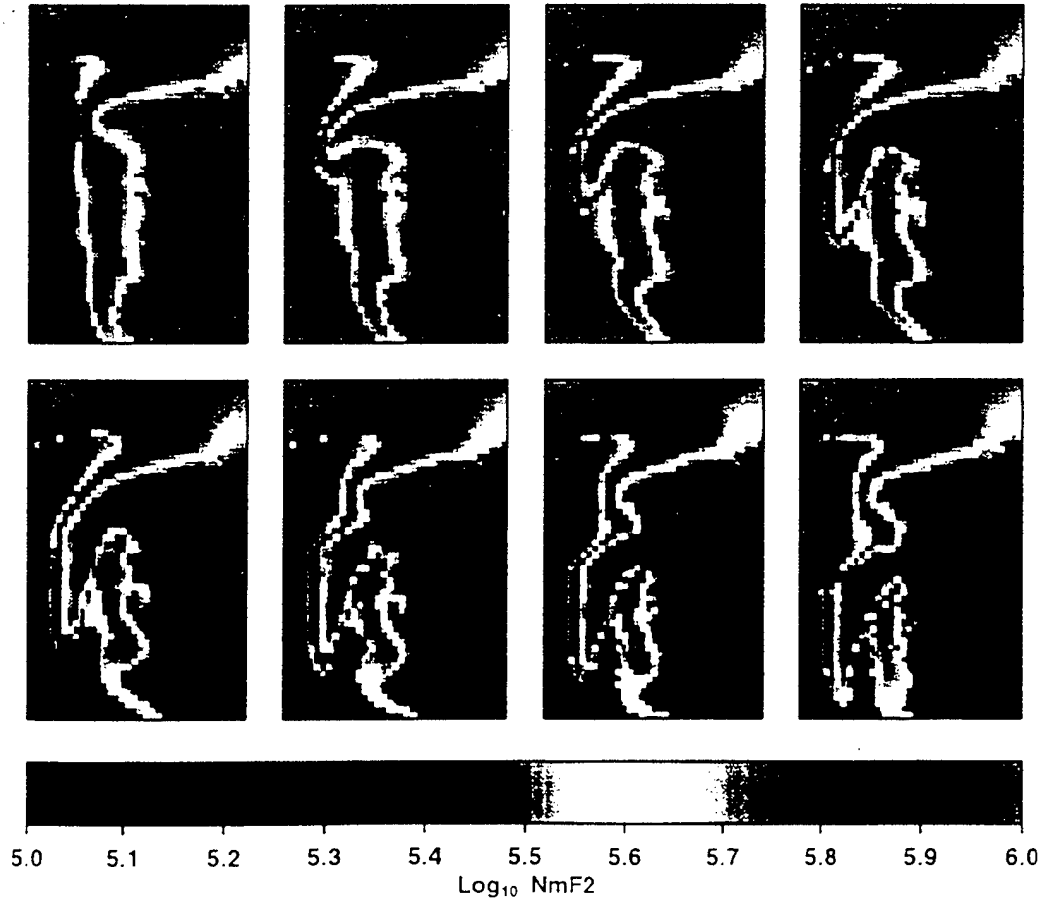


Plate 3. A series of eight color-coded $N_m F_2$ snapshots from the TDIM simulation. Each snapshot uses the same color coding of densities. The snapshots are labeled with the numbers given in the time history plot of Plate 2.

regenerate the 2100 UT TOI. However, all the other polar cap structure now uniformly drifts antisunward, as indicated by the A convection panel in Plate 2. The net result is that the structuring produced by the half-hour of DE convection is stamped on the polar cap plasma until it can drift out of the polar cap and into the auroral zone.

The final panels of Plate 3 show that the density structuring caused by the DE pattern can readily be viewed as patches. At least two distinct regions of high density are present. Each has a peak density of the order of $1 \times 10^6 \text{ cm}^{-3}$, with the density between them dropping to $2 \times 10^5 \text{ cm}^{-3}$. These patches, and those of the PL simulation, are indistinguishable in scale size, spatial complexity, and density from the plasma structures observed in the polar ionosphere. They do however lack the sub-10 km level structuring.

4. Conclusions

The PL and TDIM simulations show that the shape and extent of polar cap patches are determined by the plasma flow changes that occur while the plasma is in the cusp and polar cap. Qualitatively, the PL and TDIM simulations show, for the first time, that given the variability we know exists in the IMF and, hence, the magnetospheric convection, patches occur naturally without complex plasma source and sink mechanisms. Both models show that, under constant southward IMF conditions, a TOI extends from the cusp into the polar cap. It is this flow of dayside high-density plasma that becomes the source of patches as the convection undergoes time variations.

The role of the other patch mechanisms will not be irrelevant, but the time varying convection has been shown to have the capability of producing the order of magnitude density enhancements observed in the polar cap under southward IMF conditions that are referred to as patches. Follow-on studies are now in progress to determine the contribution of the other mechanisms as well as to explore the full consequences of the time varying convection mechanism.

Acknowledgment. This research was supported in part by NASA grant NAG5-1484 and NSF grant ATM-89-13230 to Utah State University; AF contracts F19628-88-K-0008, F19628-89-K-0001, F19628-90-K-0007, and NSF grants ATM-9000273 and ATM-9016465 to Boston College; and AF contract F19628-90-K-0001 to the University of Texas at Dallas. Helpful discussions with Jurgen Buchau and Ed Weber are acknowledged.

REFERENCES

Anderson, D. N., A theoretical study of the ionospheric F region equatorial anomaly, I. Theory, *Planet. Sci.*, 21, 409-419, 1973.

- Anderson, D. N., J. Buchau, and R. A. Heelis, Origin of density enhancements in the winter polar cap ionosphere, *Radio Sci.*, 23, 513-519, 1988.
- Buchau, J., B. W. Reinisch, E. J. Weber, and J. G. Moore, Structure and dynamics of the winter polar cap F region, *Radio Sci.*, 18, 995-1010, 1983.
- Hairston, M. R., and R. A. Heelis, Model of the high-latitude ionospheric convection pattern during southward interplanetary magnetic field using DE-2 data, *J. Geophys. Res.*, 95, 2333-2343, 1990.
- Hardy, D. A., M. S. Gussenhoven, and E. Holernan, A statistical model of auroral electron precipitation, *J. Geophys. Res.*, 90, 4229-4248, 1985.
- Heppner, J. P., and N. C. Maynard, Empirical high-latitude electric field models, *J. Geophys. Res.*, 92, 4467-4489, 1987.
- Lockwood, M. and H. Carlson, Jr., Production of polar cap electron density patches by transient magnetopause reconnection, *Geophys. Res. Lett.*, 19, 1731-1734, 1992.
- Pinnock, M., A. S. Rodger, J. R. Dudeney, K. B. Baker, P. T. Neweli, R. A. Greenwald, and M. E. Greenspan, Observations of an enhanced convection channel in the cusp ionosphere, *J. Geophys. Res.*, 98, 3767-3776, 1993.
- Robinson, R. M., R. T. Tsunoda, J. F. Vickrey, and L. Guerin, Sources of F region ionization enhancements in the nighttime auroral zone, *J. Geophys. Res.*, 90, 7533-7546, 1985.
- Schunk, R. W., A mathematical model of the middle and high latitude ionosphere, *PAGEOPH*, 127, 255-303, 1988.
- Sojka, J. J., Global scale, physical models of the F region ionosphere, *Rev. Geophys.*, 27, 371-403, 1989.
- Weber, E. J., J. Buchau, J. G. Moore, J. R. Sharber, R. C. Livingston, J. D. Winningham, and R. W. Reinisch, F layer ionization patches in the polar cap, *J. Geophys. Res.*, 89, 1683-1694, 1984.

J. J. Sojka, M. D. Bowline and R. W. Schunk, Center for Atmospheric and Space Sciences, Utah State University, Logan, UT 84322.

D. T. Decker, C. E. Valladares, and R. Sheehan, Institute for Space Research, Boston College, Chestnut Hill, MA 02154.

D. N. Anderson, Geophysics Directorate, Phillips Laboratories, Hanscom Air Force Base, MA 02159.

R. A. Heelis, Center for Space Studies, University of Texas at Dallas, Richardson, TX 75083.

(Received April 11, 1993;
accepted May 5, 1993.)

Modeling daytime *F* layer patches over Sondrestrom

D. T. Decker, C. E. Valladares, R. Sheehan,¹ Su. Basu,^{1,2} D. N. Anderson,³
and R. A. Heelis⁴

Abstract. A comprehensive, time-dependent, high-latitude, one-species *F* region model has been developed to study the various physical processes which are believed to affect the polar cap plasma density distributions as a function of altitude, latitude, longitude, and local time. These processes include production of ionization by solar extreme ultraviolet radiation and particle precipitation; loss through charge exchange with N_2 and O_2 ; and transport by diffusion, neutral winds, and convection $E \times B$ drifts. In our initial calculations we have modeled highly structured plasma densities characterized by digisonde observations at Sondrestrom using both a time-dependent global convection pattern and spatially localized regions of transient high-speed flow. We find that the model is very sensitive to the details of the time-dependent convection pattern, and both the time dependence and the high-speed flows contribute to the *F*-region structure. Further, when we use high-speed flows based on specific radar observations the simulated density structure is in reasonable agreement with that day's digisonde observations.

Introduction

Over the last 10 or 15 years observations have shown that the winter polar cap *F* region contains a variety of large-scale structures. In particular, it has been found that the type of structure observed depends on the sign of B_z , that is the z component of the interplanetary magnetic field (IMF). What is observed during periods of negative or southward directed B_z are enhanced "patches" of ionization drifting across the polar cap in an antisunward direction [Buchau *et al.*, 1983; Weber *et al.*, 1984, 1986]. These patches come in a wide variety of shapes and scale sizes [Buchau *et al.*, 1985]. The typical sizes range from a few 100 to ~ 1000 km, and the enhancements of plasma densities can be up to an order of magnitude above the surrounding background [Buchau and Reinisch, 1991].

Much of this observed structure is believed to be related to the high-latitude convection pattern and in particular its time dependence [Todd *et al.*, 1986;

Anderson *et al.*, 1988; Lockwood and Carlson, 1992]. It also has been suggested [Foster, 1989] that during storms a source of patches in the polar cap can be plasma transported through the noontime cleft from a region at mid- and low latitudes in the afternoon sector. Other suggested sources of *F*-region structure have been soft precipitation [Kelley *et al.*, 1982], transport of aurorally produced ionization [Knudsen, 1974; Weber *et al.*, 1984], and enhanced plasma loss rates [de la Beaujardiere *et al.*, 1985].

Theoretical studies of high-latitude large-scale structures have primarily involved the use of global *F* region models. Such models consist of solving sets of fluid equations over substantial portions of the globe; in particular, sets of continuity, momentum, and energy equations for various ion species. An additional feature of such models is that they require a number of geophysical parameters as inputs. (An example of the needed inputs will be given in a later section.) Two inputs that are of special interest for modeling large-scale structures are particle precipitation and the magnetospheric convection pattern. The reason this is so is that all the suggested mechanisms for producing patches that we are aware of have involved the behavior of one or both of these two inputs. For the purposes of modeling we have found it useful to classify each of the various mechanisms into one of three types: (1) particle precipitation, (2) global $E \times B$ convection,

¹ Institute for Space Research, Boston College, Newton, Massachusetts.

² Now at National Science Foundation, Washington, D. C.

³ Phillips Laboratory, Geophysics Directorate, Hanscom Air Force Base, Massachusetts.

⁴ Center for Space Research, University of Texas at Dallas.

Copyright 1994 by the American Geophysical Union.

Paper number 93RS02866.

0048-6604/94/93RS-02866\$08.00

and (3) mesoscale $E \times B$ convection. In type 1 the focus has been on spatially restricted regions of precipitation associated with such names as the cleft/cusp/dayside aurora/mantle/lower-latitude boundary layer, etc. The idea is that "dayside" precipitation produces regions of enhanced ionization which then convect into and across the polar cap. For the type 2 mechanism it is the spatial structure and time dependence of the global convection pattern that is critical. The idea is to have changes in the pattern that cause changes in the trajectories of the convecting plasma associated with the "tongue of ionization." In particular, what is wanted are changes that create patches of ionization rather than a continuous tongue of ionization. Our third category involves what we are calling mesoscale convection. The focus here is on spatially localized regions of transient high-speed flows that lead to enhanced ion temperatures which in turn create depleted ionization regions via enhanced ion loss rates. By mesoscale we are considering regions that have scales of hundreds of kilometers. Clearly, the distinction between categories 2 and 3 can be vague, and one can easily construct scenarios that involve elements of both. Nevertheless, this has been a useful division for the purposes of theoretical modeling.

The use of global F region models to study the high latitudes began over a decade ago [Knudsen *et al.*, 1977], and since that time a number of studies have been carried out. In particular, there have been studies examining the effects of various convection patterns [Rasmussen *et al.*, 1986; Sojka and Schunk, 1987] and studies on the transport of large-density structures within those patterns [Robinson *et al.*, 1985; Schunk and Sojka, 1987]. However, for the most part, over the last decade there were few theoretical studies that explicitly focused on how F region structure might be initially produced. Rather most modeling focused on either a few test trajectories and/or used smooth statistical inputs that in turn led to fairly smooth ionospheres. However, there were a few exceptions where the focus was on how to produce a large-scale ionospheric structure. Sojka and Schunk [1986] examined the type 1 mechanism in a study on "the production and decay of localized electron density enhancements in the polar ionosphere." The source of the enhancements were spatially limited regions of auroral precipitation that were designed to simulate cleft precipitation in one case and Sun-aligned auroral arcs in

another. Factor of 2 enhancements were easily produced that were then transported across the nighttime polar cap. This was essentially a feasibility study in that it focused on a few test trajectories and several generic ionization profiles. Another study of Sojka and Schunk [1988] examined the effects of mesoscale electric field structures on the polar cap F region. While this work was designed to simulate plasma trajectories during B_z northward conditions it did illustrate the possibility of enhanced electric fields creating regions of reduced ion densities.

For B_z southward conditions the one attempt that we are aware of that focused on the category 2 mechanism for producing patches was by Anderson *et al.* [1988]. In that study the ionosphere over Thule, Greenland, was simulated assuming a time-varying convection pattern. The time variation consisted of changing between one pattern characterized by an 80-kV cross-tail potential and a 12° polar cap, and another with a 100-kV cross-tail potential and a 15° polar cap radius. The result of making this change was a sevenfold enhancement in the F_2 peak density ($N_m F_2$) at Thule. This study was not a global simulation of the entire polar cap, but rather only trajectories that passed over Thule were considered. So it was not ascertained whether a patch was formed or whether just a ripple in a tongue of ionization was being produced. Thus while there were some preliminary studies in the 1980s on what causes patches, what was lacking was a quantitative demonstration of the definitive mechanism or mechanisms for patch creation.

Our approach to this problem is to continue asking the question that these earlier works essentially posed: If we take a "state-of-the-art" theoretical F region model, can we understand the large-scale ionospheric structure in terms of structure in the geophysical inputs to the model? Alternatively, we may ask if current fluid models have enough physics in them so that temporal and spatial structure in the inputs is sufficient to produce the observed large-scale F region structures? To study this question, we have developed a comprehensive and flexible time-dependent high-latitude F region model. One way we are using this model is to simulate a variety of scenarios for creating F region patches. We have completed an initial study of one such scenario and those results are presented in a recent paper coauthored with the modeling group from Utah State University [Sojka *et al.*, 1993].

However, besides testing theoretical scenarios we also want to keep a measure of reality in our work by attempting to model various observations of the high-latitude *F* region. The purpose of this paper is to describe our *F* region model and our first attempts to use satellite ion drift and incoherent radar observations from a particular day to simulate the *F* region on that day. In this case we study the ionosphere over Sondrestrom on February 19, 1990. The calculations have been designed to examine what we defined as the type 2 and type 3 mechanisms. The type 2 aspect of the work is essentially an extension of the approach of *Anderson et al.* [1988]. Here we initially use nine different convection patterns derived from actual drift measurements made during nine consecutive DMSP F8 satellite passes. This is an appealing approach because if much of the structure in the *F* region depends simply on the time dependence of the cross-tail potential and the polar cap radius, then ion drift measurements from DMSP give us the opportunity to monitor that time dependence. For the type 3 portion of the calculation we include mesoscale regions of high-speed flow as seen in five events during the 4-hour radar experiment performed on February 19.

What we will show is that the sensitivity of the density distribution to the global convection pattern depends critically on the specification of the flow trajectories in the noon and postnoon sectors. Direct measurements of the ionospheric flow in this region are not available from the DMSP F8 satellite. Thus while this data can adequately define the polar cap size and the total cross-polar cap potential, the characteristics that are most critical to our modeling are determined by statistical approximations to the latitude and local time behavior of the dayside potential distribution. Such approximations are shown to be inadequate to model the observed density structure. Besides showing how critical the global convection pattern is, we will also demonstrate the importance of the "locally" observed mesoscale high-speed jets in creating ionospheric structure. The conclusion we present is that in this case both type 2 and type 3 mechanisms are playing a crucial role in the structuring of the ionospheric density. Hence to successfully model such a situation, we need information about both the mesoscale structure as well as the global magnetospheric convection pattern.

In the next two sections we describe the theoret-

ical model and its inputs. This is followed by three sections describing our calculations. We conclude with a discussion and summary of the results and a description of our future plans.

Theoretical Model

The *F* region model used in this study calculates the high-latitude O^+ ion density as a function of altitude, location, and time. The origin of this high-latitude model goes directly back to the theoretical low-latitude *F* region model of *Anderson* [1971, 1973] which has been used over the last 20 years to study low-latitude ionospheric morphology. Over the years, this model has been generalized for use in both the mid- and high latitudes. The two major differences between the low- and high-latitude models are the vastly different electric fields required and the need to include particle precipitation in the high-latitude model. Together, these high-, mid-, and low-latitude *F* region models make up the *F* region component of the global Phillips Laboratory Ionospheric Model.

The model determines the O^+ ion density by numerically solving the time-dependent ion (O^+) continuity equation given by (1):

$$\frac{\partial N_i}{\partial t} + \nabla \cdot (N_i \mathbf{V}_i) = P_i - L_i \quad (1)$$

Here N_i is the ion density, \mathbf{V}_i is the ion velocity, P_i is the production rate, and L_i is the ion loss rate. To solve (1) requires transforming the independent variables from a spherical r, θ, ϕ coordinate system to one which defines directions parallel and perpendicular to \mathbf{B} . After some rearrangement (1) takes the form

$$\frac{\partial N_i}{\partial t} + \mathbf{V}_{i\perp} \cdot \nabla N_i = P_i - L_i - \nabla \cdot (N_i \mathbf{V}_{i\parallel}) - N_i \nabla \cdot \mathbf{V}_{i\perp} \quad (2)$$

The left-hand side of (2) gives the time rate of change of ion density in a reference frame which drifts with the $\mathbf{V}_{i\perp}$ convection velocity where $\mathbf{V}_{i\perp} = \mathbf{E} \times \mathbf{B}/B^2$. The production rate includes production by photoionization, photoelectron impact ionization, particle precipitation, and nocturnal photoionization. The loss rate occurs by charge exchange with N_2 and O_2 . The remaining quantity needed for the right-hand side of the equation is $\mathbf{V}_{i\parallel}$, the velocity parallel to the magnetic field. An expres-

sion for V_{\parallel} [Moffett, 1979] is derived by combining the ion and electron momentum equations. It is within the momentum equations that the effects of gravity, pressure, the ambipolar electric field, and the neutral wind are included in the model.

Substitution of the expression for V_{\parallel} into equation (2) gives a linear diffusion equation for the O^+ density. To solve this parabolic partial differential equation, the finite differencing scheme of Crank and Nicolson is used to produce a set of linear algebraic equations which are then solved using standard techniques for inverting a tridiagonal matrix. By applying this technique along a given magnetic field line, the O^+ density is determined along that field line as a function of time. Solving such an equation naturally requires that both initial and boundary conditions be specified. For the initial condition we can specify any O^+ profile along the field line that is desired. Normally, we use a generic profile appropriate for the initial time of the particular simulation. For the lower boundary condition at the foot of the field line (100 km) we use the local approximation to provide the O^+ density. At the upper boundary, usually above 1000 km, we specify either a O^+ density or flux. Typically, we use a zero flux condition. Finally, by going through this procedure for many field lines a global picture of the O^+ density can be produced. A detailed description of the derivation and numerical solution of (2) can be found in the works by Anderson [1973] and Moffett [1979].

Our model and the Utah State University model [Schunk, 1988; Sojka, 1989] compare in the following manner. The two models use the same approach to simulate the F region ionosphere. The basic difference is that ours is a simpler model. We solve the continuity and momentum equations for one species, while they solve continuity, momentum, and energy equations for multiple species. Obviously, theirs is the more comprehensive model, but our simpler model does give us the ability, without needing supercomputer resources, to do sensitivity studies, test scenarios, and follow the thousands of flux tubes necessary to resolve spatial structures.

Geophysical Inputs

In order to solve (2) a large variety of geophysical input parameters must be specified. It is these same parameters that we were referring to in the intro-

duction when we stated that our purpose was to see if variability in the inputs will produce the observed structure in the ionosphere. In this section we briefly describe those parameters.

1. Neutral atmospheric densities of N_2 , O_2 , and O , and the neutral temperature as a function of altitude, location, time, solar activity, and magnetic activity are obtained from the mass spectrometer/incoherent scatter (MSIS-86) neutral atmosphere model [Hedin, 1987].

2. The horizontal neutral wind as a function of location and time is obtained from one of three available wind models: the empirical model HWM-87 [Hedin et al., 1988], the empirical model HWM-90 [Hedin et al., 1991], and the theoretical model VSH [Killeen et al., 1987].

3. The ion and electron temperatures as a function of altitude and time are based on the analytic functions of Strobel and McElroy [1970] which in turn were derived from incoherent radar scatter measurements made at Millstone Hill during solar minimum. Another temperature that is needed is the effective temperature that is used in evaluating the ion loss rate. We use the simple expression due to Schunk et al. [1975] which contains an explicit dependence on the square of the magnetospheric electric field.

4. Solar extreme ultraviolet (EUV) fluxes are derived from the reference spectrum SC#21REFW and the associated $F_{10.7}$ algorithms of Hinteregger et al. [1981]. This detailed spectrum is averaged into 11 energy intervals before being used in calculating the photo production of O^+ .

5. The production of O^+ from photoelectron impact ionization is based on the work of Richards and Torr [1988], where they parameterized the results of electron transport calculations of ionization rates. The rates are given as a fraction of the photoionization rate.

6. The characteristics of the auroral electron precipitation are obtained from the statistical patterns of electron integral energy flux and average energy as measured by DMSP satellites [Hardy et al., 1987].

7. The nighttime scattered EUV photons are assumed to consist of three lines at 834Å, 584Å, and 304Å. The intensities are based on Knudsen et al. [1977] and Chakrabarti et al. [1984]. The nocturnal ionization rates are calculated by assuming that these photons are incident at the top of the ionosphere.

Potential with corotation in mag. coord.

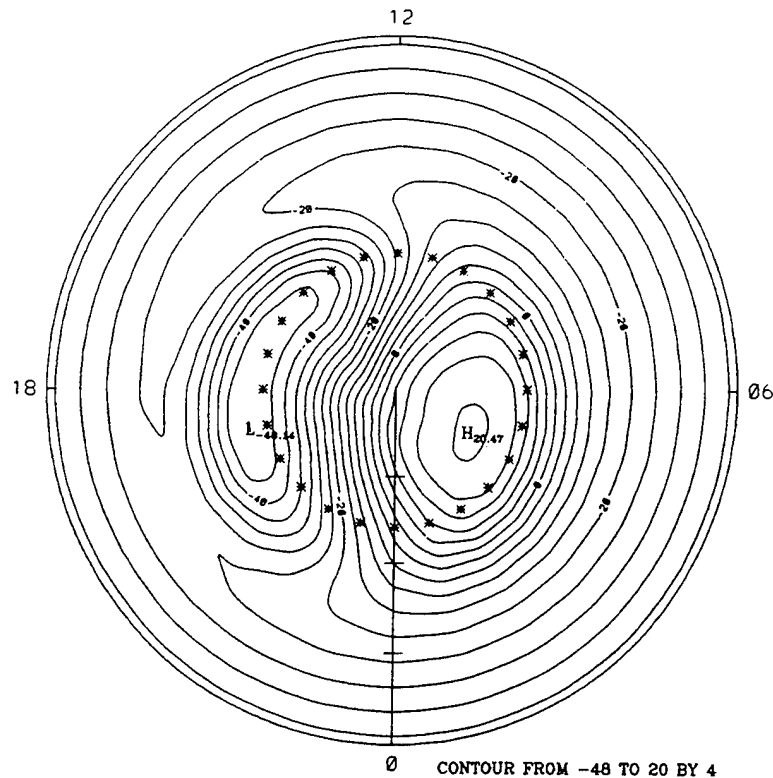


Figure 1. Contours of potential for the combination of corotation with a Hairston and Heelis magnetospheric convection pattern. The contours are drawn at 4-kV intervals and are shown in a corrected magnetic latitude (50° – 90°) and magnetic local time polar plot. The asterisks mark the position of Sondrestrom for each hour of local time.

8. Several $E \times B$ convection patterns are implemented for use in the model [Heelis *et al.*, 1982; Heppner and Maynard, 1987; Hairston and Heelis, 1990]. The inputs that specify a particular convection pattern vary, depending on which one is being used, and will be discussed later.

Preliminary Simulations

As described in the introduction, our purpose is to simulate the ionosphere over Sondrestrom for a particular day by including the effects of both a time-dependent global convection pattern and mesoscale high-speed flows. In order to provide a context for our simulations we discuss in this section several preliminary issues and calculations.

Since one of our primary interests is on the effects of time-varying convection, we begin the section with an example of one of the convection patterns that we will be using. In Figure 1 we show

contours of electric potential for a Hairston/Heelis (HH) magnetospheric convection pattern combined with the corotation potential. The contours are drawn at 4-kV intervals and are shown in corrected magnetic latitude and local magnetic time for 50° to 90° north. These contours are also the trajectories of the plasma moving due to the $E \times B$ drift that results from the presence of this potential. The asterisks mark the position of Sondrestrom for each hour of local time. This plot is UT independent because the corotation potential is calculated neglecting the difference between the geographic and geomagnetic poles. However, for all other aspects of the model the offset of the poles is included, and hence other "UT effects" can be modeled.

In Figure 1 we can identify three types of trajectories. First, there are the trajectories that make up the evening and morning cells, where the plasma motion is fairly restricted to circulation about the

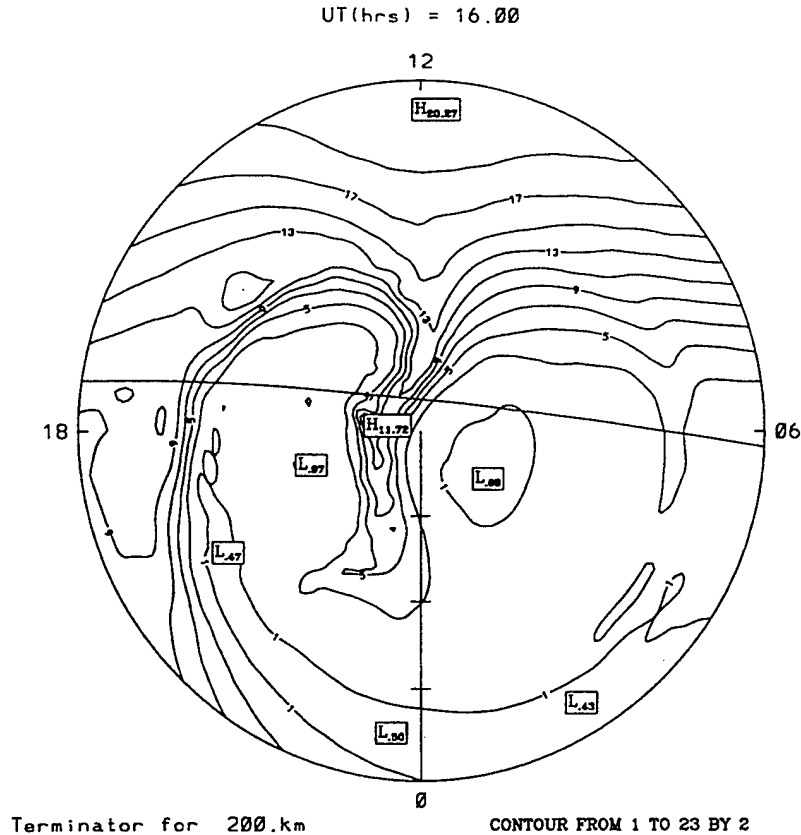


Figure 2. Contours of calculated peak electron density ($\times 10^5 \text{ el cm}^{-3}$) as a function of magnetic latitude (50° – 90°) and magnetic local time during December, solar maximum conditions at 1600 UT. Note the tongue of ionization (TOI) which crosses the polar cap as a result of strong antisunward drift. The line running across from around 1800 UT to near 0600 UT is the location of the terminator at 200 km altitude.

minimum and maximum of the potential. The second type of trajectories is the nearly circular ones out at lower latitudes where the plasma is basically corotating. Finally, the third class of trajectories are those where plasma from lower latitudes can be brought in and across the polar cap. These trajectories are very important because they provide a path by which higher-density plasma can be brought into the polar cap and form what is called a tongue of ionization (TOI), and in all the scenarios we have seen for making patches, these trajectories play a critical role.

We next want to illustrate the high-latitude *F* region that results from using a time-independent convection pattern such as given in Figure 1. In Figure 2 we present a snapshot at 1600 UT of the peak F_2 density ($N_m F_2$) from such a simulation for December solar maximum northern hemisphere

conditions. What is shown are contours of $N_m F_2$ in units of 10^5 cm^{-3} as a function of corrected magnetic latitude (50° – 90°) and magnetic local time. The straight line running across the middle of the plot is the day/night terminator for 200 km. What we see is the same generic picture that has been produced by nearly all of the earlier theoretical studies of high-latitude morphology: a TOI is created by virtue of what we labeled the third class of trajectories in the convection pattern. One difference of note compared to earlier studies is that this picture involves around 4000 individual trajectories as compared to the few hundred of earlier studies. This is no particular advantage in this steady state convection case but is necessary in cases where one wants to resolve patch structure. Another point of interest related to patches is that the TOI provides a ready supply of enhanced densities giving the level of

Millstone Feb 19 1990

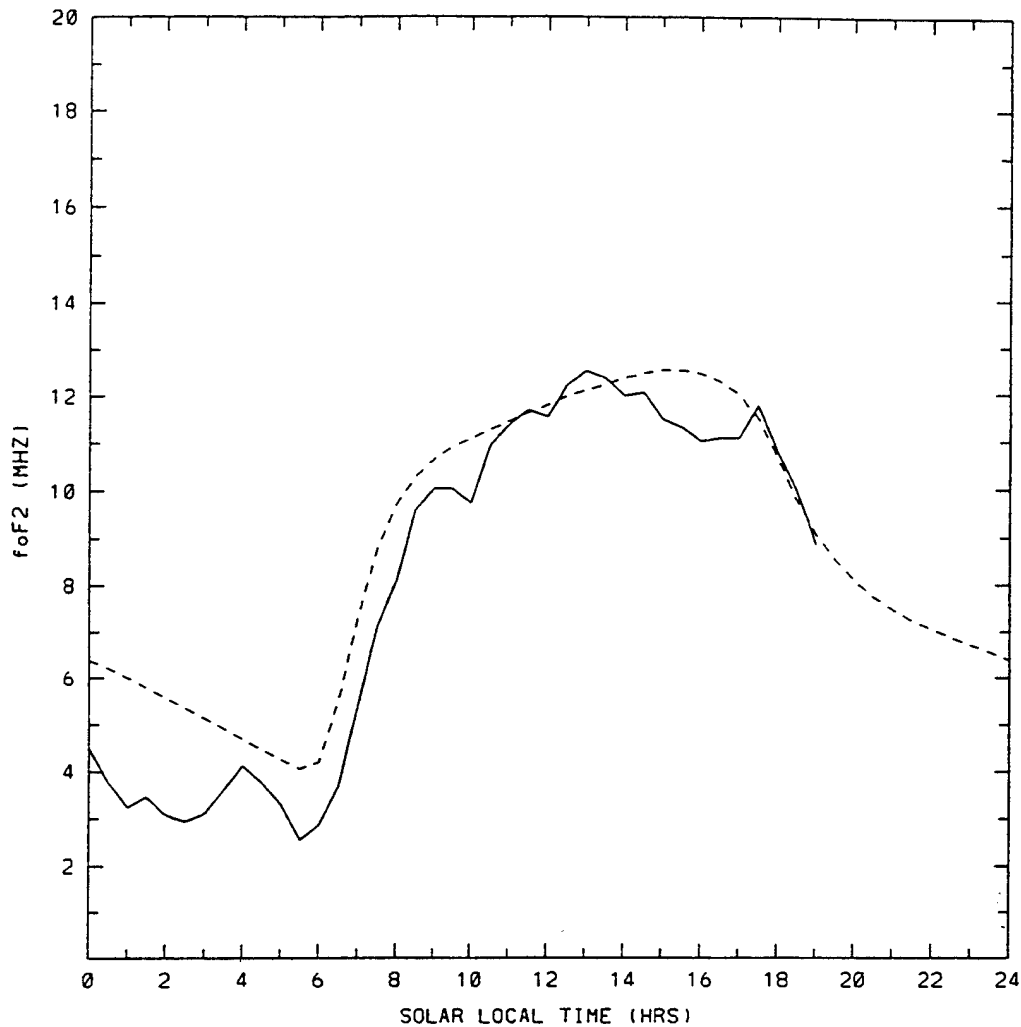


Figure 3. The critical frequency of the F_2 peak (f_oF_2) in MHz as a function of solar local time at Millstone Hill on February 19, 1990. The observed f_oF_2 (solid curve) is compared with that from a simulation (dashed curve).

contrast that is observed between patches and the background plasma. We can also understand the Anderson *et al.* [1988] results in terms of such a simulation. When they used the convection pattern with a 12° radius, Thule was not under the TOI, but saw plasma trajectories from the dusk cell and hence low N_mF_2 . When the change was made to the 15° radius pattern, a broader TOI was produced such that it then passed over Thule, resulting in a sevenfold enhancement of N_mF_2 .

We now turn to the day of interest, February 19, 1990. We begin our discussion of the day by presenting a simulation of the ionosphere above Millstone Hill and comparing with digisonde observa-

tions. This allowed testing of the model for that day without the complication of the $\mathbf{E} \times \mathbf{B}$ convection. In Figure 3 we show f_oF_2 from the simulation (dashed curve) and the observed f_oF_2 from the Millstone digisonde (solid curve). This type of agreement is typical of recent modeling results presented at the Coupling Energetics and Dynamics of Atmospheric Regions (CEDAR) Meeting, in the workshop entitled Problems Related to Ionospheric Modeling and Observations (PRIMO) and gives us some confidence that on this day we were producing reasonable densities in the daytime midlatitudes.

For the first calculation at Sondrestrom we set the magnetospheric convection to zero and again

Sondrestrom Feb 19 1990

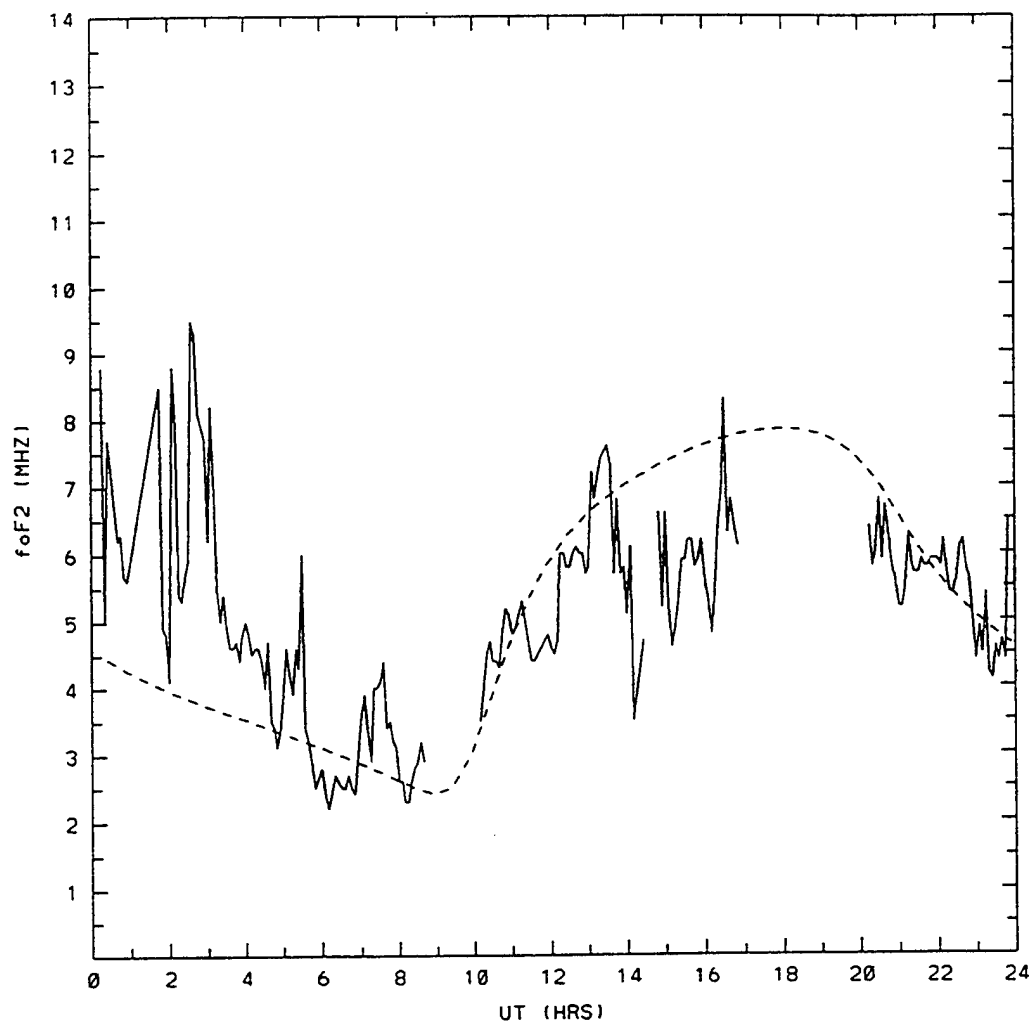


Figure 4. The critical frequency of the F_2 peak (f_oF_2) in MHz as a function of universal time at Sondrestrom, Greenland, on February 19, 1990. The observed f_oF_2 (solid curve) is compared with that from a simulation (dashed curve) having zero magnetospheric convection.

included only corotation. The idea was not that we expected corotation to be occurring at Sondrestrom, but rather we wanted to have a baseline to compare with when we did include convection. In Figure 4 we show the calculated f_oF_2 compared to digisonde data taken on February 19, 1990, at Sondrestrom. The dashed curve represents the simulation, and the solid line represents the observations. Examining the results we see that with corotation there is a complete lack of the type of structure seen in the data. In the early morning the data show considerable structure which we could speculate is due to some sort of remnants of a TOI

reaching Sondrestrom around local midnight. Turning to the afternoon we again see considerable structure in the data around the time when Sondrestrom might be coming under a TOI. Though somewhat surprising, you will note that the envelope of the observed densities are comparable to what corotation produces.

Simulating Time-Dependent Convection

In this section we describe our attempts to model the ionosphere over Sondrestrom using our type 2 mechanism: time-dependent global convection. The

approach used was an extension of the Anderson et al. scenario. That is we allowed the cross-tail potential drop and the polar cap radius to change at specific times during the simulation. Our approach differed from Anderson et al. in four ways: (1) we considered nine different convection patterns not just two, (2) the patterns were derived from DMSP satellite data on the given day, (3) all the parameters that define the Hairston/Heelis convection pattern were allowed to change, and (4) we compared calculated $N_m F_2$ with digisonde data from that day. We should mention that the point of comparing to data was not that we expected to get detailed agreement; rather the data gave us a "yardstick" to use in assessing our results.

The nine patterns that were used for the simulation were derived from ion drift measurements made during nine F8 satellite passes between 0241 and 1615 UT on February 19, 1990. During this period B_z was both positive and negative, while B_y remained mostly negative. In seven of the nine passes a two-cell pattern seemed to be established, and we used *Hairston and Heelis* [1990] patterns. For the remaining two passes we used *Heppner and Maynard* [1987] (hereinafter referred to as HM) for B_z weakly northward and B_y negative. Over these nine patterns the most dramatic differences were in the cross-tail potentials (varied from 41 to 95 kV) and the polar cap radii (ranged from 11° to 20°). For this calculation rather than running a full global simulation, we followed *Anderson et al.* [1988] and just calculated those trajectories that passed over Sondrestrom. This was done by selecting the particular ground location (Sondrestrom) and times at which we wanted to calculate altitude profiles of the O^+ density. The profiles were calculated by following flux tubes, whose trajectories passed over the station at the specified times. In this simulation we started each trajectory 6 hours before it reached Sondrestrom. The initial location was found by tracing backward from Sondrestrom along the trajectory dictated by the convection pattern. On February 19, 1990, interplanetary magnetic field measurements were available from just after 0200 UT to just before 1700 UT. Since we wanted to run the simulation during periods when we knew the IMF, this limited our simulation at Sondrestrom to just after 0800 UT to around 1700 UT. In Figure 5 we see the results of using these nine patterns. Again we compare calculated $f_o F_2$ values with observed. What is immediately obvious is the large enhancement in the simulation at around 1400 UT.

This is caused by Sondrestrom rotating under a strong TOI a little bit before local noon. Clearly, the enhancement is too large, but there is also the problem that other than one large peak no structure was produced, whereas the observations show a highly structured ionosphere.

One question that comes to mind is how much confidence can we have in the convection patterns derived from the F8 data, especially for those critical TOI-producing trajectories that pass through the noon/postnoon region, where the magnetospheric dusk cell convection and corotation are roughly equal but are in opposite directions. The first point to mention is that F8 is in a basically dawn/dusk orbit and gives no direct information about the afternoon sector. Thus the trajectories that bring the large densities into Sondrestrom are essentially defined by the assumptions used in constructing the mathematical model of Hairston and Heelis. In particular, the assumptions that the convection reversal boundary is a circle and that the decay of the magnetospheric potential equatorward of that boundary is the same at all local times are critical and in general not true. The assumed position and width of the "throat," which are also critical to the tongue trajectories, are not based on the day's F8 data, but are statistically derived from months of observations.

Another point that we need to discuss is the variability of the IMF on this day. Figure 6 shows 1-min averages of the three components of the IMF that were measured by the IMP 8 satellite on February 19, 1990. What we see is a day where B_z changes sign on almost an hourly basis with the longest period of negative B_z (1300–1400 UT) being just less than an hour. While a fairly broad consensus has been established regarding the two-cell convection pattern during periods of southward B_z , disagreements and uncertainties remain concerning the patterns during periods of northward B_z . Even more uncertainty exists during those periods when the sign of B_z is undergoing frequent change. As a result even though in seven of the nine F8 passes a two-cell pattern appeared to be established, under these highly variable conditions it seems very probable that simply changing every hour or so between different patterns may not even crudely represent the actual time evolution of the convection pattern.

Our final point concerns the radar observations that were made at Sondrestrom over a 4-hour experiment from around 1100 to 1500 UT on February 19 [Valla-

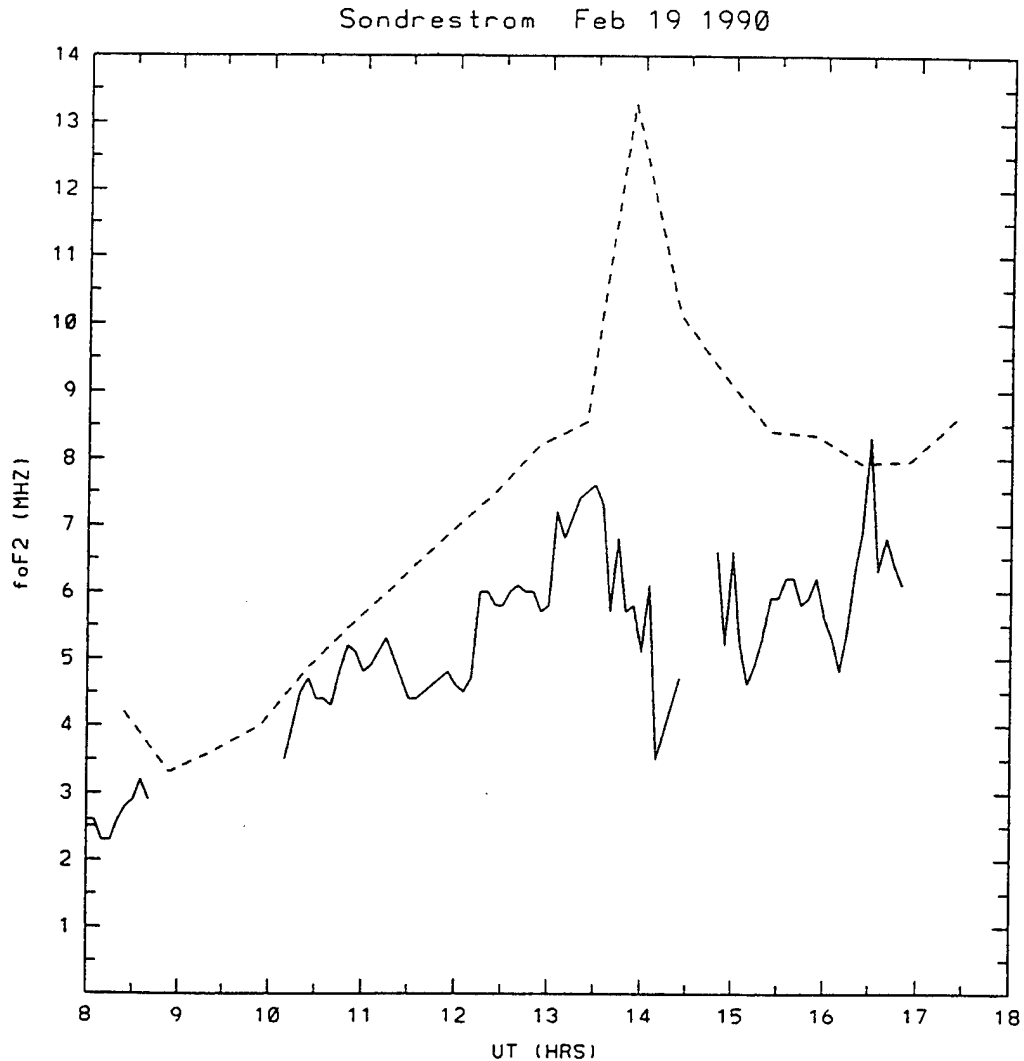


Figure 5. The critical frequency of the F_2 peak (f_oF_2) in megahertz as a function of universal time at Sondrestrom, Greenland, on February 19, 1990. The observed f_oF_2 (solid curve) is compared with that from a simulation (dashed curve) using a sequence of nine magnetospheric convection patterns (see text).

dares et al., this issue]. The experiment conducted was designed to map electron density and the velocity field over a large area. While the thrust of the experiment was to examine daytime transient events, it does provide, to the west of Sondrestrom, semicircle snapshots of the convection pattern. We can then compare these observations to what Sondrestrom would see if the patterns we used were observed by the radar. Ignoring the transient mesoscale events seen in the radar we still find that at many times serious differences exist between the radar observations and the F8-derived patterns both in the magni-

tude and the direction of the drifts. We also note that the regions viewed by the radar are not directly sampled by the F8 satellite.

Our conclusion is that the large discrepancy between the digisonde data and our model results tells us little about the F region model but most likely reflects the fact that a series of F8 passes alone are inadequate to describe accurately the time evolution of the global convection pattern under the conditions present on February 19. However, before we can move on and study the effects of the mesoscale convection events, we still have the

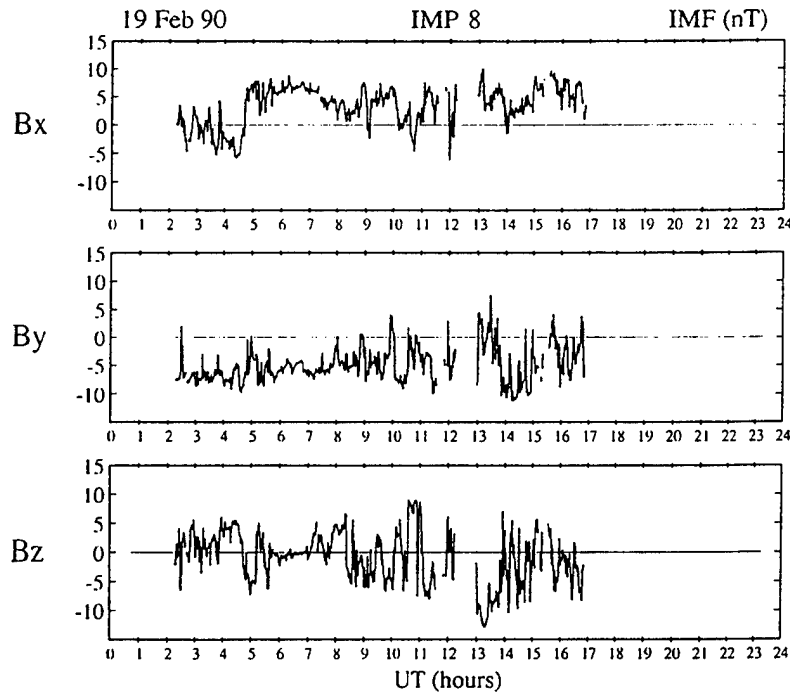


Figure 6. The interplanetary magnetic field data measured on February 19, 1990, by IMP 8. Shown from top to bottom are 1-min averages of the three IMF components in GSM coordinates. All three traces are plotted in units of nanoteslas.

problem of determining whether we can find any time-dependent convection pattern that will reproduce the large-scale behavior of the digisonde data. So the question is how sensitive are the results in Figure 5 to the details of the type 3 trajectories, or alternatively, can our model produce anything radically different by using different combinations of the patterns we have available. To answer this, we made a series of simulations using many of the convection patterns available: the Hairston/Heelis with other parameters, different versions of the Heppner/Maynard A, DE, and BC patterns, and various mixtures of all these. What we found was that the results were extremely sensitive to the type 3 trajectories. We could make what was originally in Figure 5 a 13-Mhz peak at around 1400 UT into a thinner peak (less than 30 min in length), a broader peak (3.5 hours long), an earlier peak (1300 UT), a later peak (1600 UT), a smaller peak (9 Mhz), or a double peak. However, of greatest interest in this case is a judicious combination of six Hairston/Heelis and Heppner/Maynard (HHHM) patterns that give the results shown in Figure 7. Here we again show simulated f_oF_2 (dashed line) compared

to digisonde data (solid line). We see that the large peak is gone and the results are much more in line with the observations. The points here are (1) there is great sensitivity to the details of the time-dependent global convection pattern and (2) some structure can be produced by very few changes in the global convection pattern. The 1-Mhz step just before 1400 UT results from a single change from a Hairston/Heelis pattern to a Heppner/Maynard DE pattern at 1330 UT. The 1-Mhz step just after 1600 UT comes from the change back to the Hairston/Heelis pattern. The sensitivity to different patterns can be seen by just comparing Figures 5 and 7. Another example of the sensitivity to details is if we make the switch from Hairston/Heelis to Heppner/Maynard just 30 min later at 1400 UT rather than a 1-Mhz step down to 6.5 Mhz, we get a thin peak up to 9.75 Mhz followed by the drop to 6.5 Mhz.

Simulating Mesoscale Convection

It seems appropriate at this point, given the problems discussed in the previous section to com-

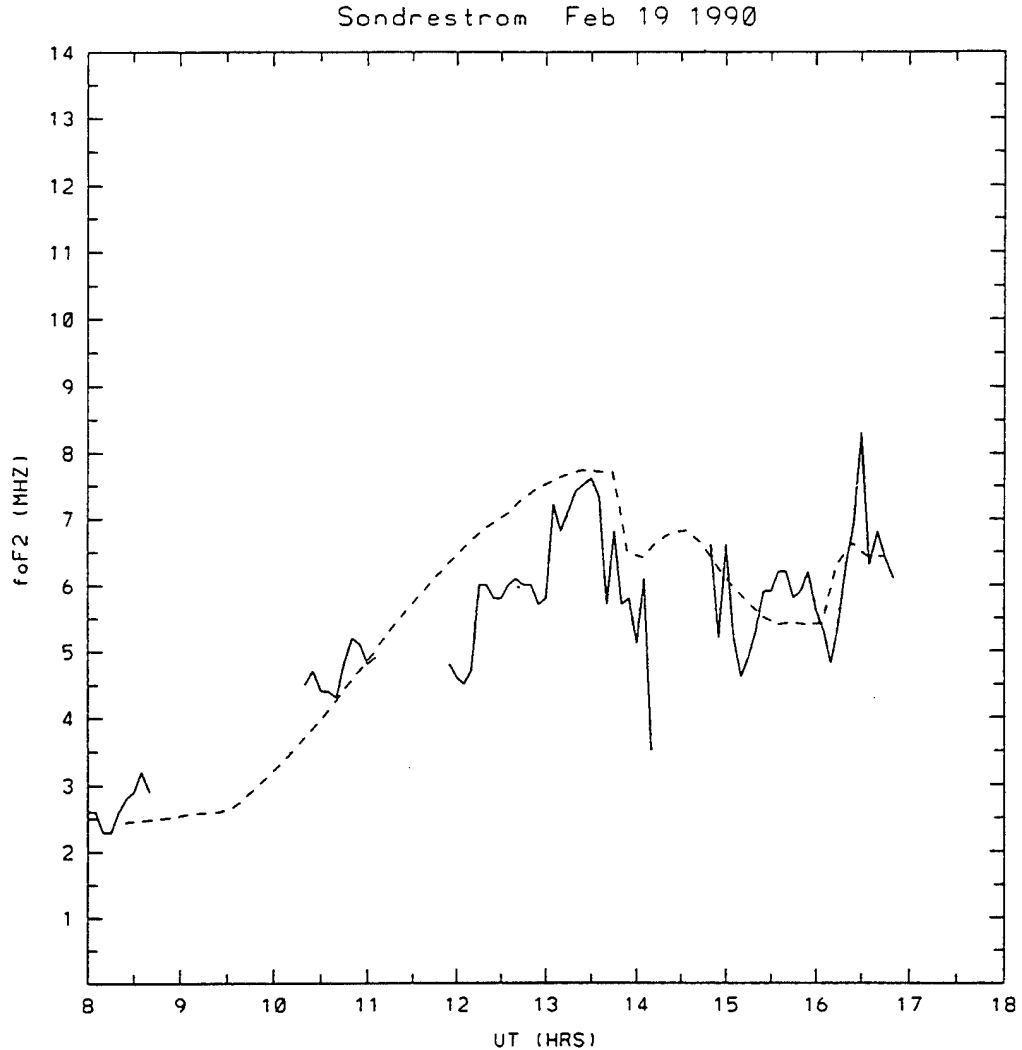


Figure 7. The critical frequency of the F_2 peak (f_oF_2) in megahertz as a function of universal time at Sondrestrom, Greenland, on February 19, 1990. The observed f_oF_2 (solid curve) is compared with that from a simulation (dashed curve) using a sequence of six magnetospheric convection patterns (see text).

ment on why we chose to study a day that appears to be so ill-suited for modeling. The sole reason was the availability of radar observations that included several transient high-speed plasma flow events that were collocated with regions of low F region density [Valladares *et al.*, this issue]. Our hope was to use the radar drift observations to model what we have labeled as the type 3 mechanism of patch formation or what in this case Valladares *et al.* called density break-off events. However, we also felt that we could not just deal with the flow events but had to treat the time-dependent global convec-

tion that these events are embedded within. Thus we found ourselves dealing with time-dependent convection under less than ideal conditions.

Having found a time-dependent convection pattern that reproduces the larger-scale behavior of the digisonde data, we then turned to the possible role of the observed flow events in creating F region structure. As already described in the previous section, the radar experiment on February 19 was designed to study transient daytime events. What was seen were five events that consisted of fast plasma flows in excess of 2 km s^{-1} (requiring

electric fields of 100 mV m^{-1}). These flows were collocated with enhanced F region ion temperatures exceeding in some cases 4000°K . These fast plasma jets were also collocated with regions of low F region density, and Valladares et al. suggest that the depletions are the result of enhanced ion loss rates due to the large ion temperatures. For the event discussed by Valladares et al. [this issue] the jet was determined to be at least 2000 km in longitude and to cover 300 km in the N-S direction. Under such conditions they estimated that a flux tube would reside in the jet at least for a time as long as 16 min. On the basis of previous theoretical calculations, they concluded that this was sufficient time for these large electric fields to cause a sizeable loss of O^+ density. By examining both radar and magnetometer data, they were able to describe the temporal evolution of one of the events. It was seen to arise west of Sondrestrom, intensify while drifting over Sondrestrom, and then turn poleward and drift up the coast of Greenland as it decayed away.

Our interest was to include these events in our simulation of the ionosphere over Sondrestrom. However, as described above, these events can have quite a complex temporal behavior that is not well understood and that we are not yet in a position to treat in a detailed manner. So we chose not to attempt a simulation of all the details of such an event but rather to include just two features of such events: (1) the time of their occurrence and (2) the order of magnitude of their electric fields. The electric fields are approximated by adding small circular regions in which the potential varies like a triangular sawtooth across any diameter. These additions are done at the observed times of the five events in the vicinity of Sondrestrom for a period of around 16 min each. The regions have a radius of 3° and a potential amplitude of 25 kV. The expected effect is that during these events, Sondrestrom will pass beneath plasma that has been heated for periods of up to 16 min.

In Figure 8 we show the results (short dashes) of including events during the following periods: 1108–1124 UT, 1138–1154 UT, 1230–1300 UT, and 1408–1424 UT. The event starting at 1230 UT is a combination of the third and fourth observed events. The long dashed curve is the simulation without the high-speed flow events that was shown in Figure 7. The solid curve is again the digisonde data. We see that the mesoscale events have created significant depletions in f_oF_2 as compared to

the no event simulation, and the times and magnitudes of these depletions are in quite nice agreement with some of the structure in the observations.

Discussion and Summary

We have seen, as have earlier modelers, that time-independent convection can lead to tongues of ionization bringing large ion densities into the polar cap. In an attempt to simulate structured enhanced plasma density observed over Sondrestrom, we performed calculations including the effects of time-dependent global convection and mesoscale convection events. While the particular day studied was chosen because of the observations of mesoscale events, it is necessary to deal with both the events and the global convection that those events are embedded within. Our initial strategy was to use DMSP F8 ion drift data to infer nine different convection patterns that were then used to construct a crude time-dependent global convection pattern. We did not expect that switching between fixed convection patterns every couple of hours was going to create the type of structure seen in the digisonde data. Examination of the observed F_2 peak concentration in Figure 4 shows that variations exist on many different scale sizes. Quite large variations are seen with a time variation of less than 30 min. Assuming that the signal is produced by density structures moving through the digisonde's field of view at about 500 m s^{-1} , this corresponds to a spatial structure with dimensions of 100 km. If all we do is change our convection pattern on the timescale of hours, we do not expect to reproduce all the small-scale variations. However, using the baseline concentration obtained by assuming a corotating ionosphere (Figure 4), we see deviations from this baseline over timescales of several hours. In particular, we note that a significant reduction from corotation is seen approximately during the period 1400–1600 hrs UT.

Our comparison made between model results and data for Millstone tells us that the amounts of ionization that we produce at midlatitudes are reasonable. Our F8 derived simulation for Sondrestrom produces a basically unstructured ionosphere with a TOI producing a single large peak. The digisonde data at Sondrestrom says just the opposite: the high-density peak is not present and the actual ionosphere is a highly structured one. We believe the major problem is that our description of

Sondrestrom Feb 19 1990

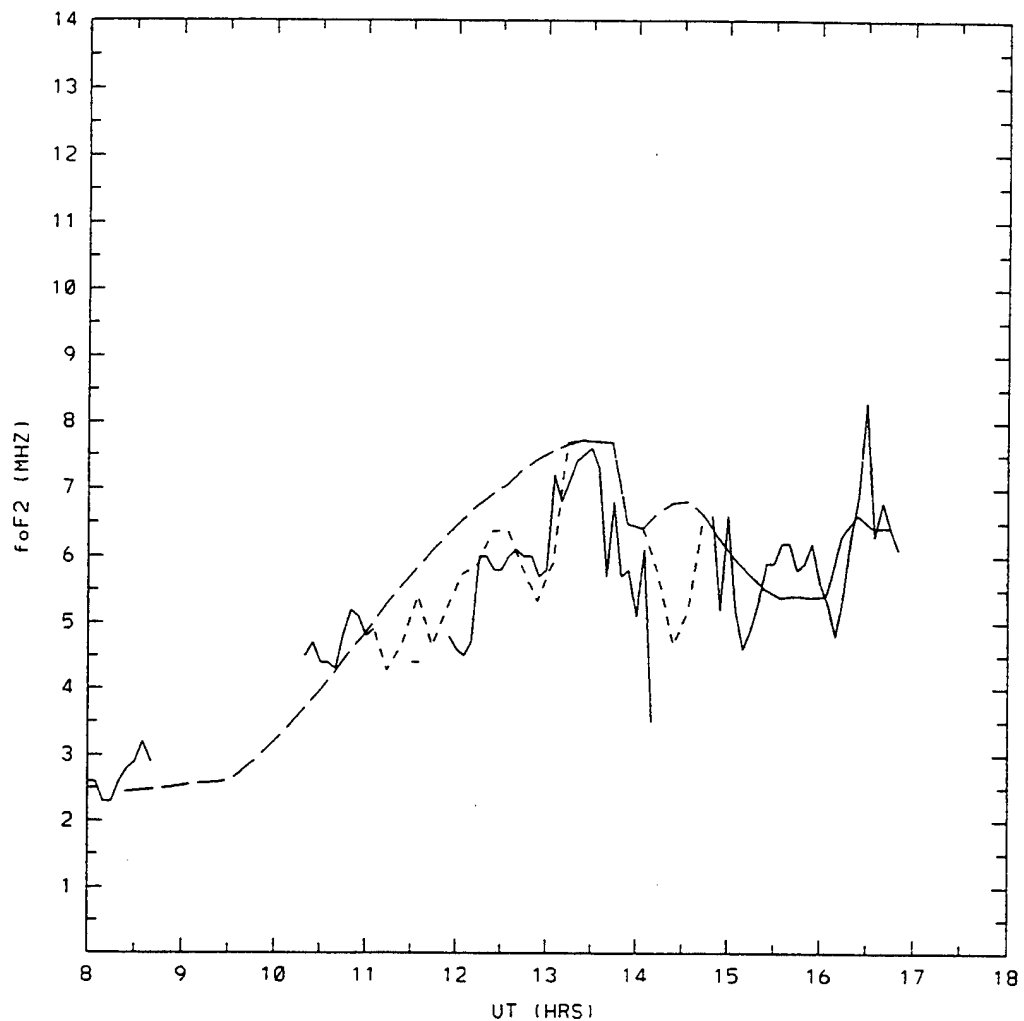


Figure 8. The critical frequency of the F_2 peak (f_oF_2) in megahertz as a function of universal time at Sondrestrom, Greenland, on February 19, 1990. The observed f_oF_2 (solid curve) is compared with results from two simulations. The long dashed curve is from the simulation shown in Figure 7. The short dashed curve is from a simulation that includes five high-speed flow events (see text) as well as the previously used sequence of six magnetospheric convection patterns.

the ionospheric convection pattern and the specification of when changes in the pattern occur are inadequate. The reasons for this are (1) F8 does not sample the critical afternoon sector, (2) the IMF is highly variable, (3) present convection models are well established only for periods of southward B_z , and (4) the observed radar drifts do not match well with the convection patterns used.

Given that we could not confidently derive the time-dependent convection from observations, we then asked if we could find any combination of

convection patterns that would reproduce the large-scale behavior of the digisonde data. We were able to find such a pattern by using a sequence of six Hairston/Heelis and Heppner/Maynard (hereinafter referred to as HHHM) convection patterns. The large difference between the F8-based simulation shown in Figure 5 and the HHHM results shown in Figure 7 can be understood by examining the trajectories that bring plasma in over Sondrestrom. In Figure 9 we show three such trajectories plotted in a geographic latitude and local solar time coordinate

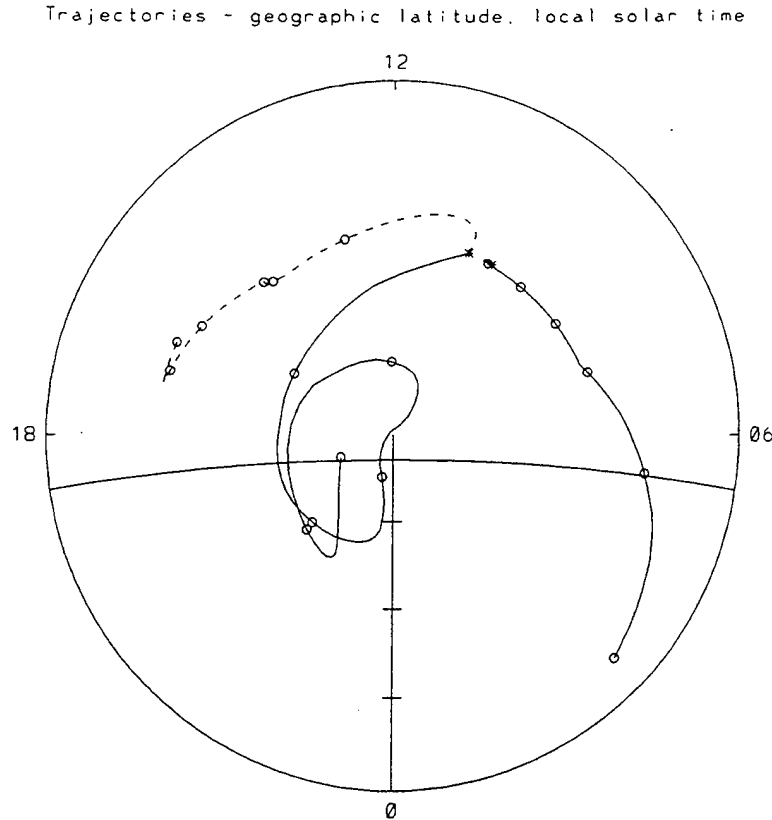


Figure 9. Plasma trajectories in a geographic latitude (50° – 90°) and local solar time coordinate system. Asterisks mark the end of the trajectories at Sondrestrom. The space between the circles on each curve represents 1 hour elapsed time. The solid curve is from the simulation using a sequence of six magnetospheric convection patterns. The dashed curve is from the simulation using a sequence of nine magnetospheric convection patterns.

system. The asterisks mark the location of Sondrestrom, and the circles mark the trajectories into 1-hour segments. The solar terminator at 300 km is also drawn in the figure to make it easy to see when a trajectory is in sunlight. The dashed trajectory is from the nine-pattern F8-based simulation, and the solid line trajectories are from the HHHM simulation (without mesoscale events). The large peak in Figure 5 at 1354 UT is the result of the dashed trajectory that is shown arriving at Sondrestrom at 1030 local solar time. We can see that the plasma spends 6 hours meandering about in the sunlit afternoon. The peak is the result of both a large photoionization source and of upward drift due to the vertical component of the $\mathbf{E} \times \mathbf{B}$ drift. This is an example of what we previously referred to as the type 3 trajectories that can produce a tongue of ionization, an example of which is shown in Figure 2. Referring to the potential pattern shown in Figure

1 we see that this trajectory is passing through the stagnant region where the magnetospheric dusk cell convection is combining with corotation to produce small electric fields and hence small drifts.

Looking at the trajectory from the HHHM simulation (the solid line) that arrives at Sondrestrom at 1354 UT we see that in that case the plasma has had a completely different history. In its final approach into Sondrestrom it has spent less than 2 hours in sunlight, and as can be seen in Figure 7 has produced a dramatically smaller F_2 peak density. This trajectory is an example where the drift is dominated by the magnetospheric dusk convection cell which, in this case, is from a Heppner/Maynard pattern.

The third trajectory shown in Figure 9 is for plasma arriving at Sondrestrom at 1324 UT and is included to illustrate the difference in trajectories before and after the sharp decrease that takes place

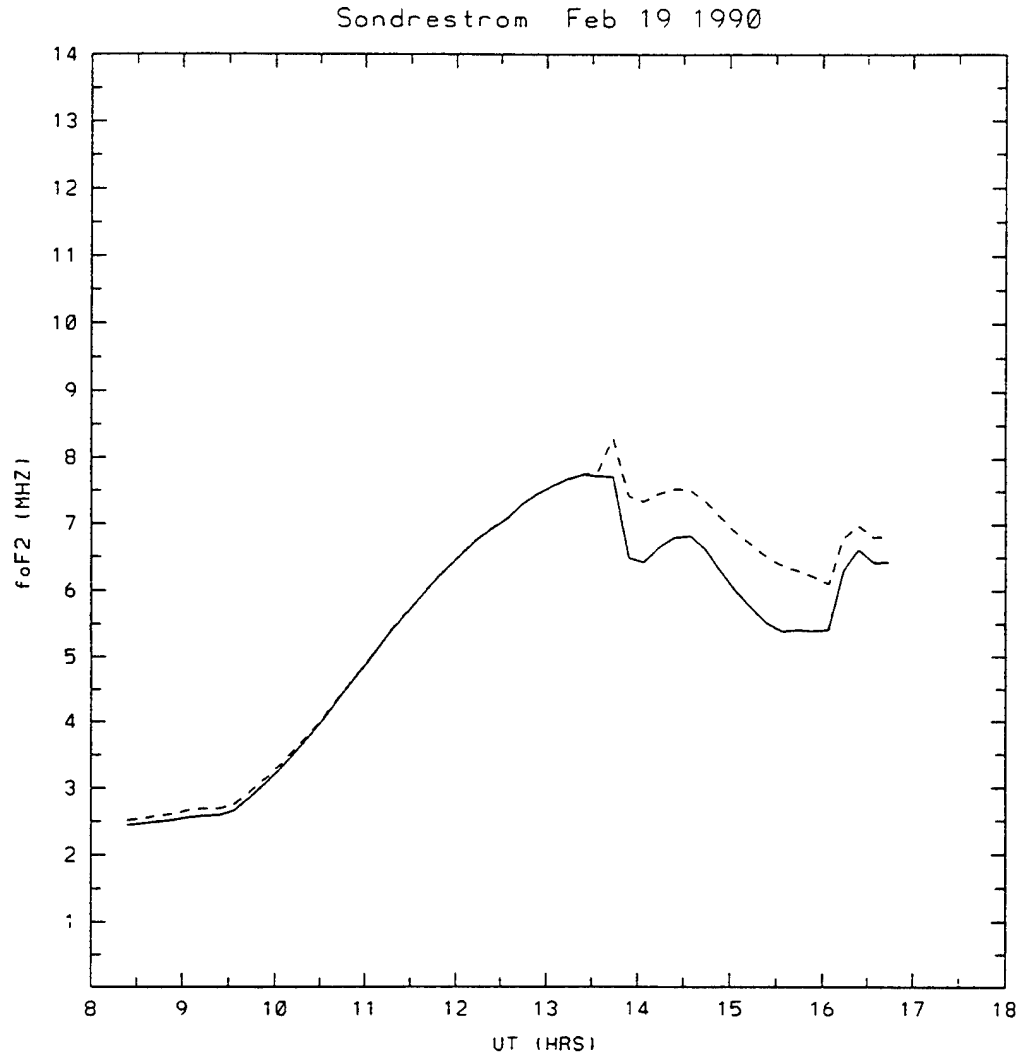


Figure 10. The simulated critical frequency of the F_2 peak (f_oF_2) in megahertz as a function of universal time at Sondrestrom, Greenland, on February 19, 1990. The solid curve is from the simulation using a sequence of six magnetospheric convection patterns (also shown in Figure 7). The dashed curve is from a simulation using the same sequence of six magnetospheric convection patterns, except the heating due to electric fields is turned off.

in the HHHM results when changing from a Hairston/Heelis to a Heppner/Maynard pattern (see Figure 7). Looking at the two HHHM trajectories, we see that they come from two very distinct regions. However, when we examine why the two trajectories produce different densities, we find it is not just because of different sources and different vertical drifts but also because they have different amounts of heating due to the electric fields. In Figure 10 we show the original HHHM simulation (solid curve) along with a calculation where the heating due to

electric fields has been turned off. We can see that after 1330 UT, when we switched to a Heppner/Maynard pattern, the f_oF_2 calculation with heating is reduced over the nonheating calculation. This reduction is due to electric fields in the Heppner Maynard pattern, causing an enhanced temperature, which in turn increases the O^+ loss rate due to the temperature dependence of the charge exchange reaction rates.

Finally, we want to emphasize that the HHHM pattern is one of expedience, not one derived from

that day's drift observations. The main point is that the sensitivity of our results to the global patterns used illustrates the key role played in ionospheric structuring by the details of time-dependent convection.

Our simulation of the high-speed flow events illustrates the potential of transient regions of high electric fields to also cause structuring of the *F* region. We find that including the five observed events in the simulations creates depletions that are of the same order of magnitude as those observed in the digisonde data. Examination of Figure 8 shows steps in the data around 1200 and 1300 UT, whose sizes are reasonably reproduced by the simulation. The step down to lower frequency at around 1400 UT is a nice example, where we see that both the time-dependent global convection and the mesoscale event contribute to the observed structure. As we have discussed, the radar data suggests that the depletions associated with these events are the result of increased ion loss rates caused by enhanced ion temperatures from electric field heating of the ions. However, on the other hand, when we add the high-speed flows into the global convection pattern we can also perturb trajectories so that the plasma that reaches Sondrestrom comes from a different location. Thus we are interested in assessing how much of the depletions are due to enhanced ion loss rates and how much are due to changing where the plasma comes from. We do this by performing a 5-event HHHM simulation with the heating due to electric fields turned off. In Figure 11 we present results from three simulations: (1) HHHM with no events and no heating (solid curve), (2) HHHM with five events and no heating (long dashes), and (3) standard HHHM with five events and heating on (short dashes). Looking at each event we see that in all cases the simulated depletions result from a mixture of both processes. The first event between 1100 and 1130 UT is roughly due in equal amounts to increased ion loss rates and changed trajectories. The second event is initially similar, but toward 1200 UT, it becomes dominated by increased ion loss. From 1215 to 1230 it is the change in trajectory that makes the difference. The combined events from 1230 to 1300 UT are seen to be dominated by increased ion loss rates (this is the event studied in detail by Valladares et al.). Finally, the event at around 1430 is another example of both processes playing a role. So the key point is that the simulated transient mesoscale events created signif-

icant structure, but they did so via enhanced ion loss rates and by changing where the plasma comes from.

Because the mesoscale events occur embedded within a global convection pattern, we can ask how dependent on the global patterns used are our conclusions concerning the mesoscale. To examine this, we performed other event simulations using quite different sets of global convection patterns. We found that the timing of the event-produced depletions and the relative depth of the depletions were comparable in all simulations. Hence we believe that our conclusions concerning the importance of the mesoscale events are independent of the convection patterns used. Finally, we want to reemphasize that these are not detailed simulations of the temporal and spatial behavior of the mesoscale events but low-order approximations of their behavior. As such, we believe their importance is due to what they say about the potential of mesoscale events to produce structure rather than to whether they can reproduce a particular day's data in great detail.

We have shown that both the type 2 and type 3 mechanisms can play a role in structuring the *F* region ionosphere. However, we have found that our division between the two mechanisms is even cloudier than we thought. The global convection pattern can have effects, not only by changing where the plasma comes from, but also via electric field heating effects. Likewise, the mesoscale high-speed flows can act, not only by electric field heating effects, but also by changing where the plasma comes from. It is not clear at this point which is the rule and which the exception: whether these mechanisms dominate over each other or act together in a complex and intertwined manner.

While we have successfully simulated the type of *F* region structuring observed on a particular day, what is obviously missing is the critical connection from actual observed ion drifts to inferred global time-dependent convection to observed *F* region structure. We used F8 data to infer a time-dependent pattern, but it failed to reproduce the large-scale behavior of the data. We used the model tools available to us to construct a time-dependent pattern that could reproduce the large-scale behavior of the data, but we have not shown that it is a pattern that has much to do with what the actual pattern was. There are several things we can do to fill in the missing connection. On this particular day

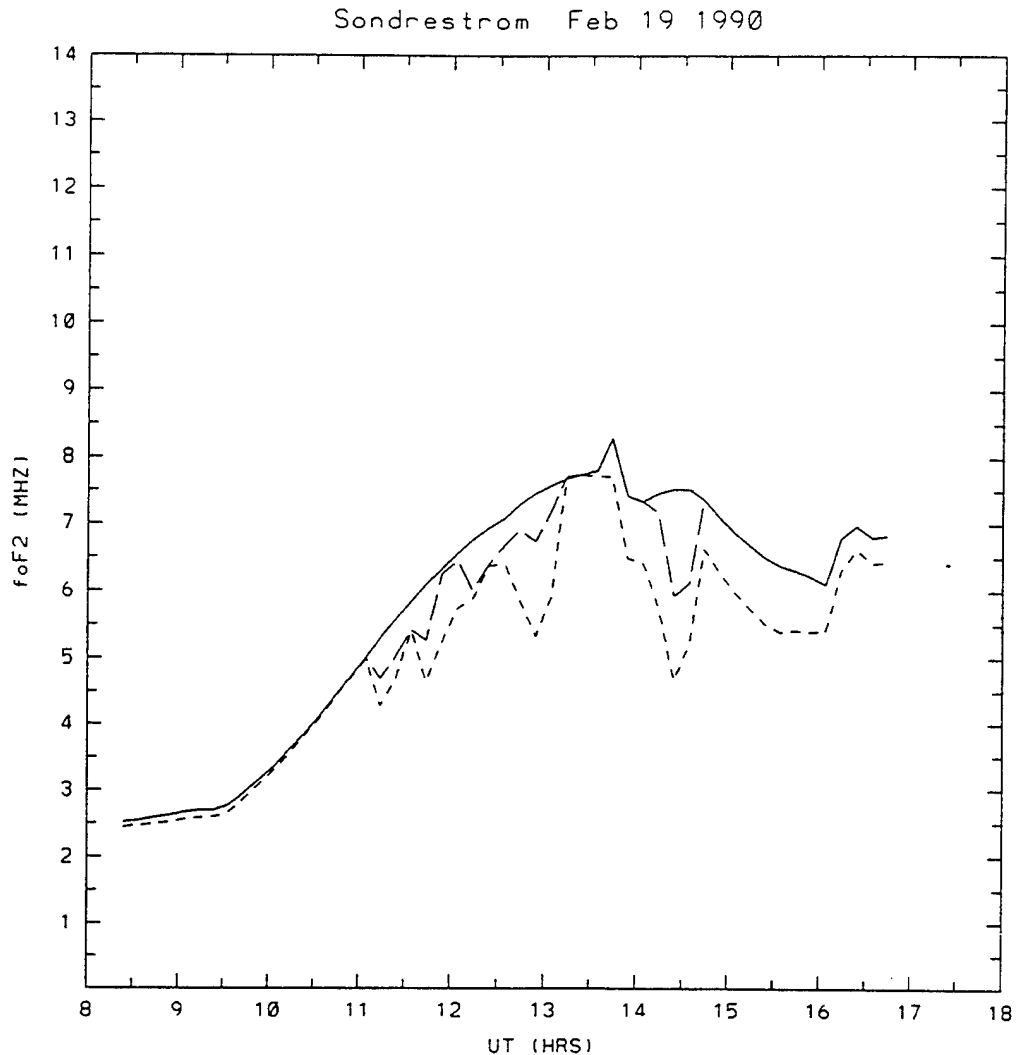


Figure 11. The simulated critical frequency of the F_2 peak (f_oF_2) in megahertz as a function of universal time at Sondrestrom, Greenland, on February 19, 1990. The solid curve is from the simulation using a sequence of six magnetospheric convection patterns with the heating due to electric fields turned off. The long dashed curve is from a simulation that also has the heating turned off and uses the same sequence of six magnetospheric convection patterns but also includes the five high-speed flow events. The short dashed curve uses the same six patterns and five events but has the heating due to electric fields turned on (also shown in Figure 8).

there were DMSP F9 satellite passes that we have yet to take advantage of. (F9 also misses the afternoon but does pass over at around 1000 LT.) We have also not taken full advantage of the radar data. To date, we have only used it to compare with patterns we are using but not to infer those patterns. Another potential source of drift information are the Sondrestrom and Qaanaaq digisondes that on February 19 did make drift measurements interspersed

with their density measurements. Clearly, we would like to use all these sources along with the full temporal behavior of the IMF to construct a time-dependent convection pattern. To do this will require more flexible convection models than we had available for this study. One of us (R. A. Heelis) has been developing such a model that contains fewer of the approximations in the present Hairston and Heelis model as well as greater flexibility.

Even if we do everything we have just described, on this particular day we may still find ourselves in great difficulty due to the large IMF variability. However successful we may or may not be with this data set, substantial progress in modeling actual observations will require more experiments designed to obtain *F* region convection and density data at high spatial and temporal resolution, ideally during periods of steady B_z south, with perhaps some interesting but not too exotic B_y variations.

Besides attempting to model actual observations, theoretical studies on critical aspects of the convection patterns time behavior will continue, that is, theoretical studies of various detailed scenarios. In one such study [Sojka et al., 1993] we found that the B_y dependence of the convection pattern can play a critical role in large-scale *F* region structuring. A follow-up study by J. J. Sojka et al. (Patches in the polar ionosphere: UT and seasonal dependence, submitted to *Journal Geophysical Research*, 1993) has studied the UT and seasonal dependence of this scenario. However, these two studies have thus far created structure mostly in the nightside polar cap and auroral oval. Many questions remain concerning the creation of *F* region structure in the cusp and dayside polar cap, the precise region that this paper has been concerned with. Also in this paper we have focused exclusively on the convection pattern, but there are other model inputs which need to be studied as sources of *F* region structure. In particular, the role of particle precipitation needs to be clarified. Of special interest is particle precipitation in the cusp and/or cleft as a potential source of ionization just before the plasma is swept into the polar cap by the high-latitude convection pattern. This mechanism will be a topic of future studies using our high-latitude *F* region model.

Acknowledgments. We would like to thank Jurgen Buchau and Ed Weber for interesting and useful discussions. The work at Boston College was partially supported by Phillips Laboratory contracts F19628-88-K-0008, F19628-89-K-0001, F19628-90-K-0007, and F19628-93-K-0001, and by NSF grants ATM-9000273 and ATM-9016465. At the University of Texas at Dallas this research was supported by the Phillips Laboratory contract F19628-90-K-0001. Finally, we want to gratefully acknowledge the contributions of Jurgen Buchau, who died suddenly on August 9, 1993. Jurgen's observations of high-latitude density structures are the foundation of our current understanding of polar cap patches. Many of the themes and ideas explored in this paper came directly

from both his papers and the many discussions we had with him. All of us, both experimentalists and modelers alike, will miss him greatly.

References

- Anderson, D. N., Daily variation of the ionospheric *F*2 equatorial anomaly in the American and Asian sectors, *NCAR Coop. Thesis*, 24, 1-144, 1971.
- Anderson, D. N., A theoretical study of the ionospheric *F* region equatorial anomaly, I, Theory, *Planet. Space Sci.*, 21, 409, 1973.
- Anderson, D. N., J. Buchau, and R. A. Heelis, Origin of density enhancements in the winter polar cap ionosphere, *Radio Sci.*, 23, 513, 1988.
- Buchau, J. E., and B. W. Reinisch, Electron density structures in the polar *F* region, *Adv. Space Res.*, 11(10), 29, 1991.
- Buchau, J. E., B. W. Reinisch, E. J. Weber, and J. G. Moore, Structure and dynamics of the winter polar cap *F* region, *Radio Sci.*, 18, 995, 1983.
- Buchau, J. E., E. J. Weber, D. N. Anderson, H. C. Carlson, Jr., J. G. Moore, B. W. Reinisch, and R. C. Livingston, Ionospheric structures in the polar cap: Their origin and relation to 250-MHz scintillation, *Radio Sci.*, 20, 325, 1985.
- Chakrabarti, S., R. Kimble, and S. Bowyer, Spectroscopy of the EUV (350-1400 Å) nightglow, *J. Geophys. Res.*, 89, 5660, 1984.
- de la Beaujardiere, O., J. D. Craven, V. B. Wickwar, G. Candal, J. M. Holt, L. A. Frank, L. H. Brace, D. S. Evans, and J. D. Winningham, Universal time dependence of nighttime *F* region densities at high latitudes, *J. Geophys. Res.*, 90, 4319, 1985.
- Foster, F., Plasma transport through the dayside cleft: A source of ionization patches in the polar cap, in *Electromagnetic Coupling in the Polar Clefts and Caps*, edited by P. E. Sandholt and A. Egeland, pp. 343-354, Kluwer Academic, Norwell, Mass., 1989.
- Hairston, M. R., and R. A. Heelis, Model of the high-latitude ionospheric convection pattern during southward interplanetary magnetic field using DE-2 data, *J. Geophys. Res.*, 95, 2333, 1990.
- Hardy, D. A., M. S. Gussenhoven, R. R. Raistrick, and W. J. McNeil, Statistical and functional representations of the pattern of auroral energy flux, number flux, and conductivity, *J. Geophys. Res.*, 92, 12,275, 1987.
- Hedin, A. E., MSIS-86 thermospheric model, *J. Geophys. Res.*, 92, 4649, 1987.
- Hedin, A. E., N. W. Spencer, and T. L. Killeen, Empirical global model of upper thermosphere winds based on atmosphere and Dynamics Explorer satellite data, *J. Geophys. Res.*, 93, 9959, 1988.
- Hedin, A. E., M. A. Biondi, R. G. Burnside, G. Hernandez, R. M. Johnson, T. L. Killeen, C. Mazaudier, J. W.

- Meriwether, J. E. Salah, R. J. Sica, R. W. Smith, N. W. Spencer, V. B. Wickwar, and T. S. Virdi, Revised global model of thermosphere winds using satellite and ground-based observations, *J. Geophys. Res.*, **96**, 7657, 1991.
- Heelis, R. A., J. K. Lowell, and R. W. Spiro, A model of the high-latitude ionospheric convection pattern, *J. Geophys. Res.*, **87**, 6339, 1982.
- Heppner, J. P., and N. C. Maynard, Empirical high-latitude electric field models, *J. Geophys. Res.*, **92**, 4467, 1987.
- Hinteregger, H. E., K. Fukui, and B. R. Gilson, Observational, reference and model data on solar EUV, from measurements on AE-E, *Geophys. Res. Lett.*, **8**, 1147, 1981.
- Kelley, M. C., J. F. Vickrey, C. W. Carlson, and R. Torbert, On the origin and spatial extent of high-latitude *F* region irregularities, *J. Geophys. Res.*, **87**, 4469, 1982.
- Killeen, T. L., R. G. Roble, and N. W. Spencer, A computer model of global thermospheric winds and temperatures, *Adv. Space Res.*, **7**, 10,207, 1987.
- Knudsen, W. C., Magnetospheric convection and the high-latitude *F*₂ ionosphere, *J. Geophys. Res.*, **79**, 1046, 1974.
- Knudsen, W. C., P. M. Banks, J. D. Winningham, and D. M. Klumpp, Numerical Model of the Convecting *F*₂ Ionosphere at High Latitudes, *J. Geophys. Res.*, **82**, 4784, 1977.
- Lockwood, M., and H. C. Carlson, Jr., The production of polar cap electron density patches by transient magnetopause reconnection, *Geophys. Res. Lett.*, **19**, 1731, 1992.
- Moffett, R. J., The equatorial anomaly in the electron distribution of the terrestrial *F* region, *Fundamental of Cosmic Physics*, **4**, 313, 1979.
- Rasmussen, C. E., R. W. Schunk, and J. J. Sojka, Effects of different convection models upon the high-latitude ionosphere, *J. Geophys. Res.*, **91**, 6999, 1986.
- Richards, P. G., and D. G. Torr, Ratios of photoelectron to EUV ionization rates, *J. Geophys. Res.*, **93**, 4060, 1988.
- Robinson, R. M., R. T. Tsunoda, J. F. Vickrey, and L. Guerin, Sources of *F* region ionization enhancements in the nighttime auroral zone, *J. Geophys. Res.*, **90**, 7533, 1985.
- Schunk, R. W., A mathematical model of the middle and high-latitude ionosphere, *Pure Appl. Geophys.*, **127**, 255, 1988.
- Schunk, R. W., and J. J. Sojka, A theoretical study of the lifetime and transport of large ionospheric density structures, *J. Geophys. Res.*, **92**, 12,343, 1987.
- Schunk, R. W., W. J. Raitt, and P. M. Banks, Effect of electric fields on the daytime high-latitude *E* and *F* regions, *J. Geophys. Res.*, **80**, 3121, 1975.
- Sojka, J. J., Global scale, physical models of the *F* region ionosphere, *Rev. Geophys.*, **27**, 371, 1989.
- Sojka, J. J., M. D. Bowline, R. W. Schunk, D. T. Decker, C. E. Valladares, R. Sheehan, D. N. Anderson, and R. A. Heelis, Modeling polar cap *F* region patches using time varying convection, *Geophys. Res. Lett.*, **20**, 1783–1786, 1993.
- Sojka, J. J., and R. W. Schunk, A theoretical study of the production and decay of localized electron density enhancements in the polar ionosphere, *J. Geophys. Res.*, **91**, 3245, 1986.
- Sojka, J. J., and R. W. Schunk, Theoretical study of the high-latitude ionosphere's response to multicell convection patterns, *J. Geophys. Res.*, **92**, 8733, 1987.
- Sojka, J. J., and R. W. Schunk, A model study of how electric field structures affect the polar cap *F* region, *J. Geophys. Res.*, **93**, 884, 1988.
- Strobel, D. F., and M. B. McElroy, The *F*₂-layer at middle latitudes, *Planet. Space Sci.*, **18**, 1181, 1970.
- Todd, H., B. J. I. Bromage, S. W. H. Lockwood, A. P. van Eyken, and D. M. Willis, EISCAT observations of bursts of rapid flow in the high-latitude dayside ionosphere, *Geophys. Res. Lett.*, **13**, 910, 1986.
- Valladares, C. E., Su. Basu, J. Buchau, and E. Friis-Christensen, Experimental evidence for the formation and entry of patches into the polar cap, *Radio Sci.*, this issue.
- Weber, E. J., J. Buchau, J. G. Moore, J. R. Sharber, R. C. Livingston, J. D. Winningham, and B. W. Reinisch, *F* layer ionization patches in the polar cap, *J. Geophys. Res.*, **89**, 1683, 1984.
- Weber, E. J., J. A. Klobuchar, J. Buchau, H. C. Carlson, Jr., R. C. Livingston, O. de la Beaujardiere, M. McCready, J. G. Moore, and G. J. Bishop, Polar cap *F* layer patches: Structure and dynamics, *J. Geophys. Res.*, **91**, 12,121, 1986.
- D. N. Anderson, Phillips Laboratory, Geophysics Directorate, Hanscom AFB, MA 01731.
- Su. Basu, National Science Foundation, Aeronomy Program, Room 644, 1800 G Street, NW, Washington, DC 20550.
- D. T. Decker, Institute for Space Research, Boston College, Newton, MA 02159.
- R. A. Heelis, Center for Space Research, University of Texas at Dallas, Dallas, TX 75083-0688.
- R. Sheehan, Institute for Space Research, Boston College, Newton, MA 02159.
- C. E. Valladares, Institute for Space Research, Boston College, Newton, MA 02159.

(Received January 26, 1993; revised July 26, 1993; accepted October 3, 1993.)

Modeling Boundary Blobs Using Time Varying Convection

David N. Anderson

Ionospheric Effects Division, Phillips Laboratory, Hanscom AFB MA

Dwight T. Decker and Cesar E. Valladares

Institute for Scientific Research, Boston College, Newton, MA

Abstract. The Global Theoretical Ionospheric Model (GTIM) has been used to study a mechanism which generates F-region electron density enhancements known as boundary blobs. The model calculates the O^+ density as a function of altitude, latitude, and local time. It includes the effects of production of ionization by solar extreme ultraviolet radiation and electron precipitation; loss through charge exchange with N_2 and O_2 ; and transport by diffusion, neutral winds, and ExB convection drifts. Using time-dependent convection patterns that previously were used to study polar cap patch formation, it was found that patches can be convected out of the polar cap and swept sunward by the dusk convection cell. The resulting structures have many of the features associated with boundary blobs; extended in local time and altitude, narrow in latitude, located in the return flow region of the aurora, and densities up to a factor of 8 over background. These results are the first quantitative, first principles verification and extension of the trajectory modeling of Robinson *et al.*, (1985).

1. Introduction

"Boundary Blob" is the name that has been given to enhanced ionospheric F region plasma densities which have been observed to exist near the equatorward edge of the auroral oval, primarily in the late afternoon and evening hours before midnight [Bates *et al.*, 1973; Rino *et al.*, 1983; Weber *et al.*, 1985]. The term boundary blob was coined by Jim Vickrey (private communication, 1994) and they are most easily observed during elevation scans of incoherent scatter radar measurements such as reported by Rino *et al.* [1983] using the Chatanika radar. Figure 1 is an example of boundary blobs observed on Nov. 11, 1981, and it can be seen that one of the characteristic features is their very narrow latitude structure which extends in altitude. Boundary blobs also extend over large distances in longitude and can persist for many hours. Figure 2, from the paper by Rino *et al.* [1983], displays the location of a boundary blob as a function of local time on Nov. 11, 1981. On this day, blobs persisted for more than 12 hours. In recent years, there has been growing evidence that there is a cause and effect relationship between macroscopic features such as blobs and the irregularities that are responsible for radio wave scintillations. This suggests that the quantitative modeling of such macroscale features as boundary blobs will be crucial in any National Space Weather Program that includes the goal of

specifying and forecasting F region irregularities. An excellent review of the observations, suggested sources, and modeling of boundary blobs can be found in Tsunoda's 1988 Reviews of Geophysics article on "High-Latitude F region Irregularities: A Review and Synthesis".

It is generally accepted that the source of boundary blobs is the reconfiguration of polar cap patches of enhanced ionization as they convect anti-sunward across the polar cap and then are distorted by the two-cell convection pattern which causes sunward flow at lower latitudes in the evening sector. Polar cap patches themselves have been shown to be high density plasma produced by solar radiation in the daylit region equatorward of the "cusp" which is then structured as it is convects through the cusp and across the polar cap (200-1000 m/sec) into the midnight sector. The formation of these patches will be discussed briefly in the next section. Robinson *et al.* [1985] investigated how the restructuring of patches into blobs takes place by performing a trajectory tracing calculation using a two-cell ($B_z < 0$) convection pattern. In this calculation, they defined a circular region that straddled both the evening and morning cells of the convection pattern and showed how this circle over a three hour period convected into an extremely elongated structure in longitude and very narrow in latitude. While they did not actually calculate electron densities inside and outside the region, they did demonstrate that a region in the shape of a circular patch could evolve into the shape of a blob.

Weber *et al.* [1985] demonstrated through a coordinated campaign involving an airborne all sky imaging photometer, the Chatanika incoherent scatter radar and DMSP overflights, that soft energetic particle precipitation need not be the primary source for boundary blobs. To date there has not been a definitive study which has demonstrated, theoretically or quantitatively, that boundary blobs with their characteristic narrow latitude extent and long longitude extent evolve from polar cap patches and are intimately connected and follow naturally from patch formation mechanisms. We demonstrate this natural evolution quantitatively in this paper.

2. Theoretical Approach

To study the formation of boundary blobs, theoretically, we use the Global Theoretical Ionospheric Model (GTIM) developed at Phillips Laboratory/Geophysics Directorate and described by Decker *et al.* [1994]. GTIM calculates electron density profiles as a function of latitude, local time and longitude by solving the coupled ion (O^+) continuity and momentum equations numerically. Since this model calculates only ion and electron densities and is not self-consistently coupled to thermospheric calculations, a number of inputs to GTIM are required. These include neutral

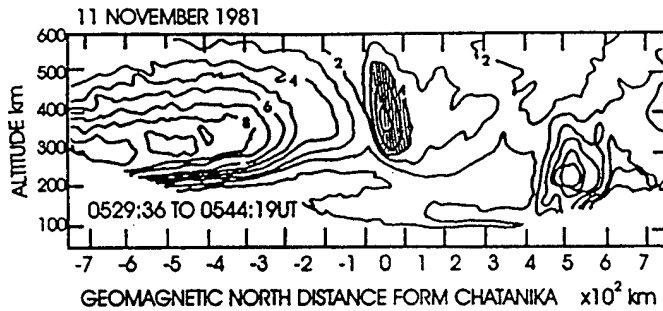


Figure 1: Plasma density contours ($\times 10^5$ el/cm³) measured by Chatanika radar (elevation scans) on 11 November, 1981. Shaded contours represent a boundary blob (after Rino et al., 1983)

atmospheric densities, winds and temperatures; solar and energetic particle ionization rates; diffusion and loss rates and transport by convection $E \times B$ drift velocities. Because we wish to study the formation of boundary blobs as a natural consequence of the formation of polar cap patches, we will utilize an already successful patch-generating investigation which was carried out using GTIM and published in a joint Geophysical Research Letters paper with colleagues at Utah State University [Sojka et al., 1993].

Briefly, it was demonstrated that polar cap patches could be formed by imposing a time-dependent variation in the two-cell $E \times B$ convection pattern which reflected a change in the Interplanetary Magnetic Field (IMF) B_y component, where B_y was initially positive (> 0), then switched to $B_y < 0$ for one and a half hours and then switched back to $B_y > 0$. Figure 3 presents polar cap potential contours for $B_y < 0$ and $B_y > 0$ from the Hairston and Heelis [1990] model assuming a cross polar cap potential of 80 kV and a polar cap radius of 12 degrees. The reader is referred to the paper by Sojka et al. [1993] for a description of the model inputs and the resulting patch formation and a discussion of calculated F region peak densities ($N_m F_2$) inside and outside the patches which were produced.

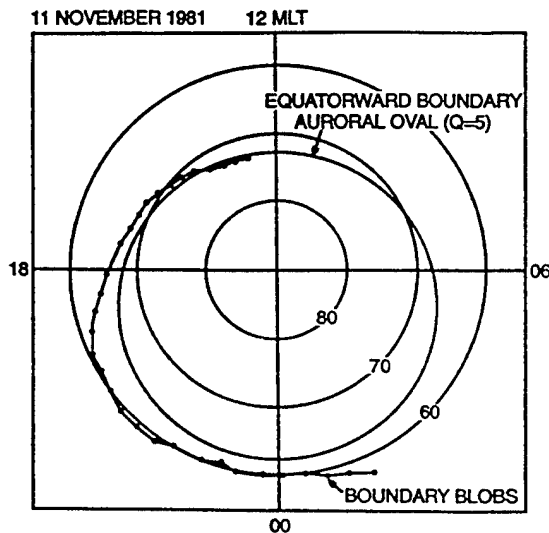


Figure 2: Location of boundary blobs as a function of MLT and MLAT measured by Chatanika radar on 11 November, 1981 (after Rino et al., 1983)

We plot in Plate 1 color-coded $N_m F_2$ values at 2030 UT and 2130 UT showing the polar cap density structures which result when B_y was switched from positive to negative at 1700 UT and back to positive at 1830 UT. These two plots present $N_m F_2$ values as a function of corrected geomagnetic latitude and local time 2 and 3 hours, respectively, after the B_y component was returned to its initial 8 nT value. Notice the existence of a longitudinally-long and latitudinally-narrow band of enhanced $N_m F_2$ values in the evening sector at auroral boundary latitudes of about 65 to 70 degrees magnetic latitude. This narrow band is the distorted remnant of what was a tongue of ionization that was caught up in the evening convection cell when B_y was switched from negative to positive. A detailed understanding of how individual regions of enhanced plasma developed cannot be readily determined from these two snapshots but requires analyzing individual trajectories that result from the time-dependent convection. Such an analysis will be the subject of another paper, in this paper it is the features of this band that we wish to investigate in greater detail.

3. Model Results

The inputs to GTIM and the conditions for generating polar cap patches as described by Sojka et al. [1993] are identical to the inputs and conditions for investigating boundary blobs in this study. The only difference is in the number of flux-tubes

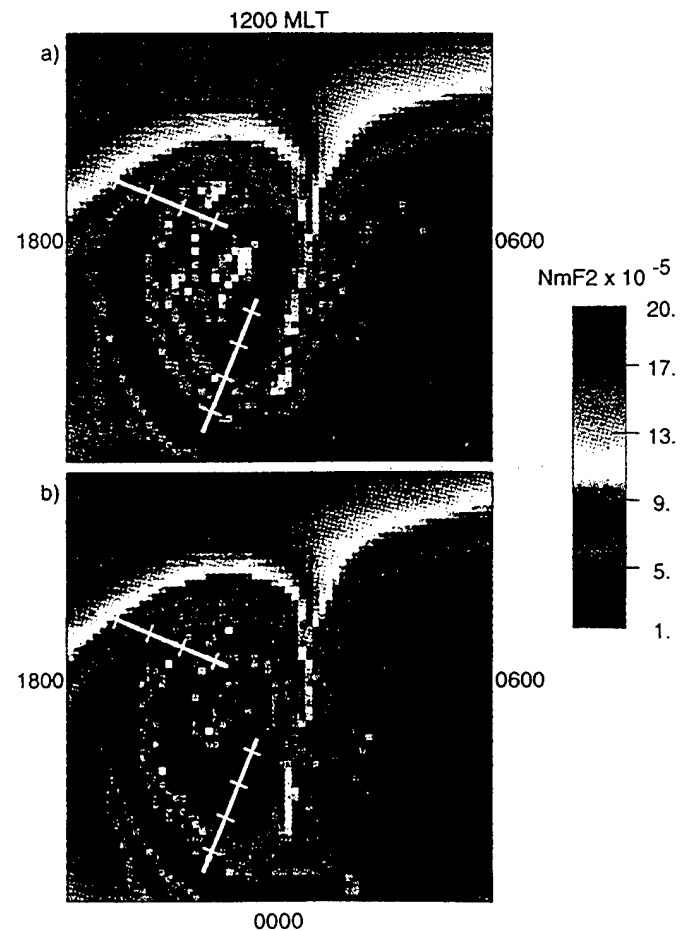


Plate 1: Contours of $N_m F_2$ at (a) 2030 and (b) 2130 UT as a function of MLT and MLAT from simulation reported in Sojka et al. (1993). See paper for details.

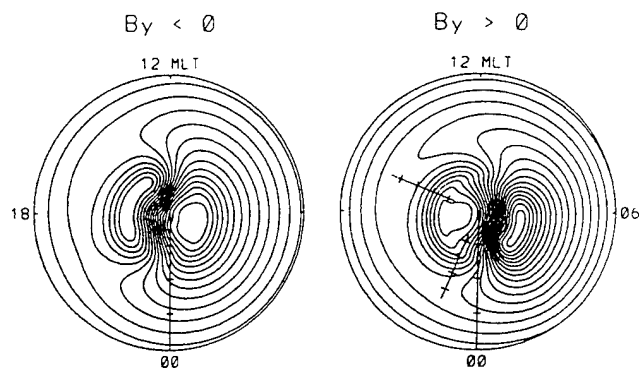


Figure 3: Hairston and Heelis [1990] convection patterns with corotation added for IMF B_z southward, where IMF $B_y = -8$ gamma (left panel) and IMF $B_y = 8$ gamma (right panel). The cross polar cap potential is 80 kV and the polar cap radius is 12 degrees. The contours are drawn at 4 kV intervals and are shown in a corrected magnetic latitude (50° - 90°) and magnetic local time polar plot.

that are followed as they convect within the high latitude/polar cap region by ExB drift. For this study and the subsequent figures which appear in this section, the latitudinal resolution is 0.2 degrees in magnetic latitude. The resolution in Plate 1, similar to that from the *Sojka et al.* paper, is on the order of one degree. Plate 1 displays the gross structure of $N_m F_2$ over the entire high latitude/polar cap region above 60° cgmlat at 2030 and 2130 UT. The figures that display our calculated boundary blobs will be contours of O^+ ion density as a function of altitude and latitude at two specified magnetic local times (MLT) and two Universal Times (UT), 2030 and 2130 UT, respectively. We then compare, in a general way, the calculated blob characteristics with those displayed in Figure 1 taken from *Rino et al.* [1983]. The location of these "latitude slices" are indicated in Figure 3 and Plate 1 as diagonal straight lines with tick marks in five degree steps from 65° to 80° .

Figure 4a and 4b show calculated O^+ density contours at 22.5 MLT at 2030 and 2130 UT, respectively. The highest density contour is $\log_{10}[O^+] = 5.6$ and the lowest contour is 4.0 where the density units are in ions/cm^3 . In Fig. 4a two

boundary blobs occur, centered at 65.5° and 68.5° magnetic latitude with peak densities inside each blob of about 8×10^5 ions/cm^3 and outside densities around 1×10^5 ions/cm^3 . Both the characteristic narrow latitude extent and the altitude extent of observed boundary blobs are captured in the calculated O^+ density contours. We have not tried to reproduce the conditions during the Chatanika elevation scans pictured in Figure 1 for this study, but simply wish to compare the general characteristics to demonstrate, quantitatively, that boundary blobs seem to naturally result from the formation of polar cap patches - at least when the patches are formed through a time-varying convection ExB drift pattern. In Figure 4b, one hour later in UT, the boundary blobs have moved slightly lower in latitude and are somewhat narrower. Also the density between the blobs is greater at roughly 2×10^5 ions/cm^3 .

Figure 5a and 5b now display calculated O^+ density contours at 16.5 MLT for UTs of 2030 and 2130, respectively. At this magnetic local time the blobs are at significantly greater latitudes and the solar produced ionosphere is readily apparent below 65° mag. lat. In this figure the maximum density contour is now 1×10^6 ions/cm^3 while the minimum is 1×10^4 ions/cm^3 . In Figure 5a two boundary blobs occur at 75° and 78.5° latitude and still have the narrow latitude extent of 1° to 2° and an enhanced altitude extent. In contrast, four blobs occur at 2130 UT and three of them are narrower and the one at 80° is wider. In the paper by *Rino et al.* they find that on Nov. 11, 1981 the boundary blobs move to higher magnetic latitude at earlier local times, in rough agreement with our findings.

4. Summary

While the observed characteristics of boundary blobs has been well documented and the source of these high latitude features has been proposed, qualitatively, in previous investigations, no quantitative, first-principles study which validated the suggested physical mechanisms has been carried out. We have shown in this paper, that many of the boundary blob characteristic features such as altitude extent, narrow latitude extent and elongated longitude/local time extent can be explained as a natural consequence of a) time dependent convection forming polar cap patches and b) the subsequent

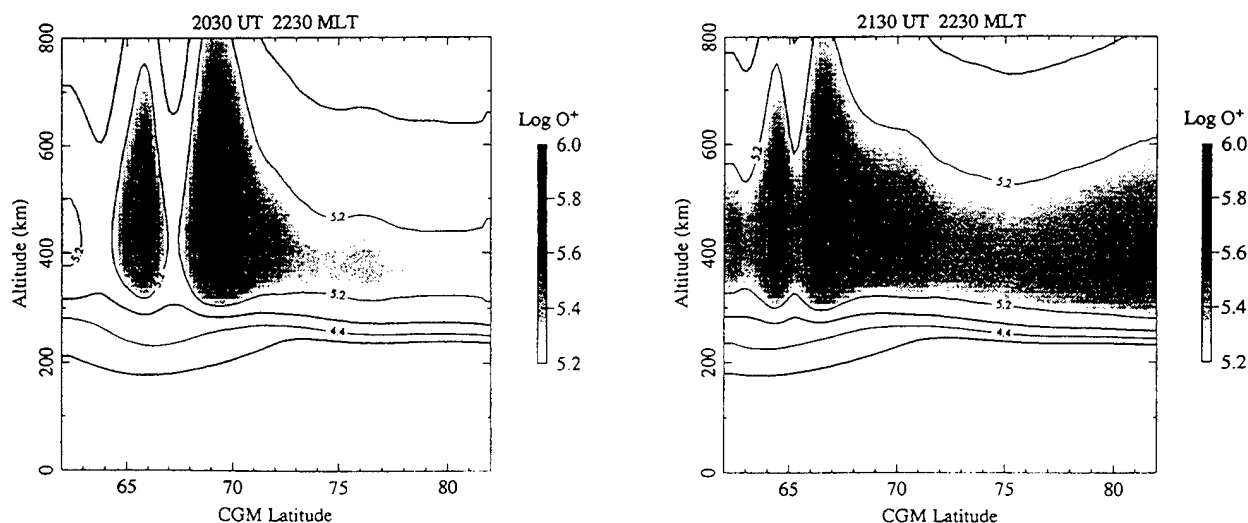


Figure 4: Calculated O^+ ion density contours at 2230 MLT as a function of corrected geomagnetic latitude and altitude for Universal Times of (a) 2030 hours and (b) 2130 hours. (see text for details)

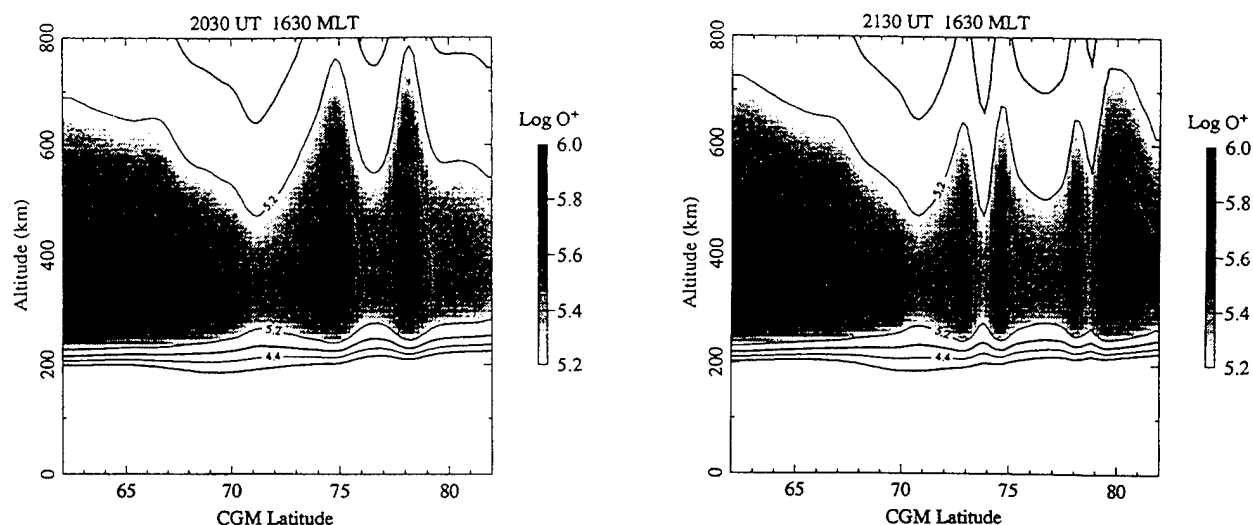


Figure 5: Calculated O^+ ion density contours at 1630 MLT as a function of corrected geomagnetic latitude and altitude for Universal Times of (a) 2030 hours and (b) 2130 hours. (see text for details)

deformation of these patches under the influence of a particular ExB convection pattern which causes the elongation of plasma density enhancements along the equatorward edge of the auroral boundary. In addition, the observation that the boundary blobs occur at higher magnetic latitudes at earlier local times is also reproduced in our simulations. The observed plasma density enhancements inside the boundary blobs compared to the density outside, about a factor of four or more, are also reproduced in these calculations.

It may be that polar cap patches are produced by other mechanisms such as a change in the polar cap radius as suggested by Anderson *et al.* [1988] and confirmed by subsequent calculations. However, once patches are formed in the dusk cell portion of a two cell convection pattern, then they will be distorted in such a way as to produce boundary blobs which extend primarily from midnight to the afternoon local time sector along the equatorward edge of the auroral boundary. While the design of our simulation favored producing blobs in the premidnight sector, one could design a simulation that would potentially produce postmidnight blobs. However, it is not at all clear whether one sector is favored over another. There are observations of blobs in both sectors, however most of the observations we are familiar with have been made in the premidnight sector. Further, while either sign of B_y is equally possible, corotation does introduce a basic asymmetry into the system. In order to resolve such issues, a study of the predicted morphology of boundary blobs will be a critical topic for future work. Finally, we should note that two other types of blobs have been identified in the literature [Tsunoda, 1988]. They are sub-auroral and auroral blobs and they are mainly identified by where they are found. Whether they are simply boundary blobs appearing in other locations or whether other processes are occurring is an open question. We want to emphasize that in this paper we have investigated just one scenario for making just one type of blob and that other scenarios for various blobs will be the subject of future work.

Acknowledgements. The work at Boston College was supported by Phillips Laboratory contracts F19628-93-K0001 and F19628-90-K-0007 and by NSF grant ATM-9404088.

References

- Anderson, D. N., J. Buchau, and R. A. Heelis, Origin of density enhancements in the winter polar cap ionosphere, *Radio Science*, 23, 513-519, 1988.
- Bates, H. F., A. E. Belon and R. D. Hunsucker, Aurora and the poleward edge of the main ionosphere trough, *J. Geophys. Res.*, 78, 648-658, 1973.
- Decker, D. T., C. E. Valladares, R. Sheehan, Su. Basu., D. N. Anderson and R. A. Heelis, Modeling daytime *F* layer patches over Sondrestrom, *Radio Science*, 29, 249-268, 1994.
- Hairston, M. R., and R. A. Heelis, Model of the high latitude ionospheric convection pattern during southward interplanetary magnetic field using DE-2 data, *J. Geophys. Res.*, 95, 2333-2343, 1990.
- Rino, C. L., R. C. Livingston, R. T. Tsunoda, R. M. Robinson, J. F. Vickrey, C. Senior, M. D. Cousins, J. Owen and J. A. Klobuchar, Recent studies of the structure and morphology of auroral zone *f* region irregularities, *Radio Science*, 18, 1167-1180, 1983.
- Robinson, R. M., R. T. Tsunoda and J. F. Vickrey, Sources of *F* region ionization enhancements in the nighttime auroral zone, *J. Geophys. Res.*, 90, 7533-7546, 1985.
- Sojka, J. J., M. D. Bowline, R. W. Schunk, D. T. Decker, C. E. Valladares, R. Sheehan, D. N. Anderson and R. A. Heelis, Modeling polar cap *F*-region patches using time varying convection, *Geophys. Res. Lett.*, 20, 1783-1786, 1993.
- Tsunoda, Roland T., High Latitude *F* Region Irregularities: A review and synthesis, *Reviews of Geophysics*, 26, 719-760, 1988.
- Weber, E. J., R. T. Tsunoda, J. Buchau, R. E. Sheehan, D. J. Strickland, W. Whiting and J. G. Moore, Coordinated measurements of auroral zone plasma enhancements, *J. Geophys. Res.* 90, 6497-6513, 1985.

D.N. Anderson, Phillips Laboratory, Geophysics Directorate(GPIM), 29 Randolph Rd., Hanscom AFB, MA 01731-3010. (e-mail: danderson@plh.af.mil)

D.T. Decker, Institute for Space Research, Boston College, 885 Centre St., Newton, MA 02159. (e-mail: decker@plh.af.mil)

C.E. Valladares, Institute for Space Research, Boston College, 885 Centre St., Newton, MA 02159. (e-mail: cesar@dlw7.bc.edu)

(Received April 5, 1995; accepted June 15, 1995.)